Université de Montréal

On the Binary Frequency of a Complete Sample of Magellanic, WC Wolf-Rayet Stars and a Spectroscopic Study of WC Binary Colliding Winds

par

Peter Bartzakos

Département de physique

Faculté des arts et des sciences

Thèse présentée à la Faculté des études supérieures
en vue de l'obtention du grade de
Philosophiæ Doctor (Ph.D.)
en physique.

Février, 1998

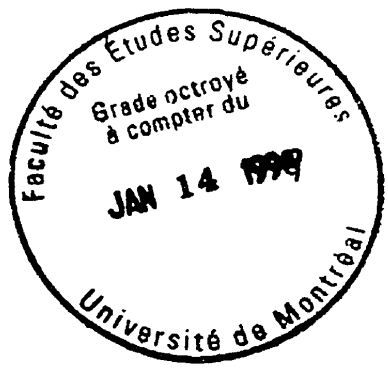

Université de Montréal
Faculté des études supérieures

Cette thèse intitulée:

On the Binary Frequency of a Complete Sample of Magellanic, WC Wolf-Rayet Stars and a Spectroscopic Study of WC Binary Colliding Winds

Présentée par:

Peter Bartzakos

a été évaluée par un jury composé des personnes suivantes:

M. le professeur Claude Carignan	président du jury
M. le professeur Anthony F.J. Moffat	directeur de recherche
Mme la professeur Nicole St-Louis	membre du jury
M. le professeur Douglas R. Gies	examinateur externe
M. le professeur Dennis Salahub	représentant du doyen

Thèse acceptée le: 13. 11. 1998

Abstract

A spectroscopic and photometric study of all 24 known WC/WO Wolf-Rayet stars of the Magellanic Clouds is made in an effort to determine the binary frequency of WR-stars in environments of low metallicity. This is followed by an investigation of colliding winds in those stars revealed to be binary.

Low metallicity has been postulated in the literature as the prime cause for the low WR/O number ratio in the Clouds. This follows from the fact that progenitor O-star winds at low Z have insufficient strength to repel the outer hydrogen envelope of all but the most massive, luminous O-stars. This removal is needed to produce a WR-star. Low-to-medium mass O-stars in low-Z environments require a companion to reduce their gravitational potential and thus ease the removal of the outer layers. By studying absolute magnitudes, line equivalent widths, and radial velocity variability, a binary frequency of only thirteen percent is found for the Large Magellanic Cloud. (The Small Cloud contains only one WC-star.) This is far less than the $52\% \pm 14\%$ frequency predicted by theory. The stellar winds appear powerful enough to accomplish the task themselves, even in a low-metallicity milieu.

As O-star winds are also strong, they should collide with the WR winds in WR+O binaries to form a bow-shaped shock front. The shocked material is heated to high temperature near its head, after which it flows along a shock cone that wraps around the weaker-wind O-star. Rapid cooling of the dense shock zone yields radiation much like that seen from the WR wind itself. Such excess emission is seen in many WR emission lines; it generally produces double-peaked spectral profiles that can be described by the model of Lührs. These

profiles depend on orbital phase, orbital plane inclination, streaming velocity of the shocked material and cone opening angle. Such profiles are modelled for CIII 5696 Å in Br22 (the only WC/WO system in the MC's to reveal significant CIII excess) in an attempt to determine these parameters. However, a Lührs' model fit to the observed CIII excess in Br22 gives only qualitative agreement. A new global approach proves more successful. The excess profile is characterised by the full width at half-maximum and mean velocity. A fit of the simplified Lührs' model in this case is used in an attempt to determine the cone parameters and orbital inclination. However, because of observational errors, the solution appears to be numerically degenerate in orbital inclination. The method, however, shows promise if more high-quality data can be used to reduce the noise. The presence of excess emission in the form of Lührs' profiles in the CIV 5808 Å line, present in all binaries of the sub-sample, shows that the colliding wind phenomenon is universal amongst close WC/WO binary stars.

Résumé

Introduction et motivation

Avec leurs spectres dominés par des fortes raies en émission, les étoiles Wolf-Rayet (WR) sont considérées comme des objets ayant atteint le stade ultime d'évolution stellaire, juste avant d'exploser en tant que supernova. Les raies d'émission sont le reflet d'une atmosphère en expansion sous forme d'un vent stellaire dense.

Une étoile WR est formée lorsqu'une étoile de type O évolue et perd son enveloppe d'hydrogène par l'entremise du vent stellaire engendré par la pression de radiation. Les produits de la nucléosynthèse stellaire comme l'hélium, l'azote, le carbone et l'oxygène sont ainsi exposés. Lorsque l'étoile a une abondance élevée en hélium et azote et faible en carbone et oxygène, elle est de sous-type WN. Celles plus évoluées qui montrent une abondance en carbone élevée (et faible en azote) sont de sous-type WC et les objets les plus évolués qui possèdent une abondance d'oxygène élevée sont désignés WO. Il est à noter qu'une étoile ne traverse pas nécessairement ces trois stades d'évolution avant de devenir un supernova.

Pour retirer l'enveloppe d'hydrogène, il faut que l'accélération du vent stellaire soit assez forte pour vaincre la force gravitationelle de l'étoile. Une façon d'engendrer un vent fort est d'avoir une étoile de grande masse. Un tel objet aura une plus grande luminosité et donc une pression de radiation plus élevée. Une masse initiale élevée favorise donc la formation des étoiles WR.

On devrait avoir un vent plus fort si la métallicité de l'étoile est plus grande. Si l'abondance en métaux de l'atmosphère est plus élevée, elle peut absorber plus efficacement la quantité de mouvement que les photons lui transmettent, étant

donné qu'elle est alors plus opaque. On a ainsi un vent plus fort. Conséquemment, la formation des étoiles WR devrait être favorisée par un milieu plus riche en métaux.

Les Nuages de Magellan sont beacoup moins riches en métaux que la Voie Lactée. Pour le Grand Nuage de Magellan, on a une métallicité de $Z = 0.006$ et pour le Petit Nuage de Magellan on a $Z = 0.002$. La Voie Lactée, quant à elle, a une métallicité de $Z = 0.02$ dans le voisinage solaire.

Une étoile O qui n'est pas assez massive ou riche en métaux pour devenir WR n'est pas nécessairement vouée à éviter la phase WR. Selon Maeder (1982, 1991) un tel objet pourrait devenir WR s'il a un compagnon proche dans un système binaire. Le compagnon réduit, effectivement, le potentiel gravitationel de l'étoile, lui permettant ainsi de perdre son enveloppe plus rapidement pour atteindre la phase WR.

Avec la théorie d'évolution à l'intérieur d'un système binaire de Maeder & Meynet (1994), on prédit qu'au moins $52\% \pm 14\%$ des étoiles WR devraient être binaires dans le Grand Nuage de Magellan pour exister comme WR à cause de sa faible métallicité. En fait, toutes les étoiles WR devraient être binaires dans le Petit Nuage de Magellan.

Puisque les étoiles O ont des vents stellaires relativement forts (mais tout de même environs un ordre de grandeur moins puissant que ceux des étoiles WR), un autre phénomène pourrait se produire dans un système binaire WR+O: la collision des vents stellaires. Dans ce cas, la matière peut même être expulsée hors du système.

Vue la faible métallicité du Grand Nuage de Magellan, il est improbable d'y trouver beaucoup d'étoiles WR simples puisqu'il faut des étoiles très massives (masse initiale plus grande que $50\,M_\odot$), qui sont relativement rares. Cependant, on a plus de cent étoiles WR dans cette galaxie. Est-ce qu'on y trouve vraiment 52% de systèmes binaires?

On peut tenter de répondre à cette question en étudiant la fréquence binaire d'un sous-échantillon complet d'étoiles WR. Dans le Grand Nuage de Magellan,

par exemple, on a 23 étoiles WC/WO, presque toutes du type WC4 et toutes formées dans le même environnement de basse métallicité où il faut une étoile très massive pour former une étoile de type Wolf-Rayet.

On peut, en plus, chercher des vents en collision parmi les étoiles binaires que l'on découvre. La perturbation introduite par ce phénomène devrait avoir un effet important sur la forme des raies spectrales. En étudiant leur variation en fonction du temps, on pourra déterminer des paramètres de la collision et même de l'orbite, comme son inclinaison.

À l'aide d'observations spectroscopiques et photométriques, on étudie donc la fréquence binaire des étoiles WC/WO du Grand Nuage de Magellan et les collisions des vents des étoiles binaires trouvées. On inclut dans cette étude la seule étoile WC/WO du Petit Nuage de Magellan ainsi que les deux étoiles WC/WO de la Voie Lactée les plus évoluées, pour comparaison.

Données et fréquence binaire

Les données spéctroscopiques ont été obtenues durant trois missions d'observation: une en 1984 et deux en 1993. Ces données furent traitées avec le logiciel IRAF pour produire des spectres calibrés et redressés au continu.

Les données photométriques furent prises par observation de service en 1994 et 1995. Ces images furent traitées avec IRAF pour séparer photométriquement les étoiles multiples apparentes dans le ciel et déterminer les magnitudes apparentes des étoiles. On trouva ensuite les magnitudes absolues, en tenant compte des raies d'émission.

Ces résultats furent utilisés pour calculer la fréquence binaire. On chercha les étoiles plus brillantes qu'attendu pour un type spectral donné, indiquant une contribution d'un compagnon. Puisque la lumière du continu d'une autre étoile diluerait l'intensité des raies d'emission des étoiles WR, on chercha des largeurs equivalentes de raies plus basses que prévues. Finalement, on devrait s'attendre à ce que l'écart-type des vitesses radiales soit élevé pour un système binaire, dû au

mouvement orbital. On compara aussi les variations de la vitesse radiale moyenne entre les époques pour la détection des étoiles binaires à plus longue période.

On trouva que seulement trois des 23 étoiles étudiées dans le Grand Nuage de Magellan sont binaires (ces trois étaient déjà connues avant cette étude). Ceci représente une fréquence de binaires de seulement 13%, ce qui est clairement incompatible avec la théorie. Il semble que les vents stellaires soient assez forts pour vaincre la gravitation même dans un environnement de basse métallicité.

Vents en collision

Puisque les compagnons de type O des étoiles WR ont aussi des vents forts, on s'attend à trouver des indices de vents en collision. Étant donné que le vent WR possède une plus grande quantité de mouvement que celui de l'étoile O, la surface du choc en forme de cône devrait être courbée autour de l'étoile O.

On s'attend à une température élevée à la tête de ce cône, soit plusieurs dizaines de millions de degrés K. La matière chaude, étant très dense, se refroidit en se déplaçant le long du cône et ce faisant émet de la radiation (en excès de celle qu'on s'attend à avoir avec une étoile simple) qui correspond à la température donnée. D'autres chercheurs ont trouvé de l'émission rayons-X qui varie avec la phase et des perturbations des raies ultravioletes et visibles. On a expliqué ces émissions par des vents en collision. On a trouvé aussi de l'émission infrarouge au périastre des binaires WC à longue période que l'on explique par la compression de la matière en poussière de carbone par les vents en collision. On a même fait, récemment, de l'imagerie radio de plusieurs systèmes WR+O ou O+O, où l'on détecte la tête d'une onde de choc de forme conique formée par une collision de vent.

On a postulé que l'onde de choc prendrait la forme d'un cône en trois dimensions autour de l'étoile O. Sur ce cône, le matériel ayant traversé le choc s'écoule et les ions se recombine, émettant ainsi de la radiation. Si on suppose qu'un type donné d'ions est distribué dans une bande optiquement mince sur le

cône d'épaisseur non-négligeable, les photons qu'ils émettront produiront un profil spectral avec deux pics situés près des ailes de la raie (similaire en apparence au profil par un anneau en expansion ou un disque en rotation). Nous appellerons ceci un profil de Lührs.

Ce profil de Lührs varie en forme, en position et en longueur d'onde avec la phase orbitale, l'inclinaison du système dans le ciel, la vitesse d'écoulement de la matière émettrice et l'ouverture du cône. En principe, on devrait être capable de déduire tous ces paramètres en ajustant le profil de Lührs aux données spectrales de la raie.

Après avoir ajusté une courbe sinusoïdale aux données de vitesse radiale pour trouver les périodes orbitales des binaires, on tenta un ajustement au profil de Lührs pour la raie très variable de CIII 5696 Å de l'étoile Br22 dans le Grand Nuage de Magellan. Le modèle explique bien le mouvement translationel en longueur d'onde de cette raie mais semble incapable de reproduire les pics des profils à certaines phases orbitales. Il est possible qu'à certaines phases orbitales, l'émission d'un pic devient saturée et donc dominée par rapport au cas optiquement mince.

On abandonna la méthode mentionnée ci-dessus pour une autre plus robuste, qui tente de déterminer la vitesse d'écoulement, l'ouverture du cône de choc et l'inclinaison orbitale selon la variation orbitale de la largeur à mi-hauteur et de la position moyenne de la raie émise par le cône. Aprés avoir soustrait un profil de base dérivé du minimum de tous les profils de la raie de CIII 5696 Å pour les étoiles Br22 et WR9 (les deux objets étudiés présentant de telles raies fortes), on ajusta une courbe à la largeur à mi-hauteur. Lorsque l'on ajusta la courbe en gardant l'inclinaison comme paramètre libre, on trouva des erreurs très grandes et des vitesses d'écoulement plus rapides que celle du vent stellaire. Quand l'inclinaison fut fixée, par contre, on obtint des valeurs plus raisonnables. Il semble que la solution de l'ajustement soit presque dégenerée numériquement en inclinaison.

Finalement, on essaya d'identifier des profils de Lührs pour la raie de CIV 5808 Å (une raie forte dans toutes les étoiles binaires). On enleva un profil minimum et on trouva des résidues montrant des profils déformés attendus qui varient

qualitativement selon la théorie dans tous ces objets.

Conclusion

Parmi les étoiles WC/WO du Grand Nuage de Magellan, on trouve une fréquence binaire de seulement 13%, ce qui est beaucoup moins élevée que la fréquence de 52% prédite par la théorie pour former des étoiles WR dans un milieu de faible métallicité. Il semble que les vents stellaires des étoiles de type O ont tout de même un taux de perte de masse suffisamment élevé — facteur obligatoire pour la transformation en WR. Ceci reste à confirmer en étudiant les étoiles plus nombreuses de type WN.

Ces vents forts semblent former des ondes de choc dues à des collisions. Un modèle de profil de Lührs a le potentiel d'expliquer la forme du choc et les profils spectraux produits en conséquence. Un essai avec ajustement du profil théorique ne réproduit pas adéquatement les détails des profils observationels. Un modèle plus simple basé sur la variation orbitale de la largeur à mi-hauteur et de la moyenne de l'excès d'émission semble d'avoir des solutions numériquement dégenerées pour l'inclinaison orbitale mais a démontré du potentiel. Il faudra des données plus nombreuses pour réduire le bruit observationel pour utiliser à l'avenir cette méthode prometteuse.

À cause de la détection de profils de Lührs pour le CIV dans toutes les étoiles WC/WO binaires étudiées, on peut conclure que le phénomène de vents en collision soit universel pour des systèmes WC/WO binaires dont la séparation des composantes est petite.

Contents

List of Tables

List of Figures

List of Abbreviations

CASLEO *Complejo Astronómico El Leoncito*

CCD Charge-coupled device

CTIO Cerro Tololo Inter-American Observatory

FWHM Full-width at half-maximum

HST Hubble Space Telescope

LMC Large Magellanic Cloud

MC Magellanic Cloud

PSF Point-spread function

RV Radial velocity

RLOF Roche-lobe overflow

SB Spectroscopic binary

SB1 Spectroscopic binary with spectral components from only one star

SB2 Spectroscopic binary with spectral components from both stars

SMC Small Magellanic Cloud

UTSO University of Toronto Southern Observatory

WC Carbon-sequence Wolf-Rayet star

WN Nitrogen-sequence Wolf-Rayet star

WO Oxygen-sequence Wolf-Rayet star

WR Wolf-Rayet star

WWC Wind-wind collision

Chapter 1

Introduction

1.1 Wolf-Rayet Stars

> *... on voit la ligne lumineuse comme parsemée de petites perles brillantes ...*

With this, the astronomers Wolf and Rayet concluded their research note presented to the French Academy of Science in 1867 (Wolf & Rayet 1867). They had turned their attention to three stars in the Cygnus constellation, attracted by their yellow tint that distinguished them from their neighbours. With their optical spectroscope, they found spectra with weak continua and barely visible colours. However, the spectra also showed a series of very bright emission lines. This was an important discovery, since γ Cassiopiæ was the only star known at that time to have emission lines.

1.1.1 Nature of Wolf-Rayet emission lines

As more Wolf-Rayet stars (as they came to be called) were discovered, the question of how the emission lines were formed was posed. Wolf and Rayet were only able to state that the lines were evidence of some kind of incandescent gas.

Beals (1929) noted that the emission lines of these stars were quite broad (10–100 Å) compared to other emission line objects. Relative to the continuum,

the lines were strong compared to those of other stars with emission lines and the wavelengths of Wolf-Rayet lines differed from those of other discovered emission line stars. Wolf-Rayet stars were clearly in a class of their own.

To Beals, the similarity of the broad bands of emission from novæ to those of the Wolf-Rayet stars was suggestive. Novæ spectra arose because of Doppler broadening from a continous outflow of material, whose atoms were ejected by radiation pressure. He proposed that Wolf-Rayet emission lines were the result of the same phenomenon.

Beals (1931) then demonstrated that an optically thin expanding shell of radiating gas would produce the surprising result of flat-topped emission lines, as is seen in many lines of Wolf-Rayet spectra (*e.g.* CIII 5696 Å, see Figure 1.1 on this page, although this line is very weak here).

Other lines, however, are not so easily explained (*e.g.* CIV 5801/5812 Å). These are the round-topped profiles from at least partly optically thick material (Castor, Abbott & Klein 1975).

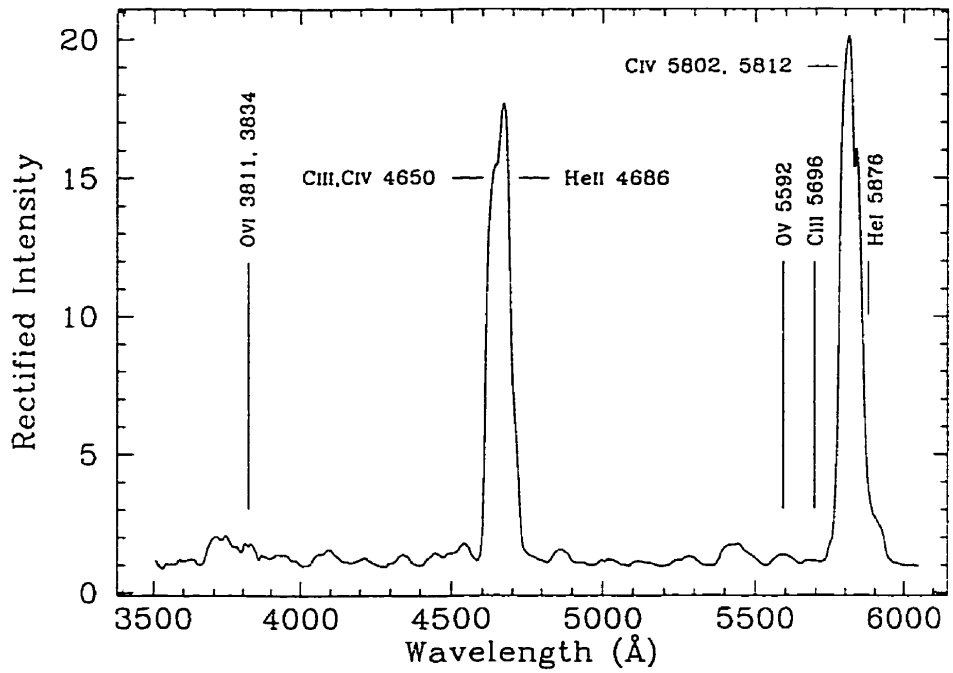

Figure 1.1: *Sample single WC4 class stellar spectrum (Br50 rectified mean of Nov. 1993 spectra). Important emission lines are labelled with their rest wavelengths in Å. Important absorption lines from an OB companion in a binary star are illustrated in Figure B.1 for the star Br22.*

1.1.2 Nature of Wolf-Rayet stars and stellar winds

Today, the emission lines of Wolf-Rayet stars are viewed, as Beals suggested, as the spectroscopic evidence of a more or less optically thin gas of low density expelled radially from the star. The terminal velocity of the wind, v_∞, is measured to be typically in the range of 1000–2500 km/s (van der Hucht 1995, Abbot & Conti 1987). This expelled matter constitutes loss of material from the star. The associated mass-loss rate, $\dot{M}$, is in the range 10^{-5} to $10^{-4}\,M_\odot$/yr (Willis 1991). For comparison, the mass-loss rate from the Sun is about $10^{-14}\,M_\odot$/yr.

WR-stars exhibit the products of advanced H- or He-nuclear burning in their atmospheres and have often been stripped of their hydrogen, brought about by internal mixing and mass-loss from their progenitorial O-stars through a stellar wind.

OB-stars were once thought not to drive winds because of the absence of emission lines in visible-range O-star spectra (Underhill 1949). When spectroscopy in the far-ultraviolet became possible with rocket-borne instruments (*e.g.* Morton 1967) and orbiting satellite observatories such as *Copernicus* (Snow & Morton 1976), emission lines and P Cygni profiles were discovered in the spectra of such objects. Evidence for expanding stellar envelopes and winds escaping from the star was then established without a doubt.

The winds of main sequence massive stars have similar terminal wind velocities as those of WR-stellar winds. However, WR winds tend to be an order of magnitude denser than those of main-sequence OB-stars (Maeder & Conti 1994).

The proposed mechanism for expulsion of material from early-type stars is radiative transfer of momentum. A photon from the photosphere is absorbed or scattered by the electron of an ion. This is much more efficient than scattering by free electrons. The absorbing particle's momentum is changed by this absorption, as well as when it emits a photon to lose this newly gained energy. In the outer region of the stellar atmosphere, the radiation has a net outward flow. The absorbing particle, however, loses its new energy isotropically. The ion receives

net momentum outwards, is accelerated radially and collides with other particles in the plasma. The medium, as a whole, is so accelerated outwards.

The continuum opacity of early-type stars is dominated by electron-scattering in the spectral region where most of the flux emerges (Mihalas 1978, p. 554). The radiative acceleration by electron-scattering, however, is only two-fifths of the opposing acceleration of gravity. Continuum scattering alone cannot account for stellar winds in hot stars.

Lucy and Solomon (1970) considered the acceleration by radiative absorption of abundant elements in hot stars with resonance lines at frequencies where the stars' continuum flux is strongest (the ultraviolet). They estimated an upper limit to the radiative acceleration by the stronger component of the CIV doublet at 1548 Å for an O-star with an effective temperature of 25 kK. This line is in the wavelength region where the continuum flux is strongest at this temperature. They found that this one line produced an acceleration 300 times that due to gravity for an O-supergiant.

Although Lucy and Solomon's result initially assumed that the radiation at this wavelength was unattenuated by photospheric absorption, they subsequently made corrections for this and found that radiation could still produce an acceleration that exceeds that of gravity. Hydrostatic equilibrium is not possible for the outer layers of early-type stars.

When the ion begins to move away from the star, the absorption line becomes Doppler-shifted from the neighbouring continuum. The line absorbs photons from the new spectral region and its acceleration is enhanced. As the layer containing the ion leaves, the underlying layers must expand to compensate for the rarefaction thus created. These layers begin to be accelerated and a flow is initiated.

With this model, Lucy and Solomon were able to derive terminal velocities comparable to those found by observation. They calculated, however, an upper mass-loss limit which is only comparable to the lower mass-loss limit observed ($10^{-8}\,M_\odot/yr$).

Castor, Abbott & Klein (1975) suggested that subordinate lines should contribute to the radiation acceleration as well as resonance lines. They found that a hundred-fold increase in the mass-loss rate could be so obtained, permitting models that give adequate predictions of the mass-loss rates for O-stars ($\sim 10^{-6}\,\mathrm{M}_{\odot}/\mathrm{yr}$).

However, the purely radiative models underestimate the observed momenta of Wolf-Rayet stars by an order of magnitude (Cassinelli 1991). There is no resolution to this problem, although multiple-scattering of photons in the envelope has been proposed (*e.g.* Springmann 1994; Gayley, Owocki & Cranmer 1995). The line-driven wind theory assumes that each photon transfers momentum to a particle in the plasma once. This is not realistic. A photon should transfer momentum several times by scattering in the envelope, providing that it is sufficiently dense and opaque.

1.2 Evolution of Wolf-Rayet stars, mass-loss, metallicity and binaries

With the absence, or nearly so, of hydrogen, and the presence of nucleosynthetic products in their atmospheres, Wolf-Rayet stars are viewed as a class of stars at the penultimate stage of massive stellar evolution before their explosion as supernovæ. According to Chiosi & Maeder (1986), single WR-stars are part of the following evolutionary scheme:

$$\begin{array}{lllllll} \mathrm{O} \rightarrow \mathrm{Of} \rightarrow & \mathrm{SG}\,\&\,\mathrm{LBV} \rightarrow & \mathrm{WN} \rightarrow & \mathrm{WC} \rightarrow & \mathrm{WO} \rightarrow & \mathrm{SN}, & M_{\mathrm{init}} > 60\,\mathrm{M}_{\odot}, \\ \mathrm{O} \longrightarrow & \mathrm{SG} \longrightarrow & \mathrm{WN} \rightarrow \mathrm{WC} & \longrightarrow & & \mathrm{SN}, & 25\,\mathrm{M}_{\odot} < M_{\mathrm{init}} < 60\,\mathrm{M}_{\odot}, \end{array}$$

where SG represents a supergiant star, LBV a luminous blue variable and SN a supernova. M_{init} is the initial mass of the progenitorial O-star. Stars of initial solar abundance in metals and an initial mass of less than $25\,\mathrm{M}_{\odot}$ are not expected to attain the WR stage. (The minimum initial mass of the WR progenitor is expected to increase with lower initial metallicity.)

With these scenarios, the main-sequence O-star begins its evolution, gradually

consuming the hydrogen in its core via the CNO cycle. Internal mixing brings some of the fused products (mainly He and N) outwards. Meanwhile, stellar winds blow away most of the hydrogen-rich outer layers, exposing the star's He and N interior. The spectral characteristics of such a star define it as Wolf-Rayet, first as WN, then WC as the He-burning products (mainly C) are exposed.

In an alternative conclusion from more recent studies (Crowther *et al.* 1995), the more massive stars bypass the SG and LBV stage completely so that

$$\begin{aligned} &\mathrm{O} \rightarrow \mathrm{Of} \rightarrow \mathrm{WN{+}abs} \rightarrow \mathrm{WN} \rightarrow \mathrm{WC} \rightarrow \mathrm{SN}, \quad M_{\mathrm{init}} > 60\,\mathrm{M}_{\odot}, \\ &\mathrm{O} \longrightarrow \mathrm{SG\,\&\,LBV} \rightarrow \mathrm{WN} \rightarrow \mathrm{WC} \rightarrow \mathrm{SN}, \quad 25\,\mathrm{M}_{\odot} < M_{\mathrm{init}} < 60\,\mathrm{M}_{\odot}, \end{aligned}$$

where WN+abs represents a WN-star with hydrogen absorption lines present in its spectrum.

As the loss of matter of the outer layers of the star is important for the formation of the WR-phase, it is necessary that the stellar wind be strong enough in the O-star progenitor to blow off this hydrogen envelope. Since this wind is mainly the consequence of radiation pressure on the ions of the photosphere, accelerating the particles in a net outward direction, the rate of mass-loss should depend on conditions that promote a strong stellar wind. One such condition is that there be a high initial mass. The higher the mass, the higher the luminosity (*e.g.* $L \propto M^3$ for most main sequence stars) and so the greater the pressure on the photospheric particles. This increases the probability that the star will reach the WR stage.

Maeder (1991) proposed that the mass-loss leading to WR-stars be related to the initial metallicity of the star. With the wind resulting from radiation pressure on the ions of the photosphere, the higher the metallicity, the greater the opacity of the material to the impinging photons. As more of the momenta from the radiation is transferred to them, particles of higher metallicity will tend to be more highly accelerated outward than those of lower metallicity. Maeder therefore argued that stars with low initial metallicity would require higher initial mass to evolve into the WR stage.

The metallicity of the Magellanic Clouds is substantially lower than the

mean metallicity of the Milky Way, which is characterised by solar abundance ($Z_{\rm SMC} = 0.002, Z_{\rm LMC} = 0.006, Z_{\odot} = 0.02$). Maeder (1982, 1991) theorised that an O-star with insufficient mass and metallicity to evolve into a WR-star could still become a WR-star if it had a close binary companion. The companion will effectively reduce the gravitional potential near the surface of the more massive evolving star, allowing it to lose mass more rapidly via Roche-lobe overflow (RLOF) and thus reach the WR phase. The results of Maeder & Meynet (1994) with evolutionary models can be used to predict that the binary frequency of WR-stars should be higher when the ambient metallicity is lower. Assuming that the fraction of stars in massive binaries undergoing Roche-lobe overflow, $\varphi[\equiv$ WR(R)/O], is independent of metallicity, they calculated the number ratio of the total number of WR-stars to O-stars (WR/O) as a function of metallicity. Their results are shown in Figure 1.2 on this page.

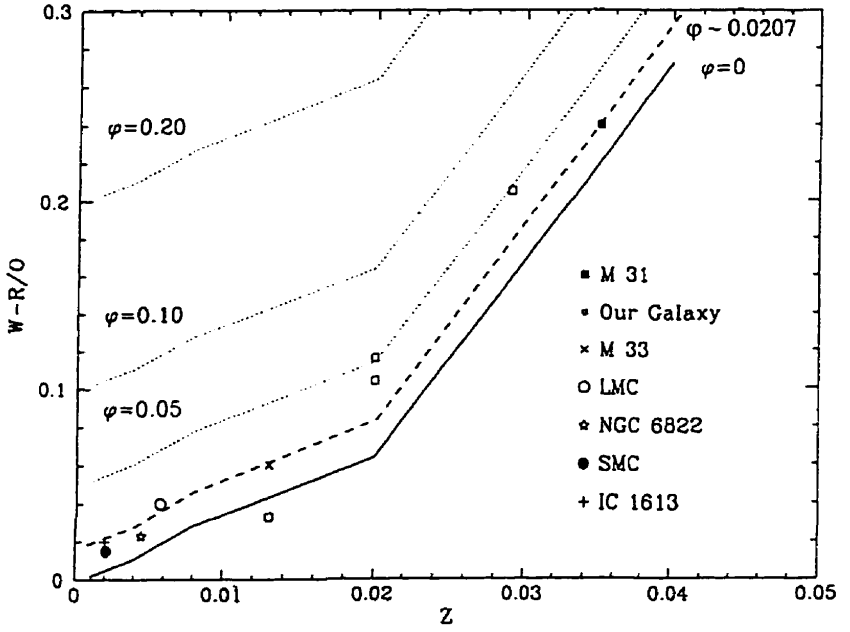

Figure 1.2: *WR to O number ratio as a function of metallicity for various values of the ratio of massive stars undergoing mass transfer in binaries, to all O-stars (curves). The values for some galaxies are included (points) (from Figure 2 of Maeder & Conti 1994; the dashed line, representing $\varphi \sim 0.0207$, has been added in this dissertation).*

The observational value of φ, for each galaxy in Figure 1.2, was found by

first determining the value of WR/O from the curve for $\varphi = 0$ at the value of Z corresponding to each galaxy. The difference between these $\varphi = 0$ values and those for the galaxies then allowed an estimate for φ for each galaxy (assuming linear interpolation between the curves for $\varphi = 0$ and $\varphi = 0.05$). By taking the mean of these galactic φ values, a universal φ is found to be approximately 0.0207 ± 0.0058. An estimate of the fraction of WR-stars that were created by Roche-lobe overflow (WR(R)/WR) may then be found with the data in Figure 1.2 by

$$\mathrm{WR(R)/WR} = \frac{\mathrm{WR(R)/O}}{\mathrm{WR/O}}.$$

The results for the SMC, LMC and the Milky Way are listed in Table 1-I on this page. The high fraction of WR-stars expected to have been formed through

Table 1-I: *Expected fraction of WR-stars formed by channel of Roche-lobe overflow for the SMC, LMC and the Milky Way.* $\varphi = 0.0207 \pm 0.0058$ *is assumed (cf. Figure 1.2).*

Galaxy	Z	WR/O	WR(R)/WR
SMC	0.002	0.017	1.24 ± 0.34
LMC	0.006	0.04	0.52 ± 0.14
Milky Way	0.02	0.104	0.199 ± 0.056

Roche-lobe overflow in the Magellanic Clouds means that the binary frequency should be at least 52% (some WR binaries may occur without RLOF) in the LMC and virtually all Wolf-Rayet stars in the SMC should be binary, as a result of their low metallicity.

1.3 Colliding winds in Wolf-Rayet binaries

Before the discovery of the strong stellar winds of O-stars, a massive binary star was viewed as two stars that would initially undergo evolution separately. However, when one star would overflow its Roche-lobe it would transfer matter to the other star. This model was also used to explain the structure of WR binary

systems (*e.g.* Sahade 1958).

With the discovery of winds in O-stars, however, there exists a new potential mechanism for one star to deliver matter to its companion. Transfer by stellar wind could, in principal, add to the matter transfered by Roche-lobe overflow. The winds could also make it easier for the stars to overflow their respective Roch-lobes, by counter-acting gravity. Actually, radiation pressure is expected to considerably modify the classical Roche-lobes (Schuerman 1972, Kondo 1996) [however, Howarth (1997) claims that the positions and shapes of the lobes should remain unchanged].

Might not also both winds collide? If so, the wind of one star could be prevented from reaching the companion's surface by the opposing wind. Instead, the material of both winds could be blown out of the system.

1.4 Dissertation motives and objectives

The LMC has relatively low metallicity, so that it is unlikely that many single WR-stars would exist at any given time in view of the negative slope of the Initial Mass Function [reading from Figure 1 of Maeder and Conti (1994), the predicted minimum mass to form a WR-star in the LMC is $\sim 50\,M_{\odot}$].

With over one hundred WR-stars in the LMC, however, there is a quandry. The low ambient metallicity in the LMC means that approximately fifty percent of WR-stars need be binary in order to be able to exist according to the binary evolutionary scenario (Section 1.2). Are there this many binaries?

One way to shed light on the situation is to study the binary frequency of a complete sub-sample of Wolf-Rayet stars in a given environment. The 23 known WC/WO subclass stars in the LMC provide such a tractable sub-sample (see Table 1-II on page 11). All have evolved in a low-metallicity environment under the same conditions. They are nearly all of the same spectral sub-type (mostly WC4 – WO4), representing an extreme (and, perhaps, the final pre-supernova) stage of evolution for massive stars. Under Maeder's theory, attainment of this

class by a single star requires that its progenitor be very massive, highly metal-rich or both.

Another benefit of this kind of study is that among the WC binaries found, one can examine the evidence for colliding winds. Furthermore, spectroscopic radial velocity studies of binary stars generally are unable to provide information on the inclination of the orbital plane relative to the line of sight to the observer. This renders ambiguous the estimates of the masses of the component stars. RV studies can also leave undetected those binaries that have such a small inclination that the motion of the stars about one another produces no observable RV variations. Colliding winds could introduce a geometric asymmetry in the orbital system. This geometric distortion could translate into perturbed spectroscopic lines, either by some form of occultation of the stellar wind or by excess emission from material that is heated to high temperature by the winds striking each other. Possibly, these effects could be measured and their variation with orbital phase be examined, in order to determine geometrical parameters, such as the orbital inclination. If so, this could render spectroscopy a very useful tool to provide orbital constraints that could only be obtained previously with more difficult techniques, such as polarimetry and photometry. In this way, spectroscopy alone would allow a convenient, reliable and complete examination of binary stars, allowing faster progress in stellar astronomy.

The goal of this Dissertation is to determine the binary frequency of the WC/WO subclass of stars in the LMC and to study any colliding winds of those binary stars that might be found. The sole WC/WO-star in the SMC and the two earliest WC/WO+O binaries in the Galaxy are added for comparison. The main method of research is observation by repeated single-slit spectroscopy in the blue – yellow range. Photometric imaging in the V-band supplements the spectroscopic work, in order to supply reliable brightnesses and eliminate apparent visual binaries. All of these data are used to determine the binary frequency of the sample in order to confirm or deny the binary model for WR formation. The spectroscopic results also allow a determination of orbital parameters for those

Table 1-II: *WC/WO-class programme stars with their coordinates (2000.0 epoch). Magnitudes are listed in Table 3-I and spectral-types are found in Table 3-IV (see Chapter 3).*

Star[a]	Right Ascension (hr : min : sec)[b]	Declination (deg : min : sec)[b]	Galaxy
Br7	04 : 56 : 11.16	−66 : 17 : 33.2	LMC
Br8	04 : 56 : 02.94	−69 : 27 : 21.7	LMC
Br9	04 : 56 : 34.57:	−66 : 28 : 31.0:	LMC
Br10	04 : 57 : 24.75	−68 : 23 : 55.7	LMC
Br22	05 : 19 : 16.47:	−69 : 39 : 20.9:	LMC
Br28	05 : 23 : 10.23	−71 : 20 : 50.8	LMC
Br31	05 : 26 : 04.13	−67 : 29 : 57.1	LMC
Br32	05 : 26 : 30.43	−68 : 50 : 26.7	LMC
Br43	05 : 30 : 12.22	−67 : 26 : 08.3	LMC
Br44	05 : 30 : 38.60	−71 : 01 : 47.7	LMC
Br50	05 : 34 : 19.40	−69 : 45 : 10.0	LMC
Br62	05 : 35 : 43.96	−69 : 10 : 58.3	LMC
Br67	05 : 36 : 54.94:	−69 : 11 : 38.9:	LMC
Br68	05 : 36 : 51.28	−69 : 25 : 55.8	LMC
Br70	05 : 37 : 29.14	−69 : 20 : 46.6	LMC
Br74	05 : 37 : 44.73	−69 : 14 : 25.4	LMC
Br83	05 : 38 : 44.50	−69 : 05 : 55.8	LMC
Br87	05 : 38 : 41.90	−69 : 05 : 11.0	LMC
Br93	05 : 39 : 34.34	−68 : 44 : 09.2	LMC
Br94	05 : 39 : 56.01	−69 : 24 : 23.9	LMC
MG1	05 : 09 : 54.07:	−68 : 52 : 53.0:	LMC
MG5	05 : 39 : 04.08	−69 : 03 : 46.3	LMC
MG6	05 : 40 : 13.08:	−69 : 24 : 02.5:	LMC
AB8	01 : 31 : 04.19	−73 : 25 : 02.1	SMC
WR9	07 : 45 : 50.22	−34 : 19 : 48.2	Milky Way
WR30a	10 : 51 : 39.12	−60 : 56 : 34.9	Milky Way

[a]Sources and alternate designations for stars are: prefix "Br"—Breysacher 1981, "MG"—Morgan & Good 1985, "AB"—Azzopardi & Breysacher 1979, "WR"—van der Hucht *et al.* 1981.

[b]Coordinates determined using Space Telescope Science Institute *Digitized Sky Survey*. A colon after the last digit of the seconds indicates uncertainty.

stars found to be binary. Wind-wind collisions are also investigated among the binaries.

Chapter 2

The Data

2.1 Spectroscopy

2.1.1 Observations

Spectroscopic data of the WC/WO-class stars listed in Table 1-II were collected during three observing missions. The first run was carried out during thirteen nights in December 1984, the second was for eight nights in January 1993 and the third was for sixteen nights during November/December 1993. All three runs were undertaken using charge-coupled device detectors (CCD's) and diffraction grating spectrometers. The technical specifications of each mission are listed in Table 2-I (page 14). The first order of the grating was used in each case and, for the wavelength ranges observed, no order-separating filter was necessary. Observations were done at times when the phase of the moon was full. This did not impede reduction of the spectral data obtained since CCD technology and reduction software allow for convenient subtraction of sky background.

Each stellar spectrum was accompanied by spectra of a comparison lamp of noble gases for wavelength calibration, the calibration spectrum being taken with the telescope at the same position required for the observation of the star. One such comparison image was taken directly before and after the stellar observation and the average was taken of the two (except for the Dec. 1984 mission, when

Table 2-I: Observing mission specifications

	1984	1993	1993
Dates (local for night begin)	Dec. 5–17	Jan. 21–28	Nov. 17–Dec. 2
Observatory	CTIO	CASLEO	CASLEO
Telescope diameter (m)	1	2.15	2.15
Approx. wavelength range observed (Å)	5000–6300	4900–6400	3500–6100
Grating (lines/mm)	600	600	400
CCD	GEC	Thompson	TEK 1024
Approx. CCD gain (e^-/ADU)	1	10	7.95
Approx. CCD read-out noise (e^-/pixel)	20	10	10.4
Spectral dispersion (Å/pixel)	2.2	2.5	2.6
Comparison lamp	He-Ar	He-Ne-Ar	He-Ne-Ar
Control star	EG-21	β Pictoris	β Pictoris

only one calibration exposure was taken after observing the star).

Each night, CCD bias frames were taken to determine the electronic bias of the detector. Flat-field exposures were made to correct for pixel-to-pixel response variations of the CCD (no flat-field frames were made during the Nov. 1993 mission—see below). To explore the dark current level, CCD dark frames of varying exposure times (from five minutes to one hour) were obtained as well on some nights.

Spectra of a control star known to possess few spectral lines in the observed wavelength range were obtained each night. This star provided a comparison spectrum in order to test for and correct any artefacts due to the method of observation or to the equipment.

2.1.2 Reduction to rectified spectra

Reduction was performed by computer using the National Optical Astronomical Observatory programs of the Image Reduction and Analysis Facility (IRAF). The overall objective was to extract wavelength-calibrated, one-dimensional rectified spectral arrays from the two-dimensional images. The procedure used for all missions is outlined in the following steps:

1. Find average bias of each night and subtract it from all image frames.

2. Determine the effect of dark current (assuming linear accumulation of dark current counts as a function of time) and subtract it from each image frame. This was only needed for the Dec. 1984 data, as the dark current during the other two missions was negligible (less than two percent of the stellar continuum).

3. Fit a curve of relatively low order to an average of the flat-field images, divide it into the average flat-field and then divide this normalised quotient into all stellar images. Division of the flat-field image by a low order curve preserves the pixel-to-pixel gain variations in the flat-field image. The result then can be used to divide out such variations in the stellar spectroscopic images. (This was not done for the Nov. 1993 data. Instead, the spectrum of the standard star was used after Step 8 below. See Appendix A.)

4. Manually remove cosmic rays found in the images.

5. Collapse the two-dimensional spectrum into one dimension, first subtracting the sky level determined from the same image using the pixels beside the stellar spectrum. This conversion is done by adding the counts of pixels at the same wavelength together, with the weight of each pixel count determined by its intensity relative to the others.

6. Remove remaining cosmic rays on the 1-D spectrum manually, with the pixel value replacing the cosmic ray count determined by neighbouring values on the spectrum.

7. Rectify the spectrum (set continuum to unity) by fitting a low order function through the sections of the spectrum that constitute the continuum and dividing the spectrum with the fit (the continuum is considered to be slowly varying). This is difficult due to the presence of the wide emission lines of the spectra of Wolf-Rayet stars. Often level parts of the spectrum between strong emission lines, called pseudo-continua, are used instead.

8. Calibrate the spectrum in wavelength using the accompanying comparison spectra. The comparison spectrum is collapsed into one dimension in the same manner as its corresponding stellar image. The comparison emission lines are then identified and are used to calibrate the pixels in terms of wavelength. The calibration function thus found is then transposed to the stellar spectrum. If two comparison spectra are available, the average of the two is used. The wavelength scale of this calibrated spectrum is then transformed to a heliocentric wavelength by removing the velocity components of the Earth's motion.

2.2 Photometry

2.2.1 Observations

Photometric broadband V-band images were taken of all programme stars (those MC stars listed in Table 1-II), with the exception of MG5, during January 19–22, 1994, at the UTSO 60 cm telescope. MG5 was observed on November 22, 1995. The observing mission was performed through service observing by staff at UTSO. The detector was a PM512 CCD with a field of $4' \times 4'$. It had a gain of $4.6\,e^-$/ADU and a read-out noise of $10.6\,e^-$ per $0.5'' \times 0.5''$ pixel.

Calibration of the V-magnitudes of the programme stars required that the instrumental magnitudes be compared with stars of known magnitude. The standard stars chosen were from the fields RU149 and RU153 (Landolt 1992), which contain a good spread in colour index.

At the beginning of each night, the standard star fields were observed. Immediately after, an image of the programme star Br50 and its surrounding field was made. This star was chosen to serve as a secondary standard since it appeared to be isolated and since spectroscopic and photometric work (this Dissertation and previous studies: Moffat, Niemela & Marracco 1990 and Seggewiß, Moffat & Lamontagne 1991) indicate that Br50 is not significantly variable. The convenience

of this procedure was that once this star was calibrated with the RU standards, it could then be used to calibrate the other WC-stars. This was justified as Br50 is of the same type as the other object stars and in the same part of the sky (allowing determination of changes in airmass, as well, during the night). This also permitted the omission of the RU standard stars from the Nov. 1995 mission, since Br50 served as the standard for this run.

Programme stars were then observed, one after the other, with an image of Br50 taken just before and just after the observation of the programme star. As many different stars as possible were observed in a given night. The mission required four nights for the observation of all stars.

Bias frames were taken before the beginning of observations on each night. Flat-field images of the twilight sky were obtained at the end of the night, followed by dark images.

Reduction of these data was performed with IRAF using the following procedure:

1. For each night, find the average of bias frames and subtract the result from the remaining images.

2. Again, for each night, find the average of flat-field images. Unlike for spectroscopy, this result is then normalised with a constant value rather than a low-order polynomial. This gives an image that represents the pixel-to-pixel variations across the face of the CCD chip. This normalised flat-field was then divided through all of the stellar images.

Compensation for dark current was not necessary.

2.2.2 Reduction to apparent visual magnitudes

To find the magnitude of a star, one must consider what happens to starlight as it leaves the star, travels through space and finally reaches the observer.

A star has a certain absolute continuum magnitude, M_V, in the V-band. Emission lines will add light at wavelengths where they occur. If the star is

binary or has a close visual companion, it will appear brighter. Interstellar matter along the line of sight to the star will redden the starlight and the brilliance of the star will diminish, depending on the amount of interstellar matter between the observer and the object. Finally, more photons will be removed from the light beam depending on the terrestrial airmass before the light impinges on the detector and is recorded as an instrumental magnitude v.

The photometric images were analysed using the routines of the DAOPHOT package in IRAF. The point-spread function (PSF) of obviously single stars was examined to determine a typical mean PSF of the stars in the image. A Gaussian function did not model well the PSF in the wings, as noted by Moffat (1969). A Penny function was found to model best the PSF and was adopted. The images were then processed again using the adopted PSF to identify stars and separate crowded objects. Calculation of instrumental magnitudes followed, with an arbitrary but fixed zero point.

To find visual magnitudes, the principal of differential photometry was used. The visual magnitude of the secondary standard (Br50), V_c, was first found (described below). As the secondary standard was chosen to be of the same type as the programme stars and was in the same region of the sky, the difference between the visual magnitude of Br50 and that of any other programme star, V_{WR}, is simply the difference between the instrumental magnitudes measured for the two stars (where the secondary standard was effectively observed at the same airmass as the programme star),

$$V_{WR} = V_c + \Delta v, \tag{2.1}$$

where Δv is the difference between the instrumental magnitudes of Br50 and the programme WR-star.

Finding the visual magnitude of Br50, V_c

The first step was to find the effect of airmass on the measured magnitude. The instrumental magnitudes found for each image of Br50 on each night were fit

as a function of airmass with a linear least-squares routine (Press *et al.*, 1992, pp. 655–660) (Figure 2.1 on this page), using the equation $v_c = a + k_v X$. The fit values of the extinction coefficient are displayed in Table 2-II on this page.

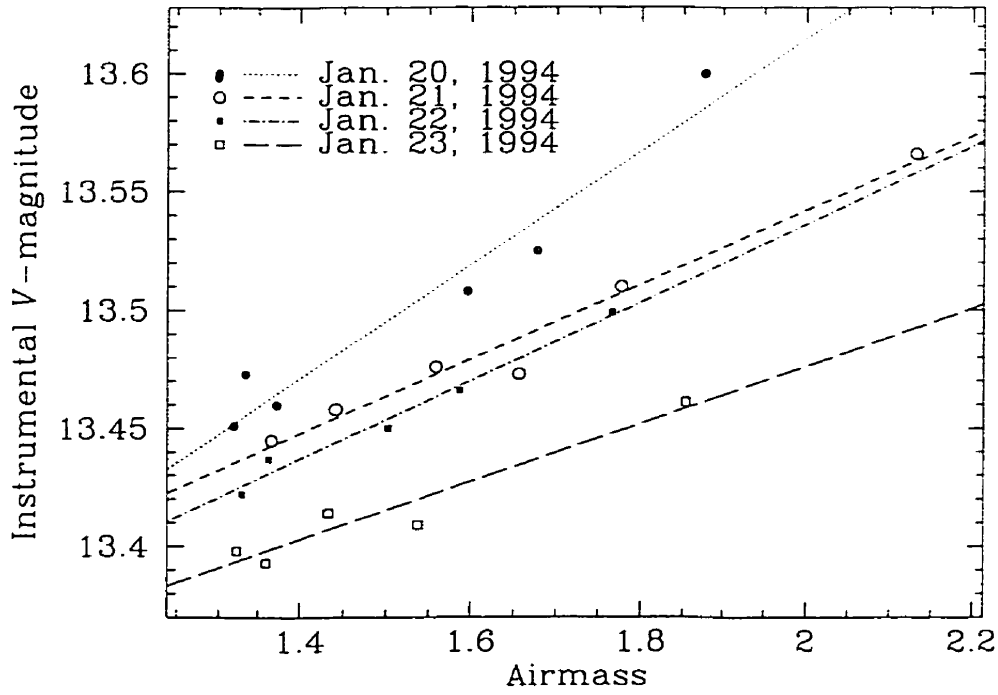

Figure 2.1: *Instrumental magnitude of Br50 versus airmass. The values and linear least-squares fit are displayed for each night of observation.*

Table 2-II: *Visual extinction coefficient for the instrumental magnitudes of Br50.*

Date	k_v
Jan. 20	0.24 ± 0.03
Jan. 21	0.16 ± 0.01
Jan. 22	0.17 ± 0.01
Jan. 23	0.12 ± 0.02

The colour of a star observed will have an effect on the value of V, which can be expressed by the relation (colour transfer equation)

$$v^0 - V = c_0 + c_1(B - V),$$

where $v^0 = v - k_v X$ is the instrumental magnitude at zero airmass, V is the standard visual magnitude of the given star, $(B - V)$ is the colour index of the

star, c_1 is the slope of the colour equation and c_0 is a zero-point. The values $v^0 - V$ of the Rubin standard stars were then plotted as a function of the colour $(B-V)$. The values of v^0 are the data from the observing mission (with exposure time taken into account) while V and $(B-V)$ come from Landolt (1992) (Figure 2.2 on this page). Given the small value of c_1 ($\simeq -0.05$), that the continuum intrinsic

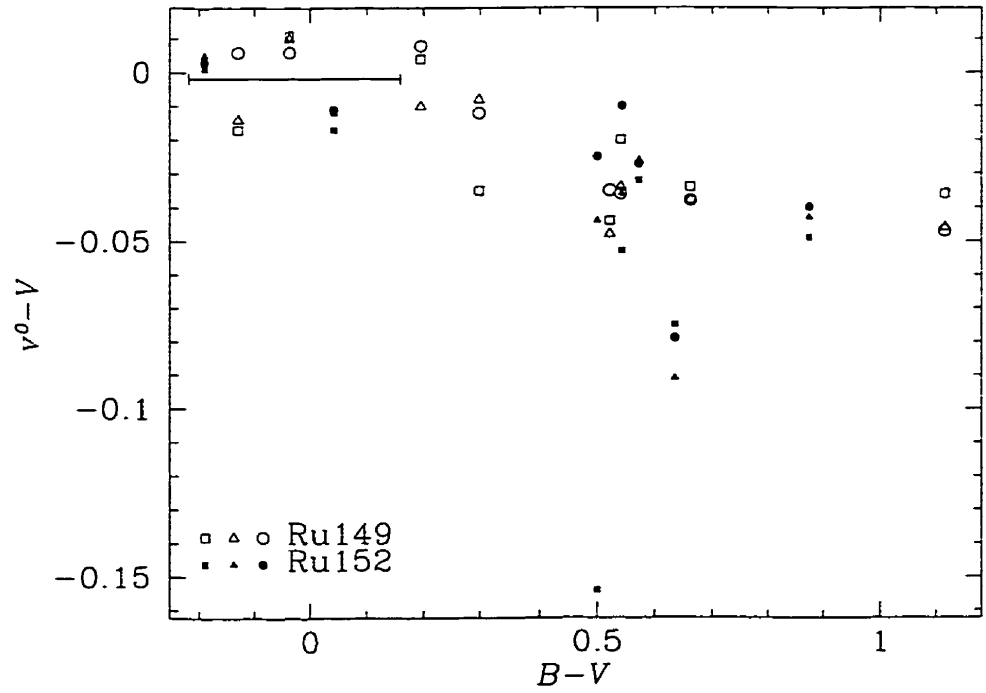

Figure 2.2: *Colour relation of Rubin standard stars. Different shapes designate data from different images of the same star. The horizontal error bar shows the region of interest.*

colours of early-type WC and WO-stars are approximately constant and that the interstellar reddening in the LMC is generally small (Smith, Shara & Moffat 1990a), a constant $B-V$ may be assumed with a value close to zero for the MC WC-stars. Therefore, $v^0 - V \simeq c_0$ is adopted to within adequate precision for this study. The zero-point c_0 was taken to be the average of the value $v^0 - V$ of those Rubin standard stars with colours close to those of the WC-stars — Ru149c, Ru149d, Ru152 and Ru152e.

The visual magnitude of the calibration star Br50, V_c, can thus be found by

$$V_c = v_c - k_v X_c - c_0, \tag{2.2}$$

with

$$\sigma_{V_c} = \sqrt{\sigma_{v_c}^2 + X_c^2 \sigma_{k_v}^2 + \sigma_{c_0}^2}. \tag{2.3}$$

Visual magnitudes of other stars

The visual magnitudes of the other stars were calculated using differential photometry with Equation 2.1. This was done by first interpolating the instrumental magnitude of Br50 at the same airmass on the same night as the programme star:

$$v_c = a + k_v X_{\mathrm{WR}},$$

which is taken from Figure 2.1. Substituting this result into Equation 2.1 yields

$$V_{\mathrm{WR}} = V_c + (v_{\mathrm{WR}} - v_c), \tag{2.4}$$

where v_{WR} is the measured instrumental magnitude of the WR-star in question. The error is taken as

$$\sigma_{V_{\mathrm{WR}}} = \sqrt{\sigma_{V_c}^2 + \sigma_{v_{\mathrm{WR}}}^2 + \sigma_a^2 + X_{\mathrm{WR}}^2 \sigma_{k_v}^2}. \tag{2.5}$$

Note that V_c and σ_{V_c} are given by Equations 2.2 and 2.3.

Adjustment for the emission lines and calculation of absolute magnitudes are dealt with in Chapter 3

2.3 Spectral and photometric atlas

In Appendix B, images and the resulting photometry, as well as mean spectra, are shown for each star (spectra only for the Galactic stars).

Chapter 3

The Binary Frequency

In this chapter, the binary frequency of the WC class stars in the Magellanic Clouds is determined. First, the calculation of the absolute visual continuum magnitude is discussed. This is followed by the extraction of radial velocity data as well as line strengths and widths from the spectrograms. The results are then used to determine which stars of the Magellanic Clouds are binary. This chapter is closed with a brief discussion of the implications of the results.

3.1 Absolute continuum magnitudes

Clearly, binary stars are brighter than single stars of the same type. Therefore, it is useful to compare brightnesses of the WC-stars in order to help determine if they are binary. To do this, absolute magnitudes (independent of reddening and distance) of the continuum emission (more or less independent of the mass loss rates) are needed. Usually, the absolute magnitude, M_V, of a star with a given visual magnitude, V, can be determined by simply adding to the value V a factor that takes into account the distance between the star and the observer, as well as the reddening of the starlight as it travels through space. In the case of WR-stars, however, this is complicated by the intense emission lines which contribute to the visual magnitude. In order to render the magnitudes compatible with the UBV photometric system, these lines must be taken into account and their

contribution to the magnitude removed.

Pyper (1966) developed a means to subtract this emission line contamination. She derived the difference between the magnitude of the continuum and that measured by the observer as

$$\begin{aligned} V'_{\rm WR} - V_{\rm WR} &= 2.5 \log \frac{E_{\rm c} + E_\ell}{E_{\rm c}} \\ &= 2.5 \log \left(1 + \frac{E_\ell}{E_{\rm c}}\right), \end{aligned}$$

where $V'_{\rm WR}$ is the corrected visual magnitude, $V_{\rm WR}$ is the measured visual magnitude, E_ℓ is the emissivity integrated over the extent of the emission lines of the star and $E_{\rm c}$ is the integrated emissivity of the underlying continuum. The calculation of $E_\ell/E_{\rm c}$ is demonstrated in Appendix C.

Having obtained the factor to correct for contamination by emission lines, as well as the extinction, all that is left is to find the distance modulus, $(m-M)_0$, to take into account the decrease in intensity with the distance between the object and the observer. Westerlund (1990) studied the results of many workers using various techniques (see references therein). He combined them to determine mean observed moduli of both Clouds. For the LMC he found a value of $(m - M)_0 = 18.50 \pm 0.15$, while for the SMC he found $(m - M)_0 = 18.9$. No uncertainty is given for the value for the SMC but it should be at least as high as that for the LMC. These values are consistent with the new values of the moduli very recently determined, by the study of many results, of $(m - M)_0 = 18.45 \pm 0.10$ for the LMC and $(m - M)_0 = 18.9 \pm 0.10$ for the SMC (Westerlund 1997, pp. 6–20, and references therein). The 1990 results were used.

The stars WR9 and WR30a were not studied photometrically. To estimate their absolute magnitudes, the data compiled by van der Hucht *et al.* (1988) were used. In their Table 4, the visual continuum magnitudes v and reddenings $E(b-v)$ [using the medium band *ubv* system of Smith (1968)] are listed. Estimates of the distance moduli of the two stars are also provided. The *ubv* values may be converted to the *UBV* system using the relations of Turner (1982):

$$V'_{\rm WR} = v - 0.033 - 0.365(b - v) \qquad \text{and}$$

$$E(B-V) = 1.22E(b-v),$$

which require the colour $b-v$, also given in their table.

Error estimates of these quantities provided by van der Hucht *et al.* are, unfortunately, not provided. The errors $\sigma_v \sim 0.015$ and $\sigma_{(b-v)} \sim 0.007$ of Smith (1968) are used. The error $\sigma_{(b-v)_0}$ (needed to calculate $\sigma_{E(b-v)}$) was roughly estimated using the values of the average standard deviations (s.d.) of $(b-v)_0$, according to spectral type, given in Table 6 of the same publication. As

$$(\text{s.d.})_s = \sqrt{\frac{\sum_i^{n_s} (\sigma_s^2)_i}{n_s}},$$

where σ_s is a hypothetical standard deviation of $(b-v)_0$ and n_s is the number of such measured deviations, for a given spectral type s (root-mean-square),

$$\sigma_s = \sqrt{n_s}\,(\text{s.d.})_s.$$

Having estimated a hypothetical σ_s for every spectral type, a global standard deviation, $\sigma_t \equiv \sigma_{(b-v)_0}$, can be estimated with

$$\sigma_t = \sqrt{\frac{\sum_s \sigma_s^2}{\sum_s n_s}} = \frac{1}{\sqrt{\sum_s n_s}} \left(\sum_s (\text{s.d.})_s^2 n_s^2 \right).$$

The errors on the distance moduli were estimated assuming that the main source of contribution to this quantity would be from σ_{M_v}, which was roughly calculated from information given in Table 6 of van der Hucht *et al.* using the same technique as for $\sigma_{(b-v)_0}$.

With all of these factors finally determined, the absolute magnitudes of the stars were calculated with

$$M_V = V + 2.5 \log \left(1 + \frac{E_\ell}{E_c} \right) - 3.1 E_{B-V} - (m-M)_0$$

and

$$\sigma_{M_V} = \sqrt{\sigma_V^2 + \left[\frac{2.5}{\left(1 + \frac{E_\ell}{E_c}\right) \ln 10} \right]^2 \sigma^2_{\frac{E_\ell}{E_c}} + (3.1)^2 \sigma^2_{E_{B-V}} + \sigma^2_{(m-M)_0}}.$$

Table 3-I on page 25 summarizes the photometric results for each star. Note that the V-data for three severely crowded stars are taken from sources whose results were based on better spatial resolution.

Table 3-I: *Magnitudes, reddenings and line-to-continuum strength ratios of observed stars. Note that V is the observed broadband visual magnitude while $E(B-V)$ and M_V are corrected for emission lines.*

Star	V	$E(B-V)^a$	E_ℓ/E_c	M_V
Br7	14.05 ± 0.07	0.30 ± 0.06	1.37 ± 0.15	-4.4 ± 0.2
Br8	14.08 ± 0.07	0.23 ± 0.06	1.19 ± 0.13	-4.2 ± 0.2
Br9	13.61 ± 0.01^b	0.10 ± 0.01	0.094 ± 0.008	-5.1 ± 0.2
Br10	13.01 ± 0.05	0.25 ± 0.04	1.05 ± 0.10	-5.5 ± 0.2
Br22	12.30 ± 0.08	0.13 ± 0.07	0.15 ± 0.02	-6.5 ± 0.3
Br28	12.72 ± 0.05	0.08 ± 0.01	0.22 ± 0.02	-5.8 ± 0.2
Br31	11.52 ± 0.08	0.11 ± 0.02	0.070 ± 0.006	-7.2 ± 0.2
Br32	12.47 ± 0.07	0.08 ± 0.02	0.16 ± 0.01	-6.1 ± 0.2
Br43	13.37 ± 0.05	0.08 ± 0.05	1.00 ± 0.10	-4.5 ± 0.2
Br44	13.17 ± 0.05	0.15 ± 0.02	0.39 ± 0.03	-5.4 ± 0.2
Br50	13.04 ± 0.04	0.11 ± 0.05	1.11 ± 0.11	-5.0 ± 0.2
Br62	13.79 ± 0.05	0.38 ± 0.18	0.59 ± 0.12	-5.3 ± 0.6
Br67	11.90 ± 0.08	0.39 ± 0.02	0.057 ± 0.005	-7.7 ± 0.2
Br68	13.00 ± 0.05	0.08 ± 0.02	0.33 ± 0.03	-5.4 ± 0.2
Br70	13.71 ± 0.05	0.18 ± 0.07	0.56 ± 0.06	-4.8 ± 0.3
Br74	14.50 ± 0.06	0.47 ± 0.06	1.12 ± 0.12	-4.6 ± 0.3
Br83	14.20 ± 0.05^c	0.46 ± 0.18	0.06 ± 0.01	-5.7 ± 0.6
Br87	12.3 ± 0.1^d	0.46 ± 0.18	0.17 ± 0.03	-7.5 ± 0.6
Br93	14.97 ± 0.06	0.18 ± 0.04	1.62 ± 0.16	-3.0 ± 0.2
Br94	13.18 ± 0.06	0.18 ± 0.02	0.33 ± 0.03	-5.6 ± 0.2
MG1	14.01 ± 0.07	0.10 ± 0.07	0.18 ± 0.02	-4.6 ± 0.3
MG5	16.17 ± 0.04	1.02 ± 0.08	1.00 ± 0.12	-4.7 ± 0.3
MG6	13.00 ± 0.06	0.23 ± 0.07	0.041 ± 0.004	-6.2 ± 0.3
AB8	12.94 ± 0.08	0.05 ± 0.04	0.16 ± 0.01	-6.0 ± 0.2
WR9	10.73 ± 0.03^e	1.33 ± 0.13	0.39 ± 0.06	-4.9 ± 0.9
WR30a	13.46 ± 0.03^e	1.11 ± 0.13	0.12 ± 0.02	-5.8 ± 0.9

[a]Reddenings (approximately independent of the emission lines) for AB8 and Br93 from $E(B-V)$ of Kingsburgh, Barlow & Storey 1995; those for Br70, MG1 and MG6 from $E(B-V)$ of Lucke 1974; those of Br83 and Br87 from $E(B-V)$ of Melnick 1983; those of WR9 and WR30a from $E(b-v)$ of van der Hucht *et al.* 1988. For all other stars the reddenings were determined from $E(b-v)$ of Smith, Shara & Moffat 1990a.

[b]HST V-magnitude from Schertl *et al.* 1995, Table 1.

[c]HST F555-magnitude from Campbell *et al.* 1992, Table 4.

[d]V-magnitude from Moffat *et al.* 1987, Table 5.

[e]Calculated from v-magnitude in van der Hucht *et al.* 1988, Table 4; hence already effectively corrected for emission lines.

3.2 Spectral parameters

The heliocentric velocities of the stars were found by evaluating the Doppler-shift of the wavelength of the CIV 5808 Å emission line. This line was chosen since it is present in all of the spectrograms available and because it is much more intense than the other lines, even though it is a doublet (5802 Å and 5812 Å) and is blended with HeI 5876 Å on its red flank. For the calculations, the line was defined to be bounded by those points where it became indistinguishable from the continuum. [The line profiles are distorted by excess emission due to wind-wind collision (discussed in Chapter 5). This was ignored since the effect is very small for CIV 5808 Å.]

The Doppler-shifted velocity of the line, $v_{\rm obs}$, was measured by finding its mean wavelength and subtracting the rest wavelength, taken somewhat arbitrarily to be 5808.0 Å (the line is a doublet of two CIV emission lines; since radial velocity searches were done mainly to determine temporal radial velocity changes and comparisons between stars, the precise choice of rest wavelength would not affect the validity of the study as long as the same wavelength was used for every spectrum; the choice of 5808 Å is that of Moffat, Niemela & Marraco 1990). The wavelength of each pixel of the line was weighted by the normalised intensity at that pixel (so that $\bar{\lambda} = \sum_i \lambda_i I_i \,/\, \sum_i I_i$, where $\bar{\lambda}$ is the mean wavelength sought, λ_i is the wavelength at a given pixel, i, of the line and I_i is the normalised intensity at that pixel after subtraction of the continuum). This calculation was performed using the statistical routine `G01AAE` of the NAG `FORTRAN` Library (NAG 1990). The results of this calculation are listed in a journal of observations contained in Appendix D. In addition to the mean, this routine also determined the standard deviation of the Doppler-shifted velocities and the sum of the weights. As the weights were the intensities at each pixel based on continuum-rectified spectrograms, the sum of the weights constituted the equivalent width ($W_{\rm e}$) of the line.

The same program also calculated the full-width at half-maximum (FWHM)

of the 5808 Å CIV line. The peak intensity of the line was also found and then the width of the line profile was determined at half of that intensity.

After having calculated the above quantities for each spectrogram of a given star, the averages of the velocities were then found ($\bar{v}_{\rm obs}$). They are given in Table 3-II on page 28, along with standard deviations and number of data points.

If the radial velocities of the stars actually reflect systemic motion, then they should be no different from the average velocity of the ambient media. To see if this was the case, the velocity of their environments (for the LMC) was estimated using the work of Feitzinger (1980).

Feitzinger's Figure 6 is a contour map of isovelocity curves of the LMC. It is reproduced in Figure 3.1 on page 29. The position of each star (superimposed on his map) was determined by subtracting the right ascension (α) and declination (δ) of the star (after precession to the 1950 epoch) from the corresponding coordinates of the centre of the chart [$\alpha = 5^{\rm h}24^{\rm m}$ and $\delta = -69°48'$ (1950)]. This brought the star's position into the map's coordinates. Since Feitzinger measured right ascension in degrees (X), the right ascension of the star was converted to those same units by

$$X = \frac{360°}{24^{\rm h}} \Delta\alpha \cos\delta.$$

[This was deduced from the formula for the length of a small arc, whose derivation is described by Smart (1977, pp. 3–4)]. No adjustment was needed for the declination.

The radial velocity of the milieu of each WR-star, $v_{\rm F}$, (with the effect of the sun's motion and the rotation of the Galaxy removed) was then read by interpolation from Figure 3.1.

The heliocentric radial velocity of the milieu of a given star, $v_{\rm mil}$ (the quantity actually sought), was then found from the sum of the milieu velocity, $v_{\rm F}$, as well as the negative of the velocity of the sun, $\vec{v}_{\odot}$, and the negative of the rotational velocity of the Galaxy, $\vec{v}_{\rm rot}$ (see Figure 3.2 on page 30), both projected in the

Table 3-II: *Heliocentric radial velocity data, for each mission, of the observed stars, where $\bar{v}_{\rm obs}$ and σ_v are in units of km/s. The velocities are based on the* CIV *5808 Å emission line.*

	Dec. 1984				Jan. 1993				Nov. 1993			
Star	$\bar{v}_{\rm obs}$	σ_v	N	$\frac{\sigma_v}{\sqrt{N}}$	$\bar{v}_{\rm obs}$	σ_v	N	$\frac{\sigma_v}{\sqrt{N}}$	$\bar{v}_{\rm obs}$	σ_v	N	$\frac{\sigma_v}{\sqrt{N}}$
Br7	365	21	9	6.9					483	39	13	10.8
Br8	426	36	9	11.9					531	43	12	12.3
Br9	534	25	9	8.2					564	51	11	15.4
Br10	549	25	9	8.4					564	64	11	19.4
Br22	665	164	9	54.8	740	115	7	43.6	624	162	15	41.7
Br28	482	29	9	9.6	533	10	7	3.7	427	41	14	10.9
Br31	514	246	9	82.1	494	199	10	62.9	470	246	16	61.5
Br32	420	160	8	56.7	511	245	9	81.7	407	203	25	40.5
Br43	543	32	9	10.5					595	37	11	11.2
Br44	363	20	9	6.7					464	46	12	13.4
Br50	543	25	10	7.8					543	50	12	14.5
Br62	417	24	11	7.4					444	32	9	10.6
Br67	592	30	9	9.8					573	48	10	15.2
Br68	549	26	10	8.3					557	28	9	9.4
Br70	199	30	10	9.4	225	6	7	2.3	195	33	12	9.7
Br74	551	34	9	11.2					561	27	9	8.9
Br83	564	59	9	19.7					534	68	11	20.4
Br87	408	40	9	13.3	438	17	6	7.0	277	49	15	12.6
Br93	176	56	10	17.8					133	45	11	13.7
Br94	628	29	9	9.5	603	48	6	19.6	481	72	15	18.6
MG1									474	43	11	13.0
MG5									556	72	8	25.4
MG6					463	14	4	7.2	210	79	12	22.9
AB8	29	98	13	27.1	153	33	7	12.6	86	137	15	35.4
WR9									343	134	15	34.6
WR30a					−72	160	4	79.8	1	164	13	45.6

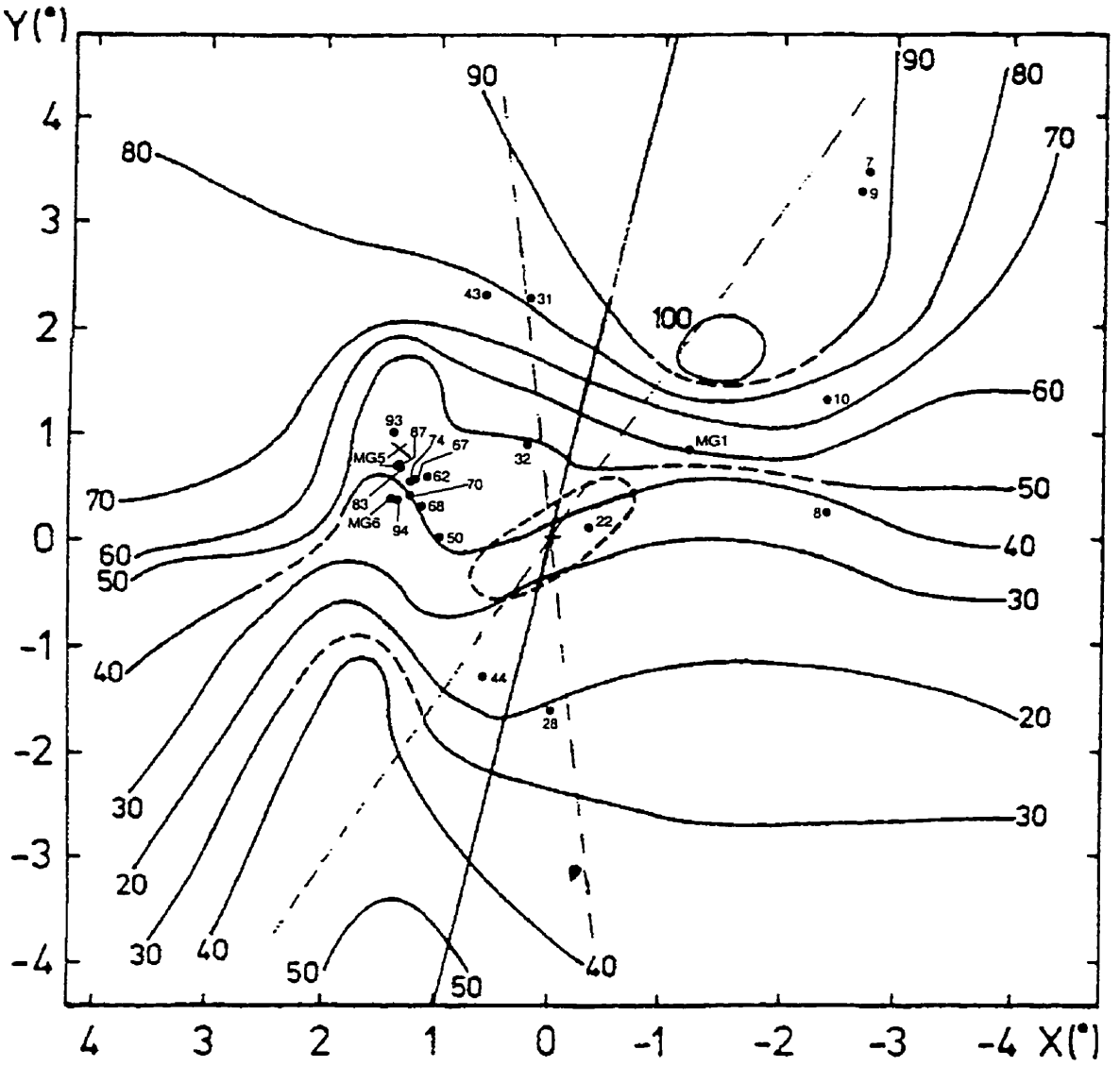

Figure 3.1: *Isovelocity contour map of the LMC from Feitzinger (1980) with superimposed positions of WR-stars. Breysacher and MG numbers are in small print while isovelocity contour line labels are in large print. The dashed ellipse is the bar of the LMC and the "X" is the position of 30 Doradus. The solid diagonal passing through the centre of the figure is the geometric line of nodes, while the dashed diagonals correspond to a sector of ±20° about this line.*

radial direction:

$$v_{\rm mil} = v_{\rm F} - \vec{v}_{\rm rot} \cdot \vec{n} - \vec{v}_{\odot} \cdot \vec{n},$$

where $\vec{n}$ is the unit vector in the direction of the star from the sun. The calculation of a scalar product with vectors expressed in equatorial coordinates is demonstrated in Appendix E. The values of $\vec{v}_{\rm rot}$ and $\vec{v}_{\odot}$ in the above equation were those used by Feitzinger in his work, allowing the reproduction of the observed heliocentric velocities on which he based his calculations.

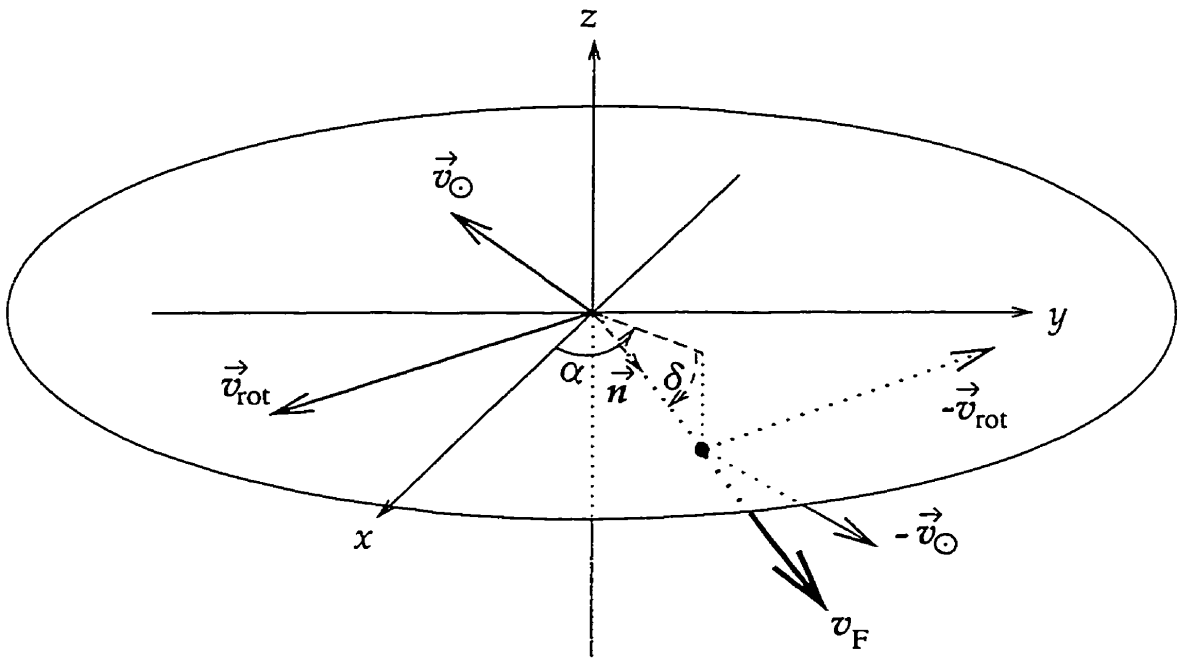

Figure 3.2: *LMC milieu heliocentric velocity vectorial components. The solid circle shows the position of a star of interest. The x–y plane is the equatorial plane (shown by the ellipse), while North is in the positive z-direction.*

Since no convincingly systematic trends were seen, the radial velocity data of all three observing missions were combined directly to produce global values of the stars. In Table 3-III on page 32 are listed the averages of the observed heliocentric radial velocities for each star, $\bar{v}^{\circ}_{\rm obs}$, except for the binaries, where the mean orbital velocity is given. The heliocentric velocities of the stars' milieu, $v_{\rm mil}$, in the case of the single LMC stars, are included, followed by $\Delta v_{\rm r}$, the difference between $\bar{v}_{\rm obs}$ and $v_{\rm mil}$. In the case of AB8 and the two Galactic WC binaries, milieu velocities are not available. For these, true systemic radial velocities based

on the O-companion orbit, γ(OB), were used to obtain $\Delta v_r = \bar{v}_{obs} - \gamma(OB)$. (The standard deviation of the average velocities, σ_{v_r}, the total number of observations, N, and the average equivalent width and full-width at half-maximum of the CIV 5808 Å line, W_e and FWHM, respectively, are also included in Table 3-III.)

3.3 Determining the binary frequency

The various quantities tabulated in Tables 3-I, 3-II and 3-III can be used to infer duplicity amongst the sample stars. Should a WR-star have an orbital companion, the light of the other star should be combined with that of the WR to give a brightness that is higher than that for a single star. Of course, a nearby optical double associated or not with the WR would have the same effect, although such cases can be separated into two stars if the crowding is not too severe.

The equivalent width of spectral lines should also be affected by the light of orbital companions (and optical doubles). The extra light should raise the proportion of the apparent continuum intensity as compared to that of an emission line. The equivalent width measured would be expected to be less than that for the same type of WR-star that was single.

The orbital motion of a binary star should produce a standard deviation of the WR-star's radial velocity that would be higher than σ_{v_r} for a corresponding single star. However, a single star in a very crowded region could have its WR spectral lines diluted, making σ_{v_r} spuriously large.

The above parameters can only effectively reveal variations over intervals up to weeks. Variations over a longer duration (*e.g.* binary orbits with periods in the range of years) would be unlikely to be detected, since the variations would be so small as to be comparable with those found for single stars. This is illustrated in Figure 3.3 on page 33, where the amplitude K of a binary WR-star is plotted as a function of the binary period and compared to the velocity standard deviation of single stars. The mass of the WR-star is assumed to be half of that of the

Table 3-III: *Spectral data of the observed stars, missions combined. The quantities* $\bar{v}^{\circ}_{\rm obs}$, $v_{\rm mil}$, γ(OB), $\Delta v_{\rm r}$, $\sigma_{v_{\rm r}}$ *and FWHM are in units of km/s,* $W_{\rm e}$ *is in Å.*

Star	$\bar{v}^{\circ}_{\rm obs}$ [a]	$v_{\rm mil}$	γ(OB)	$\Delta v_{\rm r}$ [b]	$\sigma_{v_{\rm r}}$	N	$W_{\rm e}$	FWHM
Br7	435	307		128	67	22	1847	2805
Br8	486	254		232	66	21	1569	2919
Br9	550	307		243	43	20	1114	3558
Br10	557	290		267	50	20	1425	4080
Br22	639	257	202	382	156	31	184	4133
Br28	469	241		228	54	30	297	2828
Br31	486	304	288	182	227	35	86	4018
Br32	447	273	245	174	205	42	215	4444
Br43	572	302		270	43	20	1481	3488
Br44	422	246		176	63	21	519	4130
Br50	543	265		278	40	22	1545	4002
Br62	429	268		161	31	20	870	4277
Br67	582	267		315	41	19	76	3969
Br68	553	265		288	27	19	430	3694
Br70	204	265		−61	30	29	777	5021
Br74	556	266		290	30	18	1622	3149
Br83	548	267		281	64	20	74	4158
Br87	348	267		81	84	30	218	6043
Br93	154	271		−117	54	21	2426	6062
Br94	550	263		287	90	30	436	4600
MG1	474	279		195	43	11	233	4340
MG5	556	267		289	72	8	1120	3348
MG6	273	263		10	132	16	47	5295
AB8	63	—	187	−124	116	35	178	5511
WR9	343	—	−7	350	134	15	358	3835
WR30a	−17	—	−9	−8	161	17	139	5493

[a] Replaced by the mean zero-point velocity, γ (C IV 5808 Å), for the binaries AB8, Br22, Br31, Br32, WR9 and WR30a, as calculated in Chapter 4.

[b] $\Delta v_{\rm r} = \bar{v}^{\circ}_{\rm obs} - v_{\rm mil}$ or $\bar{v}^{\circ}_{\rm obs} - \gamma$(OB) when $v_{\rm mil}$ not available.

companion, while the combined mass of both components of the binary system is 50 $M_{\odot}$. A circular orbit is assumed, since the real interest here is to check for RLOF systems, which will always have their orbits circularised if the original orbit was elliptical. A typical inclination of $i = 60°$ is assumed, as well. From

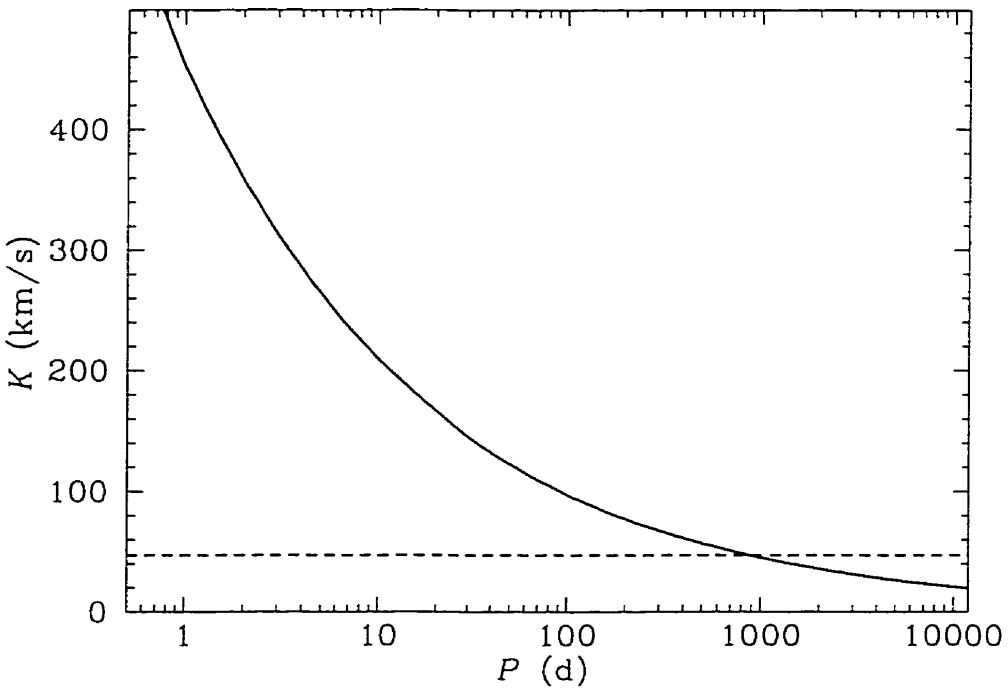

Figure 3.3: *Spectroscopic velocity amplitude as a function of period for a hypothetical binary WR-star with a combined mass of both components of* 50 $M_{\odot}$ *and* $i = 60°$. *The WR-star mass is half that of its companion. The solid curve is the amplitude function and the dashed line represents the level of the standard deviation for the Nov. 1993 mission.*

this figure it is apparent that binaries with periods of up to a few months have amplitudes that are much higher than the standard deviation of RV inherent in the spectroscopic measurements. However, a period with a duration in years will yield velocity variations indistinguishable from the scatter produced by single stars.

For detection of long-period binaries, it should be considered that such stars (with periods of several months or years) could be at different orbital phases at each epoch of observation. Its average velocity (a better measure of the typical velocity of the star at a given orbital phase than an individual velocity) at each

epoch could be different from the others. With a short period binary, however, the star could complete several orbital cycles in a given epoch and so the average velocities between epochs will be similar, although noisy.

Duplicity is unlikely to be inferred by the FWHM of the CIV emission line. Unlike W_e, FWHM should not change with a change in continuum level. However, it is conceivable that the presence of a companion could lead to an increase of the WR wind speed (by reducing the gravitational potential of the star as discussed in Section 1.2), thereby increasing the FWHM.

There is no reason to believe that the systemic velocity of the Wolf-Rayet star would be affected by a companion.

These quantities can be plotted to indentify correlations for which binary stars stand out. In Figures 3.4, 3.5, 3.6, 3.7, 3.8 and 3.9 (pages 37–40), σ_{v_r}, M_V, and FWHM are respectively plotted as a function of equivalent width; the absolute value of the velocity change between two epochs, $|\Delta\mathrm{RV}|$, is plotted as a function of σ_{v_r}. The choice of abscissa is somewhat arbitrary; the emphasis is on a parameter (such as W_e) that is most likely to be affected by the presence of a companion. In all figures, square symbols designate those stars that are certain to be binary (based on an ensemble of criteria), while circles show the rest. Filled symbols refer to stars without apparent companions diluting their light; open symbols designate stars that are optical doubles that could not be separated. Some stars also have an additional larger concentric open symbol, designating stars with OB lines in their spectra. Concentric squares show such stars whose magnitudes have been corrected for the OB light photometrically, while concentric circles mean that the magnitudes have not been so corrected.

A strong correlation with duplicity appears in Figure 3.4 on page 37, where σ_{v_r} is plotted against equivalent width. All known short-period binaries appear in the upper left-hand corner (cordoned off by the horizontal and vertical hatched bands, which are an estimation of borders that might help separate binary stars from single ones for a given parameter), a result of their high radial velocity variations and diluted light. MG6 also appears near the known binaries. Its

spectrum, however, is greatly diluted by nearby stars and is thus noisy. Varying slit placement over the complex of stars will change the composite spectrum obtained and, consequently, the radial velocity found from night to night. Such a star could, therefore, appear to have spuriously enhanced brightness and increased σ_{v_r}, but still be single. Several other stars with OB lines are diluted in W_e but have little variation in σ_{v_r}. These are unlikely to be binaries unless they are of long period or of very low inclination. The stars in the lower right-hand corner are probably single.

When absolute magnitude is plotted as a function of equivalent width (Figure 3.5 on page 38), all WC-stars with diluted light appear in the lower left-hand corner and there is a separation of stars with OB spectral lines (to the lower left-hand side) from those without. The known binary stars are mixed in this part of the plot. This plot does separate binaries from single stars, but less sharply than does Figure 3.4. It appears, however, that M_V might be correlated to W_e even for single stars (note dashed line). This might confirm the postulate of Smith, Shara & Moffat (1990a) that the flux of the emission line, F_e $(= I_c W_e)$, be approximately constant for WC-stars of the Large Magellanic Cloud. Since

$$I_c = 10^{-0.4(M_V+5)}, \qquad \text{then}$$

$$M_V = \frac{\log W_e - \log F_e}{0.4} - 5.$$

This function is plotted in Figure 3.5 as the dashed line for $F_e = 800$ (in arbitrary units since flux information is lost during rectification of the spectra). This line is not a fit and is only illustrative.

There is much scatter, however, in Figure 3.5. This might be due to the expected small variation in absolute magnitude for stars of the same spectral sub-type. The points would not fall on a thin curve but, rather, within an envelope of the same form.

The absolute value of the velocity difference between the 1984 mission and the Nov. 1993 mission is plotted *versus* σ_{v_r} in Figure 3.6 (page 38) and between Jan. 1993 and Nov. 1993 in Figure 3.7 (page 39). To test the significance of the

velocity difference, the combined normalised standard deviation was calculated in each case. Given this quantity for Epoch 1 and Epoch 2, $\sigma_{v_1}/\sqrt{N_1}$ and $\sigma_{v_2}/\sqrt{N_2}$, respectively, the combined normalised standard deviation was found from

$$\sigma_{\Delta v_{1,2}} = \sqrt{\left(\frac{\sigma_{v_1}}{\sqrt{N_1}}\right)^2 + \left(\frac{\sigma_{v_2}}{\sqrt{N_2}}\right)^2}.$$

The known short-period binaries AB8, Br22, Br31 and Br32 all fall in the lower right-hand corner of the plot of Figures 3.6 and 3.7. This is to be expected with their large combined normalised standard deviation and an average velocity that will be observed to be unchanged between epochs.

The stars Br7, Br8, Br44, Br87 and Br94 appear in the upper left-hand part of Figure 3.6. They have small combined normalised standard deviations. Stars that appear in this part of the plot could be long-period binaries, since they would be expected to show changes in velocity over epochs but have low standard deviations within an epoch, as discussed above. Niemela (1995) claimed radial velocity variations over several years for Br44 and suggested that it might be a long-period binary. Perhaps the other four stars might be long-period binaries as well, although Br7 and Br8 have no OB absorption lines in their spectra.

In Figure 3.7, MG6 (and, to a lesser extent, Br28, Br87 and Br94) has a large radial velocity difference but small combined normalised standard deviation. This could indicate that it is a long-period binary. However, the accuracy of the velocity measurements is to be doubted and its apparently large velocity difference might be due to measurement errors stemming from its noisy emission profile.

As expected, the plot of radial velocity in excess of the milieu velocity as a function of W_e shows no sensitivity to duplicity (Figure 3.8 on page 39). Although all of the known binaries are in the left-hand section of the plot, so are many other stars.

Finally, the FWHM of the CIV line does not appear to be dependent on whether or not a star is binary (Figure 3.9, page 40). Apparently, a companion does not increase the stellar wind speed significantly.

In these plots, the position of Br93 tends to stand out from the rest with an extremely high equivalent width. This is to be expected as it is a WO-star, which has a very powerful wind and will produce a line profile with great equivalent width.

Interestingly, Δv_r and FWHM tend to be negatively correlated to each other. This could have a bearing on wind structure. As well, a study of the ratios of equivalent widths of various emission lines leads to suggestions of finer sub-classification and abundance changes during evolution of stars within the WC4 class leading to WO. Both of these investigations are reported in Appendix F.

The binary status and classification criteria of the stars are summarised in

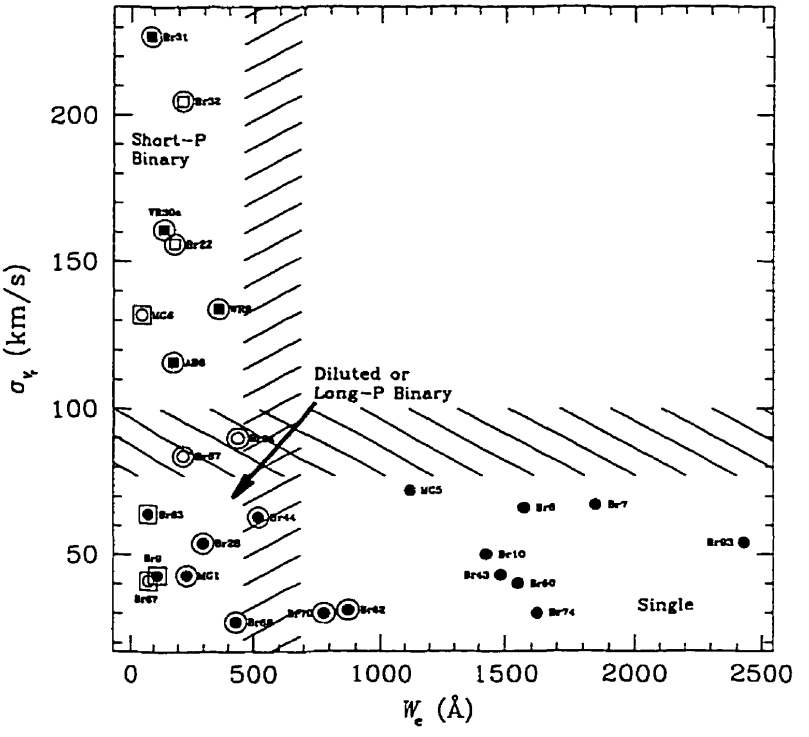

Figure 3.4: *RV dispersion (σ_{v_r}) correlation with* C IV *equivalent width (W_e). In this figure through to Figure 3.9, the symbols are: squares — certain binaries, circles — not certain binaries, filled — light not diluted by companions, open — unseparated optical doubles; concentric symbols — OB lines in spectra, concentric squares — magnitudes corrected for OB light, concentric circles — magnitudes not corrected for OB light. Hatched bands are used to attempt to separate binary stars from single ones for a given parameter.*

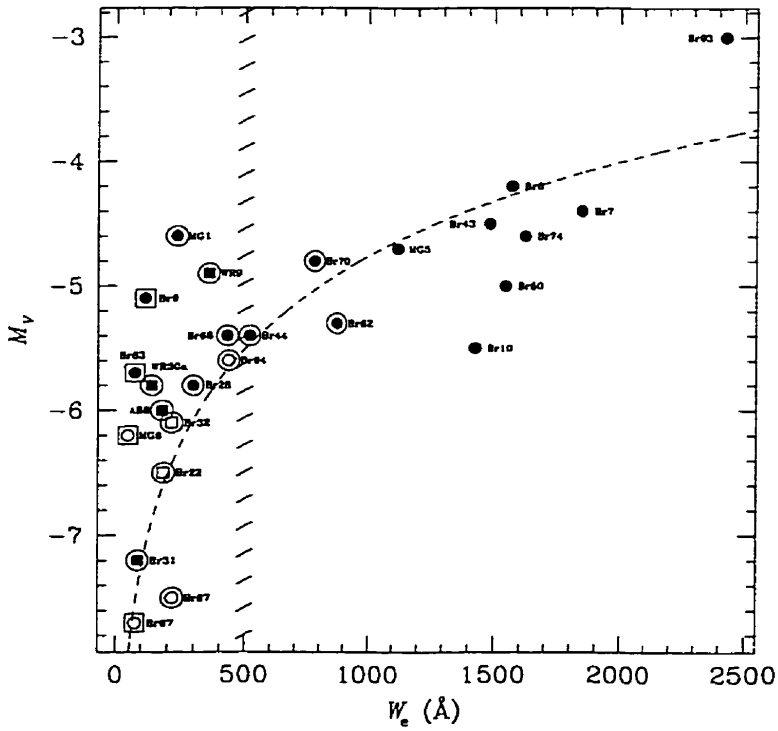

Figure 3.5: *Absolute magnitude correlation with* CIV *equivalent width (W_e). The dashed line illustrates the apparent correlation between M_V and W_e.*

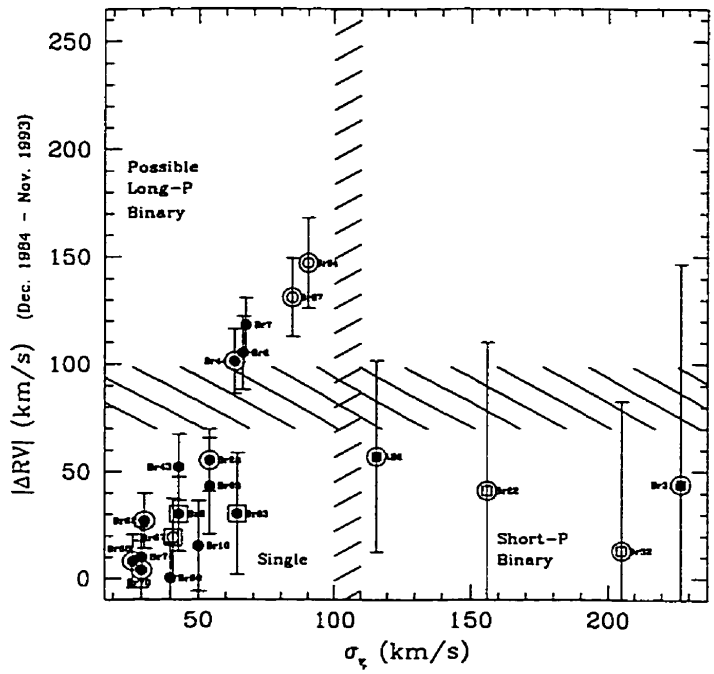

Figure 3.6: *Radial velocity difference (absolute value) versus standard deviation between the Dec. 1984 and the Nov. 1993 missions. Error bars indicate combined normalised standard deviation.*

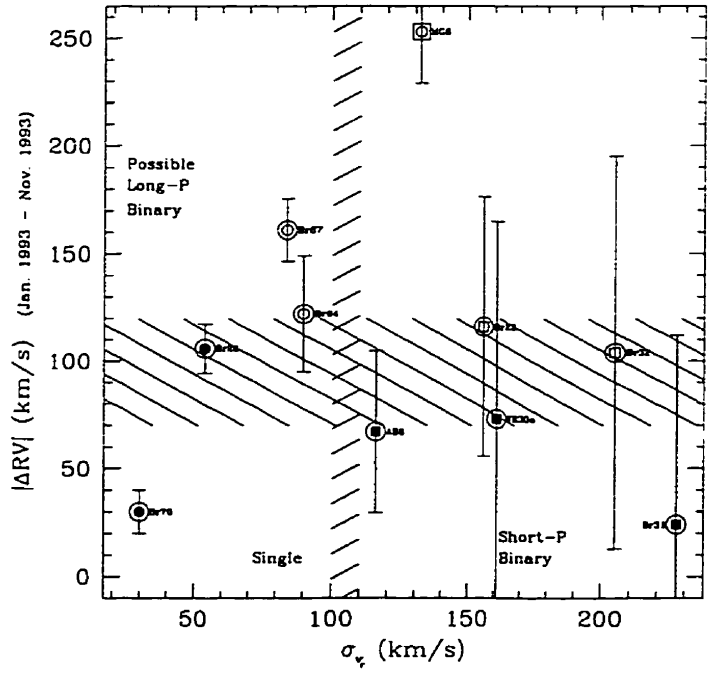

Figure 3.7: *Radial velocity difference (absolute value) versus standard deviation between the Jan. 1993 and the Nov. 1993 missions. Error bars indicate combined normalised standard deviation.*

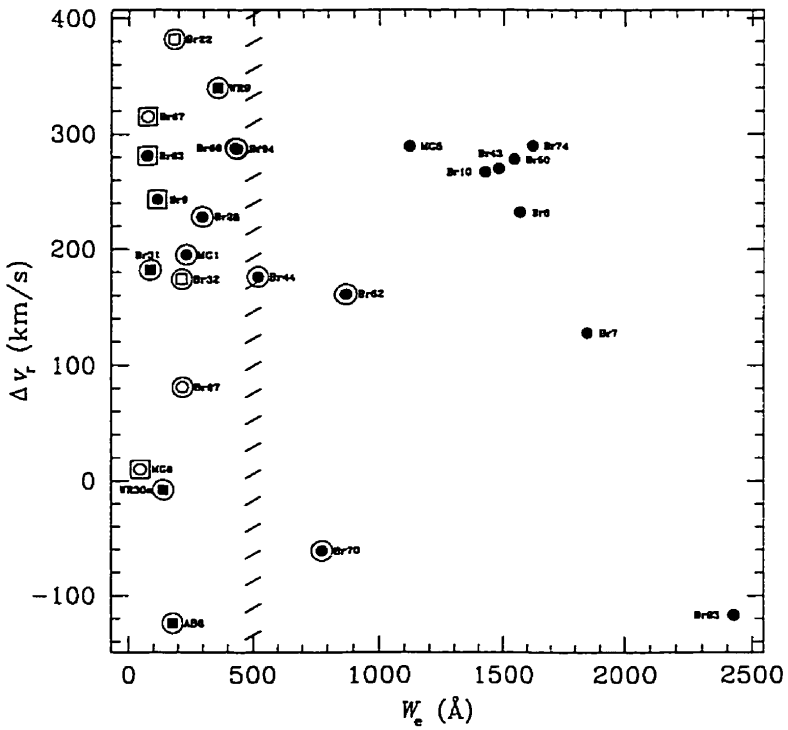

Figure 3.8: *Excess RV (Δv_r) correlation with* CIV *equivalent width (W_e).*

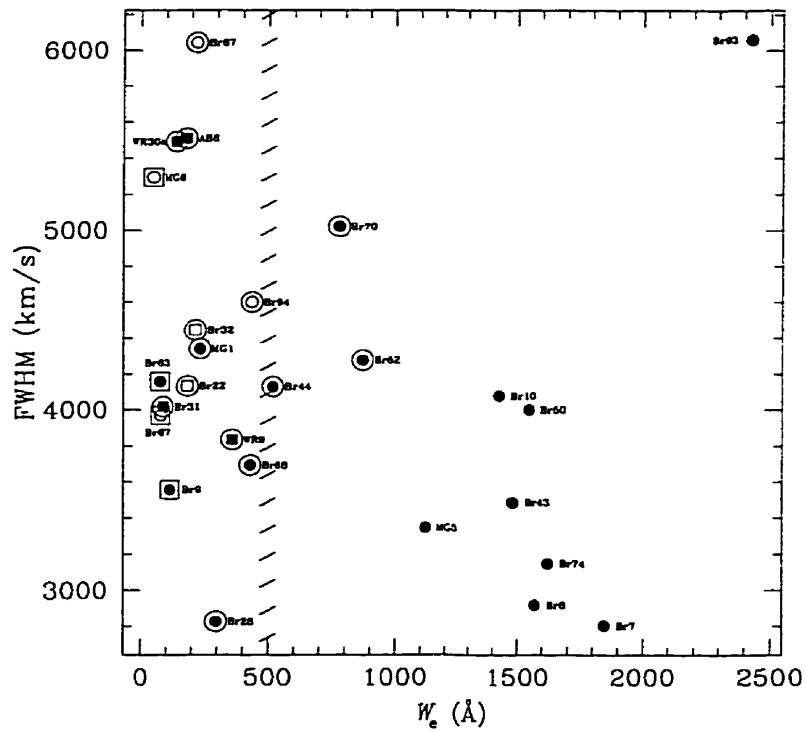

Figure 3.9: *FWHM correlation with* CIV *equivalent width* (W_e).

Table 3-IV on page 41. The previously denoted spectral type of each star is given, along with the reference from where it is obtained. This is followed by the spectral type assigned in this work. The presence of visual companions that could affect the spectrum is indicated. This was determined by inspection of the photometric results in Appendix B. Finally, the estimated binary status of each star is indicated (see below for an explanation of the choices made). The line strength ratio CIII/OV (see Appendix F) is included in this table as it is useful for stellar classification.

It is interesting to note that the line strength ratio CIII/OV is below 0.7 for all stars (after correction for wind-wind interaction, the ratio falls well below 0.7 in Br22 and WR9), consistent with all WC stars being of sub-class WC4 or WO (Figure 3 of Smith, Shara & Moffat 1990b).

Table 3-IV: *Spectral type and binarity of observed stars. The last column lists the equivalent width ratio between the* C III *5696 Å and the* O V *5592 Å lines.*

Star	Previous Sp.-type[a]	Ref.	Adopted Sp.-type[b]	Visual comp.?	Orbiting binary?[c]	$\frac{\text{C III}}{\text{O V}}$
Br7	WC4	1	WC4	no	no(?)	0.14
Br8	WC4	1	WC4	no	no(?)	0.36
Br9	WC4+O9.5II:	1	WC4(+O9.5II:)	yes	no	0.46
Br10	WC4	1	WC4	no	no	0.32
Br22	WC6+O5-6V-III	2	WC4+O5-6V-III(+O)	yes	SB2	2.96[d]
Br28	WC4+OB	1	WC4+OB	no[e]	no(?)	0.21
Br31	WC4(+O?)+O8I:	2	WC4[+O8I:]	no	SB1	0.43
Br32	WC4+O6V-III	2	WC4+O6V-III(+O)	yes	SB2	0.15
Br43	WC4	1	WC4	no	no	0.23
Br44	WC4+OB	1	WC4(+OB)	yes	no(?)	0.05
Br50	WC4	1	WC4	no	no	0.32
Br62	WC4+OB	1	WC4(+OB)	yes[f]	no	0.05
Br67	WC4+OB	1	WC4(+OB)	yes	no	0.30
Br68	WC5+OB	1	WC4(+OB)	yes	no	0.42
Br70	WC4+OB?	1	WC4+OB[g]	(no)	no	≈ 0
Br74	WC4	1	WC4	no	no	0.18
Br83	WC4+OB	1	WC4(+OB)	yes	no	0.43
Br87	WC4+WN6	1	WC4(+WN6+O)	yes	no(?)	0.06
Br93	WO4	3	WO4	no	no	≈ 0
Br94	WC4+OB	1	WC4(+OB)	yes	no(?)	0.13
MG1	WC4?+O	1	WC4+O[h]	no	no	0.04
MG5	WC4?	1	WC4	no	no	0.65
MG6	WC4?+O6	1	WC4(+O)	yes	no(?)	0.01
AB8	WO4+O7	3	WO4+O7	no	SB2	≈ 0
WR9	WC5+O7	4	WC4+O7	no	SB2	1.47[i]
WR30a	WO5+O4	3	WO5+O4	no	SB2	0.17

References: 1: Smith, Shara & Moffat 1990a
2: Moffat, Niemela & Marraco 1990
3: Kingsburgh, Barlow & Storey 1995
4: van der Hucht *et al.* 1988

[a]The previously denoted WC4? star MG4 is now known to be WN (Morgan & Good 1987).

[b]Round parentheses indicate that the absorption-line spectrum might arise in ***visual*** OB companions; the square parentheses show that there is an unresolved, non-orbiting OB-star.

[c]A question mark in parentheses indicates that there is eviidence that the star might be a long-period binary.

[d]$\approx$ 0.21 after allowing for the wind-wind collision contribution (Chapter 5)

[e]very close optical pair?

[f]very weak absorption

[g]spectrum close to WO; very weak absorption

[h]weak absorption

[i]$\approx$ 0.07 after allowing for wind-wind collision (Chapter 5)

Using the above results, the estimated binary status of the Magellanic WC-stars may be summarised as follows:

Definitely SB : Br22, Br31, Br32, AB8

Possibly SB : Br28, Br44, Br87, Br94, MG6

Probably single : Br7, Br8

Almost certainly single : Br9, Br10, Br43, Br50, Br62, Br67, Br68, Br70, Br74, Br83, Br93, MG1, MG5.

With their high velocity dispersions (*cf.* Figure 3.4) the stars Br22, Br31, Br32 and AB8 are clearly binary. They have all been noted as such by previous investigators.

MG6 is a potential binary star due to its high radial velocity dispersion shown in Figure 3.4. It also appears to have radial velocity variations between epochs (Figure 3.7). All of this, however, could be due to the very noisy spectral data obtained for this star, no doubt due to crowding (see Appendix B), yielding poor radial velocity results.

The stars Br87 and Br94 have moderately high σ_{v_r}, appearing on a borderline region to the known binaries (Figure 3.4). They also show large changes in average radial velocity between epochs (see Figures 3.6 and 3.7). Both stars, however, have unresolved companions and the spectrum of Br87 is contaminated by the light of a binary WN-star (Moffat *et al.* 1987), so that nothing certain can be said of these two.

Br28 and Br44 are listed as *Possibly SB* as well because of their RV changes between epochs (Figure 3.6 for Br44 and Figure 3.7 for Br28). They might be long-period binaries.

The stars Br7 and Br8 are listed as *Probably single* since the only evidence that they might be binary is the radial velocity differences between epochs (Figure 3.6). They have the large equivalent widths and lower brightness of single stars (*cf.* Figure 3.5) and even lack the presence of OB absorption lines.

In fact, all of the potential binary stars would require periods of at least

several months. Any star with a period of less than a month would produce radial velocity variations, σ_{v_r}, that would be noticeable (unless the inclination of the system were fortuitously very close to zero).

Without more spectroscopic data, the only Magellanic WC-stars whose orbits can be studied usefully (see Chapter 4) are the four classified as *Definitely SB*.

3.4 Implication for evolutionary scenarios

By use of Maeder's theory, the binary frequency of the LMC Wolf-Rayet stars was predicted to be at least fifty-two percent, with an error of fourteen percent (Section 1.2). He noted that, for an environment of such low metallicity, the formation of many such stars would require a companion whose gravitational potential would provoke the massive primary to lose its outer layers. This prediction must be viewed as a minimum binary frequency, since long-period binaries are not subject to such Roche-lobe effects and would evolve like single stars.

However, only three of the twenty-three LMC stars in the present study are definitely binary. This is only just over 13%. This seems to be much smaller than the prediction. Is the theory to be rejected? It must be determined if the observed binary frequency is compatible with the theory. The studied stars only constitute a sample and do not necessarily constitute the entire population of WC-stars of the LMC. There might be other stars that have yet to be discovered in this galaxy. There are those stars that might have existed in the past and have become supernovæ, while others might have yet to evolve in the future. Other galaxies might have WC-stars in environments of similar metallicity. The sample could simply be an aberration.

The statistical test of the hypothesis used was the cumulative binomial probability P that k or fewer binaries would be detected in n observed stars with a probability p that any given star would show duplicity, so that

$$P \equiv \sum_{m=0}^{k} \left(\begin{array}{c} n \\ m \end{array} \right) p^m (1-p)^{n-m},$$

where $n = 23$. These probablities were calculated for $p = 0.52 \pm 0.14$ and k varying from 0 to 23. The results are displayed in Figure 3.10 on the following page, with significance levels at one percent and five percent indicated. The data disprove the hypothesis that the binary frequency should be at least 52% at the one percent significance level. The hypothesis is disproven, at the same level of significance, even if the lower extreme binary frequency of 38% is assumed.

What of the stars judged to be possibly binary? Inclusion of such stars would provide compatibility with the predicted minimum binary frequency, except at its upper limit. However, such stars, if binary, would likely be of very long-period (more than several years). They would be expected to evolve as single stars. None of these stars have shown duplicity in this study.

Perhaps some the stars deemed single were once part of binary systems but are now runaways (former binaries whose companions became supernovæ). These could be candidates for short-period binaries that could render the sample compatible with Maeder's theory. This, however, is unlikely since the stars presumed to be single tend to have normal radial velocities (Figure 3.8). The velocities of runaways should be randomly distributed as there is no reason for the stars to be ejected from a disrupted binary system in a preferential direction. (Br93 has a significantly different radial velocity from the other almost certainly single stars, but, as mentioned briefly in Section 3.3 and discussed in Appendix F, this could very well be due to the structure of the fast wind of a single star.) With only one WC/WO star in the SMC, no conclusion can be drawn there.

With these results, it can only be concluded that Wolf-Rayet stars can evolve without the need of a binary companion, even in a low metallicity environment. Maeder's proposed evolutionary mechanism does not explain the large number of WR-stars in the Large Magellanic Cloud. Consequently, such models do not offer an explanation for the formation of WR-stars. It seems that the mass-loss rate of O-stars, Of-stars and supergiants might be higher than predicted. Perhaps the strong winds of massive stars dominate any gravitational influence by even a close companion (confirmed with Figure 3.9). Evidence for strong winds can be

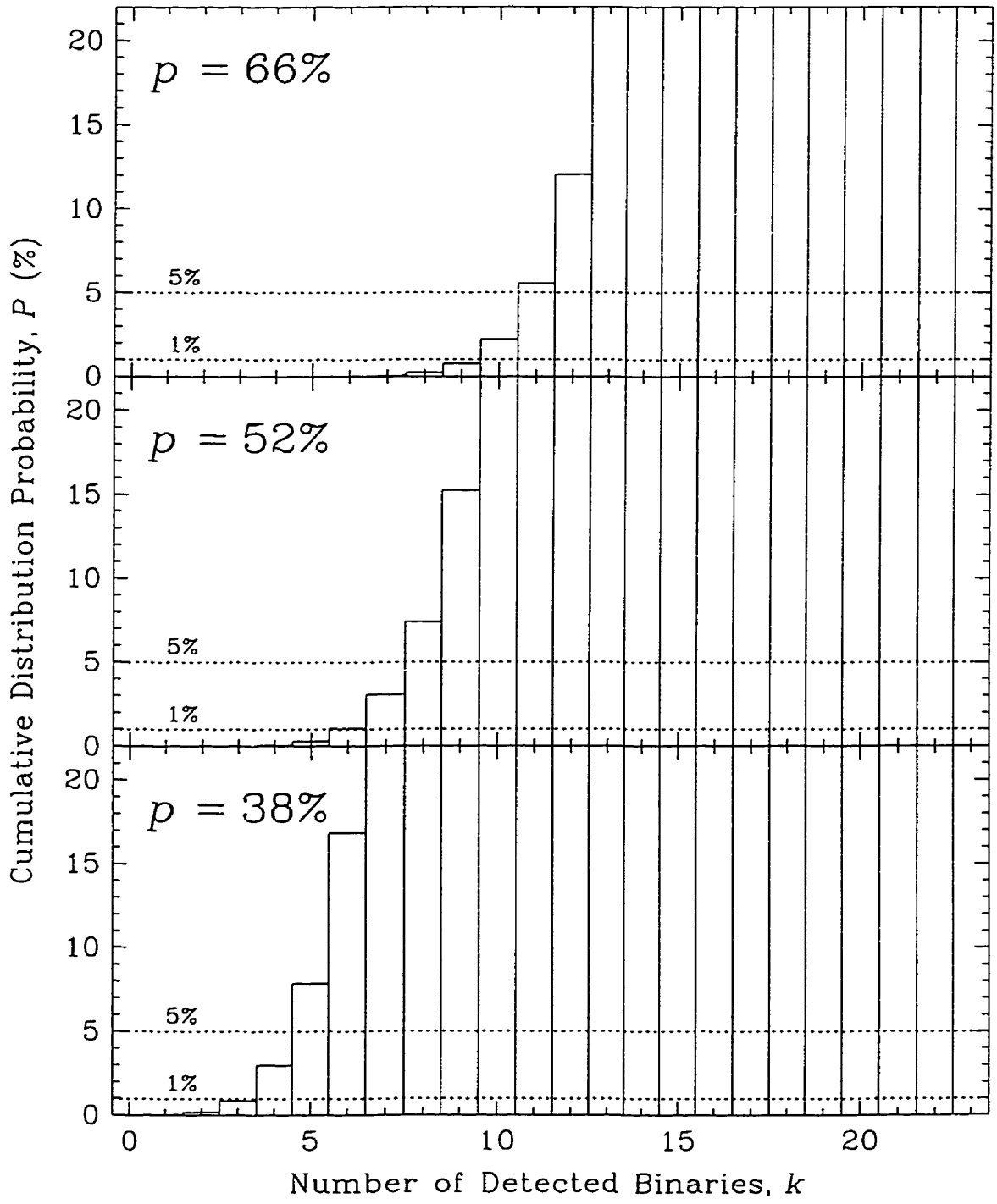

Figure 3.10: *Cumulative binomial probabilities for expected binary frequency of* $p = 0.52 \pm 0.14$. *The dotted lines show significance levels at 1% and 5%.*

seen in WR binaries *via* emission excess from wind-wind collisions.

Chapter 4

RV Orbits of the WC/WO+O Binaries

As described in the previous chapter, four certain WC+O binaries in the Magellanic Clouds were found. The next goal, as noted in Chapter 1, is to study their colliding winds. The proper study of line profile variations due to colliding stellar winds first requires the determination of an accurate orbital ephemeris for each star so as to know the orbital phase at the time of observation. An accurate period is crucial for this. To depend on previously published periods (such as those of Moffat, Niemela & Marraco 1990, hereafter MNM) for AB8, Br22, Br31 and Br32 would have been unsatisfactory, since the data used in the current study span a much longer interval (nine years). In particular, two of the stars have periods in the range of two to three days. The precision of the periods of MNM does not allow extrapolation over the more than one thousand cycles that have elapsed during the nine years without confusing the phases unacceptably.

The two Galactic WC+O binaries were also studied. This is the first publication of an orbit for WR30a.

4.1 Period search

According to MNM, the stars Br31 and Br32 have circular orbits, while the stars AB8 and Br22 have orbits of eccentricity $e \lesssim 0.2$. In view of such small values, it is fair to say that all four stars have nearly circular orbits, so that the orbital period can be estimated reliably by fitting the radial velocities determined from the CIV 5808 Å emission line to a sinusoidal curve, defined by

$$v_r(t) = v_\gamma + K \sin\left[\frac{2\pi}{P}(t - t_0)\right], \tag{4.1}$$

where $v_r(t)$ is the measured radial velocity (RV) at the time of observation t; v_γ is the mean RV, which, for well behaved lines, is the systemic RV of the mass centre; K is the RV amplitude of the orbit; P is the orbital period; and t_0 is the time of origin of the orbit at zero phase, *i.e.* when the star passes through inferior conjunction.

Equation 4.1 is non-linear and implicit in the parameters P and t_0. It can be made an explicit function of t_0 by noting that a sine function can be written as a sum of sinusoidal and cosinusoidal functions, so that

$$K \sin\left[\frac{2\pi}{P}(t - t_0)\right] \equiv K_1 \cos\left(\frac{2\pi}{P}t\right) + K_2 \sin\left(\frac{2\pi}{P}t\right),$$

where $K = \sqrt{K_1^2 + K_2^2}$. To find t_0, one can write

$$K_1 \cos\left(\frac{2\pi}{P}t_0\right) + K_2 \sin\left(\frac{2\pi}{P}t_0\right) = 0,$$

so that

$$t_0 = -\frac{P}{2\pi} \arctan\frac{K_1}{K_2}.$$

With fixed period, a general, linear least-squares fit of $v_r(t)$ can be made to determine v_γ, K_1 and K_2, from which one can calculate K and t_0.

The period, of course, is the main object of this procedure. Including P as a parameter to be fit would have required a non-linear least-squares fit. With real, noisy data, such fits are usually unstable. Instead, the period that gave the best fit was determined by fitting the sinusoidal curve successively for a series of

different periods (or, better, frequency, $f = 1/P$, since appropriate scanning of periodicity is normally done in constant steps of f). For a given fixed frequency, f, (starting at a minimum frequency, $f_{\min}$) a circular orbit was fit to the data. The resultant χ^2 value was noted (this figure-of-merit of the model, χ^2, is defined below). The frequency was then augmented by a small increment, Δf, and the fit was made again. This continued until the frequency reached a specified maximum, $f_{\max}$.

The figure-of-merit of the model is the value of χ^2,

$$\chi^2 = \sum_{i=1}^{n} \left(\frac{v_i(t) - v_r(t)}{\sigma_v} \right)^2 ,$$

where n is the number of data-points, $v_i(t)$ is the velocity of the datum i at time t, $v_r(t)$ is the corresponding velocity predicted by the model, while σ_v is the standard error of the velocity data (see below). For good fits, $\chi^2 \approx n - n_p$, where n_p is the number of free fit parameters.

Since the data were collected during three different missions with different instruments, three corresponding systemic velocities, $v_{\text{Dec84}}, v_{\text{Jan93}}$ and v_{Nov93}, were also allowed for and fitted. This takes into account any velocity shifts that were not due to changes in the velocity of the binary stars (such as inevitable systematic errors in instrumental calibration). Instead of v_γ, the vector $\vec{v}_\gamma = (v_{\text{Dec84}}, v_{\text{Jan93}}, v_{\text{Nov93}})$ was used. The model to fit then becomes

$$v_r(t) = \vec{e}(t) \cdot \vec{v}_\gamma + K_1 \cos\left(\frac{2\pi}{P}t\right) + K_2 \sin\left(\frac{2\pi}{P}t\right), \qquad (4.2)$$

where

$$\vec{e}(t) = \begin{cases} (1,0,0)\text{: } t \in \text{Dec. 1984 epoch} \\ (0,1,0)\text{: } t \in \text{Jan. 1993 epoch} \\ (0,0,1)\text{: } t \in \text{Nov. 1993 epoch.} \end{cases}$$

The routine used for the general, linear least-squares fit of the model described in Equation 4.2 was `svdfit` of Press *et al.* (1992, pp. 665–675). The standard errors of the data were chosen based on the dispersion of the radial velocities of the single WC-stars (see Appendix G). Different standard errors (σ_{v_e}) were so determined for each mission (Table 4-I on the next page).

Table 4-I: Epoch-dependent standard deviations (km/s).

Epoch	σ_{v_e}
Dec. 1984	33.4
Jan. 1993	26.1
Nov. 1993	47.2

The radial velocities used to make the period fit in CIV 5808 (and the orbital fits later) are listed in Appendix D.

The results of the fit procedure were examined to determine which frequency gave the best circular orbit fit. This frequency, however, was not necessarily the frequency ultimately chosen to be the period closest to the true period. Unpublished period searches, undertaken by MNM as part of their study of the same four WC/WO binary stars, were based mostly on other data. The period chosen was that which corresponded to a local minimum χ^2 in both cases, even if it was not necessarily the period of absolute minimum χ^2 in either case (see Figure 4.1 on the following page). Note that the minimum χ^2 is not necessarily equal to $n - n_p$; deviations by small factors can occur due to detailed variations of σ_v from one star to another that were not allowed for.

The periods of the four WC binary stars are listed in Table 4-II on page 53 in Section 4.2. The error in the period was estimated by finding the extent of the interval about the best period within which the change in the reduced χ^2 would be no greater than unity (see Appendix G). The circular fits are plotted in Figure 4.2 on page 54.

4.2 RV orbital parameters

As a test for non-zero eccentricity, an elliptical orbit was also fit to the radial velocity data of each star. The equation of such a curve is

$$v_r(t) = v_\gamma + K[\cos(\nu + \omega) + e\cos\omega], \tag{4.3}$$

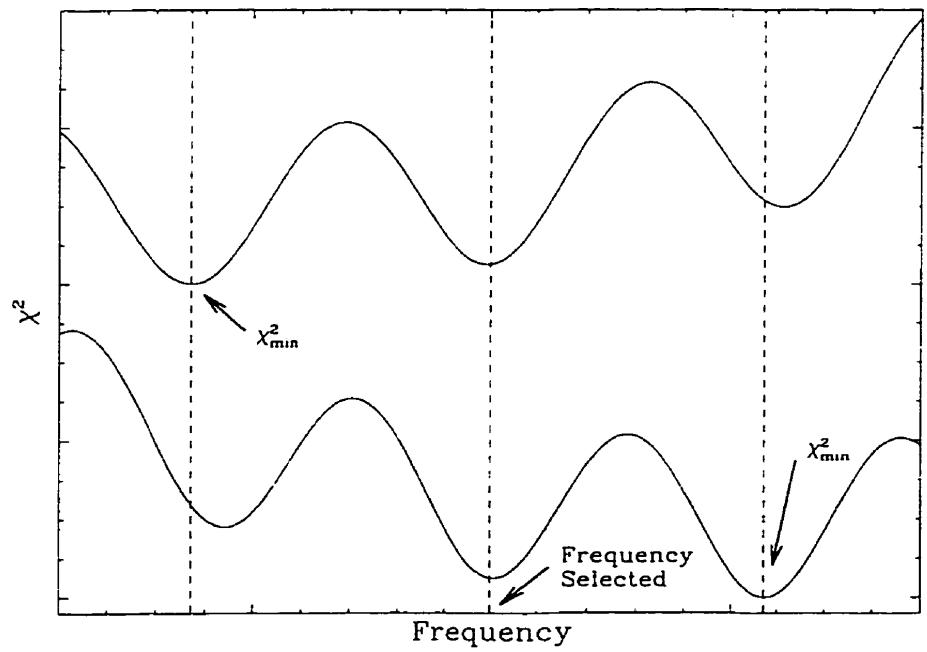

Figure 4.1: *Example of period selection. The top plot is a hypothetical periodogram from the data for a given star of this dissertation. The bottom plot is a hypothetical unpublished periodogram from MNM. The best overall period chosen is one that shows a local minimum in both periodograms, as shown.*

where ω is the angle between the ascending line of nodes of the system and the direction of periastron, ν is the true anomaly (the angle in the orbital plane from periastron to the position of the star, as seen from the centre of mass), and e is the eccentricity of the orbit. The quantities $v_r(t)$, v_γ and K are defined as in Equation 4.1. A derivation of this radial velocity curve is given by Petrie (1962). [Note that the excess emission from wind collision will distort the line profiles, even in CIV 5808 Å (see Chapter 5). This is not allowed for here since the effect is relatively small for CIV 5808 Å. As well, the orbits based on this line are in anti-phase with the undistorted O-lines (MNM).]

As for sine-wave fits, v_γ is replaced by the systemic velocity for each epoch so that Equation 4.3 is transformed to

$$v_r(t) = \vec{e}(t) \cdot \vec{v}_\gamma + K[\cos(\nu + \omega) + e\cos\omega]; \tag{4.4}$$

$\vec{e}(t)$ and $\vec{v}_\gamma$ are as in Equation 4.2.

The true anomaly is related to time *via*

$$\tan\frac{\nu}{2} = \sqrt{\frac{1+e}{1-e}}\tan\frac{E}{2},$$

with the eccentric anomaly, E, found from

$$E - e\sin E = \frac{2\pi}{P}(t-T) = M,$$

where M is the mean anomaly. T is the time of periastron passage.

The CIV 5808 Å radial velocity data were fit by Equation 4.4 using E04UPF, a non-linear least-squares optimising routine of the NAG FORTRAN library. The parameters fit were $\vec{v}_\gamma$, K, ω, T and e (P, taken from the period found from circular fits, was fixed). Errors on these parameters were estimated from the diagonal of the covariance matrix, itself derived from the Jacobian matrix that was calculated at the optimal point (Press *et al.* 1992, pp. 666–667, 676–678).

The results for both circular and elliptical fits for the MC binaries are listed in Table 4-II on the next page and are shown in Figure 4.2 (pages 54 and 55). Only circular fits for the two Galactic stars are listed in Table 4-III on the following page, with curves shown in Figure 4.3 on page 56. Both emission line curves and HeII 5412 Å absorption line orbits were studied for the Galactic stars (the absorption line velocities were estimated by applying Gaussian fits to the line profiles, with a sloping base estimated from neighbouring points of the HeII emission line of the WR-star). The standard deviations of the absorption line velocities were assumed to be unity since no errors for these velocities were available.

Included in Table 4-II is a measure of the probability that the eccentricity found could have exceeded one found for a random set of data from a circular orbit (p). This is calculated using the statistical test of Lucy & Sweeney (1971), derived from the theory of testing multivariate linear hypotheses.

In two MC cases, the elliptical model fits the data better then does the circular one. However, it cannot be assumed that the orbits are necessarily eccentric. These fits might be mathematically better simply because there are additional parameters that can be adjusted to generate curves that more closely match the

Table 4-II: *Fit parameters of C IV 5808 Å for circular and elliptical orbits for the four binary MC stars. All velocities are in km/s and dates are Heliocentric Julian Days minus 2 440 000. E_0 is the HJD of origin for the orbital phase, corresponding to the time of inferior conjunction of the WR component.*

Parameter	Br22	Br31	Br32	AB8
P (d)	14.926 ± 0.006	3.0328 ± 0.0001	1.9169 ± 0.0001	16.633 ± 0.009
Circular orbit				
v_γ (Dec. 84)	638 ± 11	453 ± 11	442 ± 13	66 ± 10
v_γ (Jan. 93)	670 ± 12	532 ± 08	468 ± 09	50 ± 12
v_γ (Nov. 93)	617 ± 12	474 ± 12	430 ± 09	74 ± 12
K	211 ± 10	322 ± 09	291 ± 08	156 ± 10
E_0	6027.1 ± 0.1	6037.80 ± 0.01	6039.820 ± 0.009	6032.9 ± 0.1
χ^2_ν	0.49	0.89	1.64	0.50
Elliptical orbit				
v_γ (Dec. 84)	638 ± 08	451 ± 16	451 ± 26	66 ± 10
v_γ (Jan. 93)	666 ± 09	532 ± 07	455 ± 03	50 ± 13
v_γ (Nov. 93)	614 ± 09	474 ± 12	435 ± 10	74 ± 13
K	223 ± 09	325 ± 14	296 ± 18	157 ± 12
T	9022.7 ± 0.6	9017.5 ± 0.5	9038.41 ± 0.15	9322.8 ± 6.6
E_0	6056.8 ± 0.8	6043.874 ± 0.020	6042.88 ± 0.19	6057.88 ± 0.15
ω (degrees)	160 ± 15	83 ± 60	2 ± 28	197 ± 141
e	0.12 ± 0.03	0.04 ± 0.04	0.13 ± 0.05	0.03 ± 0.06
χ^2_ν	0.26	0.89	1.26	0.53
p (%)	0.018	34	0.38	78

Table 4-III: *Fit parameters of C IV 5808 Å for circular orbits for the Galactic binaries WR9 and WR30a. All velocities are in km/s and dates are Heliocentric Julian Days minus 2 440 000. E_0 is the HJD of origin for the orbital phase, corresponding to the time of inferior conjunction.*

Parameter	WR9		WR30a	
P (d)	14.305[a]		4.625 ± 0.006	
Circular orbit	Emission	Absorption	Emission	Absorption
v_γ (Dec. 84)	—	—	—	—
v_γ (Jan. 93)	—	—	-90 ± 14	-22 ± 55
v_γ (Nov. 93)	321 ± 12	-7 ± 19	-68 ± 13	3 ± 30
K	186 ± 19	56 ± 28	207 ± 13	102 ± 37
E_0	6032.95 ± 0.20	6039.2 ± 1.1	6038.696 ± 0.051	6036.15 ± 0.28
χ^2_ν[b]	0.65	—	1.01	—

[a]Period from Niemela, Massey & Conti (1984), since they based it on more observations and over several epochs. They give no error and it is assumed here to be 0.001. The period found with the data described in this Dissertation is 15.6 ± 3.2 d, based on only one epoch.

[b]For the absorption, no error estimates are available to yield χ^2_ν.

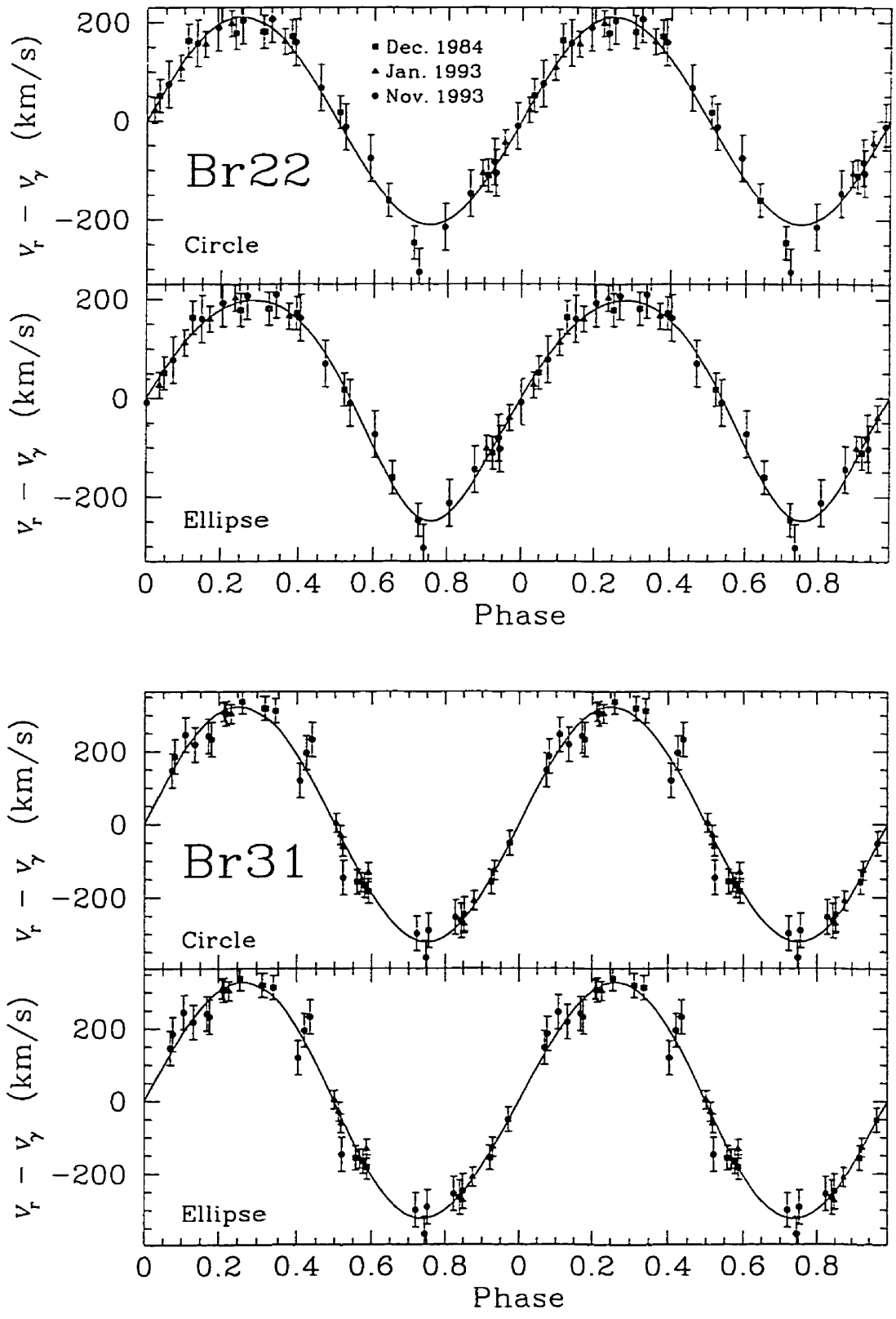

Figure 4.2: *Circular and elliptical RV fits to* C IV *5808 of the four certain MC binaries. The velocities shown are the observed radial velocities with the epoch-dependent systemic velocities subtracted. The point shape denotes epoch of observation. The origin of the phases are based on E_0 for circular orbits and T for elliptical orbits.*

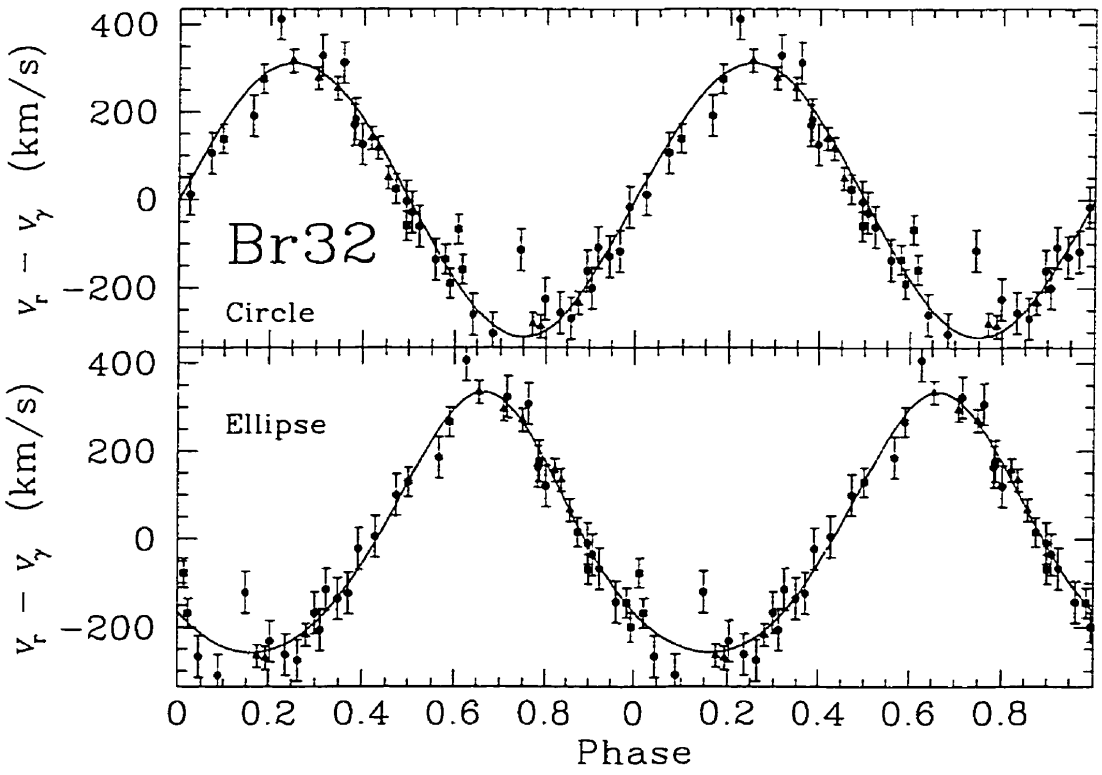

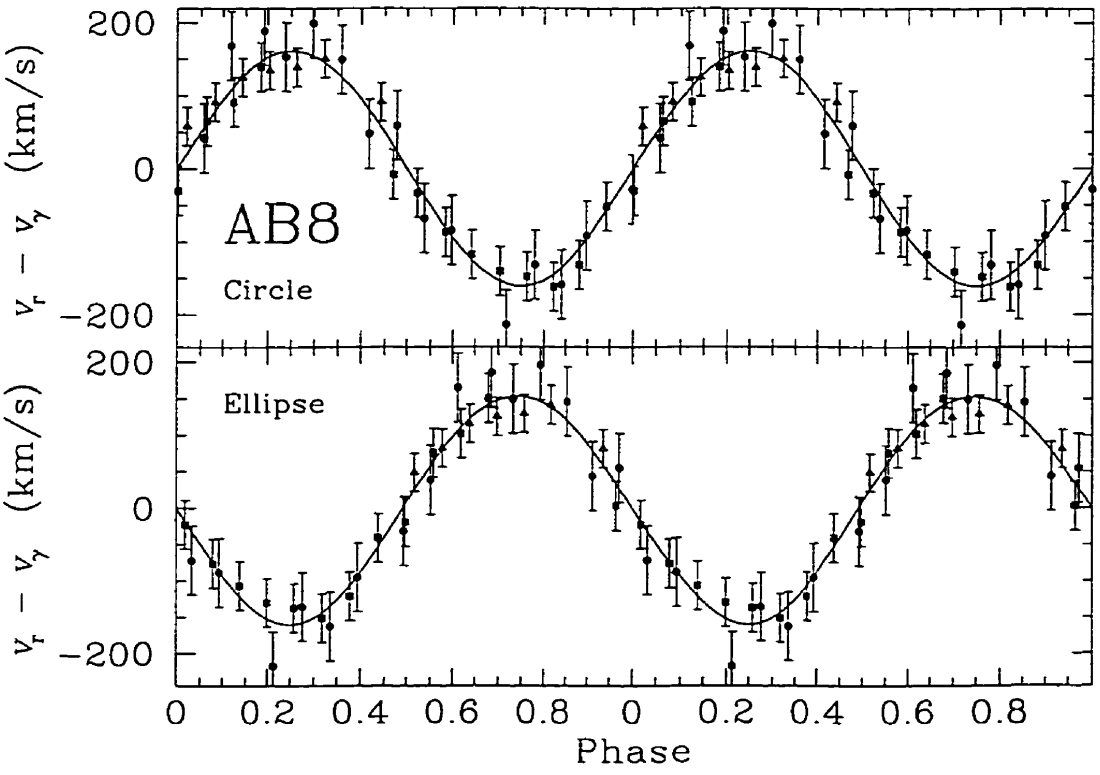

Figure 4.2 ... continued.

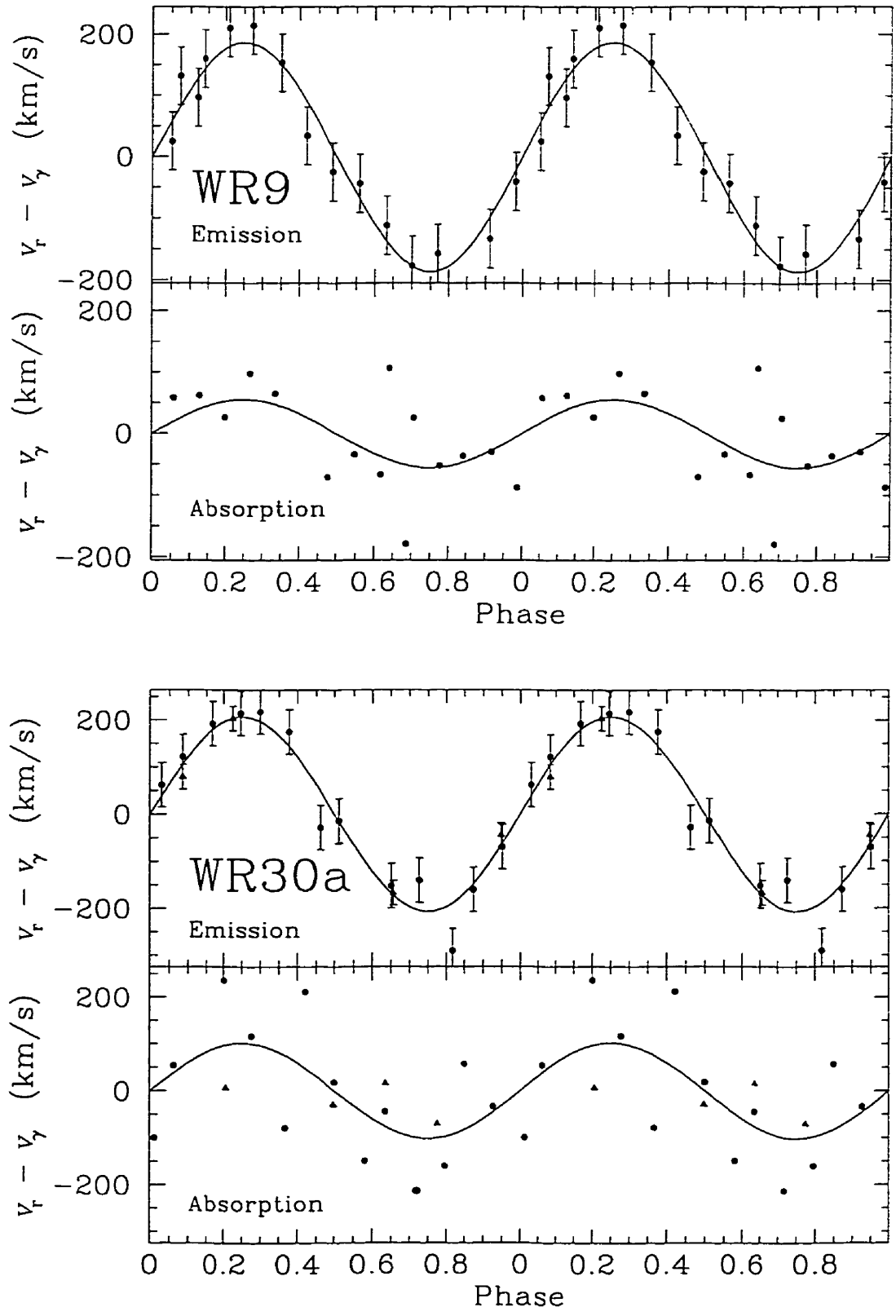

Figure 4.3: *Circular RV fits of absorption and emission features of the two Galactic WC-stars. Phase 0 (absorption): O-star in front; phase 0 (emission): WR-star in front. The symbols are the same as in Figure 4.2.*

data. The model, however, might be physically less plausible than its circular counterpart.

In the cases of Br31 and AB8, the ratio of χ^2_ν of the circular fit to that of the eccentric orbital fit is very close to unity (1.00 and 0.94, respectively). Their p values are well above the five percent significance level. In addition, the error in the eccentricities for the elliptical models of both stars is comparable to the fit eccentricities themselves, making them indistinguishable from zero. (MNM claimed, however, an eccentric orbit for AB8 based on fewer, noisier data.)

The elliptical fit for the star Br22 yields an eccentricity that is far greater than its formal error. As well, the ratio of circular fit to elliptical fit χ^2_ν values is considerably greater than one (1.85). It also has a very small value for p. Br22 might have an elliptical orbit (but see later).

For Br32, MNM asumed a circular orbit because of its very short period. However, its fit eccentricity in the present data set is significantly larger than its error. Its ratio of circular-to-elliptical fit χ^2_ν is 1.28, greater than equivalent ratios for Br31 and AB8 but substantially less than that for Br22. It also has a low value for p, suggesting that the eccentricity might not be spurious.

Should it be assumed that Br32 has a physically real elliptical orbit on the basis of this mathematical result? A brief theoretical discussion on binary rotation might be enlightening:

A system has the least mechanical energy when it rotates uniformly. The motions of stars in binaries that do not have circular orbits have stresses and strains that dissipate energy as heat that is radiatively lost to space. Such stars eventually reach a state of minimum mechanical energy with circular orbits (and synchronised spins) (Tassoul & Tassoul 1996).

Stars of short period (and, therefore, closer together) will have greater straining and energy loss-rate than those of longer period. Zahn (1975) calculated that, for binary massive stars of short period (such as Br32), the circularisation and synchronisation time (10^5 yr) is much less than the nuclear lifetime of approximately 10^7 yr. As Br32 is of Wolf-Rayet class, it is near the end of its

nuclear burning time and its orbit is expected to have become circularised long ago. Br32 is presumed, therefore, to have a circular orbit and that the mathematically superior model with non-zero eccentricity is probably not physically real.

To study further the possibility of eccentricity in the orbit of Br22, a radial velocity fit was made using the velocities determined from the HeII 5412 Å absorption line. In this fit, the period and the eccentricity were fixed to the corresponding values shown in Table 4-II. The resulting fit had a very high error on ω (129°). Although these data are noisy, this suggests that there must be little or no eccentricity and that the result from fitting the velocity of the emission profiles may merely be mathematical, without physical meaning. Br22 is thus considered to have a circular orbit. All known MC binary stars, therefore, probably have circular orbits. In any case, RLOF, if any, should help circularise these orbits.

The orbits of the O-companions of the MC binaries were not studied further. They were better determined by MNM. The blue absorption lines that are best used for determining the motion were observed during only one epoch. However, such an attempt was made for the Galactic binaries with the HeII 5412 Å absorption feature. The results are listed in Table 4-III on page 53, with the fit models displayed in Figure 4.3 on page 56. Note that this is the first publication of a proposed orbit for WR30a and the second for a WO+O binary after AB8. The times of zero phase for emission and absorption differ by 6.2 ± 1.1 d$[(0.43 \pm 0.08)P]$ for WR9 and 2.5 ± 0.3 d $[(0.54 \pm 0.06)P]$ for WR30a. Within the errors, these differences are compatible with half an orbital cycle, as expected if they reflect truly orbital motion.

The mass ratio for WR9 is $M_{\rm WR}/M_{\rm O} = 0.30 \pm 0.15$ and that for WR30a is 0.50 ± 0.18. These are in the range found for WC binaries (Cherepashchuk 1991).

Neglecting Br31 and Br32, whose O-companion radial velocities may be reduced by visual companions (see Table 3-IV), the mass ratios $M_{\rm WR}/M_{\rm O}$ are in the range 0.3–0.4, within the errors, for the four remaining systems. Assuming

initial ratios greater than one, these small values are expected for highly evolved WR-stars reaching the WC4/WO stage *via* extreme mass-loss (*e.g.* Moffat 1995).

Chapter 5

Colliding Stellar Winds

A description of previous theory and observations of colliding winds is presented. This is followed by theoretical models that were developed to predict what line profiles should be obtained. The actual spectroscopic data are then modeled using these theories. An effort to obtain some parameters of the binary system, such as the inclination of the orbit and the opening angle of the colliding shock cone, was made from these models.

5.1 Theoretical aspects of colliding winds

Should there be any collision at all? Could not the two stellar winds simply diffuse into one another instead of striking in a shock? This will depend on the mean-free-path of the wind particles at the point of contact between the two winds. If this quantity is small, compared to the distance between the two stars, then each wind will suffer a discontinous jump in their respective densities and produce a shock.

Huang & Weigert (1982) estimated the mean-free-path for the winds of an early-type binary star consisting of neutral hydrogen. They calculated the ratio of the mean-free-path to the distance between the two stars to be about 2×10^{-7}. For the more realistic case of ionised particles in a wind, this quantity is even smaller. There should be virtually no diffusion of one stellar wind into the other

and shocked collisions are to be expected from massive binary stars.

5.1.1 The contact discontinuity

The shock of one wind will be separated from that of the other by a surface of contact discontinuity. This surface is defined by the momentum flux balance on the line joining the two winds. A wind's momentum flux is defined by ρv^2, where ρ is the density of the wind and v is its velocity. An equivalent expression for the momentum flux can be derived:

$$\begin{aligned} \rho v^2 &= \frac{dM}{dV}\frac{dl}{dt}v \\ &= \frac{dM}{dt}\frac{dl\,v}{dA\,dl} \\ &= \frac{\dot{M}v}{dA}, \end{aligned}$$

so that

$$\rho v^2 = \frac{\dot{M}v}{4\pi d^2}, \tag{5.1}$$

where dM is the mass of an infinitesimally thin cylindrical parcel of gas, dV is the volume of the parcel, dl is the height and dA is the area of the face of the cylinder. This parcel is at distance d from the star.

Assuming that the flows of both winds are at their respective terminal velocities and that orbital motion of the stars is neglected, the point of momentum flux balance between the two components (Star 1 and Star 2) of the binary system is described by the equation

$$\rho_1 {v_1}^2 = \rho_2 {v_2}^2,$$

where the numerical subscripts denote quantities that correspond to Star 1 and Star 2, respectively. By substitution of the formula of Equation 5.1 this relation becomes

$$\frac{\dot{M}_1 v_1}{4\pi {d_1}^2} = \frac{\dot{M}_2 v_2}{4\pi {d_2}^2}$$

so that (Stevens, Blondin & Pollock 1992)

$$\mathcal{R} \equiv \left(\frac{\dot{M}_1 v_1}{\dot{M}_2 v_2}\right)^{1/2} = \frac{d_1}{d_2}. \tag{5.2}$$

If the momentum flux of Star 1 is sufficiently stronger than that of its companion, d_2 can be (formally) less than the radius of Star 2. The wind of the first star will then strike the photosphere. This will occur even more readily when proper allowance is made for the lower wind velocities close to the star. In the case of two winds of equal momentum flux, the surface of momentum flux balance, by symmetry, will be a plane bisecting the axis joining the two stars (see Figure 5.1 on this page). In the intermediate case where $\mathcal{R} > 1$ and the contact

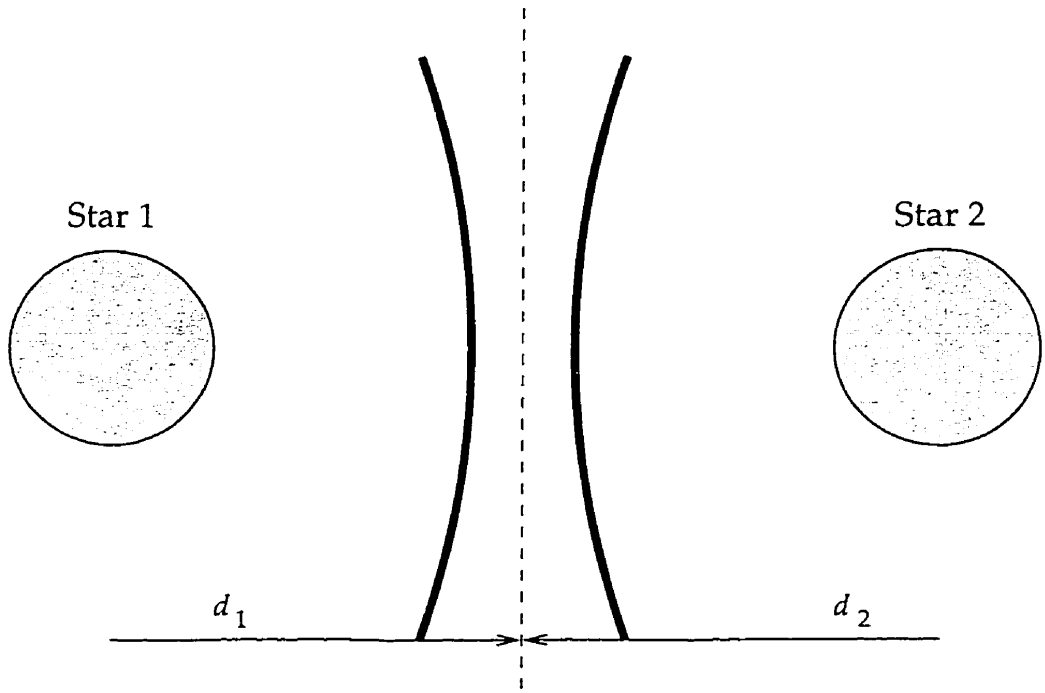

Figure 5.1: *Schematic diagram of colliding stellar winds for stars of equal $\dot{M}v$. The dashed line is where equal momentum flux occurs ($d_1 = d_2$). The solid curves show where the shocks begin for each wind (see Subsection 5.1.2).*

surface does not strike the photosphere of Star 2, the surface of momentum balance becomes curved with the concave side facing the star with the weaker wind. The slope of this surface is found by using the conservation of normal momentum flux (Figure 5.2, page 63) (Stevens, Blondin & Pollock 1992). The momentum flux normal to the surface of one wind is

$$\rho(v\cos\phi)^2 = \rho v^2\cos^2\phi = \frac{\dot{M}v}{4\pi d^2}\cos^2\phi.$$

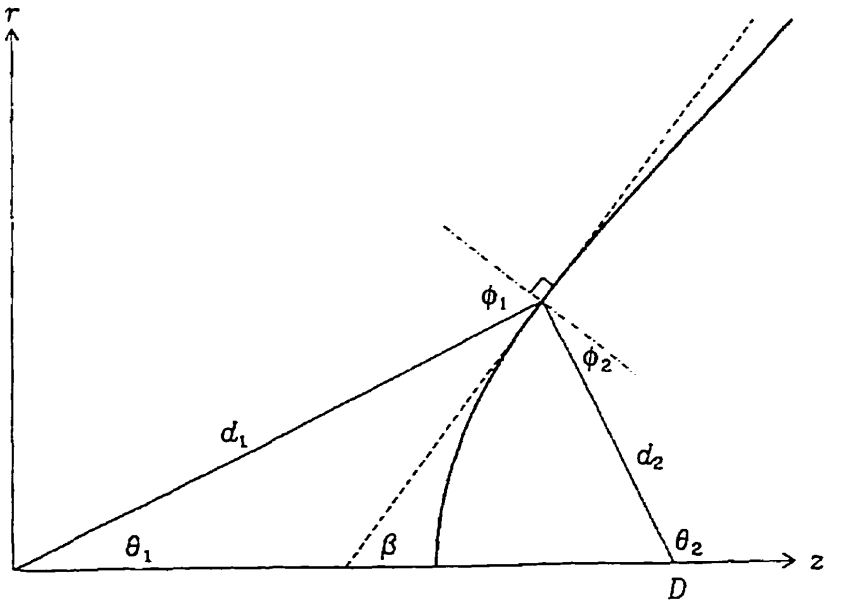

Figure 5.2: *Schematic diagram of the momentum balance surface for unequal winds. The momentum balance surface is the bold line, the dashed line is the tangent to this surface at a given point and the dot-dash line designates its perpendicular. Star 1 and Star 2 are at $z = 0$ and $z = D$, respectively. The lines d_1 and d_2 represent distances from Star 1 and Star 2, respectively, to the point on the balance surface, while θ_1 and θ_2 show their corresponding angles from the z-axis. The slope of the balance surface forms an angle β with the z-axis. The perpendicular forms angles ϕ_1 and ϕ_2 with d_1 and d_2, respectively. (from Stevens, Blondin & Pollock 1992).*

The balance of normal momentum flux is then

$$\frac{\dot{M}_1 v_1}{4\pi {d_1}^2} \cos^2 \phi_1 = \frac{\dot{M}_2 v_2}{4\pi {d_2}^2} \cos^2 \phi_2, \tag{5.3}$$

where ϕ_1 and ϕ_2 are the angles between the normal of the momentum flux balance surface and the wind velocities of Star 1 and Star 2, respectively. If θ_1 and θ_2 are the angles between the z-axis and the line from each star to the point on the momentum balance surface and β is the angle of the slope of the surface at that point (so that $\tan\beta = dr/dz$), trigonometry can be used to show that

$$\phi_1 = 90^\circ + \theta_1 - \beta = 90^\circ - (\beta - \theta_1)$$

and

$$\phi_2 = 90^\circ + \beta - \theta_2 = 90^\circ - (\theta_2 - \beta).$$

This allows $\cos\phi_1$ and $\cos\phi_2$ to be expressed with

$$\begin{aligned}\cos\phi_1 &= \sin(\beta-\theta_1)\\ &= \sin\beta\cos\theta_1-\cos\beta\sin\theta_1\\ &= \frac{z}{d_1}\sin\beta-\frac{r}{d_1}\cos\beta\end{aligned}$$

and

$$\begin{aligned}\cos\phi_2 &= \sin(\theta_2-\beta)\\ &= \cos\beta\sin\theta_2-\sin\beta\cos\theta_2\\ &= \frac{r}{d_2}\cos\beta+\frac{D-z}{d_2}\sin\beta.\end{aligned}$$

Equation 5.3 is rewritten as

$$\frac{\dot{M}_1 v_1}{\dot{M}_2 v_2}\left(\frac{d_2}{d_1}\right)^2\left(\frac{z}{d_1}\sin\beta-\frac{r}{d_1}\cos\beta\right)^2=\left(\frac{r}{d_2}\cos\beta+\frac{D-z}{d_2}\sin\beta\right)^2.$$

Division by $\cos\beta$ on both sides of the last equation and extracting the terms d_1 and d_2 leads to

$$\mathcal{R}\left(\frac{d_2}{d_1}\right)^2(z\tan\beta-r)=r+(D-z)\tan\beta.$$

Isolation of $\tan\beta$ gives

$$\left[\mathcal{R}\left(\frac{d_2}{d_1}\right)^2 z-(D-z)\right]\tan\beta=\left[\mathcal{R}\left(\frac{d_2}{d_1}\right)^2+1\right]r$$

and so

$$\tan\beta=\frac{dr}{dz}=\frac{(\mathcal{R}{d_2}^2+{d_1}^2)r}{(\mathcal{R}{d_2}^2+{d_1}^2)z-{d_1}^2 D}. \tag{5.4}$$

As the values d_1 and d_2 are coupled, in a complex way, to z and r, Equation 5.4 cannot be integrated analytically. In Figure 5.3 on the next page are displayed the results of a numerical integration for various values of $\mathcal{R}$. The surfaces are bow-shaped cones. These results do not take into account the centrifugal force (due to orbital revolution) applied to the flowing gas along the surface of balance. This force will cause the surfaces of the cones to curve like a comet in the plane of the orbit.

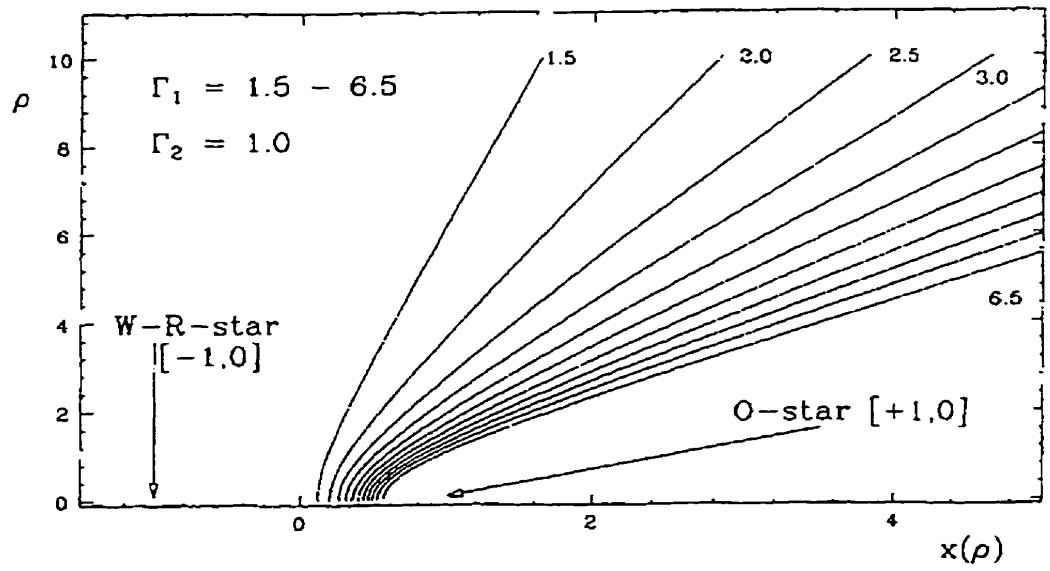

Figure 5.3: *Momentum flux balance surfaces (from Kallrath 1991). Here $D = 2$. In this figure, ρ and $x(\rho)$ are the same as r and z in equation 5.4 and Γ_1 and Γ_2 represent the momentum fluxes of the WR-star and O-star, respectively, so that $\Gamma_1/\Gamma_2 = \mathcal{R}$.*

Radiative braking by companion light

Since radiation pressure is probably the driving force of the winds of massive stars, it stands to reason that the great luminous flux of the companion O-star might have an effect on the approaching wind of the primary WR-star. Recently, Gayley, Owocki & Cranmer (1997) included the effect of the reflection of O-star photons off of the WR wind material for calculation of the momentum flux balance curve. They found that it could repel the WR wind sufficiently to weaken its effective momentum flux. This could prevent it from striking the companion's photosphere and render the shock cone more planar. The X-ray flux predicted for colliding winds of WR binaries due to the high temperature of the shock (Prilutskii & Usov 1976 and Cherepashchuk 1976) might be lower in reality due to the weaker collision and, thus, lower temperature of the shock. X-ray fluxes that are lower than expected have been observed for V444 Cygni (Corcoran *et al.* 1996).

5.1.2 Adiabatic and radiative collisions

The location of the shock in each wind does not coincide with the surface of contact discontinuity, otherwise this would imply that an infinite density would exist behind (after) the shock. In fact, for an adiabatic shock — the case for very wide binaries, where the gas densities are low and n^2-dependent radiation is less effective in dissipating energy (n is the number density of gas particles) — there is a maximum to the density of the gas that occurs behind the shock, regardless of the pressure difference on each side of the shock. This may be understood qualitatively by recognizing that when mono-atomic gas particles undergo shock, their kinetic energy of motion is tranformed into stochastic motions, whose energy will create a pressure opposing further compression. In a strong shock (where the pressure behind the shock is much greater than that in front of the shock), the pressure from the thermalised particles behind the shock prevents further compression.

Quantitatively, the maximum ratio of the density behind an adiabatic shock, ρ_{b}, to that in front of the shock, ρ_{f}, for mono-atomic gases can be derived (Scheffler & Elssässer 1988, p. 418):

$$\frac{\rho_{\mathrm{b}}}{\rho_{\mathrm{f}}} \approx \frac{\gamma+1}{\gamma-1} = 4,$$

where $\gamma = 5/3$ for a mono-atomic gas. An adiabatic collision between two winds of unequal strength, calculated with a hydrodynamic computer code, is shown in Figure 5.4 (page 67) (Stevens, Blondin & Pollock 1992).

It is possible for the shocked gas to lose energy by radiation — the case for close binaries where the gas densities are high and n^2-dependent radiative cooling is effective — giving rise to a radiative shock. If this happens, there is less available energy for stochastic motions. There will be less resistance to compression. The density of the post-shock gas can be compressed to arbitrarily high values in strong shocks with nearly instantaneous cooling by radiation. In this case, the shock region will collapse to a thinner but more chaotic configuration. The ratio between the time for cooling of the gas to interstellar temperatures, t_{cool}, to that

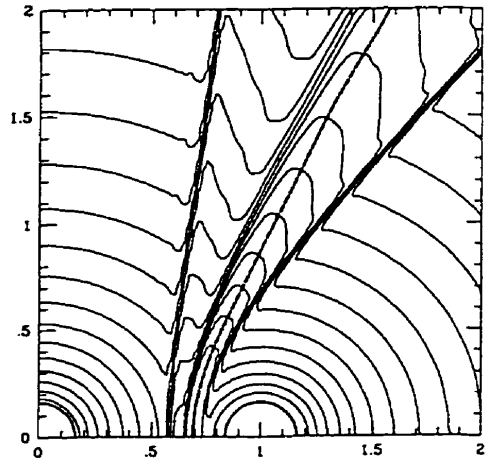

Figure 5.4: *Colliding winds with adiabatic shocks. The momentum flux balance curve is indicated by the dashed line. The shocks of the two winds occur where the density contours become very compressed. The contact discontinuity is the convergence of the contours to the left of the momentum flux balance curve.* $\mathcal{R} = \sqrt{5}$ *in this simulation. (From Stevens, Blondin & Pollock 1992).*

of escape of the gas from the shock region, $t_{\rm esc}$, is expressed by (Stevens, Blondin & Pollock 1992)

$$\chi = \frac{t_{\rm cool}}{t_{\rm esc}}.$$

For $\chi > 1$, the wind can be assumed to be adiabatic, while for $\chi \ll 1$, the wind is roughly isothermal.

5.2 Some observational aspects of hot colliding winds

X-ray, ultraviolet, visible, infrared and radio observational evidence of colliding winds from some previous work is briefly reported in this section.

5.2.1 X-ray observations

Willis, Schild & Stevens (1995) have obtained ROSAT X-ray observations in the 1 keV range of the closest known WR-star, γ^2 Velorum (WC8+O9I, $P = 78$ d). As seen in Figure 5.5 on the following page, the X-ray flux increases when the

O-star is most in front and returns to a base value as seen in single WR winds outside of these phases. The explanation for this behaviour lies in the high X-ray

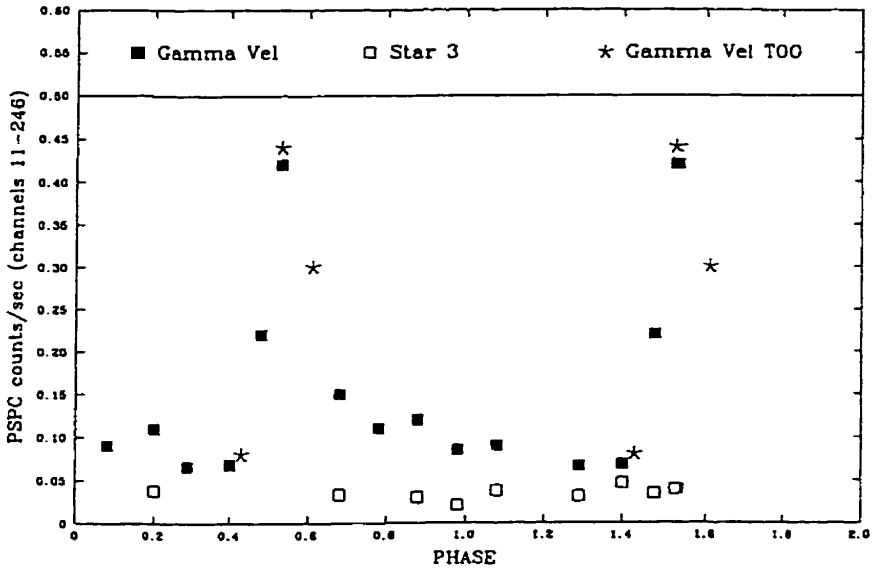

Figure 5.5: *X-ray counts in keV range of γ^2 Velorum as a function of orbital phase. The WR-star is in front at phase 0. The O-star passes in front at phase 0.5, just after periastron passage. Open squares refer to a nearby star with constant flux. From Willis et al. 1995.*

opacity at keV energies of the WR wind compared to the lower opacity of the O-star wind. Since the X-rays are produced mainly in the extended region in the bow-shock head between the two stars (Stevens *et al.* 1996), closer to the weaker-wind O-star, they can only escape to the observer when the O-star wind cavity points towards him.

5.2.2 Ultraviolet observations

The Wolf-Rayet binary V444 Cygni was studied in the ultraviolet range to find evidence of colliding winds (Shore & Brown 1988). The binary consists of a WN5 star and an O6 star with a separation of 40 $R_\odot$ and an orbital inclination of 78°. The variations with phase of the strong P Cygni lines HeII 1640 Å, NIV 1718 Å and CIV 1548/51 Å were studied. Shore & Brown noted that the P Cygni profile of HeII varied with phase and, in particular, the absorption component

disappeared near secondary eclipse (when the O-star is in front) (Figure 5.6, page 69). The same phenomenon occurred in the NIV line.

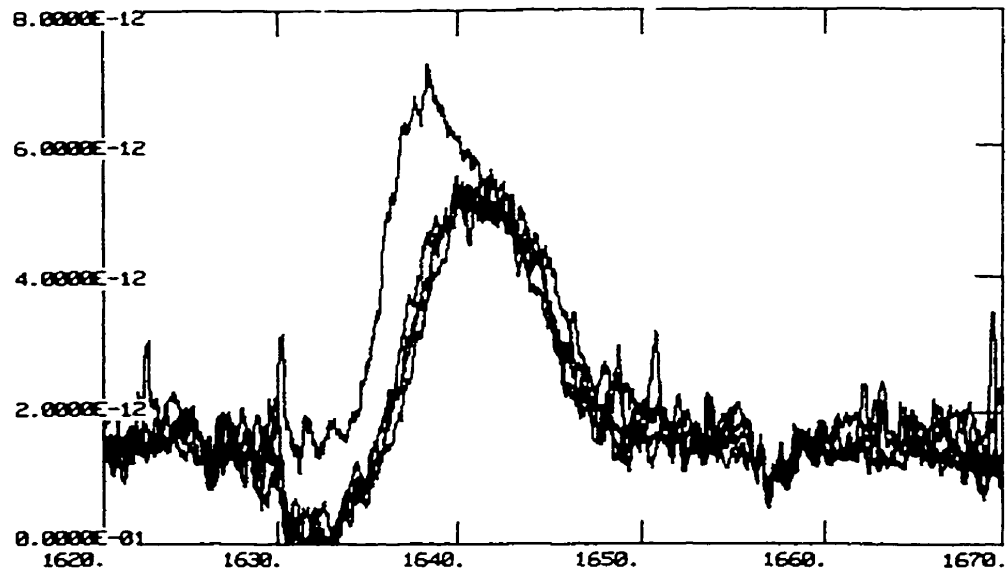

Figure 5.6: *Comparison of* HeII *1640 Å line profiles near primary eclipse ($\varphi = 0$; the more heavily absorbed spectrum) with those at phase* 0.6 *for V444 Cygni. Ordinate: wavelength* (Å), *abscissa: flux in* erg/cm/s/Å *(from Shore & Brown 1988).*

The ultraviolet HeII and NIV lines normally appear in the spectra of single O6 stars only as absorption lines with no sign of P Cygni emission. In V444 Cygni, all of the emission and much of the absorption must, therefore, be assumed to arise in the Wolf-Rayet wind, so that variations in the line profiles are indicative of effects in this wind. The absence of absorption around secondary eclipse is a sign that the part of the Wolf-Rayet wind that blows towards the observer has reduced density (is blocked), eliminating the absorption component of the P Cygni profile at this orbital phase.

The CIV 1548/51 Å lines occur in both Wolf-Rayet stars and O6 stars, so both stars contribute to the CIV P Cygni line in V444 Cygni. The terminal velocity measured from the absorption component of the CIV P Cygni profile in V444 Cygni is plotted as a function of the binary phase in Figure 5.7 on the next page.

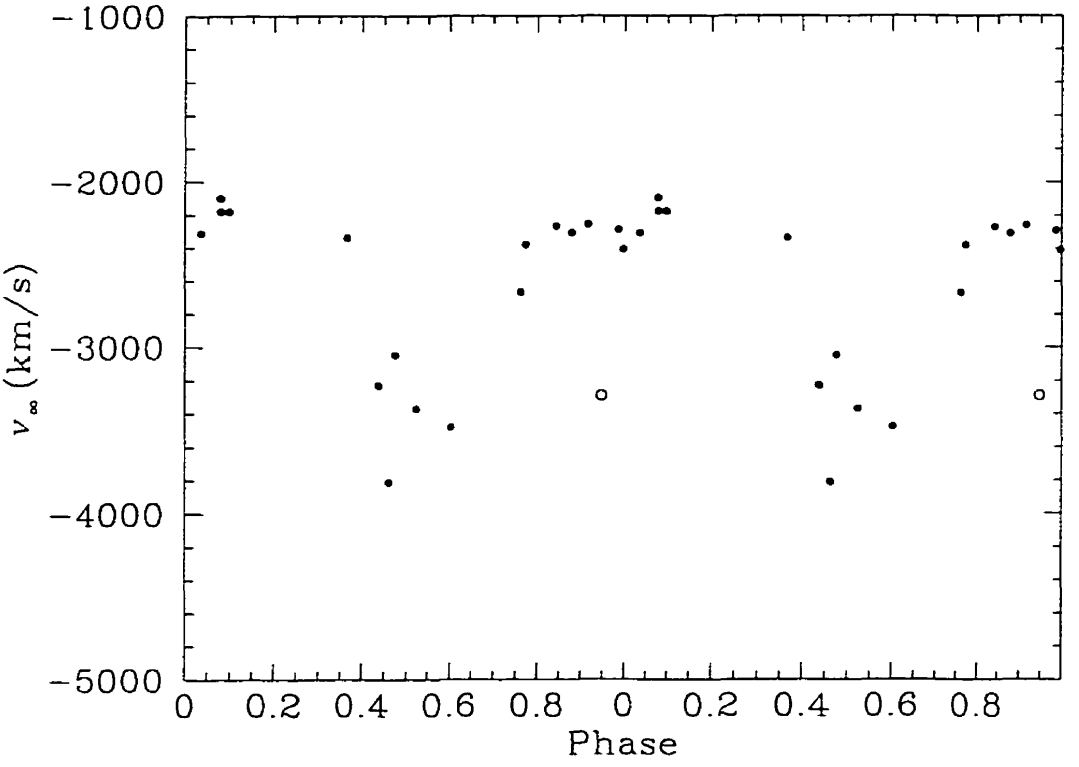

Figure 5.7: *1548/51 Å terminal velocity as a function of phase in V444 Cygni (plotted from data of Table 2 of Shore & Brown 1988; the open circle is a point in their table that appears at a different velocity in their Figure 9 of the same data). The O-star is in front at phase 0.5.*

A high-velocity blue-shaded tail appears in the absorption wing of the P Cygni profile of CIV during secondary eclipse. The increase in velocity coincides with the elimination of absorption in the P Cygni profiles of HeII and NIV.

Shore & Brown interpreted their results as a manifestation of colliding winds. They proposed that the wind of the O-star produces a cavity in the Wolf-Rayet envelope (Figure 5.8, page 71), which otherwise surrounds the entire system. At most phases, the wind of the WR-star prevents the faster O-star wind from reaching its blue-shifted terminal velocity. The result is a terminal velocity of lower magnitude at most phases. When the O-star wind begins to eclipse the Wolf-Rayet wind along the line of sight, the HeII and NIV ions from the Wolf-Rayet wind travelling towards the viewer are blocked, so that the absorption component of the P Cygni profile disappears. At these phases, the viewer sees only absorption components from the P Cygni lines of ions (CIV) in the O-star

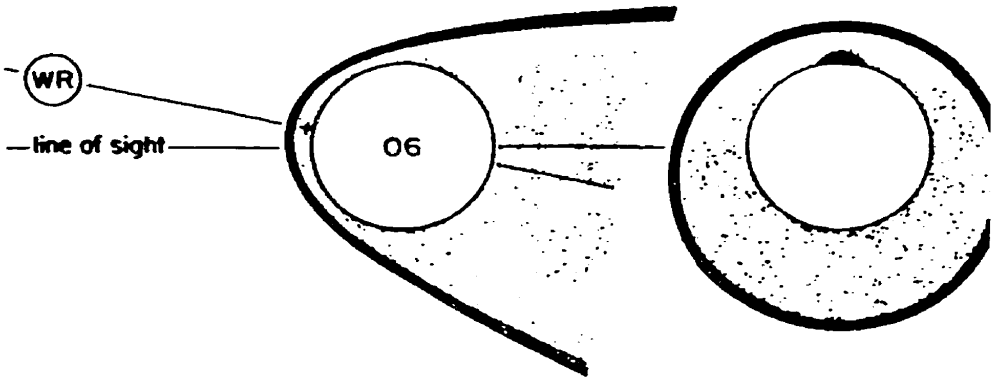

Figure 5.8: *Quadrature and conjunction schematic views of the V444 Cygni system, showing the expected cross-section of the wind-wind collision (thick line) (from Shore & Brown 1988).*

wind, which is less dense, has less abundant HeII and NIV and, at this point, has a greater, unrestrained blue-shifted terminal velocity.

5.2.3 Optical variations in emission profiles

Gies & Wiggs (1991) studied the O-star binary AO Cassiopeiæ in the visible spectral range (Hα). This is a system of two O9 stars with an orbital inclination $i \approx 63°$ (although not a WR system, it illustrates a phenomenon that is studied in Section 5.3). By subtracting a synthetic photospheric component of the spectrum, they isolated an emission component of the Hα line (Figure 5.9 on the following page). This in itself was significant, since emission lines are not expected in the visible spectroscopic range of most O-stars. There must be a region of high-temperature in the stellar envelope. The emission consists of two peaks, one blue and one red of the rest wavelength of Hα. Hence, there must be two components of this region, one moving towards the observer and one away. Velocity measurements as a function of phase were made and were used to show that both peaks follow parallel, sinusoidal paths (Figure 5.9). Also, the centroid of the emission orbits about the centre of mass of the binary system. The mean velocity of both peaks follows the systemic velocity of the binary.

Gies and Wiggs postulated that since the systemic velocity was about equal to

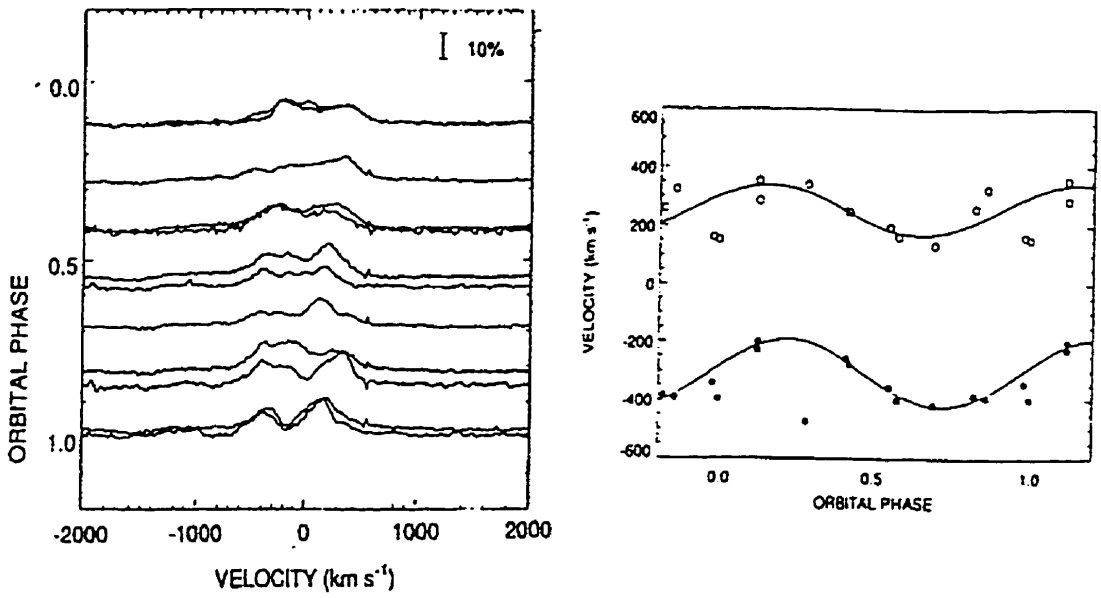

Figure 5.9: *Hα profile gallery of AO Cas with orbital phase. The error bar shows 10% of the continuum intensity. To the right are corresponding radial velocity curves of the blue (solid dots) and red (open dots) peaks (from Gies & Wiggs 1991).*

the mean velocity of the circumstellar peaks, the location of the emission centroid was fixed in the binary system with respect to the two stars. They then assumed that the emission centroid was situated between the two stars. After noting that there were no large changes in emission strength at conjunction phases, where part of the emission region could be occulted by the stars, they claimed that the Hα-emitting region was considerably extended away from the line joining the two stars. They explained the observed phenomenon as the manifestation of a bow shock from colliding winds.

Study of Hα in Plaskett's star (Wiggs & Gies 1992) and in V Sagittæ (Gies, Shafter & Wiggs 1998) has revealed evidence of circumstellar gas in the form of a bow shock as well, while for 29 UW Canis Majoris (Wiggs & Gies 1993) the Hα spectroscopic variations were interpreted as the manifestation of a planar shock.

5.2.4 Infrared evidence and dust production

Between 1976 and 1977, WR140 was discovered to have brightened by more than an order of magnitude in infrared luminosity over several months. This luminosity decreased over the following months. After monitoring the star in the infrared for several years, it was seen to brighten again in 1985 (Williams *et al.* 1987, Williams *et al.* 1990). Assuming that the brightening was cyclic, the interval between successive maxima in infrared luminosity led to an orbital period of 7.94 years. During these large variations in infrared flux, the ultraviolet luminosity was found not to change, which led to the conclusion that the overall luminosity of the two stars remained constant.

The infrared light curve was then phased to the ephemeris found from absorption line radial velocities (this assumed that the star was binary). Maximum infrared flux was then found to coincide with periastron passage. The increase in infrared emission was explained as the condensation of hot carbon dust in the envelope of the WC7 star, which subsequently cooled, emitting infrared radiation. That the carbon dust was only produced at periastron passage was explained as the result of the orbit being very eccentric ($e = 0.84$). At periastron, the colliding winds provided sufficient compression of the gas to allow dust condensation to occur. Away from periastron, the shock was not as strong, the density was insufficient and no more dust was created. The dust that was formed near periastron continued to cool, yielding gradually fading luminosities.

5.2.5 Radio evidence for colliding winds

Most massive stars emit thermal radiation in the mm – m domain, but some have a non-thermal component. In the case of WR146 (WC6+O) and WR147 (WN8+O), the non-thermal components have been spatially resolved by the European Very Long Baseline Interferometer (Dougherty *et al.* 1996 ,Williams *et al.* 1997). As illustrated in Figure 5.10 on the next page, the non-thermal emission in WR147 (WR146 is similar) arises in a bow-shaped region between the stars,

but much closer to the weak wind O-star, while the thermal component, also resolved, arises in the WR wind. This is the first time that a wind-wind collision (WWC) has been directly imaged. The non-thermal radio emission comes from the extremely hot bow-shock head, where Fermi acceleration must play a role. In short-period binaries, this radiation is normally absorbed in the dense WR wind.

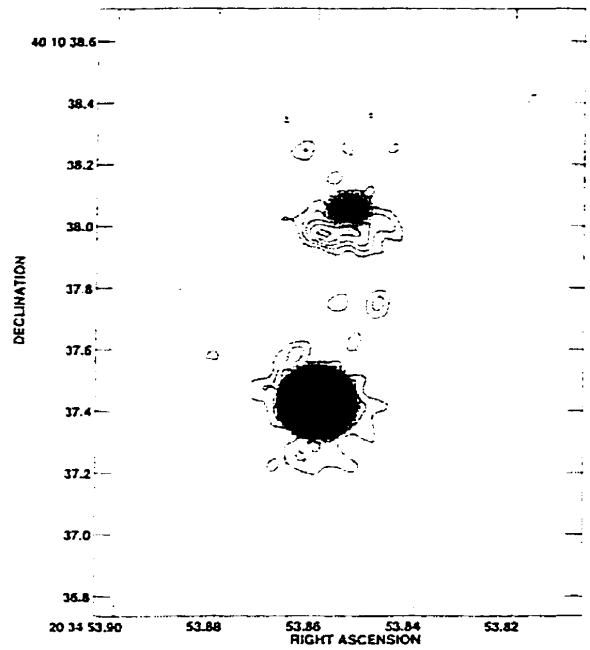

Figure 5.10: *Image of radio emission from WR147 (from Williams et al. 1997). The shaded areas show thermal emission from stars (larger area: WR-star, smaller area: O-star). The contour lines indicate non-thermal emission from the bow shock head on the WR side of the O companion and thermal emission from the wind of the brighter WR.*

5.3 Excess emission and Lührs' model

During the wind collision, the gas between the two shock fronts illustrated in Figure 5.4 is heated to a high temperature, reaching $\lesssim 10^6$ K at the bow-shock head. When the highly ionised gas flows outwards, it will cool and recombine, yielding emission line radiation in addition to that produced, if any, in the stellar winds. In the case of the six WC+O binaries studied here, a montage is presented

for each star in Figures 5.11, 5.12, 5.13, 5.14, 5.15 and 5.16 (pages 76–81). Note the strong profile changes in some lines. Are these due to wind-wind collisions?

5.3.1 CIII 5696 Å emission in Br22 and WR9

Among the four MC WC/WO+O binaries (in fact among all 23 LMC WC-stars), Br22 is special because it is the only WC/WO star to exhibit relatively strong CIII 5696 Å emission. This line is also highly variable. All lines that follow the orbital motion of the WR-star should move in phase with the WR-star. This is not the case for the CIII 5696 line. It shifts in a sinusoidal pattern with the orbital period, but approximately one-quarter of an orbit behind the WR orbit. The emission must come from another part of the binary system.

Another interesting feature of the CIII 5696 line is that it varies in form as well as in position. It is wider at some phases and its asymmetry changes; the blue wing is sometimes more intense than the red wing and at other times *vice-versa*. As shown in the next subsections, this is exactly the behaviour expected if the variable CIII emission arises in a shock cone that wraps around the weaker-wind O-star, with a flow pattern directed away from the WR-star.

The same phenomenon is seen in WR9 (Figure 5.15). However, there appears to be a base CIII 5696 Å emission upon which there is emission that moves independently of this base. Apparently, the inherent CIII from the WR-star is stronger here than in Br22.

Besides the CIII 5696 line, other lines (mostly the stronger lines) in Br22 and the five other binaries do vary. However, these variations are more subtle, since they are superposed on much brighter emission lines produced in the WR wind. Do these variations also arise in the WWC zone? An attempt to answer this will be described later in Section 5.5, after dealing with an emission-excess model for the WWC.

Why is CIII 5696 excess only seen in Br22 and WR9 among the six WC+O binaries? Usov (private communication) has studied the energy produced in

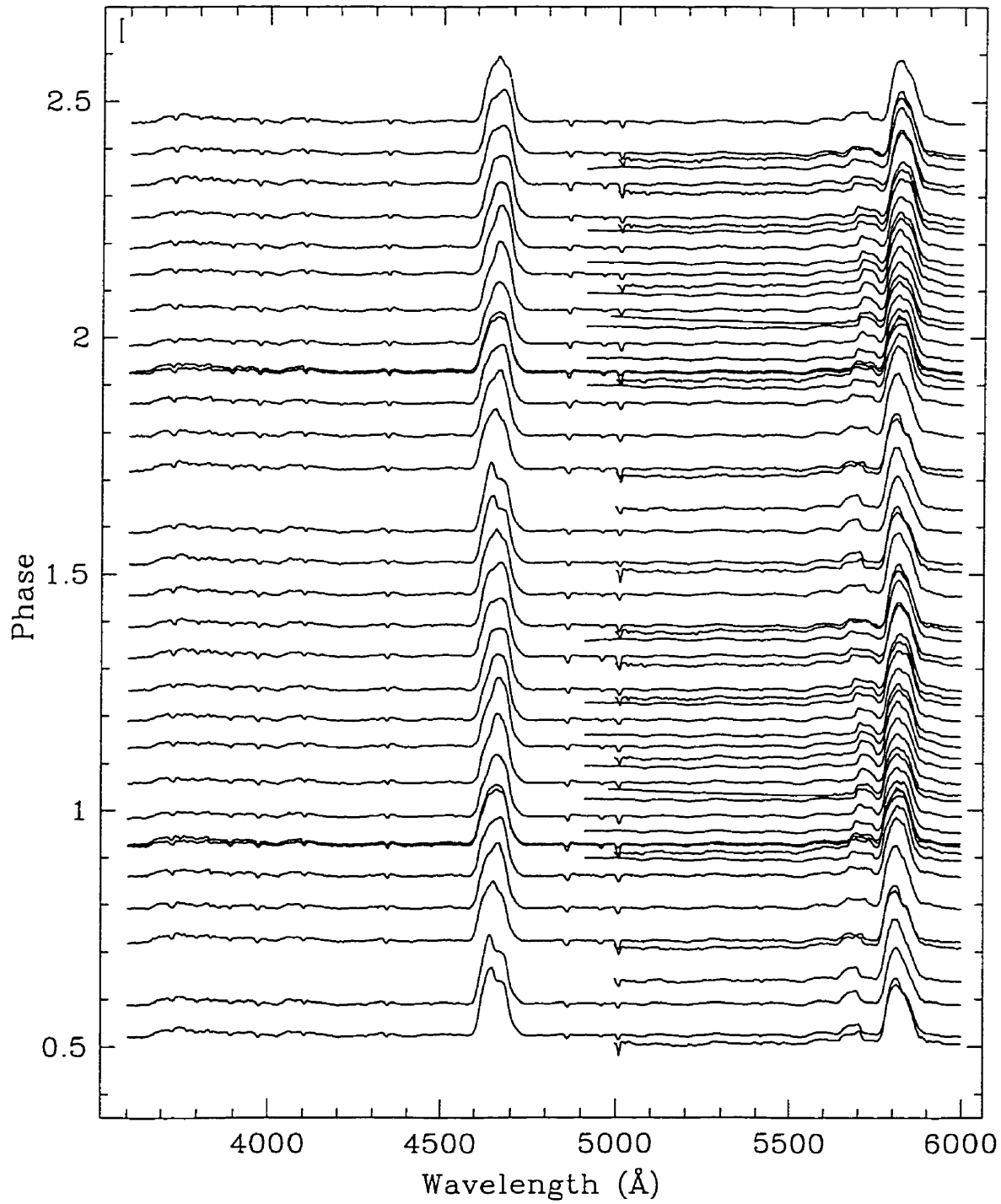

Figure 5.11: *Montage of phased Br22 spectra. The same data are repeated over two cycles. The bar in the upper left-hand corner shows the intensity of the continuum. For line identification, see Figure 1.1 (emission lines) and the average spectra of Br22 in Figure B.1 (absorption lines).*

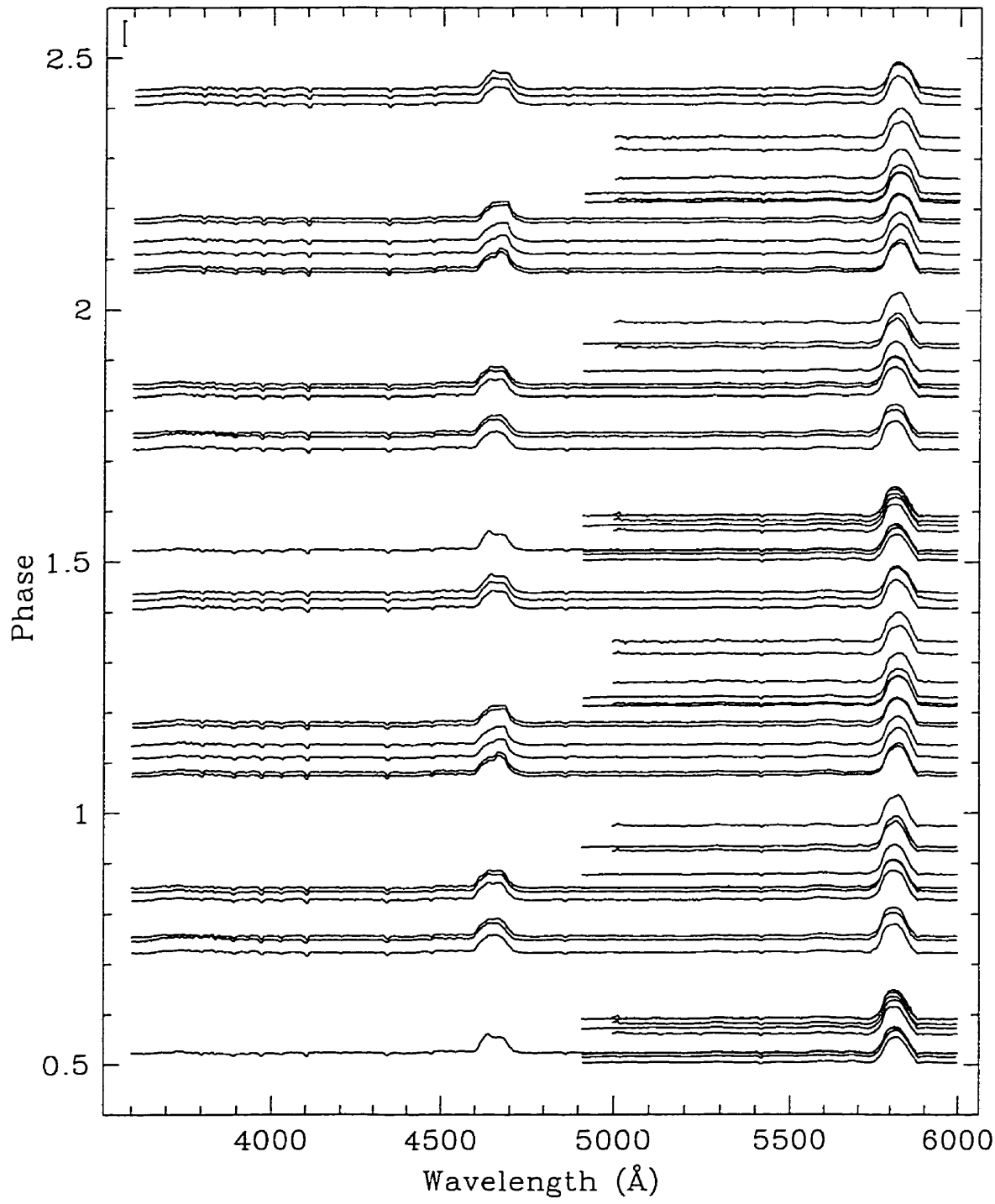

Figure 5.12: *Montage of phased Br31 spectra. The same data are repeated over two cycles. The bar in the upper left-hand corner shows the intensity of the continuum. For line identification, see Figure 1.1 (emission lines) and the average spectra of Br22 in Figure B.1 (absorption lines).*

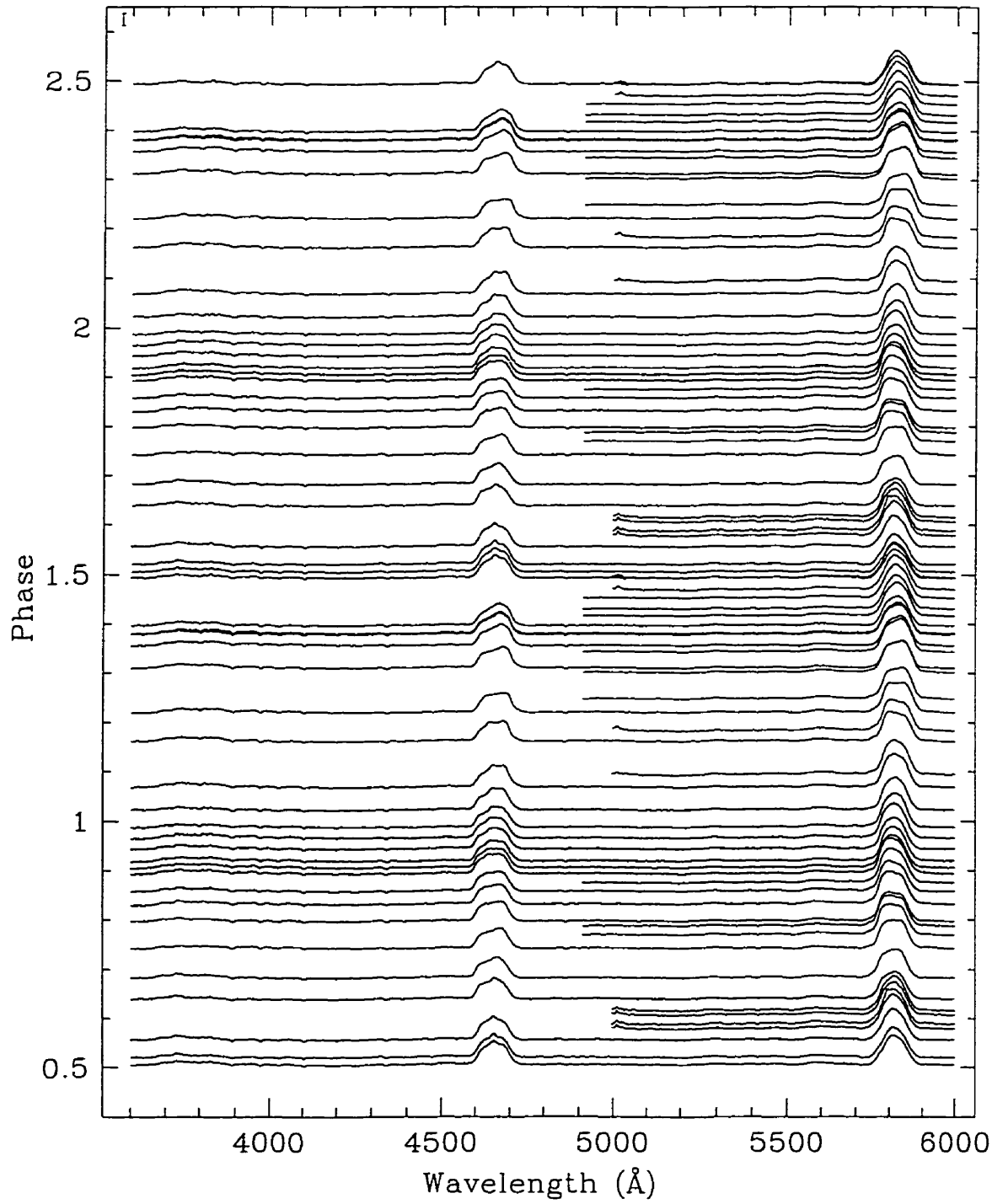

Figure 5.13: *Montage of phased Br32 spectra. The same data are repeated over two cycles. The bar in the upper left-hand corner shows the intensity of the continuum. For line identification, see Figure 1.1 (emission lines) and the average spectra of Br22 in Figure B.1 (absorption lines).*

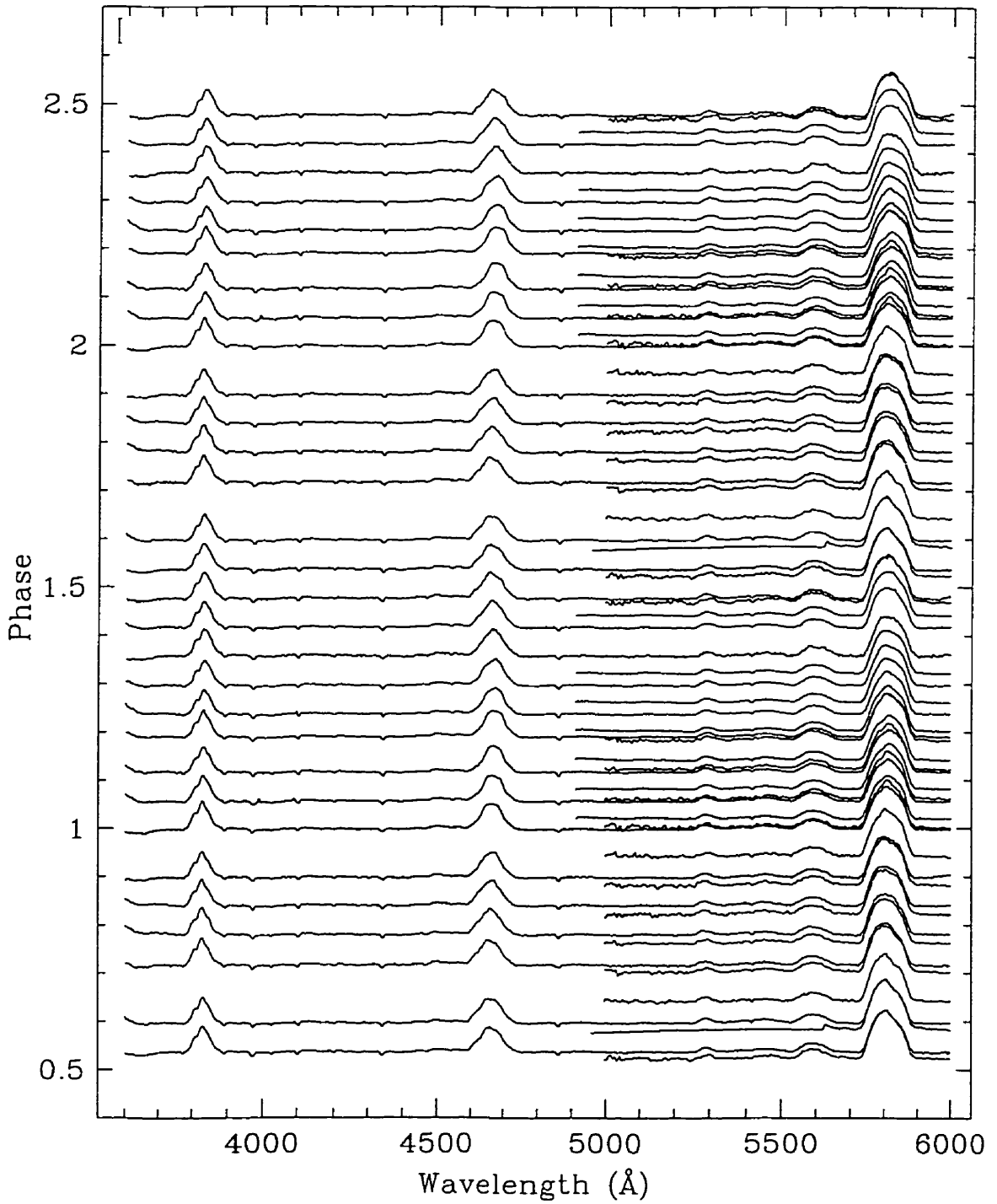

Figure 5.14: *Montage of phased AB8 spectra. The same data are repeated over two cycles. The bar in the upper left-hand corner shows the intensity of the continuum. For line identification, see Figure 1.1 (emission lines) and the average spectra of Br22 in Figure B.1 (absorption lines).*

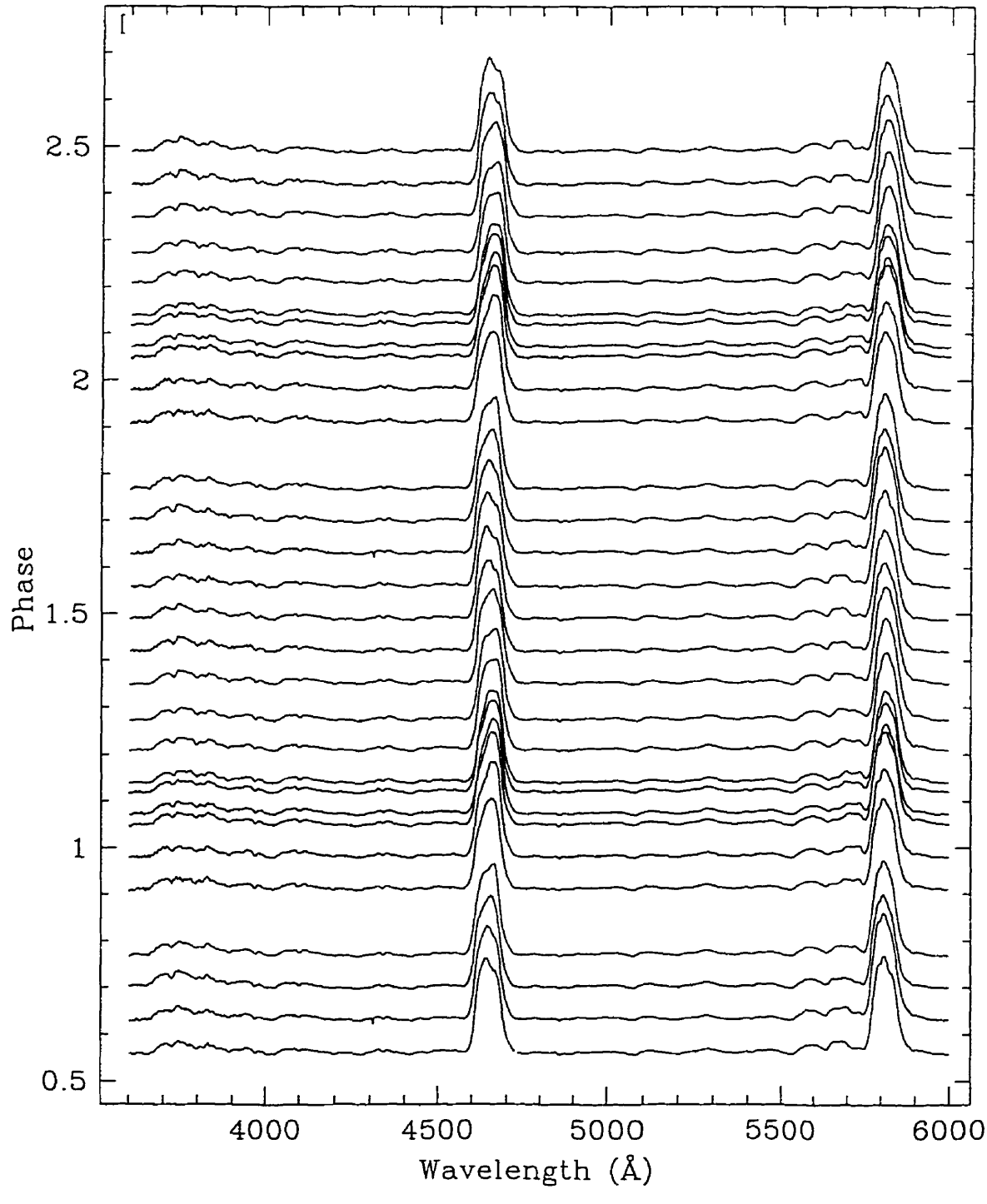

Figure 5.15: *Montage of phased WR9 spectra. The same data are repeated over two cycles. The bar in the upper left-hand corner shows the intensity of the continuum. For line identification, see Figure 1.1 (emission lines) and the average spectra of Br22 in Figure B.1 (absorption lines).*

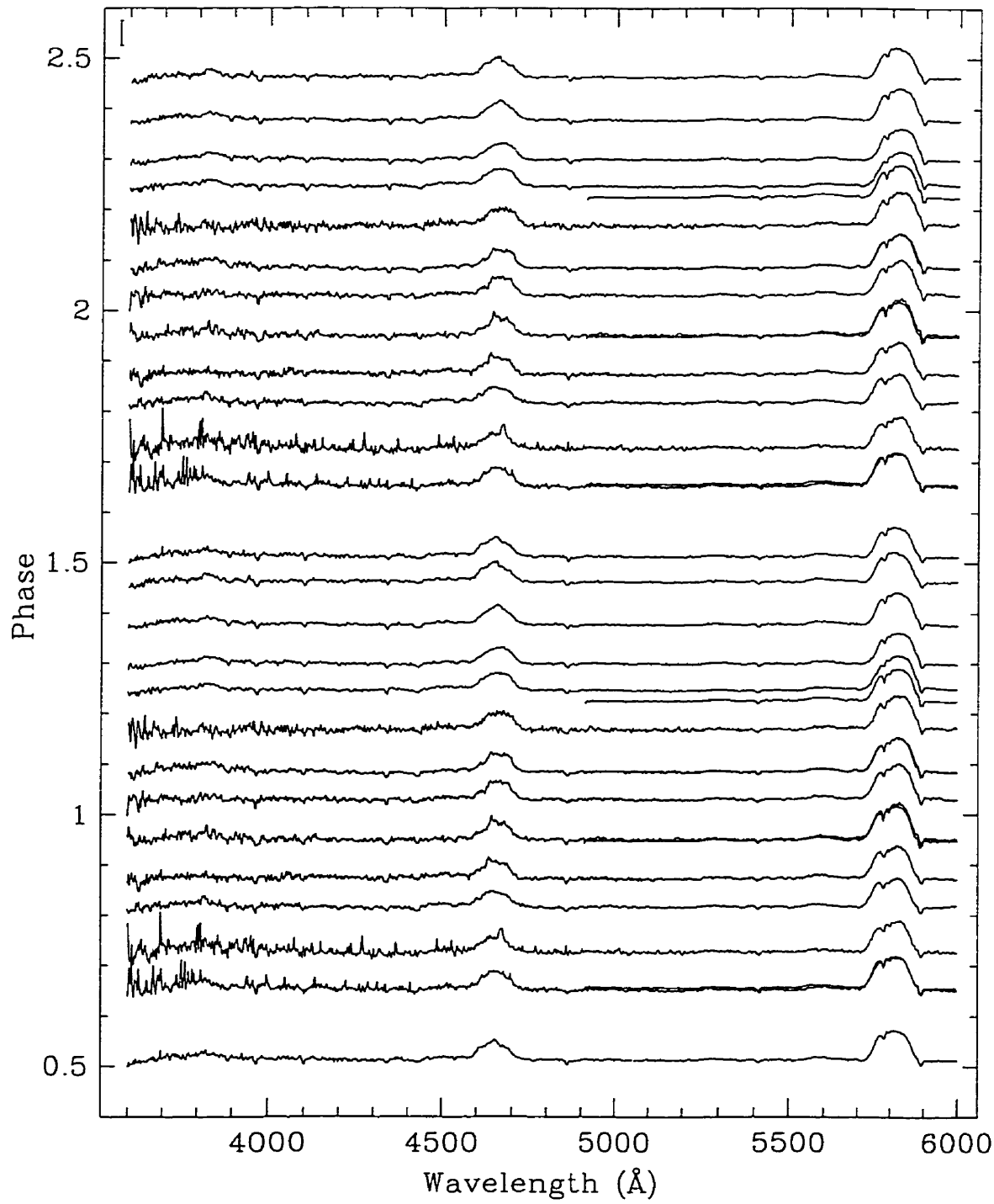

Figure 5.16: *Montage of phased WR30a spectra. The same data are repeated over two cycles. The bar in the upper left-hand corner shows the intensity of the continuum. For line identification, see Figure 1.1 (emission lines) and the average spectra of Br22 in Figure B.1 (absorption lines).*

WWC; it tends to peak in WR+O systems of intermediate orbital separation (or periods of approximately one month), as is the case for Br22 and Wr9. Radiative breaking might also play a role by preventing the WR wind from reaching its full speed and reducing the force of the WWC, changing the conditions in which the ions are created. Not all ions that could be theoretically expected might form in such a case and those that do might not be as abundant (perhaps the CIII excess even in Br22 and WR9 might have been greater without radiative breaking). However, AB8 has a similar period; presumably its WWC zone does not lead to CIII excess for a different reason: its WO component has a much hotter wind.

Why is CIII 5696 enhanced more than other lines in Br22 and WR9? Empirically, this line is considered to be very sensitive to wind clumping in single WC-stars (*e.g.* Moffat 1996), and so also sensitive to density enhancements as expected in WWC zones.

5.3.2 Line profiles expected for a thin emitting annulus

What kind of line profile is to be expected from the excess emission of the ions in a shock cone? For an idealised case of a binary system where both winds are of equal momentum flux, the region between the two shock fronts contains shocked, optically thin material expanding outwards with its centre of symmetry along a plane that is perpendicular to the axis connecting the two stars. It has a constant streaming velocity of expansion, $v_{\rm strm}$. As the shocked material cools as it flows, there will be a decreasing radial temperature gradient. The ions of interest (such as CIII 5696) would only be expected to form in an annular section of this plane where the temperature is conducive to this species. (Figure 5.17 on the following page; *cf.* also Figure 5.1, page 62).

For initial simplicity, the annulus is taken to be viewed edge-on by the observer, with the two stars in quadrature. Following the usual conservation laws, the energy flux per unit Doppler-shifted observed velocity is equal to the energy

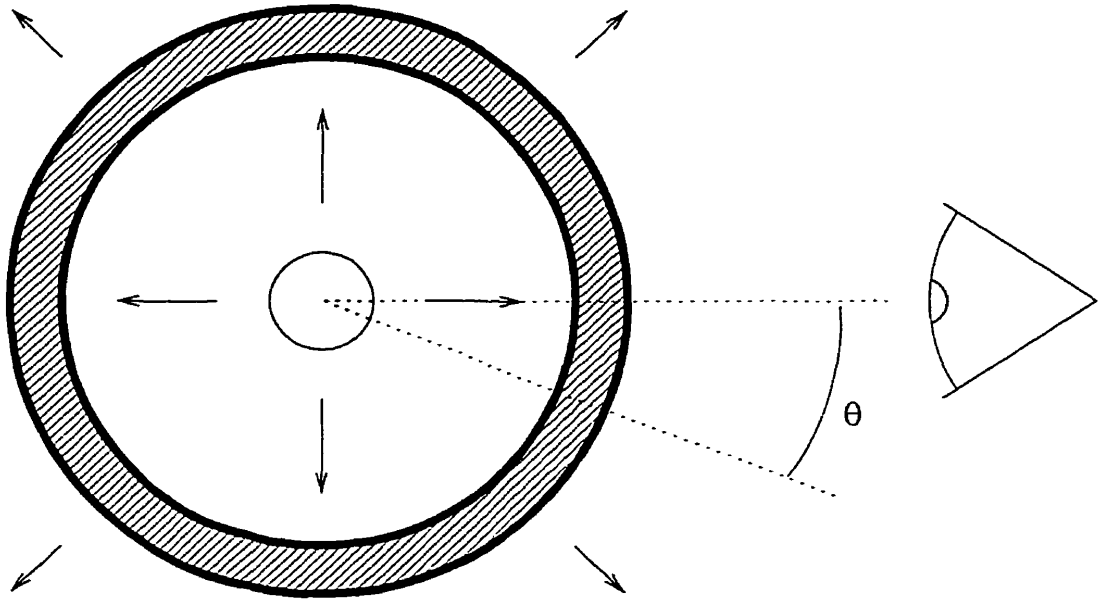

Figure 5.17: *Schematic diagram of a thin expanding annulus of shocked material expanding in a plane half-way between two stars with equal wind momentum flux, seen along the line joining the stars. A small section of the annulus forms an angle θ with the line of sight ($\theta \equiv \vartheta$ of the text).*

flux per unit angular section of the annulus, so that

$$I(v_o)\, dv_o = I(\vartheta)\, d\vartheta, \tag{5.5}$$

where v_o is the Doppler-shifted, observed velocity. The velocity seen by the observer for an infinitesmally thin section of the annulus making an angle ϑ with the line-of-sight is

$$v_o = -v_{\rm strm} \cos\vartheta,$$

so that

$$dv_o = v_{\rm strm} \sin\vartheta\, d\vartheta.$$

Thus, in Equation 5.5:

$$I(v_o) = \frac{I(\vartheta)\, d\vartheta}{dv_o} = \frac{I(\vartheta)}{v_{\rm strm} \sin\vartheta}.$$

The intensity is considered to be constant over the annulus, $I(\vartheta) = I/2\pi$, where I is the total intensity of the annulus. Since $v_o = -v_{\rm strm} \cos\vartheta$, $\sin\vartheta =$

$\sqrt{1-(v_o/v_{strm})^2}$. With this, the line profile may finally be described by

$$I(v_o) = \frac{I\pi}{\sqrt{v_{strm}^2 - v_o^2}}. \tag{5.6}$$

The profile described by Equation 5.6 is illustrated in Figure 5.18 on this page.

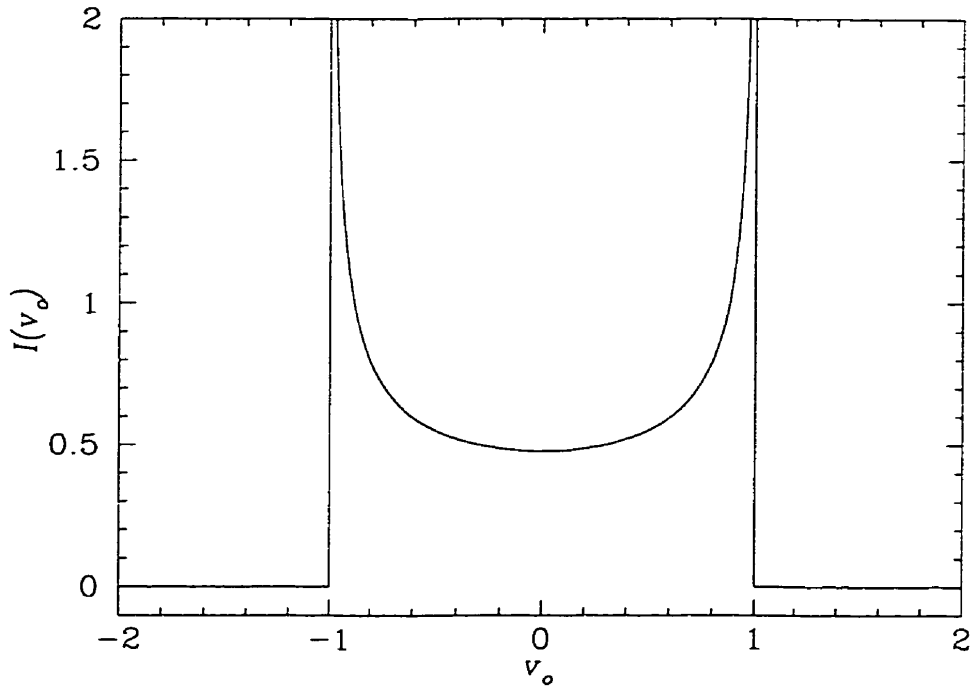

Figure 5.18: *Line profile of an optically thin, expanding annulus. The velocity v_o is normalised to $v_{strm} = 1$ and I is arbitrarily set to 1.5.*

Although the extreme wings of this function are physically unrealistic ($\lim_{|v_o| \to v_{strm}} I(v_o) = \infty$), this derived profile is useful to see what kind of spectroscopic line is produced by excess emission. It is a double-peaked profile. Note that the line profiles of AO Cas studied by Gies and Wiggs (described in Subsection 5.2.3) were also double-peaked.

This profile will vary with orbital phase, inclination and ratio of momentum flux between stellar winds. All are mutually coupled and the results are variations of the basic profile illustrated in Figure 5.18. Such variations will be shown with a more realistic model in the next sub-section.

5.3.3 Lührs' model for the excess emission line profiles

Lührs (1991, 1997) has used the same thin annulus model as presented in restricted form in Subsection 5.3.2 to give a more complete function for the excess emission profiles from colliding winds. He found (using the notation of this Dissertation):

$$I(v_{\rm o}\ ) = \frac{I/2\pi}{\sqrt{(v_{\rm strm}\sin\theta)^2(1-\sin^2 i\cos^2\varphi) - (v_{\rm o}\ - v_{\rm strm}\cos\theta\cos\varphi\sin i)^2}}. \quad (5.7)$$

Equation 5.7 does not include a shift in the axis of the cone angle ($\delta\varphi$) due to the Coriolis forces associated with the orbital motion. To allow for this, one should replace φ by $\varphi - \delta\varphi$ (see the illustration of Figure 5.19 on this page).

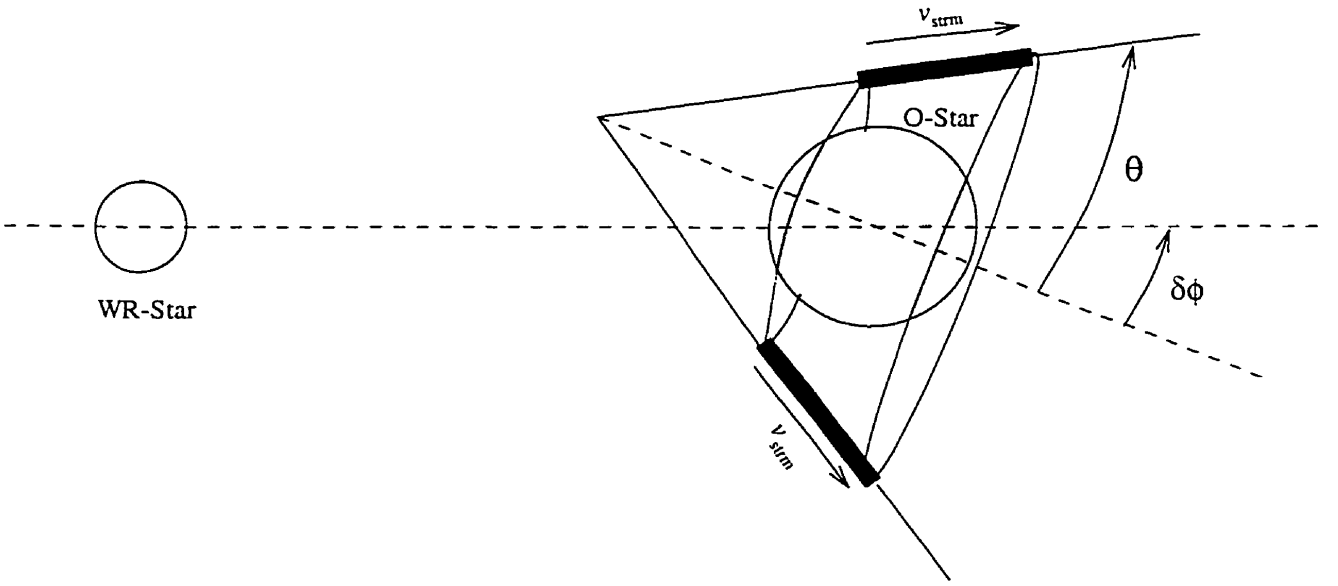

Figure 5.19: *Lührs' model for an optically thin region of emission, where a shock cone has an opening half-angle angle θ and forms an angle $\delta\phi$ with the line joining the two stars ($\delta\phi \equiv \delta\varphi$ of the text). Note that the dark rectangles represent only a cross-section of the homogeneous region of emission (with streaming velocity $v_{\rm strm}$) around the three-dimensional conical surface.*

Unfortunately, equation 5.7 still produces profiles that have infinite cusps at their outer boundaries. This is clearly not physical. Lührs attempted to introduce more realistic geometry by assuming that the excess emission occurs not in an infinitesimal cone but rather between two cone angles θ_1 and θ_2, following a

parabolic distribution function in $\cos\theta$:

$$f(\theta) = C(\cos\theta_1 - \cos\theta)(\cos\theta - \cos\theta_2),$$

where C is a constant, while θ_1 and θ_2 are the inner and outer cone boundaries, respectively, such that $f(\theta_1) = f(\theta_2) = 0$ (see Lührs 1991, p. 82).

After some algebra (Lührs 1991, pp. 82–83), this leads to the intensity distribution

$$I(u) = \frac{6J(u)/v_{\mathrm{strm}}}{\pi(\cos\theta_1 - \cos\theta_2)^3}, \tag{5.8}$$

where

$$\begin{aligned}
u &= v_{\mathrm{o}}\ /v_{\mathrm{strm}} \\
J(u) &= [(u\sin j - \cos\theta_2)(\cos\theta_1 - u\sin j) - 0.5(1-u^2)\cos^2 j](\psi_1 - \psi_2) \\
&\quad - \left[(\cos\theta_1 + \cos\theta_2 - 2u\sin j)\sqrt{(1-u^2)\cos^2 j}\right](\cos\psi_1 - \cos\psi_2) \\
&\quad + 0.25(1-u^2)\cos^2 j[\sin(2\psi_1) - \sin(2\psi_2)],
\end{aligned}$$

and

$$\begin{aligned}
\sin j &= -\sin i\cos\varphi_{\mathrm{c}} \\
\cos j &= \sqrt{1 - \sin^2 i\cos^2\varphi_{\mathrm{c}}} \\
\varphi_{\mathrm{c}} &= \varphi - \delta\varphi - \pi \\
\psi_1 &= \arcsin y_1(\cos\theta_1, u) \\
\psi_2 &= \arcsin y_2(\cos\theta_2, u) \\
y_1 &= \min\left[+1, \frac{\cos\theta_1 - u\sin j}{\sqrt{(1-u^2)\cos^2 j}}\right] \\
y_2 &= \max\left[-1, \frac{\cos\theta_2 - u\sin j}{\sqrt{(1-u^2)\cos^2 j}}\right].
\end{aligned}$$

Examples of Equation 5.8 for various phases, inclinations and cone opening half-angles are shown graphically in Figure 5.20 on the next page. A brief description of the profile variations with various orbital parameters, as illustrated in Figure 5.20, follows. Although the effects of different parameters are coupled, each parameter is discussed independently of the others.

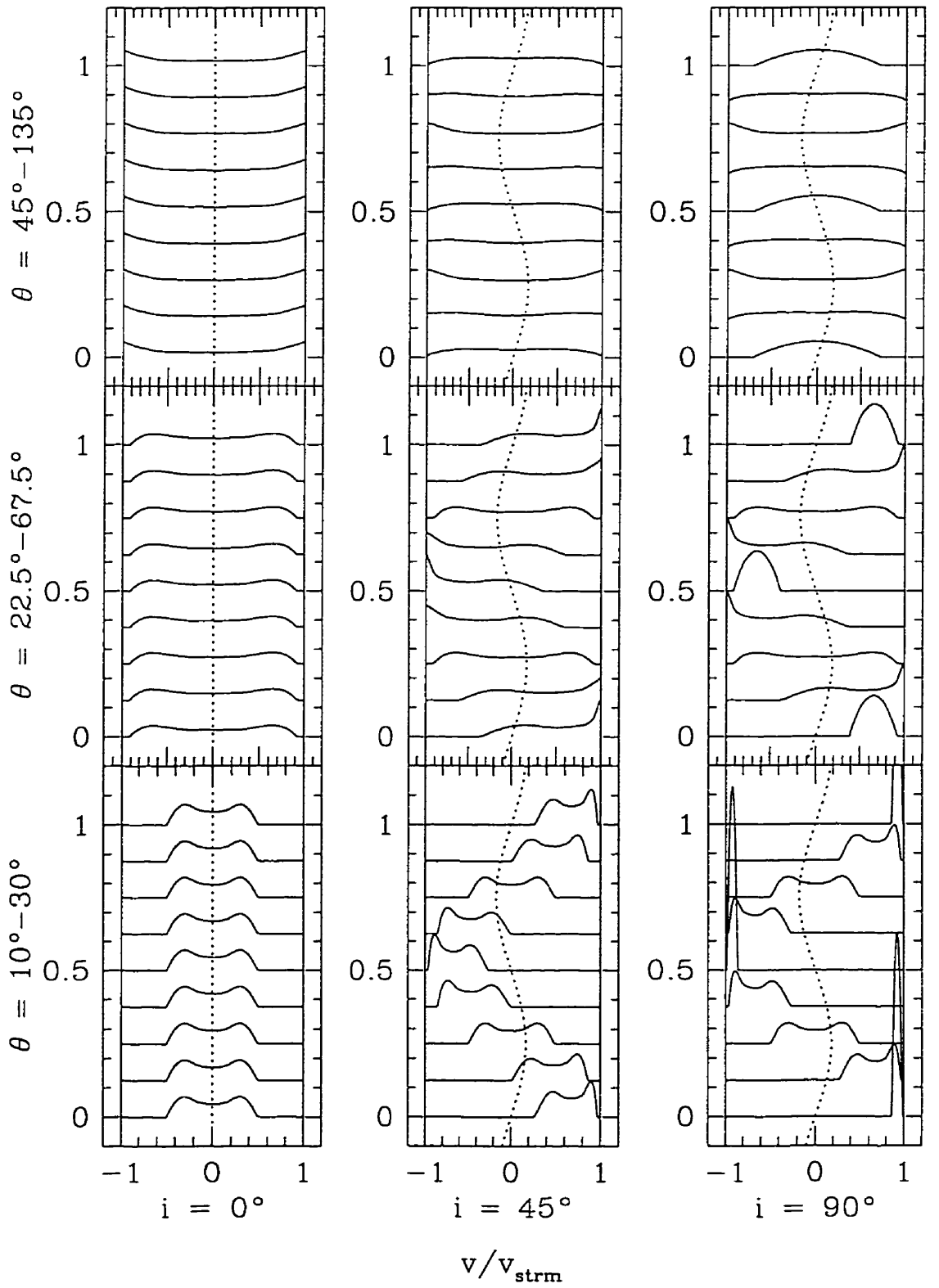

Figure 5.20: *Lührs' profiles at various inclinations and phases, with* $\delta\varphi = 0$. *The velocity scale is normalised to* $v_{\rm strm}$. *The dashed curve depicts the RV orbit of the WR-star (amplitude of* $0.2v_{\rm strm}$*). The range in cone opening half-angle* θ *goes from* θ_1 *to* θ_2 *in the context of the model, such that* $\Delta\theta \equiv \theta_2 - \theta_1 \approx \bar{\theta} \equiv (\theta_1 + \theta_2)/2$ *i.e. the adiabatic case. Phase is shown on the abscissa of each plot, where phase* $\varphi = 0$ *is when the WR-star is in front of the O-star.*

Variation with orbital phase

The flow of matter along the thick mantle of the cone will cause the mean position of Lührs' profile to vary sinusoidally with phase. At phase $\varphi = 0$, the WR-star is in front of the O-star and the cone material flows away from the observer. The mean position is at its extreme red-shifted velocity. As the stars revolve about one-another, the cone opening swings about through $\varphi = 0.25$, when the profile mean is at zero redshift. The profile reaches maximum blue-shift at $\varphi = 0.5$ when the O-star is in front of the WR-star and the mean cone flow is towards the observer. As revolution continues, the mean profile eventually returns to maximum red-shift. This effect is seen most clearly for $\theta = 10°$–$30°$ with $i = 45°$.

At $\varphi = 0$, the shock-flow's velocities at different parts of the cone tend to be compressed in a small region of velocity-space (when projected to the observer). This yields profiles with relatively small FWHM. As the stars reach quadrature, the projected velocities are most separated and the FWHM is largest. The FWHM decreases thereafter until $\varphi = 0.5$; then the cycle is repeated from $\varphi = 0.5$ through $\varphi = 1$. The FWHM varies sinusoidally at twice the frequency of the orbital revolution.

For similar reasons the height of the emission peaks vary with phase. At phase zero most of the projected velocities are crowded near the extreme red-shift. The red-shifted peak becomes higher in intensity than the blue-shifted one (with systems of $i = 90°$, the two peaks degenerate into one). With increase in phase, the projected velocities spread until quadrature, when both peaks are of equal height (and lower than the red peak at conjunction). Here, an equal amount of flux is heading towards the observer as is receding from him. As $\varphi = 0.5$ is approached, the velocities cluster more towards the blue extreme and the blue peak becomes higher in intensity. After $\varphi = 0.5$, the described cycle is reversed until $\varphi = 1$ is reached.

Variations with inclination

With no orbital inclination, there is no change in how the system is viewed with phase and so no change in profile. Note, however, that the double peaks exist nevertheless as a result of projected velocities heading towards and away from the observer.

A non-zero inclination permits observation of the phase-variations described above. The width of the profile also varies with inclination, with systems viewed edge-on permiting the most compression and dilution of intensities in Doppler velocity-space.

Variations with opening angle

The opening angle determines the spread of projected velocities of the cone material. Systems with small cone angles have material flowing in a similar direction so that the projected velocities will be compressed about that of the centroid. Wide cones have greater extent in velocity-space, with the widest having shocked matter flowing outwards along almost a disk for a shock surface, giving the widest differential velocities. These will have the widest Lührs' profiles. This is best illustrated with the profiles for $i = 0°$.

5.4 Shock-cone parameters from CIII 5696

If the theory of Section 5.3 is correct, then it should be possible to determine the form of the shock-cone using the equations derived in that section. To do this, Lührs fit each observed profile of his CIII 5696 excess emission data of the WC7+O6 binary WR79 individually for each spectrum to derive a global set of mean parameters. Here, an attempt will be made to find the parameters by fitting the profile curves to all the excess emission line data for Br22 simultaneously.

5.4.1 Fitting to the Lührs profile

A non-linear, least-squares routine was used to fit Equation 5.8 to excess emission line data from the WWC (see below). The fit parameters were $\theta_1, \theta_2, i, \delta\varphi$ and $v_{\rm strm}$. A zero-point velocity for the profiles, v_0, was included as a fit parameter, to locate the *a priori* unknown line centre of the normalised velocity $u = (v_{\rm o} - v_0)/v_{\rm strm}$, where, as before, $v_{\rm o}$ is the observed velocity of an element in the profile. A final parameter was a constant of proportionality for the intensity of the line, $I(u)$.

To allow for the possible presence of a flat-top profile of C III 5696 from the WR wind itself, a square line profile, S, was added to the excess emission fit. This new profile was assumed to move in phase with the WR-star and independently of the excess emission. Fit parameters for S were its intensity, velocity at $\varphi = 0$, line width and radial velocity amplitude. Its intensity could be set to zero when desired. The total profile fit was

$$P(u)\,du = I(u)\,du + S(u)\,du.$$

The χ^2 function of the above equation was fit with the routine PIKAIA [pre-release version (Charbonneau 1995)], a modeling program whose method of optimisation is analogous to the process of genetics and the theory of natural selection. This was chosen since it is very effective for models that are highly non-linear, is very unlikely to find erroneously a solution that is at a secondary extremum and requires no initial estimate of the solution.

A fit of Lührs' model simultaneously, according to the above technique, was made for the C III line in the Nov. 1993 epoch for Br22. The results are shown in Figure 5.21 on the following page. It is apparent from the figure that the model qualitatively follows, with phase, the overall displacement and width of the profile very well. There are, however, discrepancies at the extremes of the line profiles. When the profile approaches its extreme red or blue displacement, the outer peak expected by the theory does not appear in the data. The values of the parameters of the best fit are listed in Table 5-I on page 92. The long process

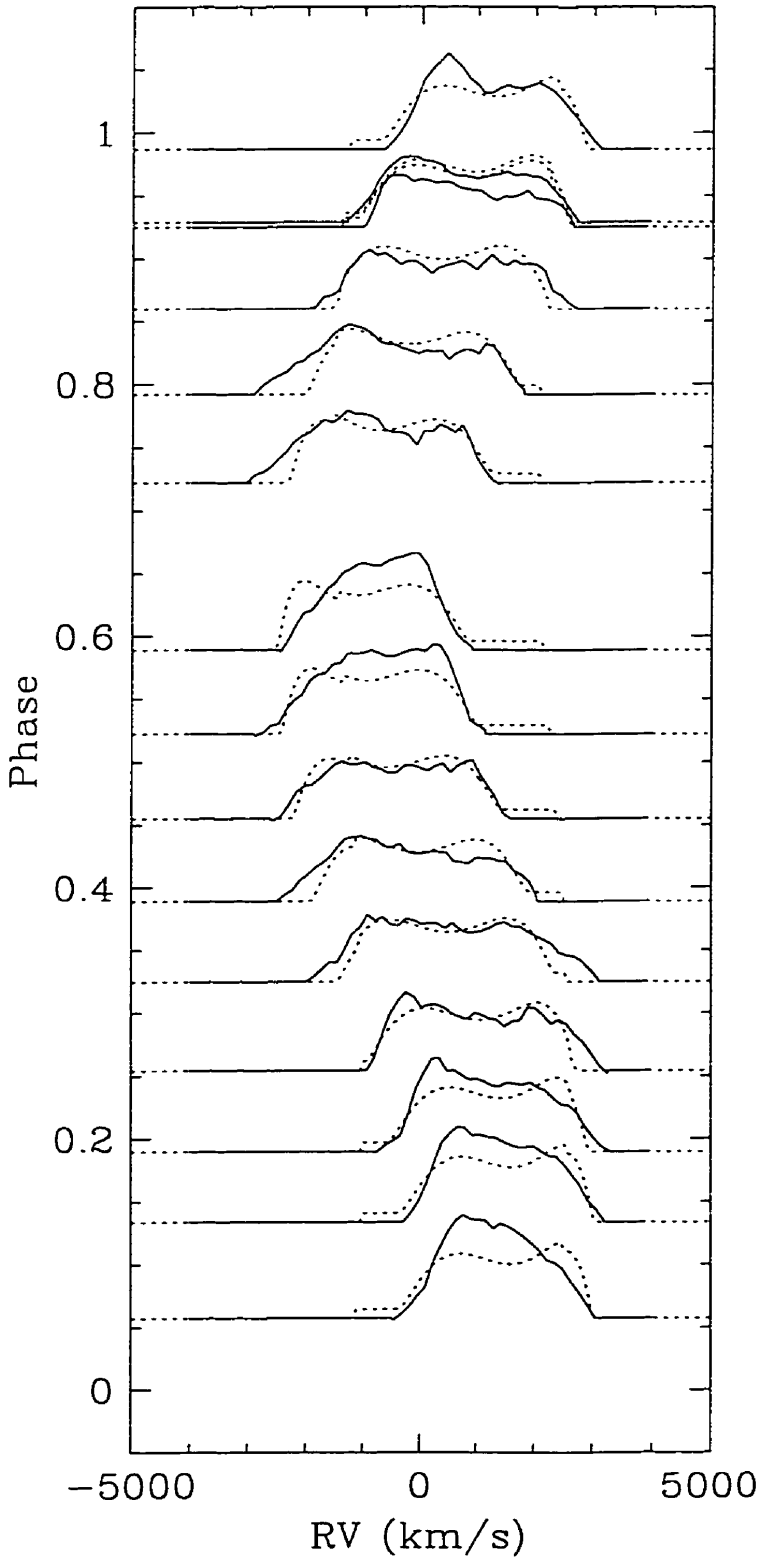

Figure 5.21: *Lührs' model fit to spectra of Br22. The solid lines represent the data while the dotted lines show the corresponding model fits. Here the wavelength is in the inertial frame of the centre-of-mass.*

of calculating errors of the coefficients was not undertaken, given the systematic problems encountered. In any case, the inclination determined by the fit of the

Table 5-I: *Parameters values of Lührs' model fit to Nov. 1993 spectra of* CIII *5696 Å line. Included are results from an attempt to determine cone parameters from arbitrary estimated peak locations (see Subsection 5.4.2) and the estimated inclination from other methods.*

Parameter	Simultaneous fit	Peak Estimates[a]	Photometry[b]	Polarimetry[c]	Spectroscopy (O-star)[d]
θ_1 (degrees)	3	$\bar{\theta} = 47$	—	—	—
θ_2 (degrees)	40		—	—	—
i (degrees)	29	63	76	71	71
$\delta\varphi$ (degrees)	47	—	—	—	—
v_{strm} (km/s)	2991	1570	—	—	—
v_0	270 (km/s)	—	—	—	—
S (int.)	0.04	—	—	—	—
$S(\varphi = 0)$ (km/s)	544	—	—	—	—
S (width) (km/s)	3639	—	—	—	—
S (amp.) (km/s)	272	—	—	—	—

[a]Bartzakos, Moffat & Niemela 1995
[b]Seggewiß, Moffat & Lamontagne 1991
[c]Moffat, unpublished data
[d]MNM

Lührs' model is much smaller than that found by four other methods! For this reason, no attempt is made to fit the Lührs' profile to WR9.

What process can produce a spectroscopic profile where the peak at a velocity extremum is not produced? The first idea that comes to mind is some sort of occultation of the shock cone by the O-star, so that the material that would produce the extreme peak is hidden from view (Figure 5.22 on the following page). At all orbital phases, however, only the most red-shifted material can be occulted by the O-star. Only the reddened peak could be eliminated, yet the blue peak, when the profile is at its extreme blue velocity, is missing as well (*cf.* Figure 5.21).

Another idea might be that the line profile of the WR-star is partly deleted by the O-star wind, replaced by WWC emission at only slightly lower RV seen by the observer (see Figure 5.23 on page 94). When the WR-star is in front, the O wind cavity occurs at high RV in the CIII base, thus depressing the outside (red) peak of the excess emission, as observed. When the WR-star is behind, the

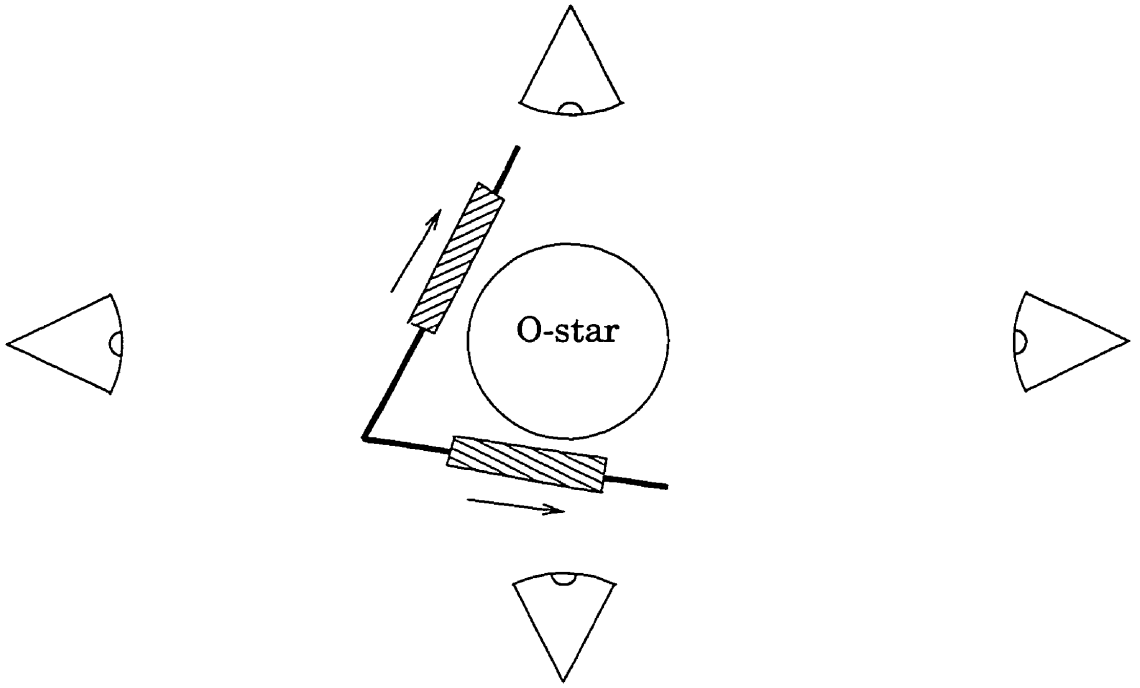

Figure 5.22: *Occultation of shock cone by companion O-star, as viewed from various directions. The emitting region of interest is illustrated with hatched rectangles.*

blue peak is depressed, also as observed. At opposition, the cavity occurs close to zero RV.

Another explanation that qualitatively works is as follows: when the shock cone is seen pointing away from the observer (maximum mean redshift) it is possible that its far edge is observed along the line-of-sight (*i.e.* $\bar{\theta} \approx i$). Under these conditions the emission from this part of the cone, moving at approximately constant speed at different distances along the cone, could be optically thick and so reduced in intensity. This corresponds to the red peak. When the shock cone points towards the observer (maximum mean blue shift), the same reasoning explains the reduction of the blue peak intensity.

One other possibility might be narrow CIII emission arising in the O-star wind, as seen in many late-type O-type supergiants (*e.g.* Walborn 1980). In fact, there is a variable and narrow CIII 5696 feature occuring at about the same RV in the binaries Br31 and Br32.

In any case, the true origin of this problem remains to be found with certainty.

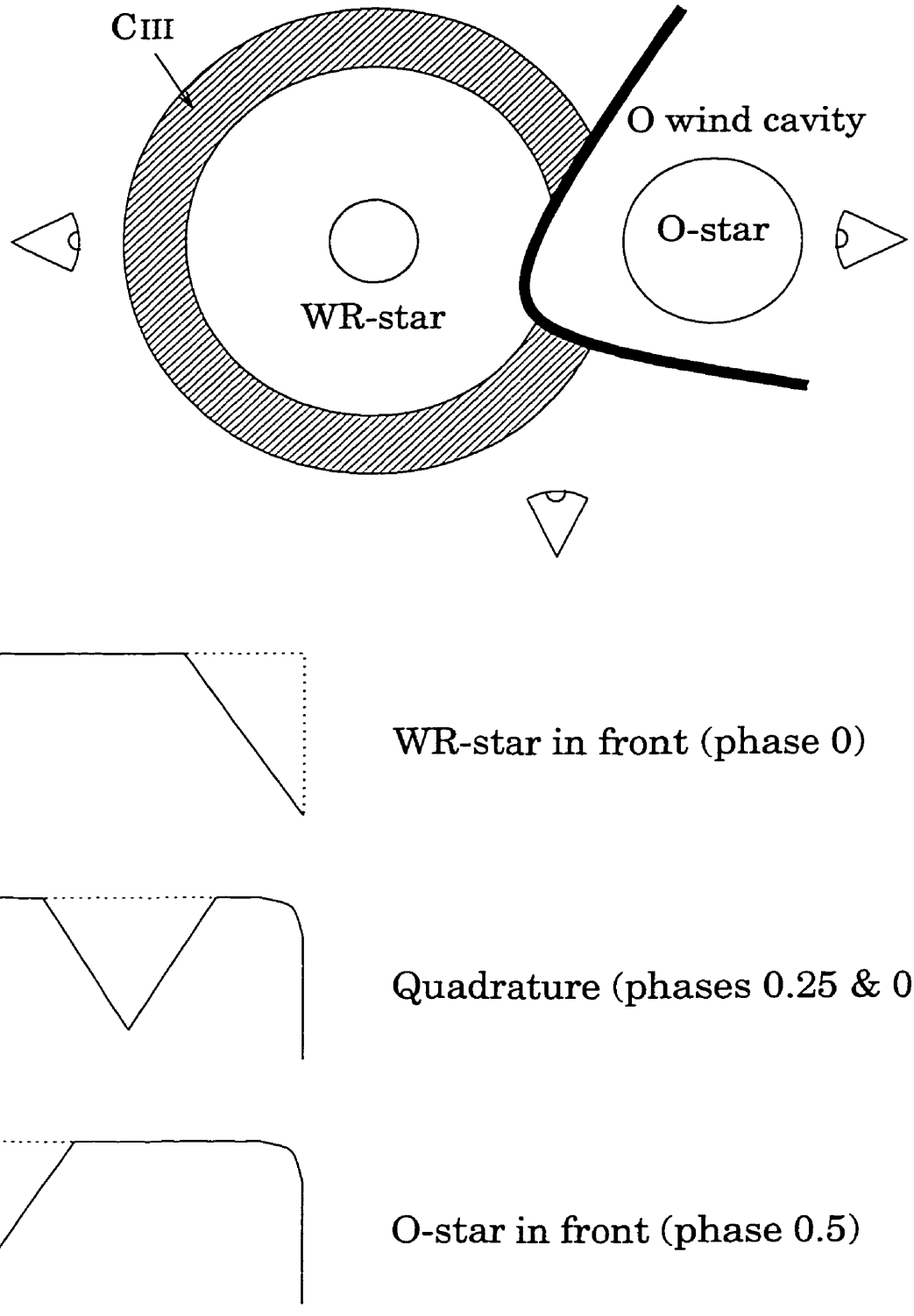

Figure 5.23: *Schematic illustration of the effect of O-star wind cavity on line profile. The top illustration shows the binary from various viewpoints while the bottom one presents expected* CIII *line profiles at various orbital phases.*

It could entail several or none of the above effects. For the time being, an attempt to determine the WWC parameters from CIII 5696 in Br22 and WR9 is made using a simple approach, in the next section, that is less sensitive to detailed profile fitting.

5.4.2 Wind-wind collision parameters from excess mean RV and FWHM variations

As an alternative to profile fitting, Lührs also measured the location of the double peaks of the excess emission of CIII 5696 Å for WR79. He then fit $v_{x_o} + v^*$ and $v_{x_o} - v^*$ to the corresponding blue and red peak positions, respectively, to obtain various parameters of the shock cone and the inclination of the binary system (Lührs 1991; see also Lührs 1997), where $v_{x_o} = v_{\rm strm} \cos\theta \cos\varphi \sin i$ and $v^* = v_{\rm strm} \sin\theta \sqrt{1 - \sin^2 i \cos^2\varphi}$. These values yield $I(v_{\rm o}) \rightarrow \infty$. Although they have the merit of being directly derived from the physical quantities described by these equations, locating the peak positions can be difficult. The two peaks might not even be obvious (as in many spectra of Br22). Attempting to use the method of fitting to peak positions thus becomes unreliable. Such an effort, for Br22, was made by Bartzakos, Moffat & Niemela (1995); the positions of missing peaks were roughly compensated for by choosing the location where the profile intensity appeared to be at an extremum before falling off rapidly.

Another alternative that is impervious to arbitrary location of the two peaks is to measure and fit the mean RV and the FWHM of the excess emission as a function of orbital phase. To do this, one can write

$$\bar{v}_{\rm ex} = \text{constant} + v_{x_o} \tag{5.9}$$

$$= a_1 + a_2 \cos 2\pi(\varphi - a_3) \tag{5.10}$$

and

$$\text{FWHM}_{\rm ex} = \text{constant} + 2v^* \tag{5.11}$$

$$= c_1 + c_2 \sqrt{1 - c_3 \cos^2[2\pi(\varphi - c_4)]} \tag{5.12}$$

in which

$$a_1, c_1 = \text{constants}, \tag{5.13}$$

$$a_2 = v_{\text{strm}} \cos\theta \sin i, \tag{5.14}$$

$$a_3 = c_4 = \delta\varphi, \tag{5.15}$$

$$c_2 = 2v_{\text{strm}} \sin\theta \qquad \text{and} \tag{5.16}$$

$$c_3 = \sin^2 i. \tag{5.17}$$

To illustrate the dependence of $\text{FWHM}_{\text{ex}}(\varphi)$ on i, equation 5.12 is plotted for various values of orbital plane inclination in Figure 5.24 on this page.

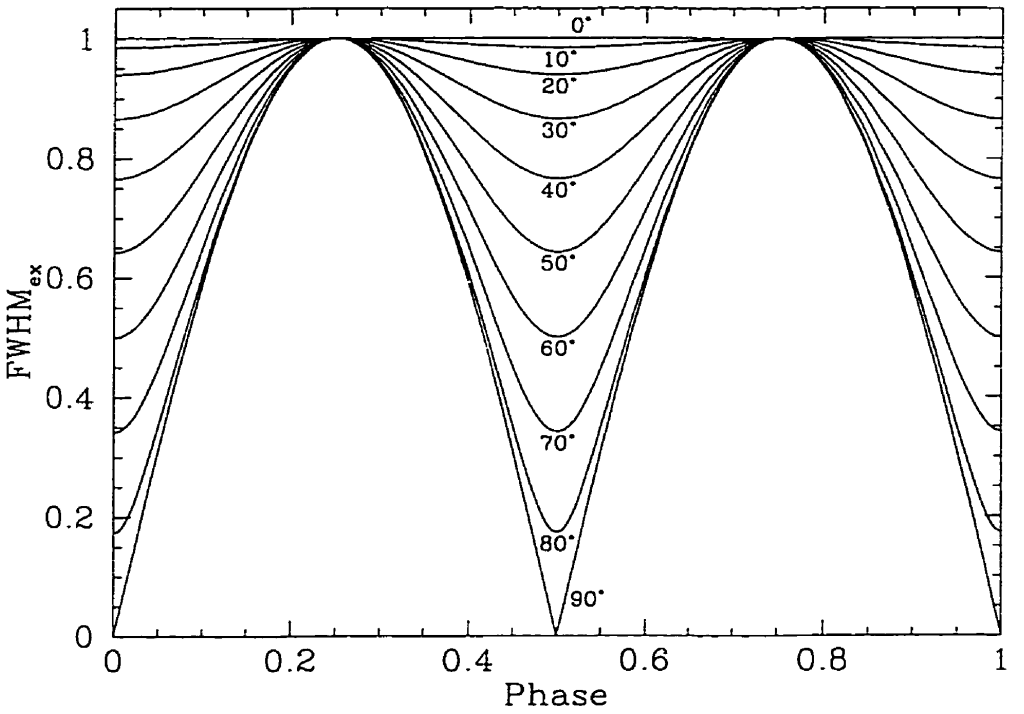

Figure 5.24: FWHM_{ex} *as a function of orbital phase plotted for various inclinations at* 10° *increments. Each curve is labelled with its inclination. Here* $c_1 = 0, c_2 = 1$ *and* $c_4 = 0$.

It is assumed here that the separation of the two peaks and the observed FWHM differ by the same constant for all phases, which might not be precisely true. For lack of a better objective technique, this was used nevertheless as a working model. This method was applied to CIII 5696 on both Br22 and WR9 for the Nov. 1993 data (the best and most complete set).

Before a fit was made with equations 5.10 and 5.12, an estimate of the base profile of CIII 5696 Å inherent in the wind of the WR-star was done. All of the Nov. 1993 spectra of the star were shifted to the same mean velocity by subtracting the orbital velocity measured from the CIV 5808 Å emission line of each spectrum. This put the spectra in the frame of the WR-star. All spectra were then adjusted to the same wavelength dispersion, superimposed upon one another and a minimum profile was defined by the lowest intensity of all spectra at each pixel (see Figure 5.25 on the next page).

The purpose of this minimum profile was to define a maximum possible emission of CIII 5696 from the star. This emission line is expected to be flat-topped. The peak in the minimum profile was, therefore, replaced by a line manually interpolated between the two wings of the minimum profile to finally yield the pedestal profile assumed for the star (dashed lines in Figure 5.25). (The equivalent width of this profile was used to find the true CIII 5696 Å to OV 5592 Å W_e ratio of the WR-star corrected for WWC; see footnotes of Table 3-IV.)

This pedestal line was then subtracted from each spectrum to estimate the net excess emission of CIII due to WWC (subtracting the same flat profile at all phases is an approximation since it is possible that different sections of the profile are partially deleted by the effect of the O-star wind cavity, as illustrated in Figure 5.23, rendering the profile variable rather than constant). The redshifts of the spectra were then added back to return the excess emission profiles to the frame of the observer. These profiles are illustrated in Figure 5.26 on page 99.

The radial velocity of the excess emission, as well as the FWHM, was calculated in the same way as they were for the CIV 5808 Å line described in Chapter 3. The radial velocities were fit to equation 5.10 in the same manner as were the radial velocities were fit to circular orbits in Chapter 4, with a fixed period taken from Tables 4-II and 4-III. The FWHM were fit to equation 5.12 with the non-linear least-squares routine `mrqmin` of Press *et al.* (1992, pp. 675-683). The error on each data point was taken to be unity.

The results of the radial velocity fits of the excess emision for both Br22 and

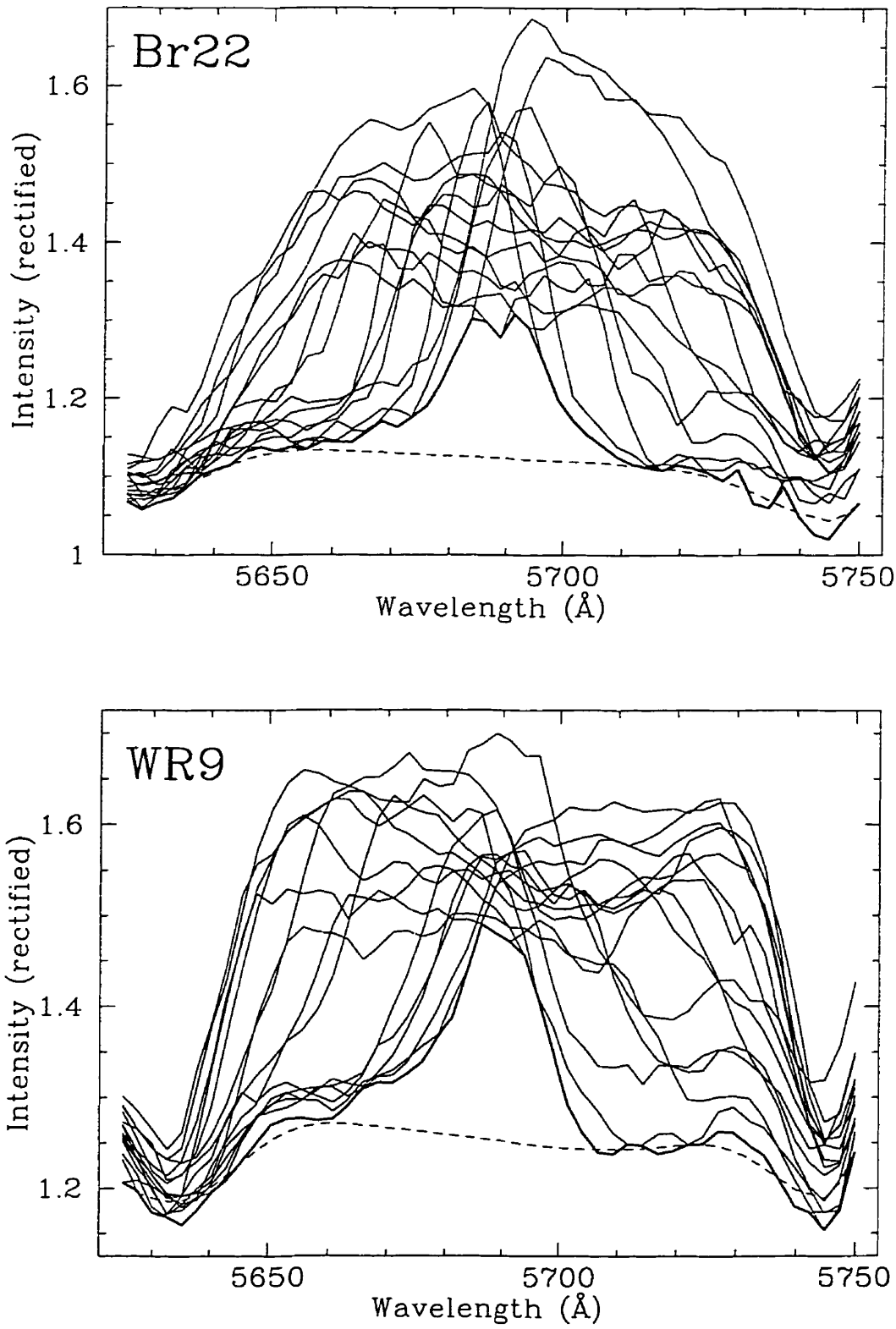

Figure 5.25: *Superposition of spectra, minimum profile (thick line) and assumed pedestal WR-star emission of* C III *5696 Å (dashed line) for Br22 and WR9.*

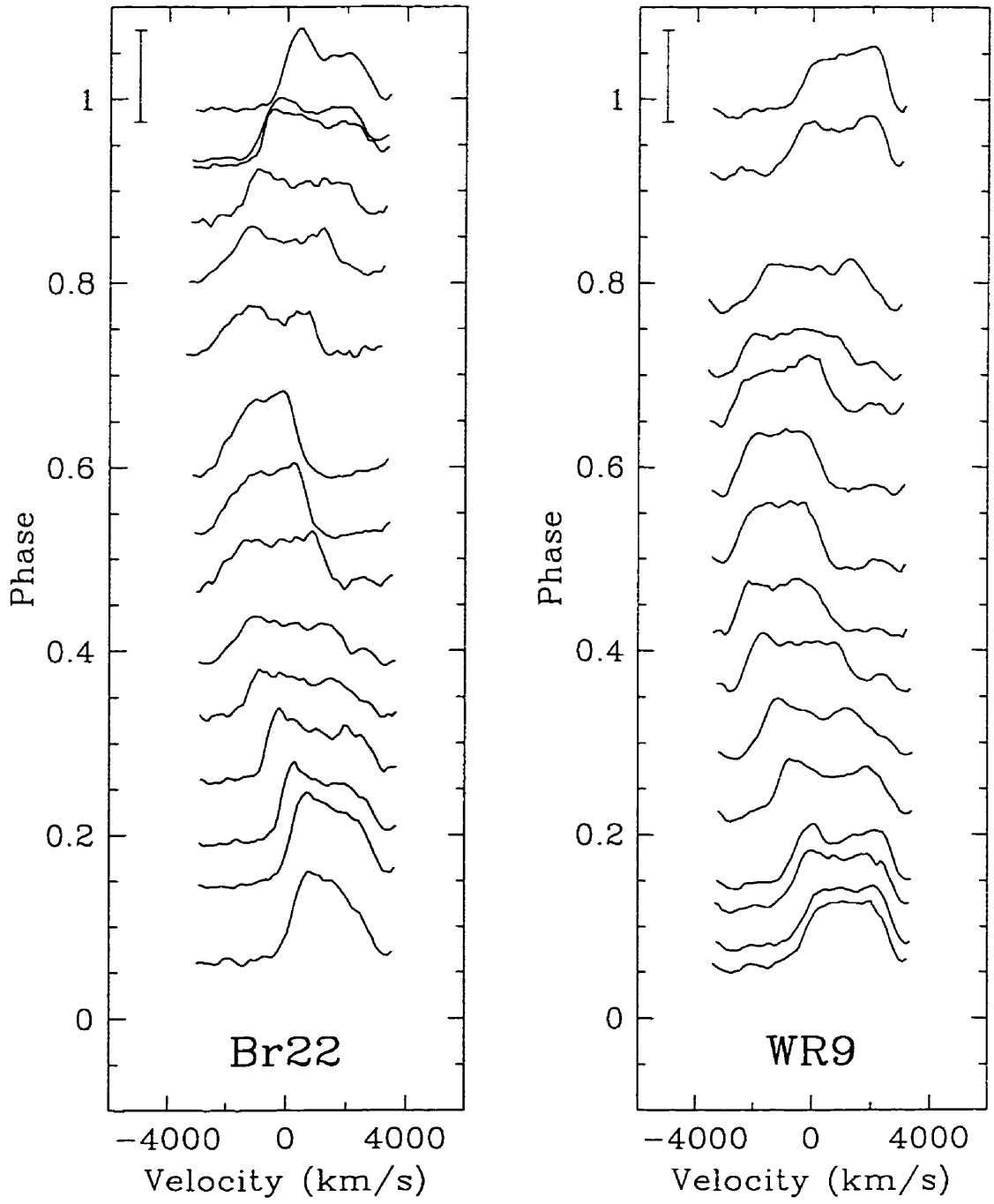

Figure 5.26: *C III 5696 Å net excess emission profiles for Br22 and WR9. The error bar height indicates fifty percent of the intensity of the continuum.*

WR9 are illustrated in Figure 5.27 on the next page while those for the FWHM fit are illustrated in Figure 5.28 (page 102). The values of the WWC parameters are listed in Table 5-II on this page, as derived from equations 5.14, 5.15, 5.16 and 5.17. Results for variable as well as fixed inclination are shown.

Table 5-II: *Shock cone parameters derived from RV and FWHM fits to* C III *5696 Å excess emission. Results for both variable and fixed inclination are shown.*

Parameter	Br22		WR9	
a_1 (km/s)	245 ± 22		-19 ± 24	
a_2 (km/s)	1097 ± 32		1187 ± 32	
a_3 (degrees)	38 ± 14		22 ± 44	
	Variable i	Fixed $i = 71°$[a]	Variable i	Fixed $i = 68°$[a]
c_1 (km/s)	$-2800 \pm 13\,700$	1680 ± 120	1500 ± 2600	2230 ± 120
c_2 (km/s)	$6600 \pm 13\,800$	1980 ± 150	2300 ± 2700	1610 ± 16
c_3	0.36 ± 0.67	0.894 ± 0	0.666 ± 0.565	0.860 ± 0
c_4 (degrees)	32 ± 2	32 ± 2	2 ± 3	2 ± 3
i (degrees)	37 ± 40	(71)	55 ± 34	(68)
v_{strm} (km/s)	3800 ± 6100	1520 ± 55	1870 ± 970	1510 ± 53
θ (degrees)	60 ± 58	40 ± 2	39 ± 37	32 ± 3

[a]Moffat, unpublished polarimetric data

It is quite clear that the fit with variable inclination yields results that are absurd. The errors on some parameters are very high (c_1, c_2 and v_{strm}). In fact, the values of the parameters themselves are unrealistically high: v_{strm} is higher than the expected speed of Wolf-Rayet winds. As well, there is a negative result for c_1 in Br22 while FWHM should always be a positive quantity. The fit with fixed inclination gives parameter results and errors that are much more reasonable.

It appears that the fit is little sensitive to inclination. In Figure 5.29 on page 103 equation 5.12 is plotted for various values of i. All curves are normalised to the same amplitude. Relatively little change occurs between solutions for different inclinations, except for values near $i = 90°$. The fit solution could very well be numerically degenerate in i, given the scatter in the data.

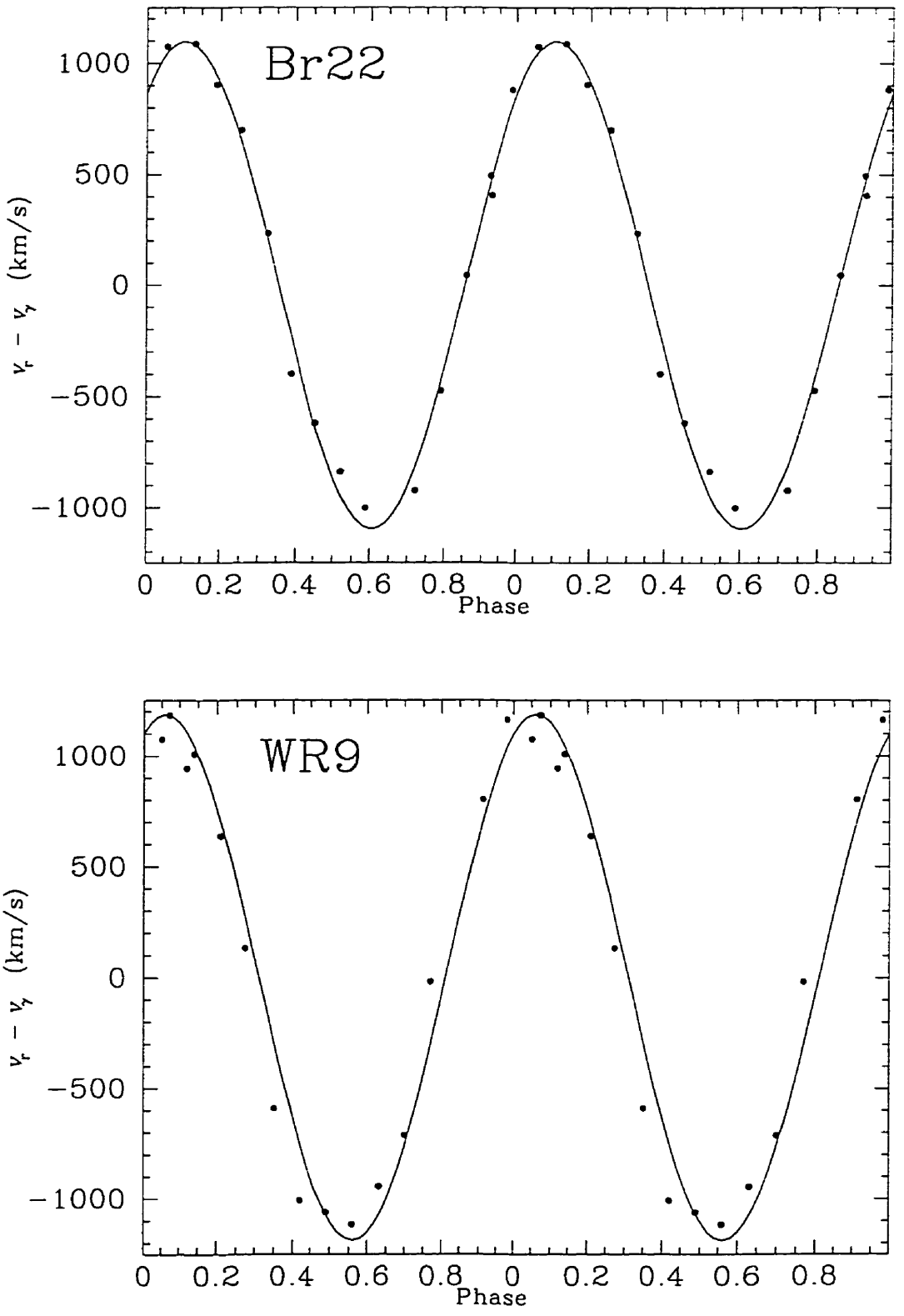

Figure 5.27: *Fit to* C III *RV of excess profiles of Br22 and WR9. The same data are repeated over two orbital cycles. Phases are based on the WR-star orbit.*

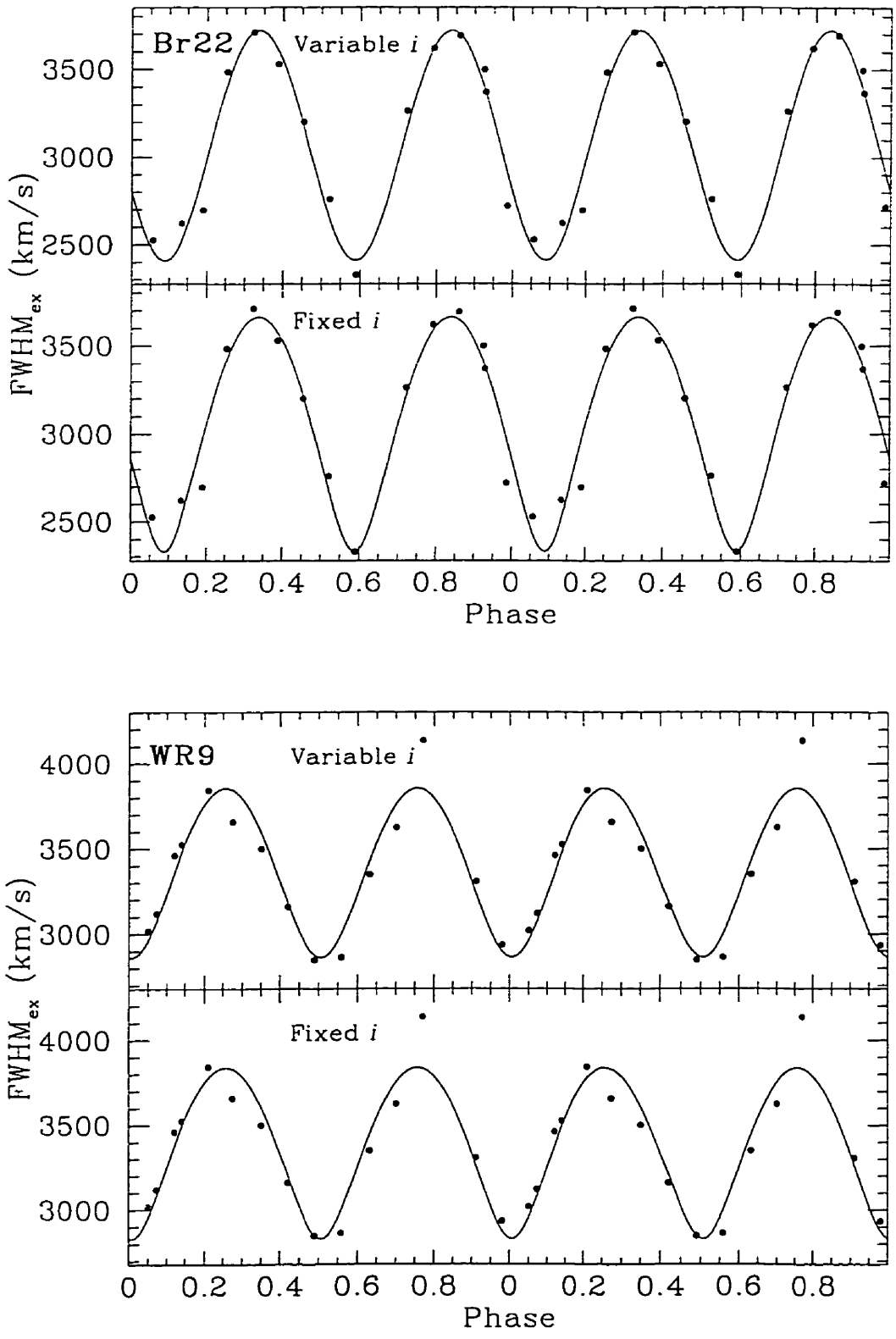

Figure 5.28: *Fit to* C III *FWHM of excess profiles of Br22 and WR9 (variable and fixed inclination). The same data are repeated over two orbital cycles.*

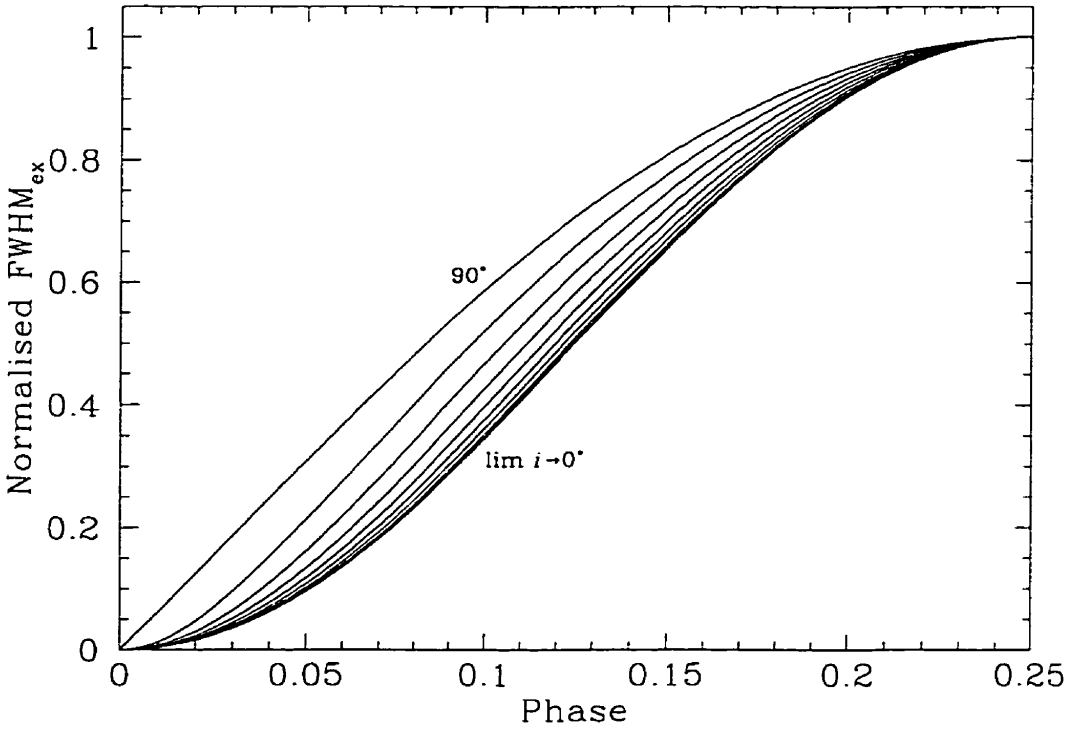

Figure 5.29: *Normalised profiles of* $\mathrm{FWHM_{ex}}$ *for* 10° *increments in inclination from phase* $\varphi = 0$ *to* $\varphi = 0.25$. *The curves with inclinations of* 90° *and* $\lim_{i \rightarrow 0}$ *are labelled.*

5.5 Excess emission in CIV 5808

Other emission lines in the binary WR-stars exhibit profile variations (see Figures 5.11, 5.12, 5.13, 5.14, 5.15 and 5.16). In particular, the strong CIV 5808 Å doublet and the CIII/CIV 4650 Å + HeII 4686 Å complex show clear variations with time. If it can be established that these variations are due to WWC excess emission, then it can be concluded that WWC is probably universal amongst close WR binaries. A description of the qualitative study of the CIV 5808 line follows. Note that this line is a doublet (5802/5812), although the 10 Å separation of the two components is relatively small compared to the overall line width in all cases (FWHM > 50 Å). Worse than this is the superposition of the blue edge of HeI 5876 Å on the red wing of CIV 5808, on which the FWHM depends. However, HeI 5876 is relatively weak in WC4/WO-stars and it can be neglected to first approximation. The 4650 Å emission is much more complicated and it is ignored, despite its large variations. As well, the strength (W_e) of the CIV 5808

line shows no significant change with phase in any of the binaries, nor with time in any of the single WC-stars.

5.5.1 FWHM variations of the CIV 5808 line

In Subsection 5.4.2, the variation of the FWHM of the CIII 5696 Å excess was used as a measure of certain parameters of the WWC shock cone. Phase-dependent FWHM variations should be present in other lines if a WWC is present and excess emission is produced for the same reason as that for CIII.

Without trying to isolate any excess emission initially, the FWHM of the CIV 5808 line was studied with the assumption that excess emission would cause some variation in the overall line. The results for the four MC binaries are displayed in Figure 5.30 on the following page, with those for the two Galactic binaries and the constant stars Br50 and Br70 in Figure 5.31 (page 106).

Both single stars show no significant variation in FWHM. All binaries, however, have a FWHM that varies with phase. The clearest example is Br32. Here, the frequency of variation is twice that for the orbit of the star. This is to be expected for WWC, in view of equation 5.12 and Figure 5.24. All other stars, except for Br22, tend to show a similar variation, although this is not strongly apparent for AB8. Br22 shows FWHM variation with the same main frequency as the orbit, an unexpected result that currently lacks explanation.

5.5.2 Excess emission profiles for CIV

The excess emission profiles for CIV 5808 Å were found in the same manner as were those for CIII 5696 Å (see Subsection 5.4.2). A minimum profile was defined, but unlike the CIII line, this profile was much higher and was also assumed to be round-topped. The minimum profile was arbitrarily taken as the maximum possible base profile of the WR wind (see Figure 5.32 on pages 107 through 109).

The minimum profile was then subtracted from each spectrum in the WR

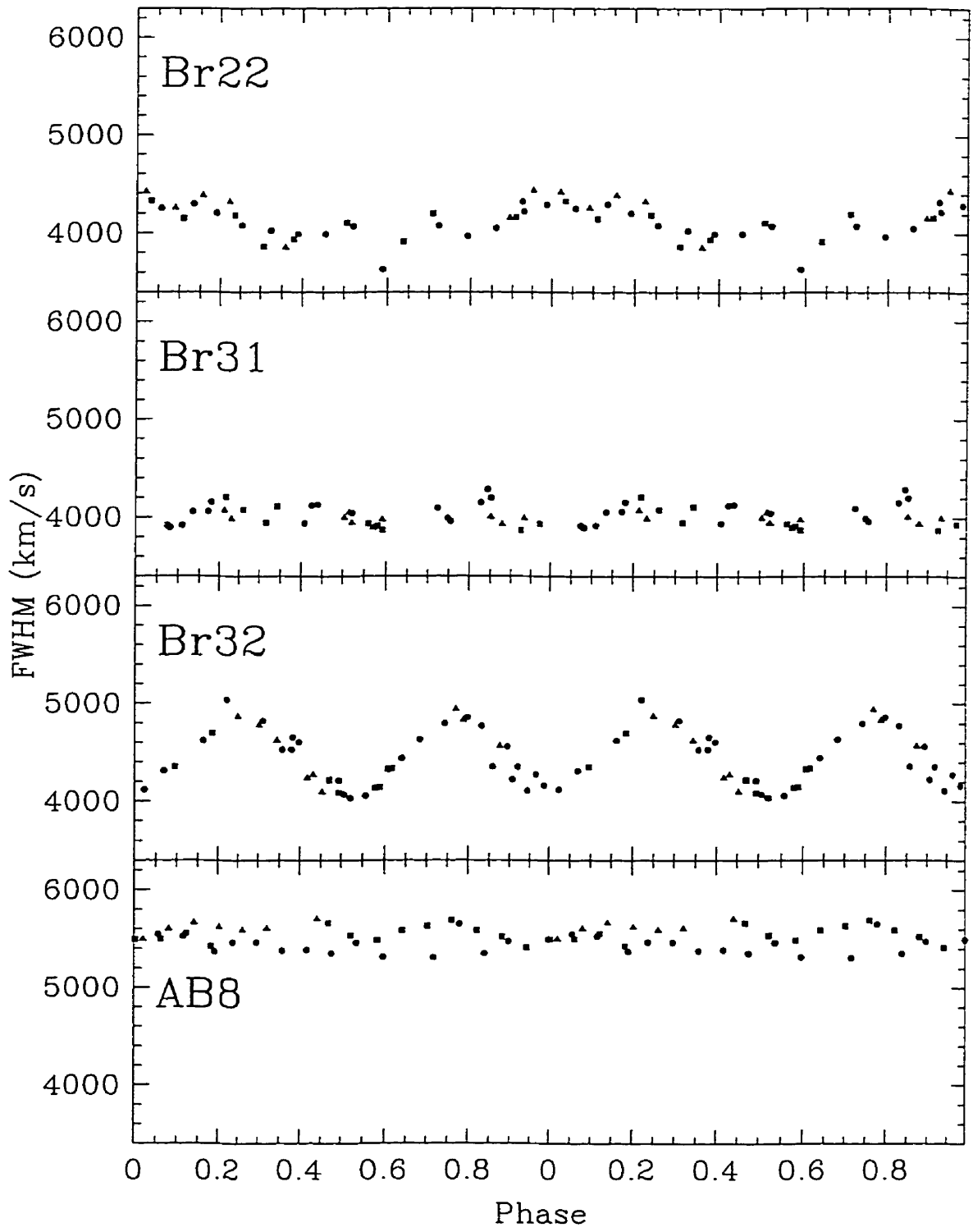

Figure 5.30: *CIV 5808 Å FWHM variations for MC binaries (squares indicate data from Dec. 1984 epoch, triangles for those of the Jan. 1993 epoch and circles denote the Nov. 1993 data).*

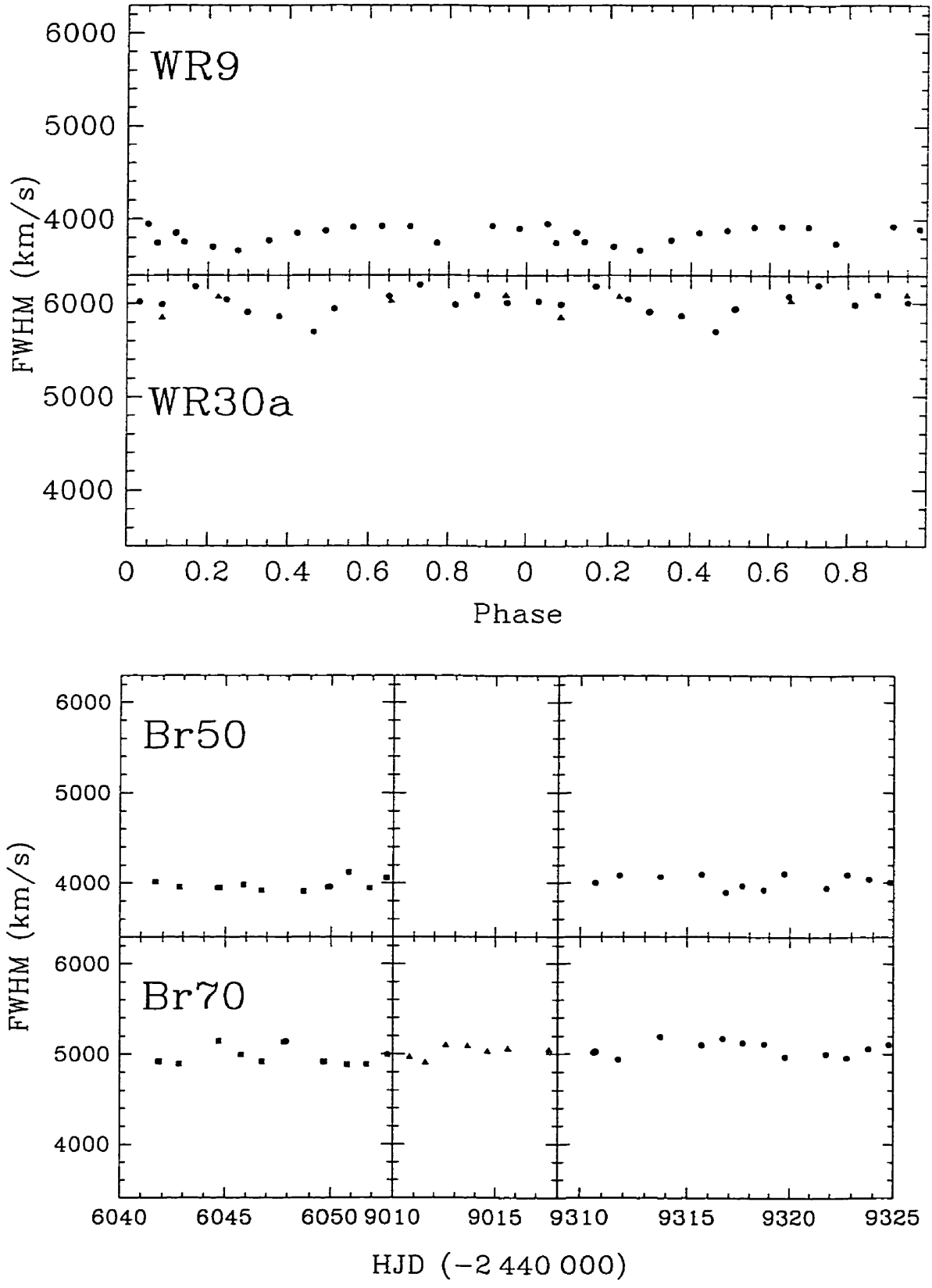

Figure 5.31: *CIV 5808 Å FWHM variations for the galactic binaries and two single WC4 stars in the LMC (squares indicate data from the Dec. 1984 epoch, triangles for those of the Jan. 1993 epoch and circles denote the Nov. 1993 data).*

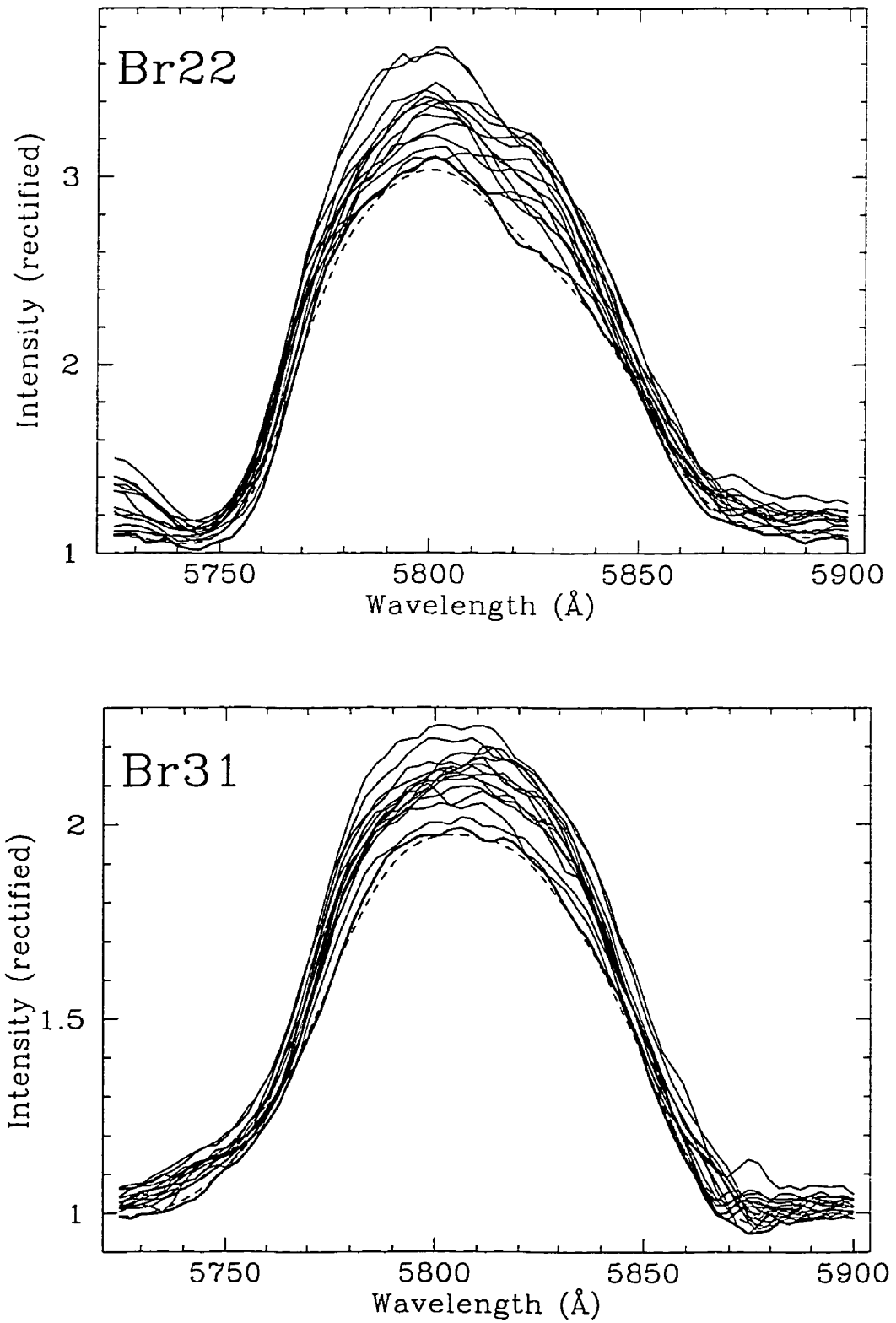

Figure 5.32: *Superimposed spectra and derived minimum profile of* C IV *for the binaries. The solid heavy line is the minimum profile while the dashed line is the smoothed minimum profile used for subtraction.*

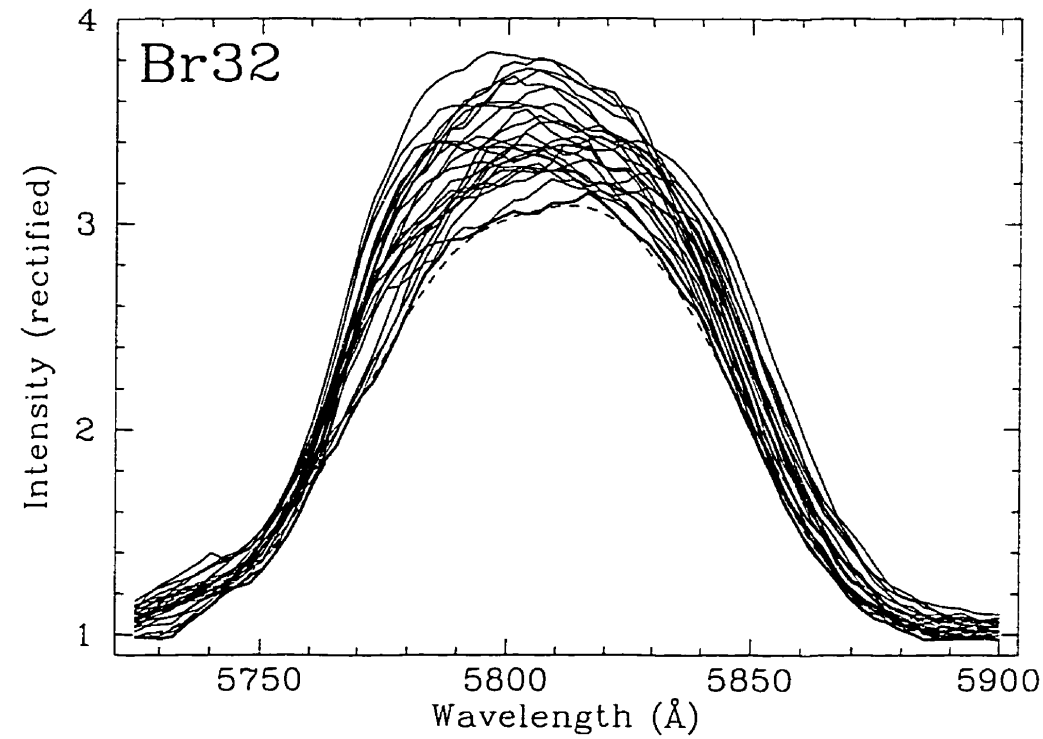

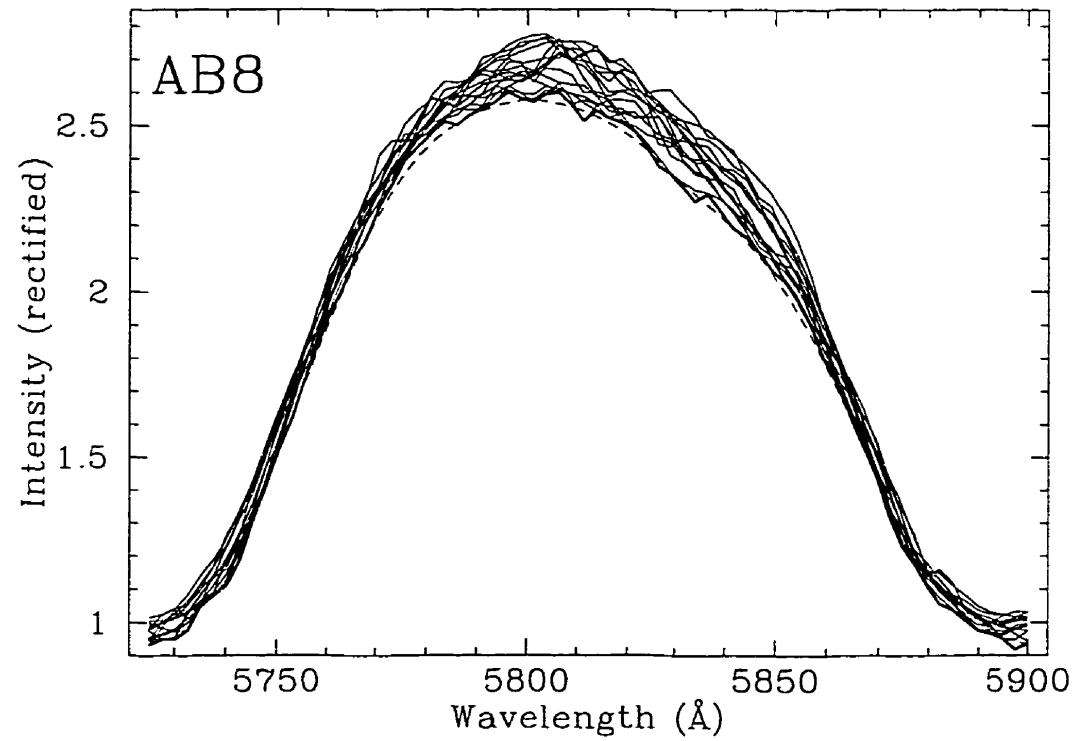

Figure 5.32 . . . continued. . .

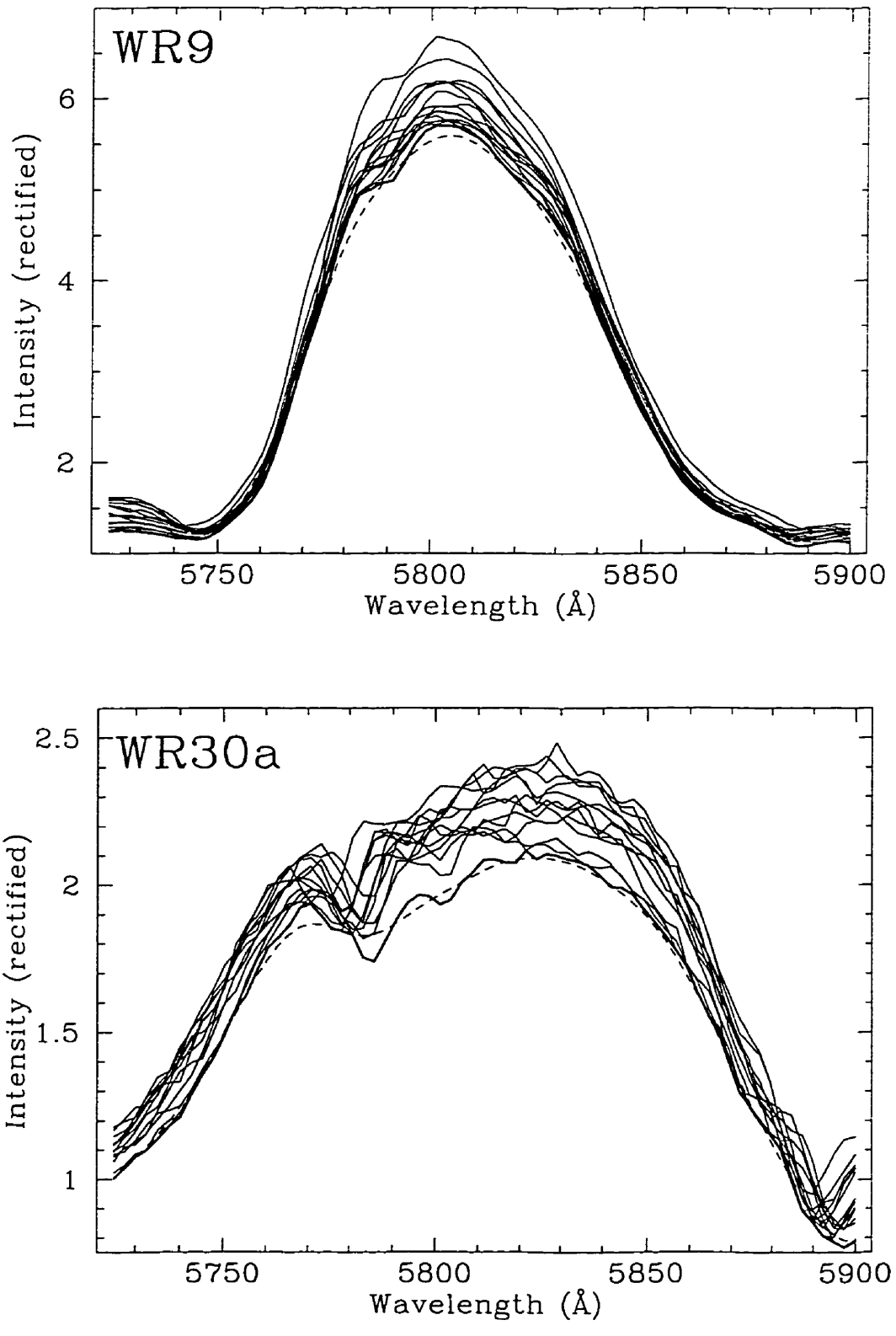

Figure 5.32 ... continued.

frame and the remainder was shifted back to the observer's frame of reference. The results are illustrated in Figure 5.33 from pages 111 to 113.

The plots of the MC stars in Figure 5.33 reveal profiles that vary with phase (this effect is not as clear for the Galactic stars WR9 and WR30a; subjected to greater interstellar extinction they have spectra with a diffuse interstellar absorption feature interfering with the emission line (Herbig 1975); it was manually corrected for in the spectra before obtaining the excess emission profiles shown; these net profiles appear to vary nevertheless). For Br32, and to a lesser extent Br31, which has large phase gaps, the net profiles tend to have a single peak near phases zero and 0.5 (when the binary is at conjunction). As the system rotates towards quadrature, the single peak spreads into two peaks that reach maximum separation near phases 0.25 and 0.75. The mean velocity of the profile does not appear to change much, however. This should be compared to the Lührs' plots for a cone opening half-angle $\theta = 45°$–$135°$ (Figure 5.20). Such a shock cone is akin to a rotating plane between the stars of the binary. Such an effect could be produced for a nearly planar shock cone for winds of equal momentum flux.

In the case of AB8, the peaks also merge and separate twice per orbital cycle, yet the point of merging and separating appear to be phase-shifted by about 0.06. This is likely due to a Coriolis deflection ($\delta\varphi$) of the part of the shock cone where this excess emission is produced. As well, the mean velocity of the feature varies strongly with orbital phase. This is characteristic of a cone with low to moderate opening angle (see the plots for $\theta = 10°$–$30°$, $\theta = 22.5°$–$67.5°$). Such material could be travelling down the sides of a shock cone.

The case of Br22 is similar to those of Br31 and Br32. It has two peaks that tend to separate and merge as well. Like Br32, the mean velocity of the profile varies little, indicating a large cone opening angle. The Coriolis shift of the emitter is also apparent by the phase shift of the points of merging of the peaks (as in AB8). This does not necessarily contradict the results for the study of CIII excess emission, where a narrow cone opening angle was expected. The CIII ions could be formed far from the apex of the shock cone, where the flow would appear

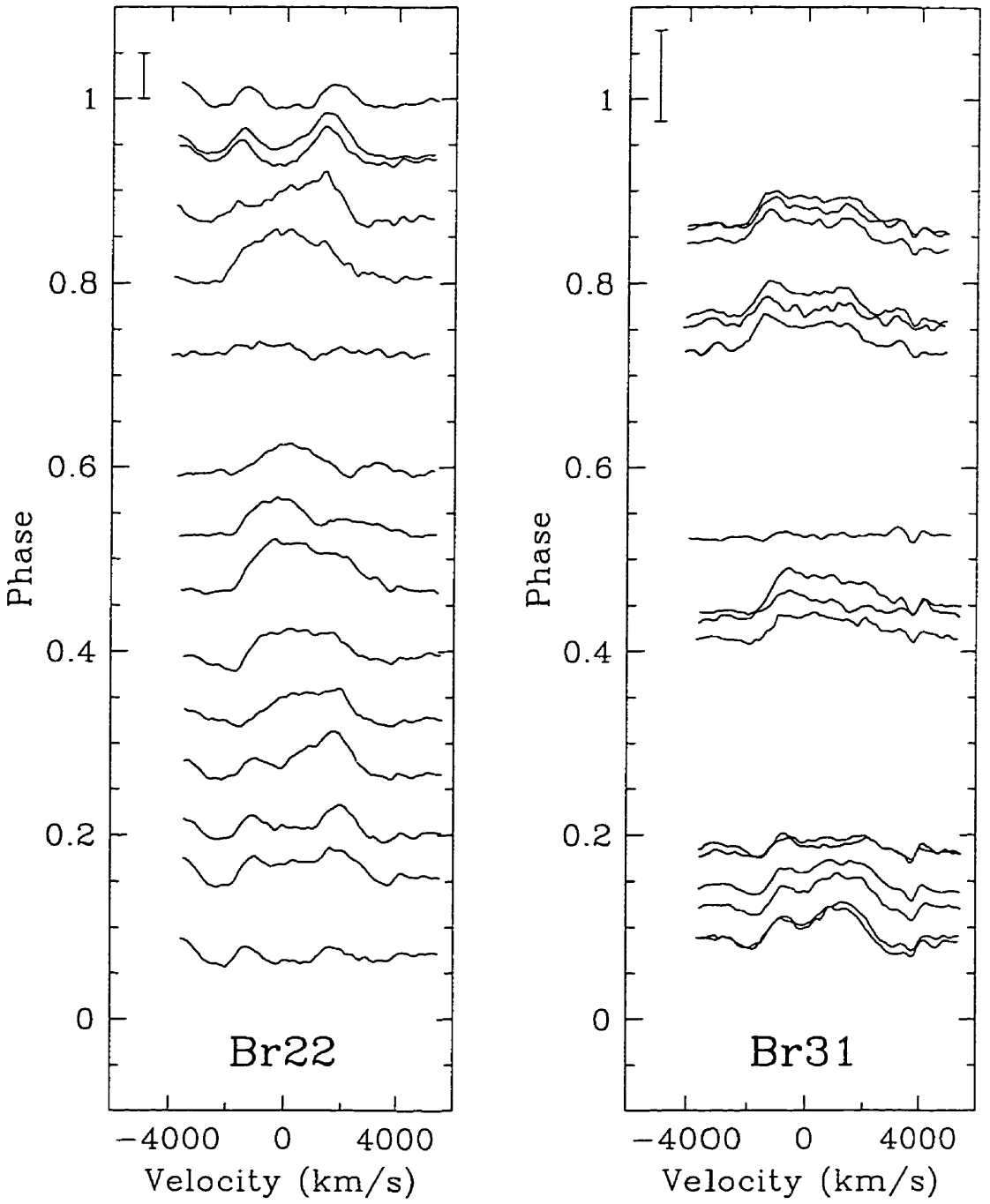

Figure 5.33: *CIV 5808 Å excess emission profiles for the binary programme stars. The height of the error bar shows fifty percent of the continuum intensity.*

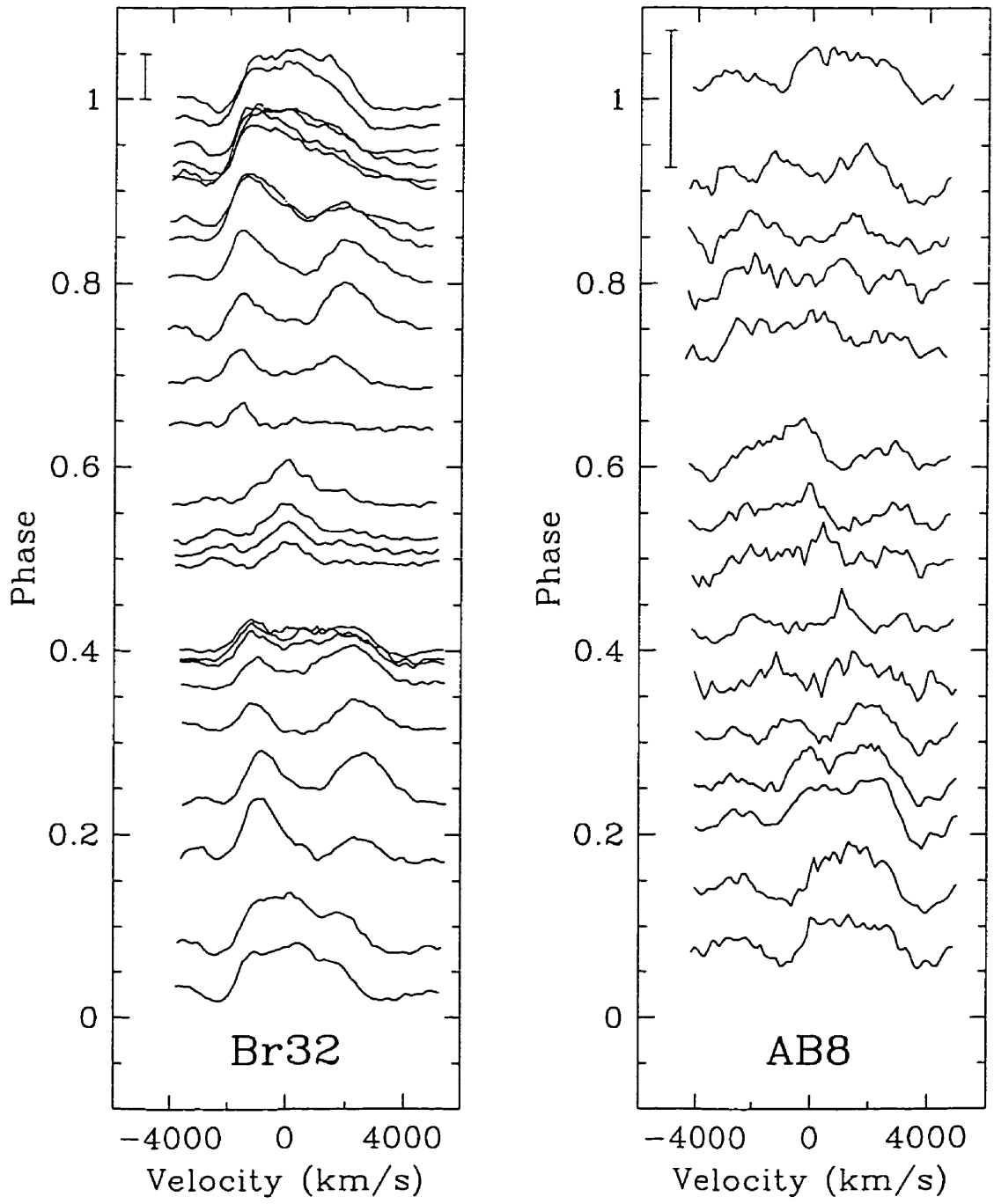

Figure 5.33 . . . continued. . .

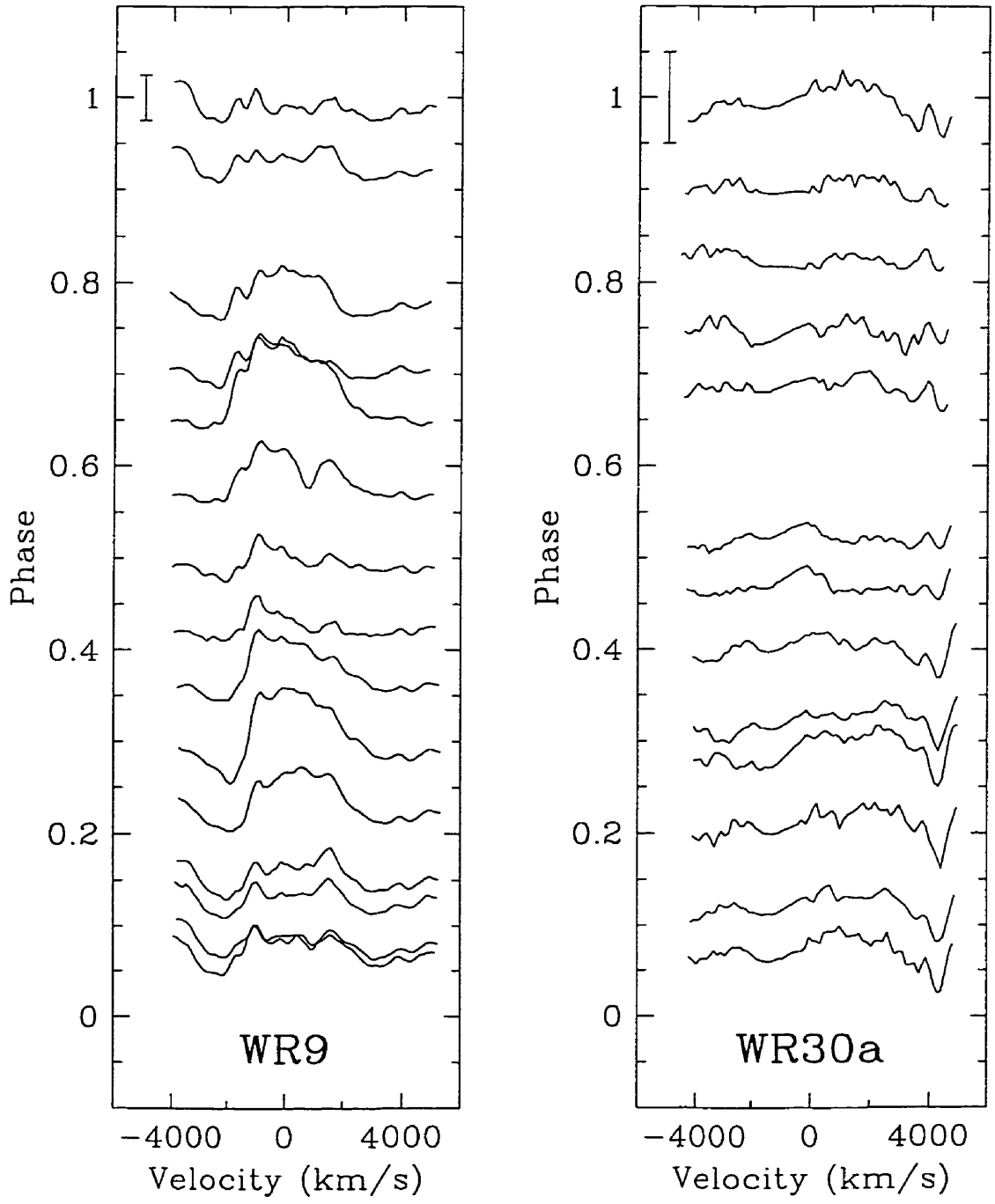

Figure 5.33 . . . continued.

as if it were along the surface of a narrow cone. The more highly ionised CIV would be expected to form closer to the hotter apex, where the curvature is wider and would give the appearance of a wider cone opening angle (as the cone apex would be expected to be curved and not sharp as in the simplified Lührs' model (*cf.* Figure 5.2). This suggests the possibility that a study of excess emission of many ions could permit the shock cone to be mapped-out.

Chapter 6

Conclusion

Binary frequency and Roche-lobe overflow

This is the first comprehensive study for binarity among a viable, uniform subsample of WR-stars. Only thirteen percent of the LMC WC/WO stars were found to be binary with any certainty. This is much lower than the minimum $52\% \pm 14\%$ prediction derived from models of Roche-lobe overflow. It would thus appear that a companion is not required for a star to shed its envelope and become WR in the LMC. The stellar wind seems sufficient to accomplish this, even in environments of low metallicity, where Maeder's theory proposes that this should be less likely.

What of the stars that might be long-period binaries but have been classified as single simply because RV variations were not detected? Could they not weigh in favour of the theory that Roche-lobe overflow helps create WR-stars in low-metallicity environs? It must be considered that a binary with a period of several years and a circular orbit will have a much larger orbital separation of component stars. The tidal influence of a star on its companion will be much smaller in this case. As well, since systems of long-period tend to have elliptical orbits of high eccentricity (unless significant RLOF had occurred, in which case the orbit would have been circularised), much of the star's time will be spent near apastron, which is very far away from the companion. It is to be, therefore, doubted that the

star will exert more than a very feeble gravitational influence and so RLOF will be negigible. A long-period binary star should behave like a single star. RLOF probably plays no role in the evolution of stars to the WR stage, except possibly in the very closest systems.

Uniformity of MC WC/WO stars

There is a remarkable uniformity amongst the 24 MC WC/WO stars. Twenty-two are subclass WC4 and the remaining two are WO (which is probably nothing more than an extension of WC-stars at the hot extreme). However, there does appear to be a significant spread in excitation/abundance even within the WC4 subclass. More remarkable, though, is the strong variation in terminal wind speed, as reflected by the large dispersion in FWHM of the CIV 5808 Å emission line from star to star. Why would all stars be otherwise virtually the same?

Due to the low environmental metallicity, the mass-loss rates of the progenitor stars is low. It takes longer for the O-star to become WR and the WR-star remains longer in the WN stage before becoming WC. This gives the star more time to produce the triple-α products of fusion before the hydrogen envelope is completely stripped away to reveal them. By this time, the star is spectroscopically well advanced in the WC sequence with increased O/C (*e.g.* Smith & Maeder 1991).

Colliding winds

The WWC phenomenon is seen in all six WC/WO binaries studied. It is probably a universal characteristic of binary WC/WO stars (perhaps even all WR subtypes) — not only for those of small separation between components observed here but also in very widely separated systems like WR140 and WR146 (*cf.* Williams *et al.* 1990, Dougherty *et al.* 1996). The bow shock model has been strengthened by the study of double-peaked Lührs' profiles, as excess emission,

in the CIII 5696 Å and the CIV 5808 Å emission lines.

The WWC can be be used, in principle, to find the inclination of the binary system, although in practice it appears that the solution is numerically degenerate when an attempt to model the variation of $FWHM_{ex}$ was made. However, if i is known *a priori*, parameters of the WWC can be found, such as the streaming velocity along the shock cone, the deflection from the line joining the two stars of the cone due to Coriolis effects, and the cone opening angle. This last quantity reflects the ratio of wind momentum fluxes between the two component stars.

An attempt to fit Lührs' profiles directly to the CIII 5696 Å emission line of Br22 did not succeed well in matching the double peaks of the line. This might have been due to variable optical thickness or other effects, as discussed. It is to be noted that Hill (1997) did succeed with the same method to model the excess CIII profiles for WR79, giving credence to the theory.

Future work

A stronger test of the binary frequency predictions at low metallicity would be to observe the WNE-stars in the Magellanic Clouds. WNE-stars should show a higher binary frequency than WC-stars at low Z (Shaerer & Vacca 1997). There are few WNE-stars in the SMC (8) but quite enough in the LMC ($\sim$ 50) to conclude statistically whether or not the creation of WR-stars in low-metallicity environments requires Roche-lobe overflow. The temporal spacing between epochs need not be as long as several years, since long-period binaries may be considered to evolve as do single stars. [Moffat (1988) studied the eight SMC WR-stars known at the time and concluded that at least five were binary. This is compatible with a binary frequency of anywhere from $\sim$ 15% to $\sim$ 99%, at the one percent significance level (Kreyszig 1975, p. 420).]

More spectral data with high signal-to-noise are needed, with good phase coverage, in order to study further the WWC. This would reduce the influence of noise — both instrumental and intrinsic — and could better constrain the

WWC parameters and increase the chance of finding reliable systemic inclinations. This would make spectroscopy a valuable tool to study binary stars, since other methods of finding i, such as photometry and polarimetry, require more stringent observing conditions and are thus more difficult to carry out.

Radio interferometry is already permiting direct observation of the collision shock cone, at least for wide systems, where the non-thermal emission arising mainly near the bow shock head can penetrate the dense winds and be observed (*e.g.* Dougherty *et al.* 1996; Williams *et al.* 1997).

References

Abbot,D.C. & Conti,P.S. 1987, *ARA&A*, **25**, 113

Allen,C.W. 1973, *Astrophysical Quantities*, Athlone Press, University of London

Azzopardi,M. & Breysacher,J. 1979, *A&A*, **75**, 120

Bartzakos,P., Moffat,A.F.J. & Niemela,V.S. 1995, in *Wolf-Rayet Stars: Binaries, Colliding Winds, Evolution*, IAU Symposium No. 163, van der Hucht, K.A. and Williams, P.M. (eds.), Kluwer, Dordrecht, p. 406

Beals,C.S. 1929, *MNRAS*, **90**, 202

Beals,C.S. 1931, *MNRAS*, **91**, 966

Bessel,M.S. 1990, *PASP*, **102**, 1181

Breysacher,J. 1981, *A&AS*, **43**, 203

Campbell,B., Hunter,D.A., Holtzman,J.A., Lauer,T.R., Shaya,E.J., Code,A., Faber,S.M., Groth,E.J., Light,R.M., Lyndo,R., O'Neil,E.J.,Jr. & Westphal,J.A. 1992, *AJ*, **104**, 1721

Cassinelli,J.P. 1991, in *Wolf-Rayet Stars and Interrelations with other Massive Stars in Galaxies*, IAU Symposium No. 143, van der Hucht,K.A. and Hidayat,B. (eds.), Kluwer, Dordrecht, p. 289

Castor,J.I., Abbott,D.C. & Klein,R.I. 1975, *ApJ*, **195**, 157

Charbonneau,P. 1995, *ApJS*, **101**, 309

Cherepashchuk,A.M. 1976, *Sov Astron Lett*, **2**, 138

Cherepashchuk,A.M. 1991, in *Wolf-Rayet Stars and Interrelations with Other Massive Stars in Galaxies*, IAU Symposium No. 143, van der Hucht,K.A. & Hidayat,B. (eds.), Kluwer, Dordrecht, p. 187

Chiosi,C. & Maeder,A. 1986, *ARA&A*, **24**, 329

Corcoran,M.F., Stevens,I.R., Pollock,A.M.T., Swank,J.H., Shore,S.N. & Rawley,G.L. 1996, *ApJ*, **464**, 434

Crowther,P.A., Smith,L.J., Hillier,D.J. & Schmutz,W. 1995, *A&A*, **293**, 427

Dougherty,S.M., Williams,P.M., van der Hucht,K.A., Bode,M.F. & Davis,R.J. 1996, *MNRAS*, **280**, 963

Feitzinger,J.V. *1980*, *Space Sci Rev*, **27**, 35

Gayley,K.G., Owocki,S.P. & Cranmer,S.R. 1995, *ApJ*, **442**, 296

Gayley,K.G., Owocki,S.P. & Cranmer,S.R. 1997, *ApJ*, **475**, 786

Gies,D.R. & Wiggs,M.S. 1991, *ApJ*, **375**, 321

Gies,D.R., Shafter,A.W. & Wiggs,M.S. 1998, *AJ*, in press

Herbig,G.H. 1975, *ApJ*, **196**, 129

Hill,G. 1997, in preparation

Howarth,I.D. 1997, *Observatory*, **117**, 335

Huang,R.Q. & Weigert,A. *1982*, *A&A*, **112**, 281

van der Hucht,K.A. 1995, in *Wolf-Rayet Stars: Binaries, Colliding Winds, Evolution*, IAU Symposium No. 163, van der Hucht,K.A. and Williams,P.M. (eds.), Kluwer, Dordrecht, p. 7

van der Hucht,K.A., Conti,P.S., Lundström,I. & Stenholm,B. 1981, *Space Sci Rev*, **28**, 227

van der Hucht,K.A., Hidayat,B., Admiranto,A.G., Supelli,K.R. & Doom,C. 1988, *A&A*, **199**, 217

Kallrath,J. 1991, *MNRAS*, **248**, 653

Kingsburgh,R.L., Barlow,M.J. & Storey,P.J. 1995, *A&A*, **295**, 75

Kondo,Y. 1996, *Rev Mex Astron Astrofis (Serie de Conferencias)*, **5**, 5

Kreyszig, E. 1975, *Statistische Methoden und ihre Anwendungen*, Vandenhoeck & Ruprecht, Göttingen

Landolt,A.U. 1992, *AJ*, **104**, 340

Lucke,P.B. 1974, *ApJS*, **28**, 73

Lucy,L.B. & Solomon,P.M. 1970, *ApJ*, **159**, 879

Lucy,L.B. & Sweeney,M.A. 1971, *AJ*, **76**, 544

Lührs,S. 1991, Ph.D. Dissertation, Westfälische Wilhelms-Universität Münster

Lührs,S. 1997, *PASP*, **109**, 504

Maeder,A. 1982, *A&A*, **105**, 149

Maeder,A. 1991, *A&A*, **242**, 93

Maeder,A. & Conti,P.S. 1994, *ARA&A*, **32**, 227

Maeder,A. & Meynet,G. 1994, *A&A*, **287**, 803

Melnick,J. 1983 *ESO Messenger*, **32**, 11

Mihalas,D. 1978, *Stellar Atmospheres*, second edition, W.H. Freeman & Company, New York

Moffat,A.F.J. 1969, *A&A*, **3**, 455

Moffat,A.F.J. 1988, *ApJ*, **330**, 766

Moffat,A.F.J. 1995, in *Wolf-Rayet Stars: Binaries, Colliding Winds, Evolution*, IAU Symposium No. 163, van der Hucht,K.A. and Williams,P.M. (eds.), Kluwer, Dordrecht, p. 213

Moffat,A.F.J. 1996, in *Wolf-Rayet Stars in the Framework of Stellar Evolution*, 33rd Liège International Astrophysical Colloquium, Vreux,J.M., Detal,A., Fraipont-Caro,D., Gosset,E. & Rauw,G. (eds.), Institut d'Astrophysique, Liège, p. 199

Moffat,A.F.J., Niemela,V.S. & Marraco,H.G. 1990, *ApJ*, **348**, 232

Moffat,A.F.J., Niemela,V.S., Phillips,M.M., Chu,Y.-H. & Seggewiß,W. 1987, *ApJ*, **312**, 612

Morgan,D.H. & Good,A.R. 1985, *MNRAS*, **216**, 459

Morgan,D.H. & Good,A.R. 1987, *MNRAS*, **224**, 435

Morris,P. & Lamers,H.J.G.L.M. 1995, preprint

Morton,D.C. 1967, *ApJ*, **147**, 1017

NAG 1990, *NAG* FORTRAN *Library Manual*, Mark 14, Vol. 6.

Niemela,V.S. 1995, in *Wolf-Rayet Stars: Binaries, Colliding Winds, Evolution*, IAU Symposium No. 163, van der Hucht,K.A. and Williams,P.M. (eds.), Kluwer, Dordrecht, p. 223

Niemela,V.S., Massey,P. & Conti,P.S. 1984, *PASP*, **96**, 549

Petrie,R.M. 1962, in *Stars and Stellar Systems, Vol. II, Astronomical Techniques*, Hiltner,W.A. (ed.), University of Chicago, Chicago, p. 560

Press,W.H., Teukolsky,S.A., Vetterling,W.T. & Flannery,B.P. 1992, *Numerical Recipes in* FORTRAN — *The Art of Scientific Computing, Second Edition*, Cambridge University Press

Prilutskii,O.F. & Usov,V.V. 1976, *Sov Astron*, **20**, 2

Pyper,D.M. 1966, *ApJ*, **144**, 13

Sahade,J. 1958, in *Étoiles à raies d'émission*, Institut d'Astrophysique, Cointe-Sclessin, 46

Schaerer,D. & Vacca,W.D. 1997, *ApJ*, **497**, 618

Scheffler,H. & Elssässer,H. 1988, *Physics of the Galaxy and Interstellar Matter*, Springer-Verlag

Schertl,D., Hofmann,K.-H., Seggewiss,W. & Weigelt,G. 1995, *A&A*, **302**, 327

Schuerman,D.W. 1972, *Ap&SS*, **19**, 351

Seggewiß,W., Moffat,A.F.J. & Lamontagne,R. 1991, *A&AS*, **89**, 105

Shore,S.N. & Brown,D.N. 1988, *ApJ*, **334**, 1021

Smart,W.M. 1977, *Text-Book on Spherical Astronomy*, sixth edition, Cambridge University Press, Cambridge

Smith,L.F. 1968, *MNRAS*, **140**, 409

Smith,L.F. & Maeder,A. 1991, *A&A*, **241**, 77

Smith,L.F., Shara,M.M. & Moffat,A.F.J. 1990a, *ApJ*, **348**, 471

Smith,L.F., Shara,M.M. & Moffat,A.F.J. 1990b, *ApJ*, **358**, 229

Snow,T.P. Jr. & Morton,D.C. 1976, *ApJS*, **32**, 429

Springmann,U. 1994, *A&A*, **289**, 505

Stevens, I.R., Blondin,J.M. & Pollock,A.M.T. 1992, *ApJ*, **386**, 265

Stevens,I.R., Corcoran,M.F., Willis,A.J., Skinner,S.L., Pollock,A.M.T., Nagase,F. & Koyama,K. 1996, *MNRAS*, **283**, 589

Tassoul,J.-L. & Tassoul,M. 1996, *Journal of Cosmic Physics*, **16**, 377

Turner,D.G. 1982, in *Wolf-Rayet Stars: Observations, Physics, Evolution*, IAU Symposium No. 99, de Loore,C.W.H. and Willis,A.J. (eds.), Reidel, Dordrecht, p. 57

Underhill,A. 1949, *MNRAS*, **109**, 563

Walborn,N.R. 1980, *ApJS*, **44**, 535

Westerlund,B.E. 1990, *A&AR*, **2**, 29

Westerlund,B.E. 1997, *The Magellanic Clouds*, Cambridge Astrophysics Series 29, Cambridge University Press, Cambridge

Wiggs,M.S. & Gies,D.R. 1992, *ApJ*, **396**, 238

Wiggs,M.S. & Gies,D.R. 1993, *ApJ*, **407**, 252

Williams,P.M., Dougherty,S.M., Davis,R.J., van der Hucht,K.A., Bode,M.F. & Setia Gunawan,D.Y.A. 1997, *MNRAS*, **289**, 10

Williams,P.M., van der Hucht,K.A., van der Woerd,H., Wamsteker,W.M., Geballe,T.R., Garmany,C.D. & Pollock,A.M.T. 1987, in *Instabilities in Luminous Early Type Stars*, Lamers,H.J.G.L.M. & de Loore,C.W.H. (eds.), Astrophysics and Space Science Library; **136**, 221

Williams,P.M., van der Hucht,K.A., Pollock,A.M.T., Florkowski,D.R., van der Woerd, H. & Wamsteker,W.M. 1990, *MNRAS*, **243**, 662

Willis,A.J. 1991, in *Wolf-Rayet Stars and Interrelations with other Massive Stars in Galaxies*, IAU Symposium No. 143, van der Hucht,K.A. and Hidayat,B. (eds.), Kluwer, Dordrecht, p. 265

Willis,A.J., Schild,H. & Stevens,I.R. 1995, *A&A*, **298**, 549

Wolf,C. & Rayet,G. 1867, *CR Acad Sci (Paris)*, **65**, 292

Zahn,J.-P. 1975, *A&A*, **41**, 329

Appendix A

Flat-Field for November 1993 Data

Due to a misunderstanding at the telescope, no flat-fielding of the Nov. 1993 data was carried out. Unfortunately, the counts of all spectra in the wavelength range from 5650 Å to 5850 Å were much lower than those of the neighbouring regions (Figure A.1, page a-ii). This does not reflect the behaviour of the true continuum of the stars studied.

This region includes the CIII 5696 Å and CIV 5808 Å emission lines and so cannot be fit as continuum during rectification of the spectrum. Instead, the spectrum of the nearly line-free (in the yellow) A-star β Pictoris was modelled each night with a cubic spline of approximately sixtieth order in the wavelength range from 5500 Å to 6100 Å (see Figure A.1). The value of the intensity of the fit at wavelengths shorter than 5500 Å was set to a constant value equal to that at 5500 Å. The entire fit was then divided by this value to give a rectified model. This fit function was then divided into all wavelength calibrated spectra observed during the same night as their corresponding β Pictoris fit.

No spectra of β Pictoris were taken during the nights of November 17 and November 18, 1993. For correction of the spectra of these two nights, the fit function of November 19, 1993 was used.

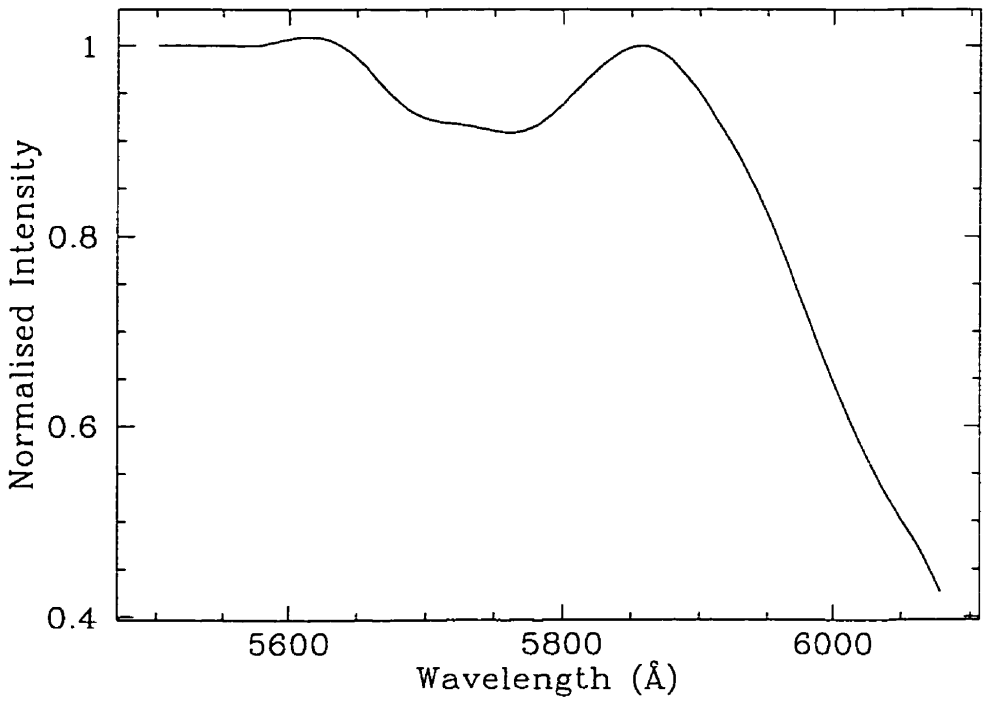

Figure A.1: *Fit of β Pictoris spectrum between 5500 Å and 6100 Å.*

Appendix B

Photometric and Spectral Atlas of the Programme Stars

In Figure B.1 on pages a-iv–a-xvi an atlas of the programme stars is presented. For each star, the V-filter CCD image of its field (from the UTSO photometric mission) is displayed, with a cursor to identify the given star. The scale of each image is $4' \times 4'$. North is at the top of the image and East is at the left. To the right of the field image is the crowded-star photometric solution using `DAOPHOT` in IRAF. Stars are shown by circles; the larger the diameter of the circle, the greater the brightness. Below these two frames is the mean spectrum of the programme star, found by taking the average of reduced spectra from the Nov. 1993 mission at CASLEO. Two vertical scales are used for clarity.

For Br22, important absorption lines of the OB companion star are labelled. The two crosses designate poorly subtracted interstellar absorption lines that do not arise in the OB-star.

Br7

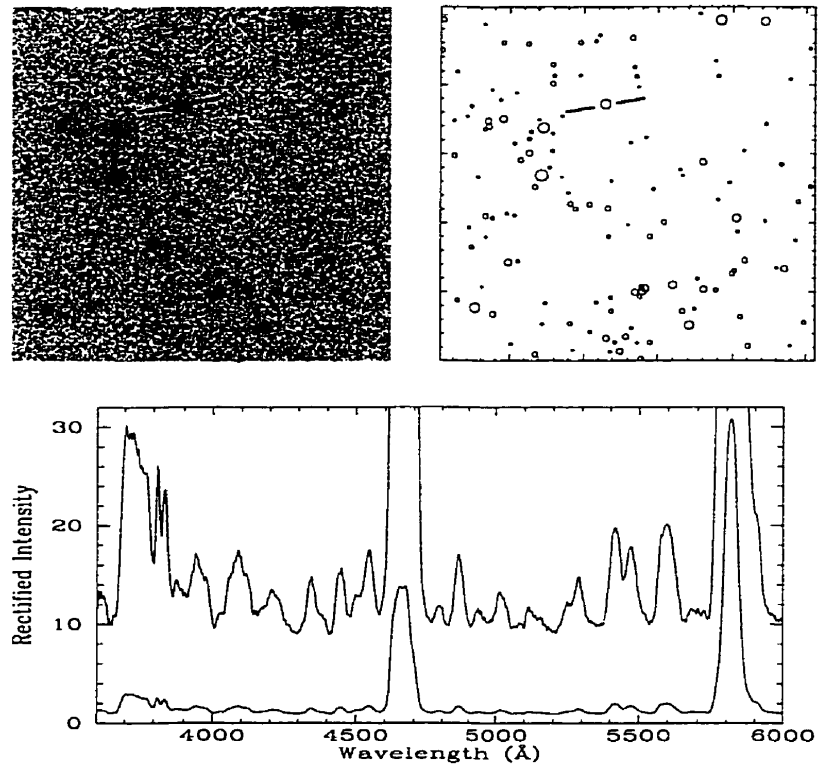

Br8

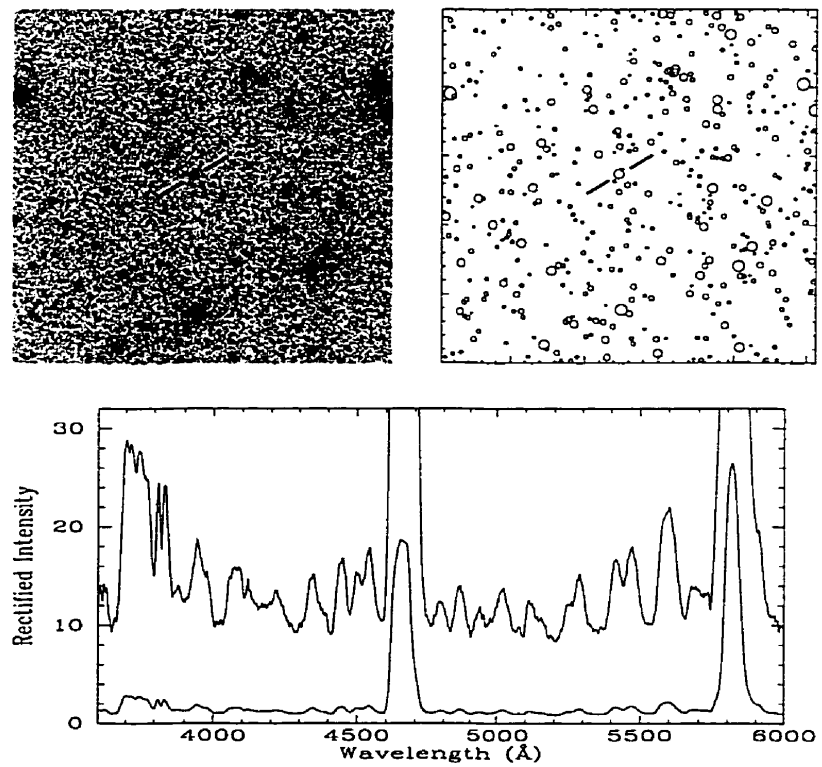

Figure B.1: *Photometric resolutions and average spectra of programme stars.*

Br9

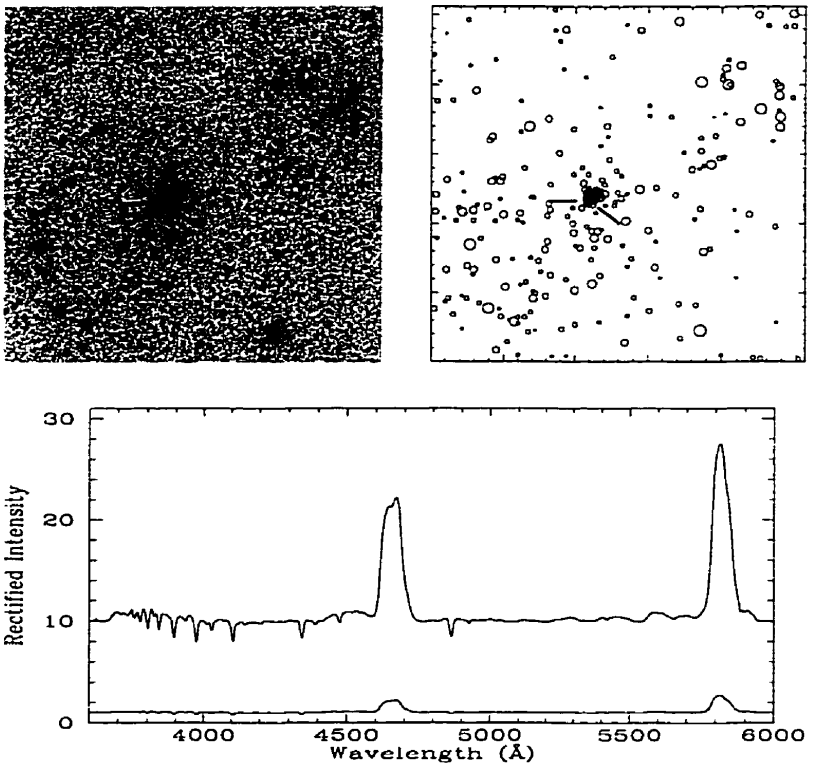

Br10

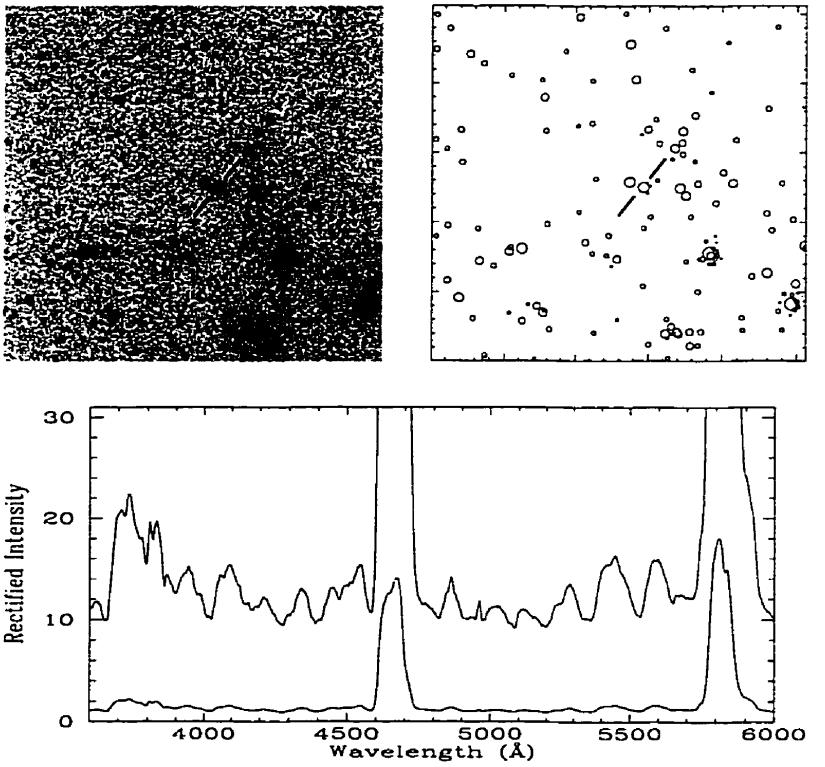

Figure B.1 . . . continued. . .

Br22

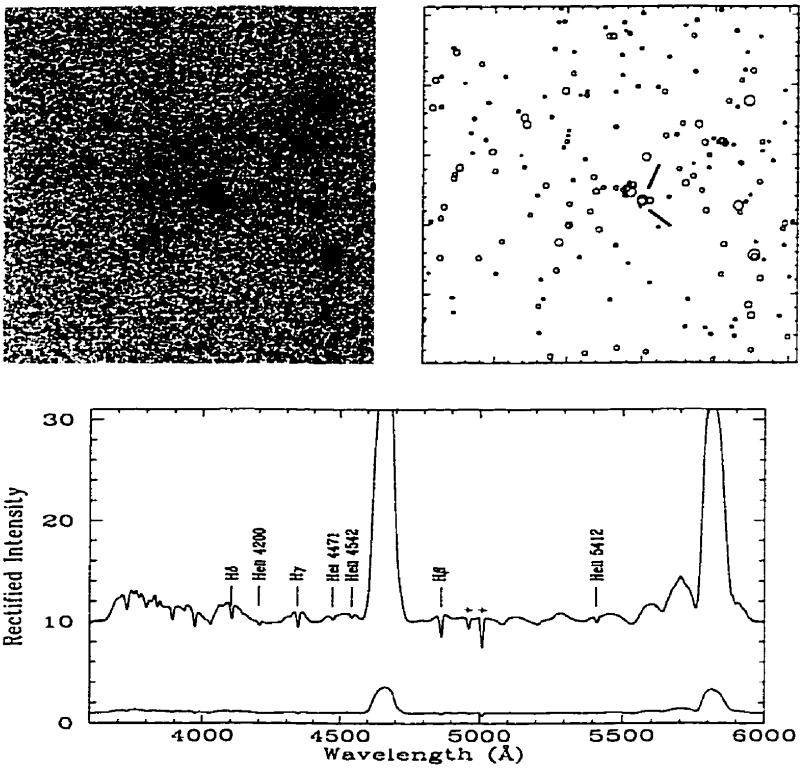

Br28

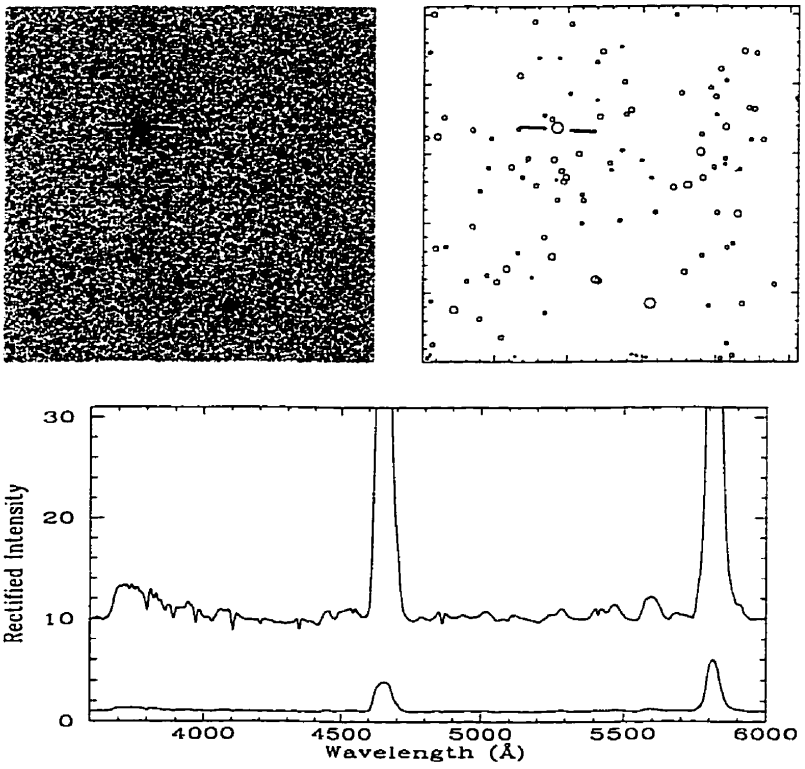

Figure B.1 ...continued...

Br31

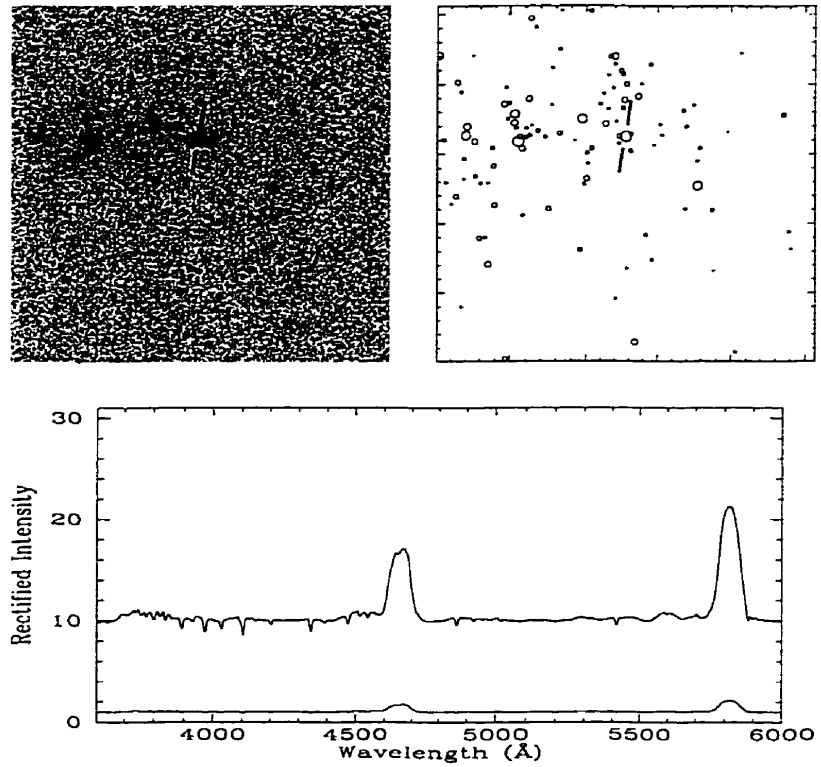

Br32

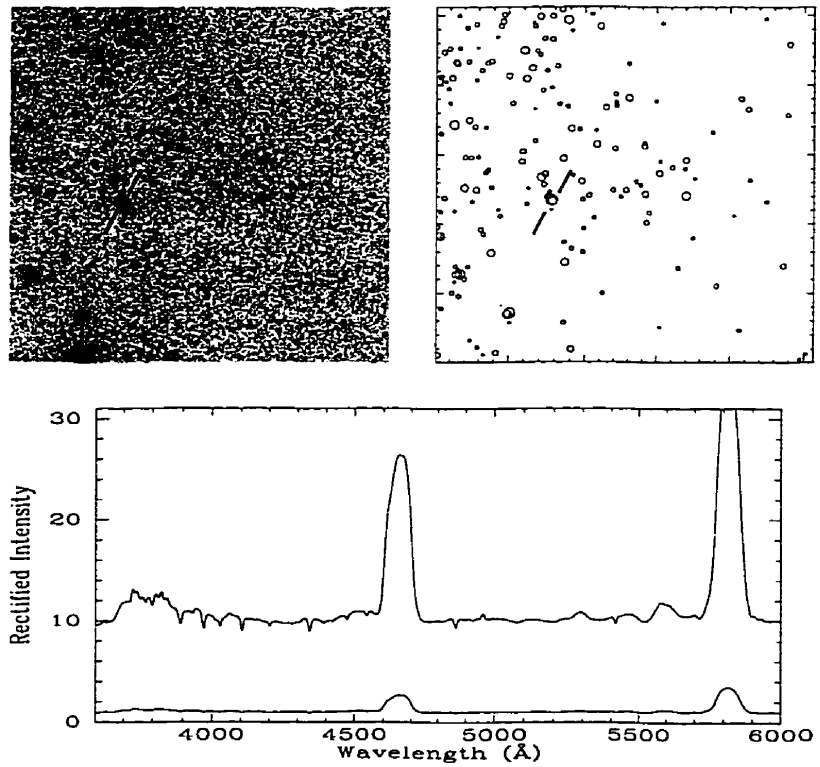

Figure B.1 ...continued...

Br43

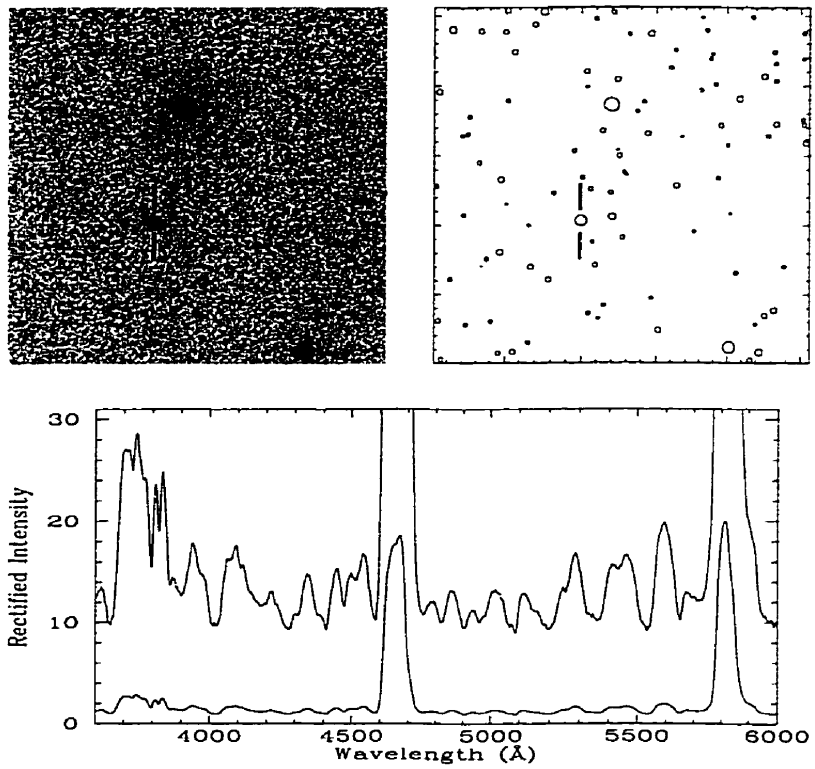

Br44

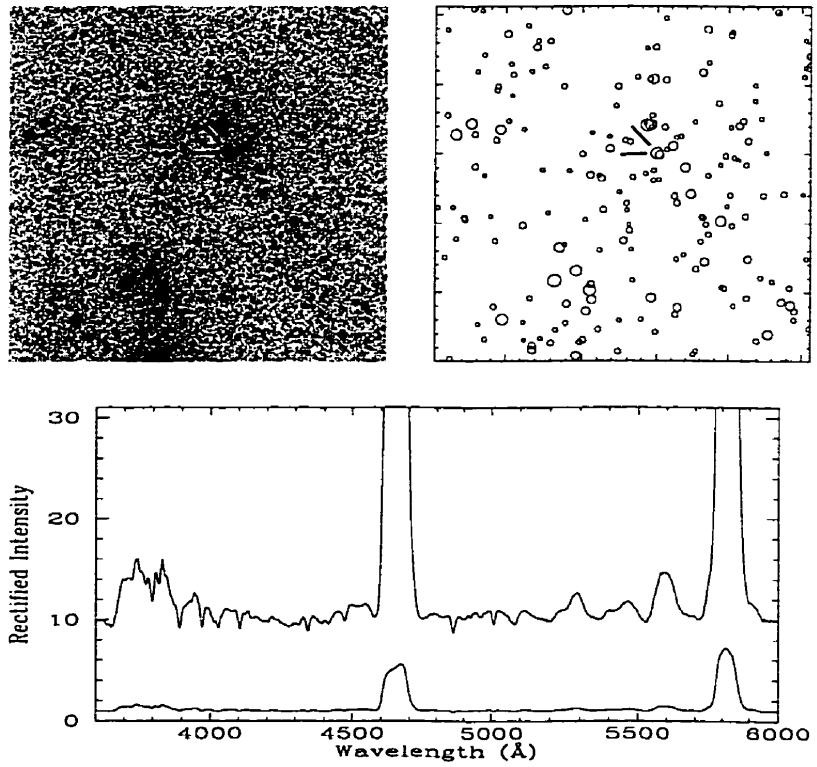

Figure B.1 . . . continued. . .

Br50

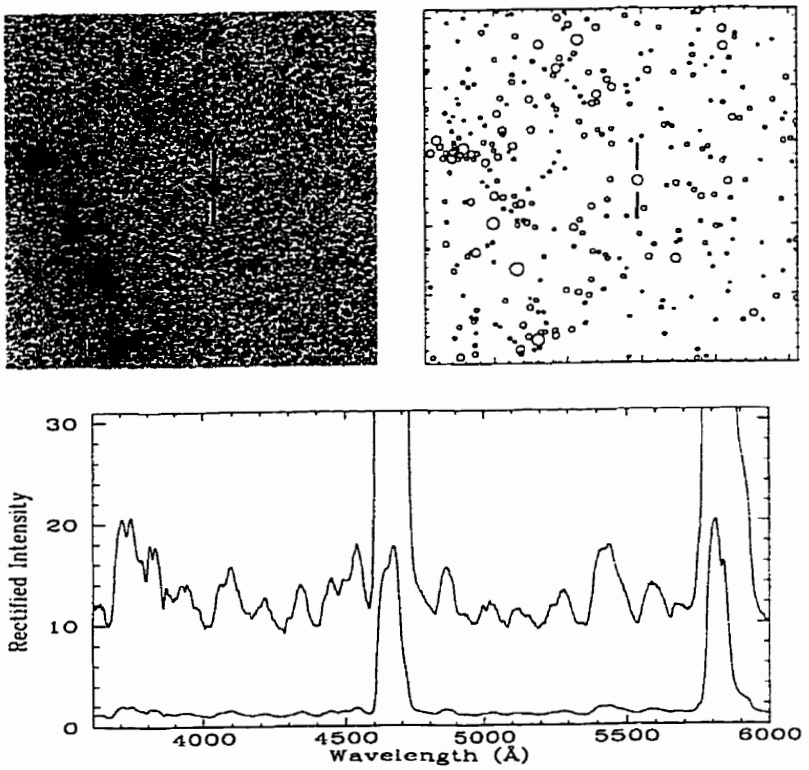

Br62

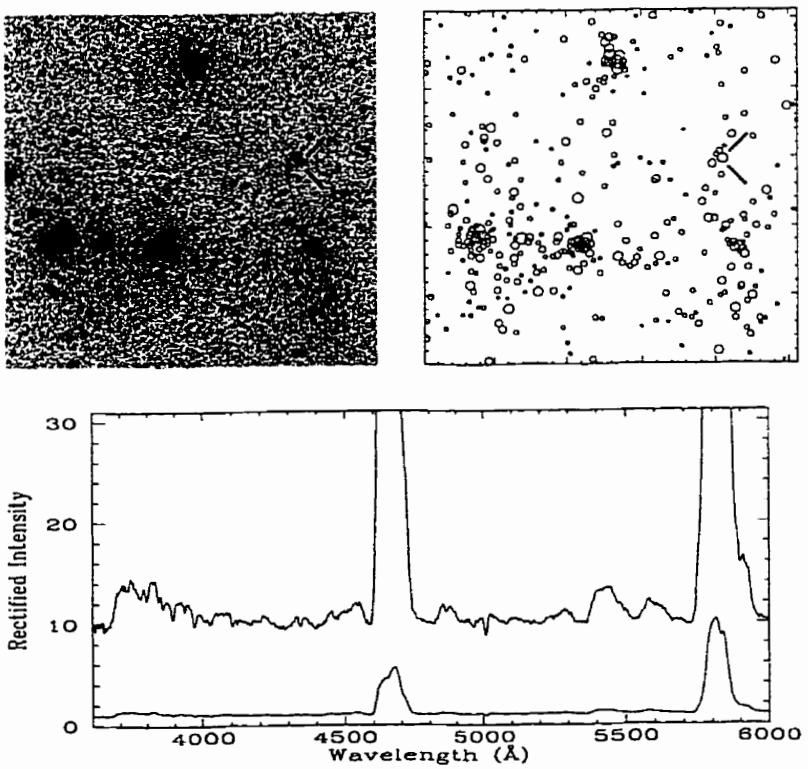

Figure B.1 ... continued...

Br67

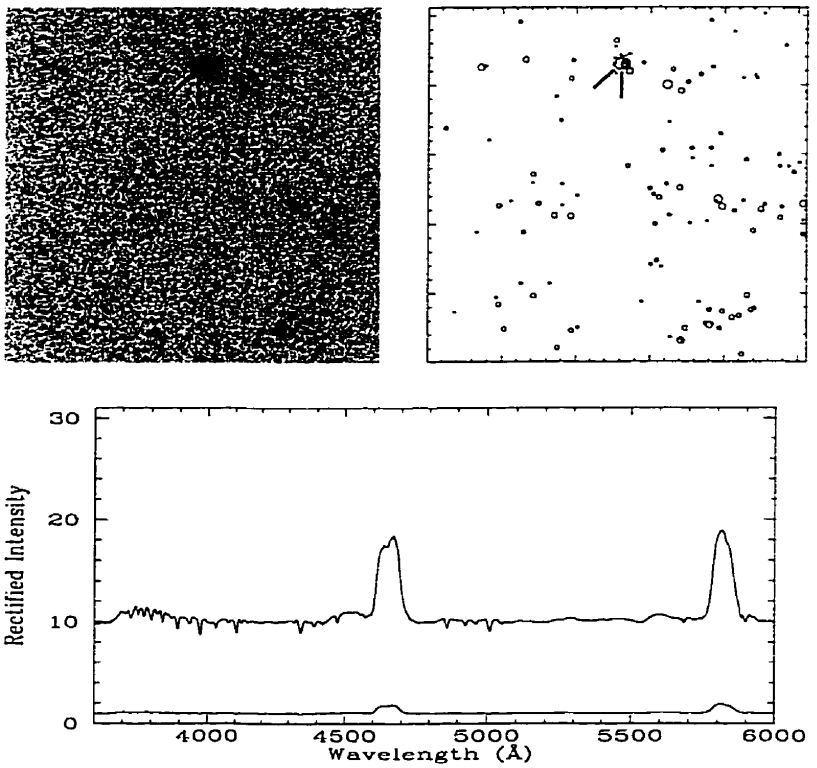

Br68

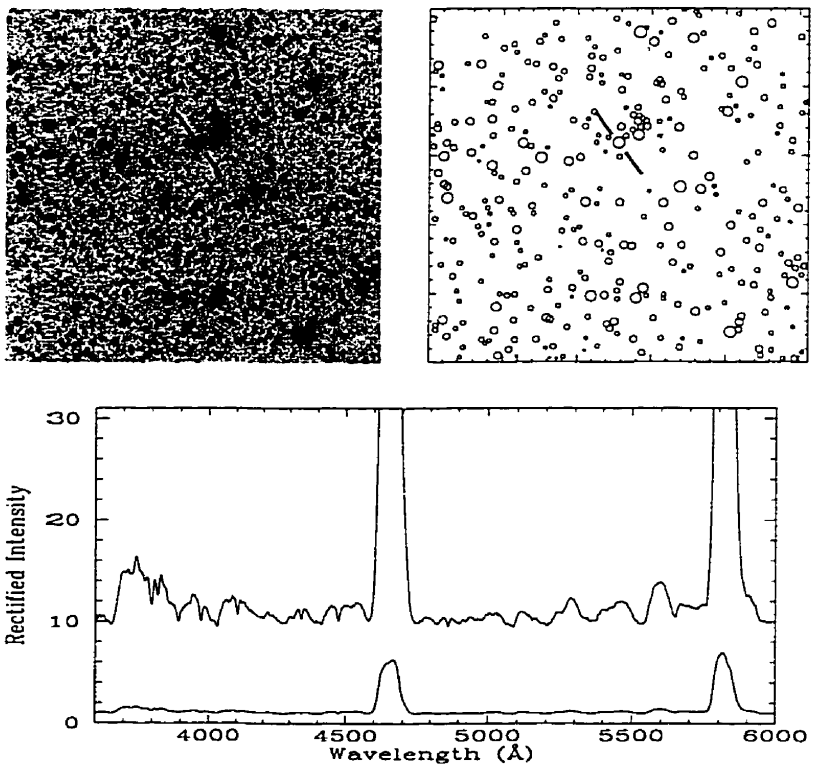

Figure B.1 . . . continued. . .

Br70

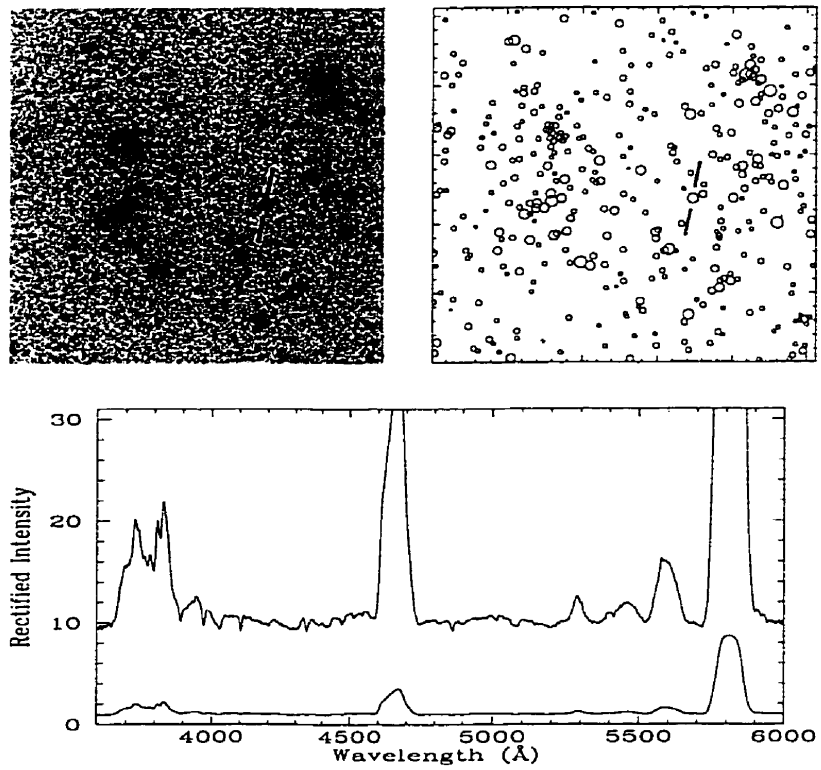

Br74

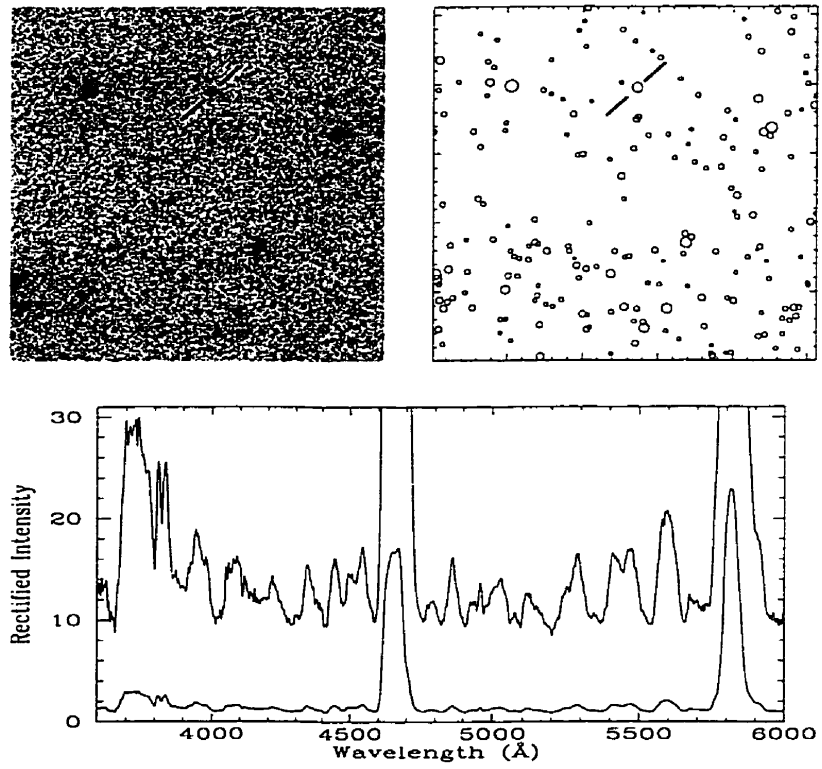

Figure B.1 ...continued...

Br83

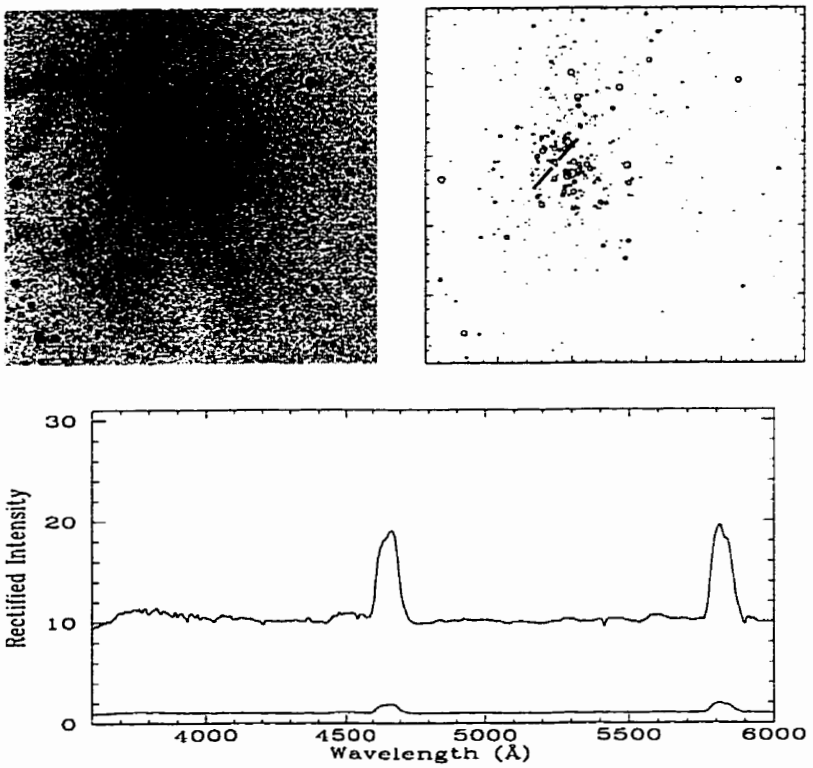

Br87

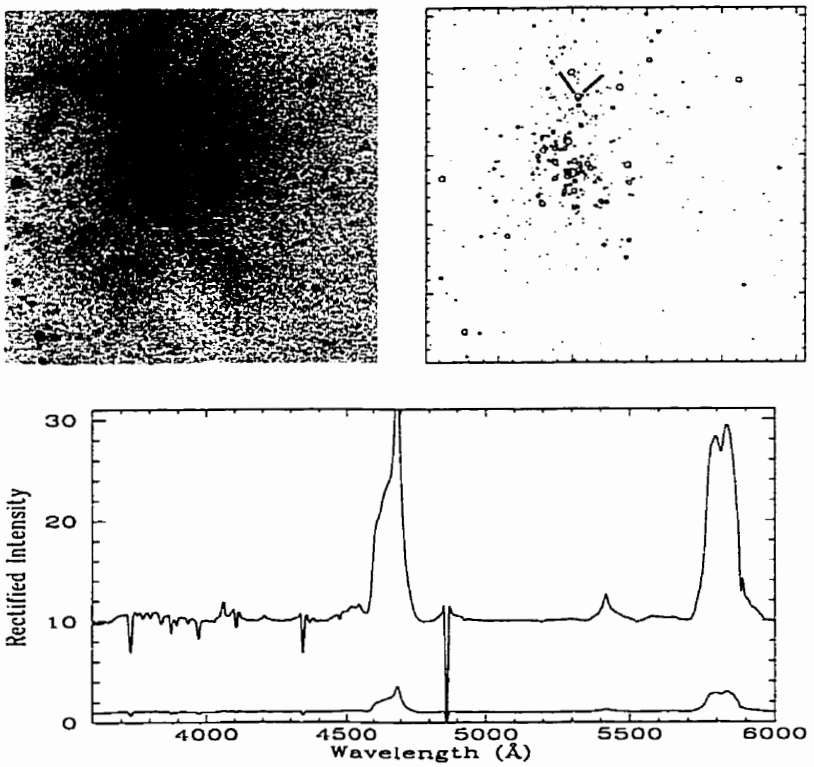

Figure B.1 ... continued...

Br93

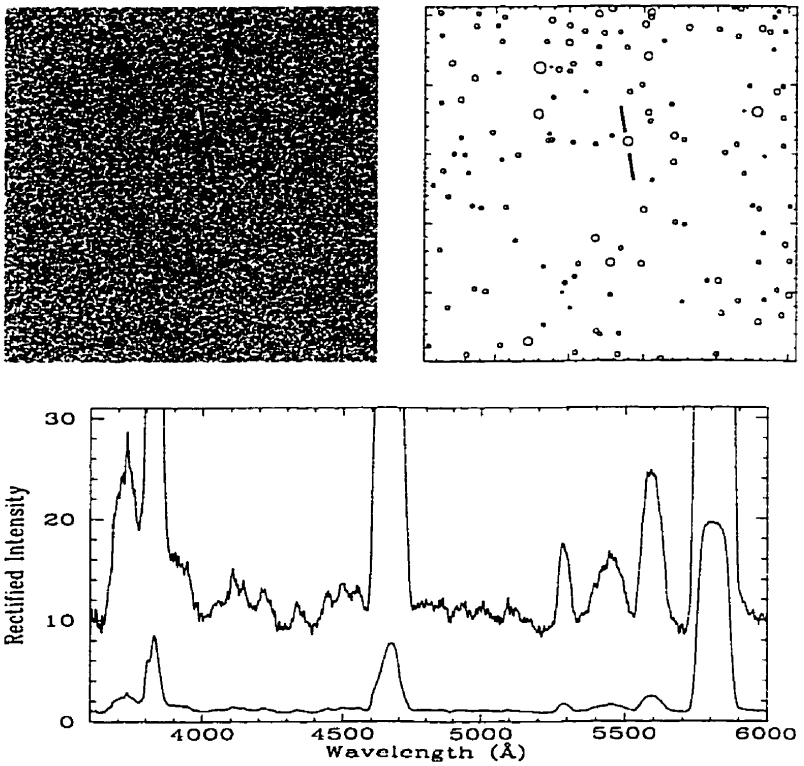

Br94

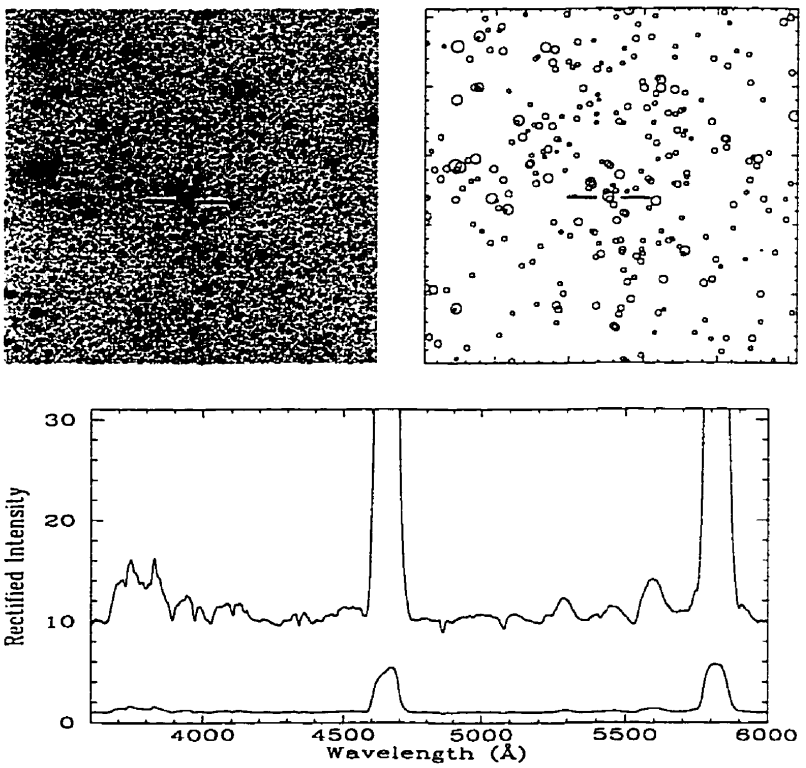

Figure B.1 . . . continued. . .

MG1

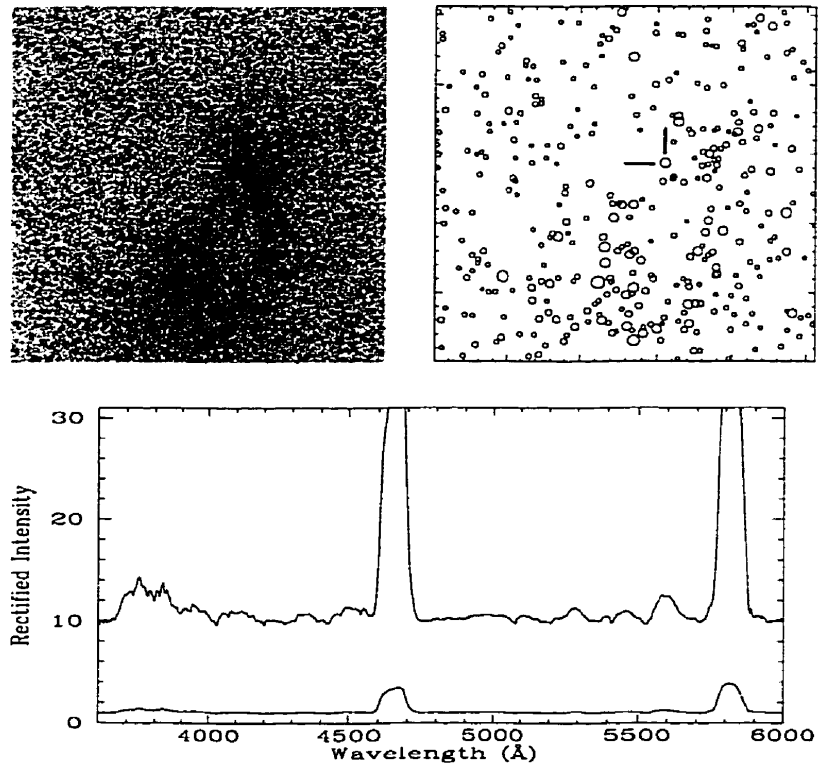

MG5

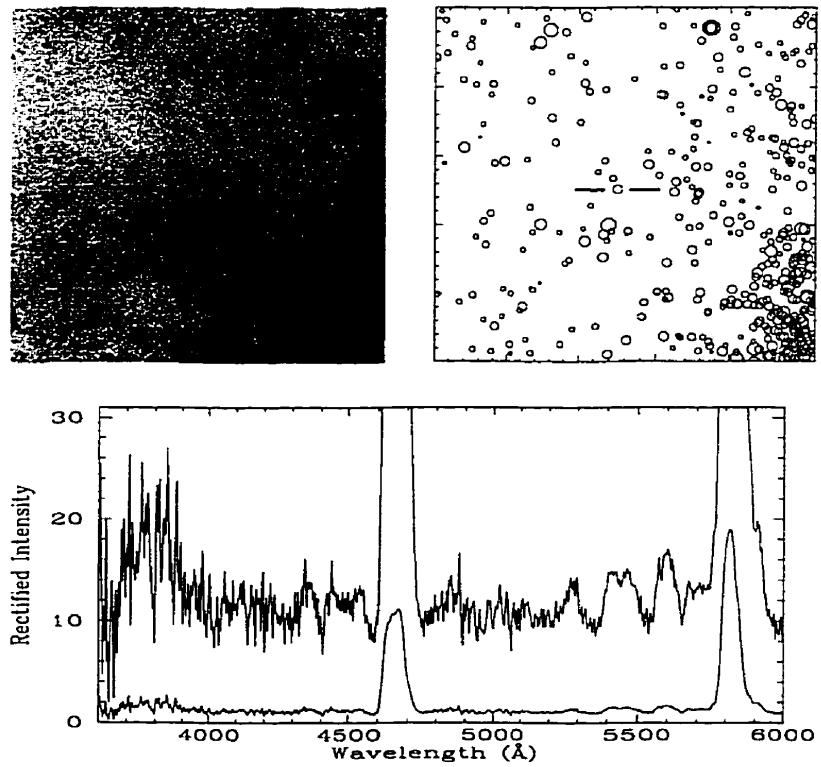

Figure B.1 ... continued...

MG6

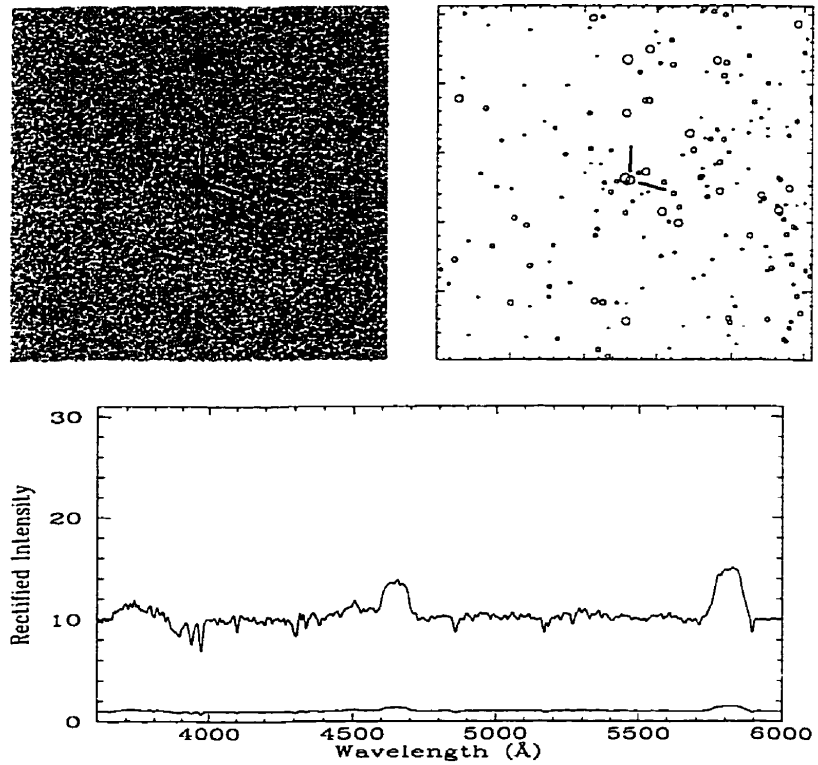

AB8

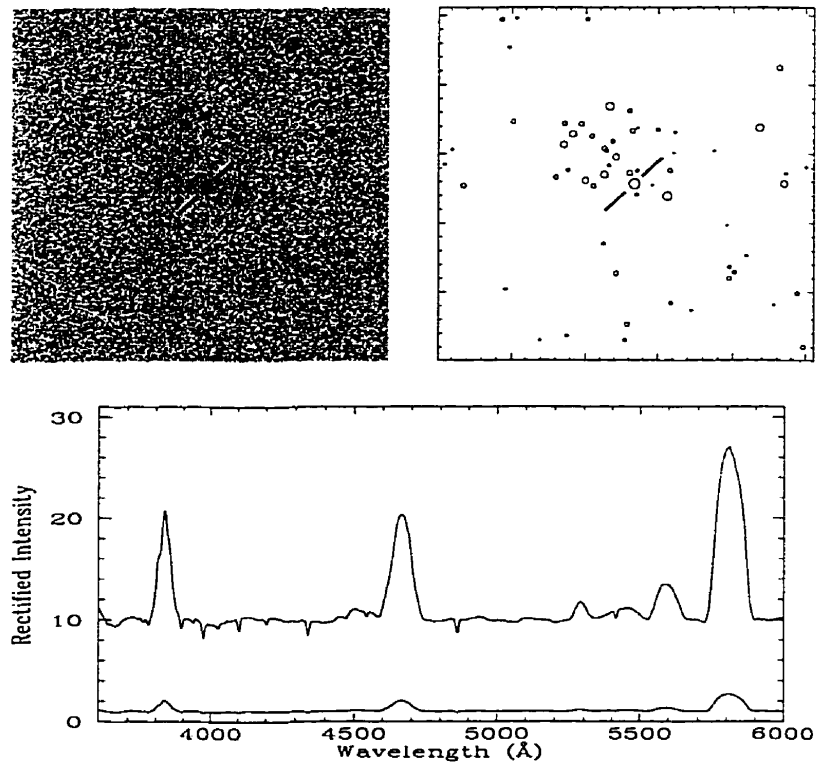

Figure B.1 . . . continued. . .

WR9

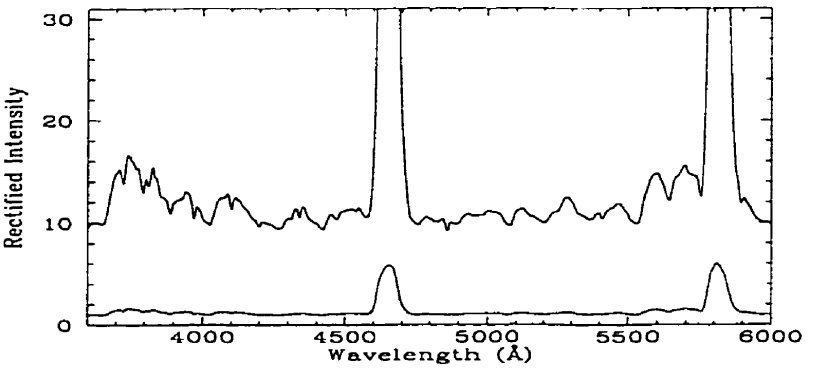

WR30a

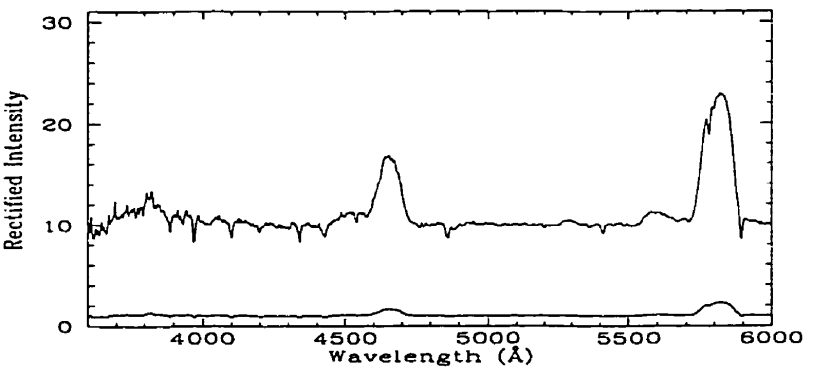

Figure B.1 . . . continued.

Appendix C

Ratio of Line Emissivity to Continuum Emissivity

The measured continuum emissivity, E_c, and the line emissivity, E_ℓ, are defined by

$$E_c = \int I_c(\lambda) T(\lambda)\, d\lambda$$

and

$$E_\ell = \int [I(\lambda) - I_c(\lambda)] T(\lambda)\, d\lambda,$$

where $I(\lambda)$ is the intensity at a given wavelength, λ; $I_c(\lambda)$ is the continuum intensity at the same wavelength; $T(\lambda)$ is the transmissivity of the measuring system at that wavelength and the integral is carried out over the whole observed spectrum.

Emissivity of lines

The emissivity of each individual emission line can be described by

$$E_{\ell_i} = \left[\int [I(\lambda) - I_c(\lambda)] T(\lambda)\, d\lambda \right]_i,$$

where the line is assigned an index i while other lines are suppressed.

The equivalent width of a line is defined by

$$W_e = \int \frac{[I(\lambda) - I_c(\lambda)]d\lambda}{I_c(\lambda)}.$$

With the approximation that $T(\lambda)$ and $I_c(\lambda)$ are about constant for a given line over its entire narrow width, one can have

$$E_{\ell_i} \approx W_{e_i} I_c(\lambda_i) T(\lambda_i),$$

where λ_i is the mean wavelength of the line of index i.

The emissivity ratio becomes

$$\frac{E_\ell}{E_c} \approx \frac{\sum_{i=1}^{n} W_{e_i} I_c(\lambda_i) T(\lambda_i)}{\int I_c(\lambda) T(\lambda)\, d\lambda}, \tag{C.1}$$

where n is the total number of lines under consideration.

Effect of reddening

The effect of reddening is to diminish the original intensity that would be observed, I_{oc}, to that which is actually seen, I_c, such that

$$\frac{I_c}{I_{oc}} = 10^{-0.4 A_\lambda},$$

where A_λ is the wavelength-dependent interstellar extinction (in magnitudes) of the star. In the optical domain, one has, to good approximation:

$$\frac{A_\lambda}{A_V} \cong \frac{k}{\lambda},$$

where A_λ is the V-band extinction, hence $k = 5500$. Finally (with the wavelength λ in Ångstrøms),

$$\frac{I_c(\lambda)}{I_{oc}(\lambda)} = 10^{-0.4 \frac{A_V \times 5500}{\lambda}} \tag{C.2}$$

The extinction is linearly related to the reddening, $E_{B-V}[\equiv (B-V) - (B-V)_0]$, in the V-band, by $A_V = \mathrm{R} E_{B-V}(\mathrm{R} = 3.1)$. Reddening values are taken mostly in Smith's (1968) narrow-band continuum system, *ubv*, as E_{b-v}. The relation between the two reddening values is $E_{B-V} = 1.22 E_{b-v}$ (Turner 1982), so that

$$A_V = 3.1 \times 1.22 E_{b-v}.$$

Continuum intensity and summation approximation

According to Morris & Lamers (1995), the unreddened continuum intensity for WR-stars, $I_{oc}(\lambda)$, is related to the wavelength by

$$I_{oc}(\lambda) = K\lambda^{-2.8},$$

where K is a constant of proportionality. This is valid from near-ultraviolet to near-infrared wavelengths. With equation C.2 the reddened intensity becomes

$$I_c(\lambda) = K\lambda^{-2.8} \times 10^{-0.4\frac{A_V \times 5500}{\lambda}}.$$

Substitution of this expression for I_c in equation C.1 gives

$$\frac{E_\ell}{E_c} \approx \frac{\sum_{i=1}^{n} W_{e_i} \lambda_i^{-2.8} \times 10^{-0.4\frac{A_V \times 5500}{\lambda_i}} T(\lambda_i)}{\int \lambda^{-2.8} \times 10^{-0.4\frac{A_V \times 5500}{\lambda}} T(\lambda)\, d\lambda}.$$

Since the filter transmission data are given in wavelength increments of 100 Å (see next section), the integral in the denominator is approximated with a summation, so that, finally, the sought-after ratio is

$$\frac{E_\ell}{E_c} \approx \frac{\sum_{i=1}^{n} W_{e_i} \lambda_i^{-2.8} \times 10^{-0.4\frac{A_V \times 5500}{\lambda_i}} T(\lambda_i)}{\sum_{\lambda=4700}^{7000} \lambda^{-2.8} \times 10^{-0.4\frac{A_V \times 5500}{\lambda}} T(\lambda)\Delta\lambda}, \qquad \text{(C.3)}$$

where all wavelengths are in units of Ångstrøms and the summation in the denominator is performed in increments of $\Delta\lambda = 100$.

Calculation of transmission

The V-band filter was not the only element affecting the transmission, $T(\lambda)$, of light in the observing system. The aluminium mirror and the atmosphere were not completely reflecting or transparent, nor did the CCD detector have the same quantum efficiency at all wavelengths. The V-band filter transmissivity as a function of wavelength, $F(\lambda)$, is listed in Table 2 of Bessel (1990). The

reflectivity of the aluminium mirror, $m(\lambda)$, is given by Allen (1973, p. 108) as well as the transmission of the atmosphere, $a(\lambda)$ (p. 126). The CCD response curve, $c(\lambda)$, was determined from data provided by the UTSO staff. In all cases, the transmission at 100 Å intervals was calculated with linear interpolation between the listed values. The transmission to be used in equation C.3 was then

$$T(\lambda) = F(\lambda) \times m(\lambda) \times a(\lambda) \times c(\lambda).$$

Error in E_ℓ/E_c

The error from two sources was considered. The first was the error in the equivalent width measured from the emission lines. The main source of such an error is from the rectification of the spectrum during data reduction. This error is estimated as not being greater than ten percent. Further, the error from the equivalent width of the CIV 5808 Å line, $\sigma_{W_{\rm eCIV}}$, dominated over the errors for the other lines. The second factor was the error in the reddening $\sigma_{E_{B-V}}$.

The error in E_ℓ/E_c was calculated by

$$\sigma_{\frac{E_\ell}{E_c}} = \sqrt{\left[\frac{\partial\left(\frac{E_\ell}{E_c}\right)}{\partial W_{\rm eCIV}}\right]^2 \sigma^2_{W_{\rm eCIV}} + \left[\frac{\partial\left(\frac{E_\ell}{E_c}\right)}{\partial E_{B-V}}\right]^2 \sigma^2_{E_{B-V}}}.$$

The first term, due to the error in equivalent width, was found with

$$\begin{aligned}
\left[\frac{\partial\left(\frac{E_\ell}{E_c}\right)}{\partial W_{\rm eCIV}}\right]^2 \sigma^2_{W_{\rm eCIV}} &= \left[\frac{\lambda_1^{-2.8} \times 10^{-0.4\frac{A_V \times 5500}{\lambda_1}} T(\lambda_1)}{\sum_{\lambda=4700}^{7000} \lambda^{-2.8} \times 10^{-0.4\frac{A_V \times 5500}{\lambda}} T(\lambda)\Delta\lambda} \sigma_{W_{\rm eCIV}}\right]^2 \\
&= \left[\frac{\lambda_1^{-2.8} \times 10^{-0.4\frac{A_V \times 5500}{\lambda_1}} T(\lambda_1)}{\sum_{\lambda=4700}^{7000} \lambda^{-2.8} \times 10^{-0.4\frac{A_V \times 5500}{\lambda}} T(\lambda)\Delta\lambda} \times 0.1 W_{\rm eCIV}\right]^2 \\
&= \left[0.1 \times \frac{W_{\rm eCIV} \lambda_1^{-2.8} \times 10^{-0.4\frac{A_V \times 5500}{\lambda_1}} T(\lambda_1)}{\sum_{\lambda=4700}^{7000} \lambda^{-2.8} \times 10^{-0.4\frac{A_V \times 5500}{\lambda}} T(\lambda)\Delta\lambda}\right]^2,
\end{aligned}$$

where $W_{\rm eCIV}$ is the equivalent width of the CIV 5808 Å line and $\lambda_1 = 5808$. Note that the numerator is simply the contribution of the equivalent width of the CIV line to the summation in the numerator of equation C.3 and that the denominator is the same as in that equation.

The error in the second term, that due to the reddening, was calculated with

$$\left[\frac{\partial\left(\frac{E_\ell}{E_c}\right)}{\partial E_{B-V}}\right]^2 \sigma^2_{E_{B-V}} = \left[\frac{\sum_{i=1}^{n} W_{e_i}\lambda_i^{-3.8} \times 10^{-0.4\frac{A_V \times 5500}{\lambda_i}} T(\lambda_i)}{\sum_{\lambda=4700}^{7000} \lambda^{-3.8} \times 10^{-0.4\frac{A_V \times 5500}{\lambda}} T(\lambda)\Delta\lambda}\right]^2 \sigma^2_{E_{B-V}}.$$

It should be noted that most of the terms of the derivative of the exponent appear in both numerator and denominator and so cancel one another.

Values of E_ℓ/E_c for each star are given in Table 3-I on page 25.

Appendix D

Journal of Binary Spectroscopic Observations

Table D-I, on pages a-xxiii through a-xxxv, contains a journal of radial velocity spectroscopic observations of the programme stars. The heliocentric Julian date of the observation is given with its corresponding orbital phase (for binaries, as determined from the emission line circular orbital elements of Tables 4-II and 4-III on page 53). This is followed by the CIV 5808 Å emission line radial velocity. In addition, the velocities measured from the HeII 5412 Å absorption line are listed for Br22 and the Galactic stars.

In this table, the dates are given in Heliocentric Julian Days (HJD) minus 2 440 000. The radial velocities are given in km/s.

Table D-I: Journal of observations.

Br7

HJD	Phase	Radial Velocity Emission	Radial Velocity Absorption
6041.582	—	410	—
6042.736	—	376	—
6043.561	—	373	—
6045.666	—	357	—
6046.565	—	368	—
6047.622	—	334	—
6049.559	—	358	—
6050.615	—	351	—
6052.560	—	360	—
9309.641	—	451	—
9311.565	—	505	—
9313.546	—	530	—
9314.541	—	533	—
9315.797	—	455	—
9316.545	—	531	—
9317.521	—	507	—
9318.524	—	514	—
9319.529	—	491	—
9321.532	—	444	—
9322.696	—	446	—
9323.710	—	440	—
9324.647	—	433	—

Table D-I . . . continued. . .

Br8

HJD	Phase	Radial Velocity Emission	Radial Velocity Absorption
6041.605	—	411	—
6042.753	—	437	—
6043.580	—	398	—
6045.642	—	432	—
6046.585	—	487	—
6047.600	—	416	—
6049.582	—	412	—
6050.635	—	371	—
6052.579	—	471	—
9309.663	—	507	—
9311.572	—	581	—
9313.556	—	567	—
9315.584	—	553	—
9316.530	—	552	—
9317.533	—	600	—
9318.532	—	544	—
9319.541	—	539	—
9321.542	—	481	—
9322.705	—	481	—
9323.818	—	492	—
9324.655	—	474	—

Table D-I . . . continued. . .

Br9

HJD	Phase	Radial Velocity Emission	Radial Velocity Absorption
6043.609	—	511	—
6044.584	—	511	—
6045.630	—	530	—
6046.608	—	499	—
6047.586	—	560	—
6048.570	—	536	—
6050.602	—	573	—
6051.625	—	553	—
6052.599	—	536	—
9309.677	—	476	—
9311.586	—	609	—
9313.577	—	545	—
9315.620	—	554	—
9316.538	—	630	—
9317.542	—	627	—
9318.540	—	619	—
9319.674	—	508	—
9321.706	—	531	—
9323.684	—	552	—
9324.664	—	550	—

Table D-I . . . continued. . .

Br10

HJD	Phase	Radial Velocity Emission	Radial Velocity Absorption
6041.630	—	536	—
6042.773	—	574	—
6043.680	—	552	—
6045.612	—	508	—
6046.623	—	531	—
6047.569	—	537	—
6049.604	—	553	—
6051.562	—	594	—
6052.612	—	556	—
9309.691	—	541	—
9311.611	—	577	—
9313.591	—	630	—
9315.639	—	650	—
9316.564	—	591	—
9317.551	—	595	—
9318.556	—	630	—
9319.682	—	455	—
9321.733	—	470	—
9323.693	—	546	—
9324.673	—	519	—

Table D-I . . . continued. . .

Br22

HJD	Phase	Radial Velocity Emission	Absorption
6040.707	0.909	527	245
6042.551	0.033	689	—
6043.698	0.110	801	105
6045.598	0.237	816	158
6046.639	0.307	819	162
6047.719	0.379	809	109
6049.622	0.507	655	214
6051.579	0.638	476	356
6052.628	0.708	391	132
9010.670	0.894	563	238
9011.553	0.953	626	237
9012.553	0.020	692	170
9013.593	0.090	778	162
9014.584	0.156	826	208
9015.591	0.224	868	190
9017.613	0.359	831	159
9309.701	0.929	511	114
9310.567	0.987	606	226
9311.620	0.057	692	193
9312.771	0.134	775	209
9313.603	0.190	807	88
9314.558	0.254	821	140
9315.610	0.325	824	240
9316.572	0.389	776	179
9317.559	0.455	684	177
9318.563	0.522	604	231
9319.561	0.589	541	308
9321.541	0.722	311	142
9322.586	0.792	402	188
9323.605	0.860	469	269
9324.565	0.925	533	272

Table D-I . . . continued. . .

Br28

HJD	Phase	Radial Velocity Emission	Absorption
6040.731	—	467	—
6042.608	—	515	—
6043.713	—	462	—
6045.580	—	457	—
6046.652	—	437	—
6047.701	—	526	—
6049.641	—	486	—
6051.592	—	498	—
6052.641	—	493	—
9010.756	—	531	—
9011.552	—	547	—
9012.552	—	522	—
9013.713	—	542	—
9014.733	—	539	—
9015.733	—	523	—
9017.715	—	529	—
9309.730	—	450	—
9310.589	—	486	—
9311.739	—	406	—
9313.678	—	371	—
9314.568	—	483	—
9315.663	—	463	—
9316.579	—	451	—
9317.567	—	408	—
9318.570	—	402	—
9319.571	—	452	—
9321.596	—	343	—
9322.594	—	425	—
9323.597	—	433	—
9324.557	—	410	—

Table D-I . . . continued. . .

Br31

HJD	Phase	Radial Velocity Emission	Radial Velocity Absorption
6040.752	0.974	400	—
6041.866	0.342	764	—
6042.625	0.592	269	—
6044.823	0.317	770	—
6046.669	0.925	295	—
6047.687	0.261	789	—
6048.597	0.561	294	—
6050.589	0.218	757	—
6051.691	0.581	285	—
9010.670	0.231	835	—
9011.553	0.522	470	—
9012.553	0.851	259	—
9012.800	0.933	405	—
9013.650	0.213	841	—
9014.567	0.516	502	—
9014.796	0.591	399	—
9015.666	0.878	322	—
9017.564	0.504	535	—
9017.773	0.572	372	—
9309.749	0.844	209	—
9310.556	0.110	719	—
9311.551	0.439	706	—
9312.731	0.828	219	—
9313.665	0.135	692	—
9314.840	0.523	327	—
9315.838	0.852	226	—
9316.832	0.180	706	—
9317.575	0.425	669	—
9318.578	0.755	183	—
9319.564	0.081	659	—
9319.843	0.172	715	—
9321.589	0.748	108	—
9322.576	0.074	621	—
9323.589	0.408	593	—
9324.545	0.723	174	—

Table D-I . . . continued. . .

Br32

HJD	Phase	Radial Velocity Emission	Radial Velocity Absorption
6040.768	0.494	382	—
6042.639	0.470	466	—
6044.836	0.616	283	—
6046.681	0.579	306	—
6047.670	0.095	581	—
6048.617	0.589	252	—
6050.569	0.607	374	—
6051.674	0.184	718	—
9010.670	0.788	185	—
9011.553	0.249	789	—
9012.553	0.770	190	—
9013.573	0.302	750	—
9013.793	0.417	611	—
9014.671	0.875	238	—
9015.570	0.344	725	—
9015.779	0.453	521	—
9017.654	0.431	589	—
9309.797	0.832	173	—
9310.542	0.221	841	—
9310.850	0.382	612	—
9311.542	0.743	314	—
9311.855	0.906	229	—
9312.762	0.379	599	—
9313.565	0.798	203	—
9313.844	0.944	300	—
9314.549	0.311	758	—
9315.598	0.858	160	—
9315.845	0.987	412	—
9316.553	0.357	742	—
9316.839	0.506	400	—
9317.583	0.894	267	—
9318.548	0.397	555	—
9318.853	0.557	292	—
9319.548	0.919	320	—
9319.835	0.069	535	—
9321.554	0.966	312	—
9322.567	0.494	425	—
9322.847	0.640	168	—
9323.580	0.023	440	—
9323.848	0.162	620	—
9324.536	0.521	368	—
9324.846	0.683	126	—

Table D-I . . . continued. . .

Br43

HJD	Phase	Radial Velocity Emission	Absorption
6041.655	—	538	—
6042.789	—	588	—
6044.597	—	528	—
6045.564	—	503	—
6046.698	—	554	—
6048.662	—	516	—
6049.845	—	572	—
6051.608	—	580	—
6052.658	—	511	—
9309.778	—	592	—
9311.674	—	604	—
9313.700	—	620	—
9315.647	—	675	—
9316.706	—	605	—
9317.591	—	604	—
9318.585	—	556	—
9319.690	—	530	—
9321.741	—	569	—
9323.701	—	603	—
9324.681	—	592	—

Table D-I . . . continued. . .

Br44

HJD	Phase	Radial Velocity Emission	Absorption
6040.788	—	381	—
6042.655	—	376	—
6044.852	—	350	—
6046.718	—	357	—
6047.646	—	351	—
6048.683	—	325	—
6050.655	—	372	—
6051.637	—	363	—
6052.674	—	393	—
9310.606	—	536	—
9311.748	—	500	—
9313.715	—	502	—
9315.655	—	538	—
9316.724	—	467	—
9317.599	—	436	—
9318.592	—	442	—
9319.697	—	415	—
9321.772	—	404	—
9322.815	—	467	—
9323.809	—	415	—
9324.688	—	442	—

Table D-I . . . continued. . .

Br50

HJD	Phase	Radial Velocity Emission	Absorption
6041.676	—	545	—
6042.805	—	508	—
6044.613	—	566	—
6045.853	—	531	—
6046.737	—	564	—
6048.704	—	551	—
6049.861	—	562	—
6050.858	—	500	—
6051.862	—	537	—
6052.691	—	572	—
9310.691	—	481	—
9311.817	—	599	—
9313.723	—	599	—
9315.673	—	550	—
9316.823	—	535	—
9317.620	—	629	—
9318.694	—	467	—
9319.726	—	564	—
9321.816	—	530	—
9322.784	—	512	—
9323.801	—	555	—
9324.817	—	492	—

Table D-I . . . continued. . .

Br62

HJD	Phase	Radial Velocity Emission	Absorption
6041.699	—	406	—
6042.714	—	425	—
6043.729	—	431	—
6044.627	—	365	—
6045.834	—	428	—
6047.835	—	404	—
6048.722	—	385	—
6049.825	—	430	—
6050.836	—	442	—
6051.654	—	443	—
6052.704	—	427	—
9310.705	—	419	—
9312.796	—	489	—
9314.577	—	455	—
9315.829	—	469	—
9317.627	—	476	—
9318.702	—	421	—
9319.734	—	389	—
9322.665	—	446	—
9324.610	—	432	—

Table D-I . . . continued. . .

Br67

HJD	Phase	Radial Velocity Emission	Absorption
6041.722	—	612	—
6043.750	—	595	—
6044.648	—	556	—
6045.818	—	585	—
6048.746	—	589	—
6049.780	—	539	—
6050.675	—	616	—
6051.704	—	608	—
6052.724	—	631	—
9310.805	—	576	—
9312.805	—	595	—
9314.635	—	598	—
9316.587	—	631	—
9317.650	—	636	—
9318.711	—	535	—
9319.766	—	607	—
9321.825	—	513	—
9322.792	—	518	—
9324.619	—	517	—

Table D-I . . . continued. . .

Br68

HJD	Phase	Radial Velocity Emission	Absorption
6040.810	—	540	—
6042.676	—	551	—
6044.665	—	507	—
6045.801	—	519	—
6046.752	—	556	—
6047.855	—	543	—
6049.662	—	533	—
6050.820	—	583	—
6051.723	—	582	—
6052.744	—	579	—
9310.730	—	567	—
9312.826	—	564	—
9314.644	—	581	—
9316.596	—	592	—
9317.658	—	582	—
9318.734	—	527	—
9319.773	—	523	—
9322.674	—	516	—
9324.627	—	558	—

Table D-I . . . continued. . .

Br70

HJD	Phase	Radial Velocity Emission	Absorption
6041.845	—	231	—
6042.820	—	210	—
6044.684	—	198	—
6045.782	—	164	—
6046.770	—	173	—
6047.814	—	182	—
6049.687	—	173	—
6050.800	—	193	—
6051.740	—	208	—
6052.760	—	261	—
9010.782	—	220	—
9011.553	—	228	—
9012.553	—	224	—
9013.611	—	221	—
9014.607	—	236	—
9015.616	—	226	—
9017.587	—	218	—
9310.642	—	245	—
9311.763	—	167	—
9313.732	—	189	—
9315.681	—	252	—
9316.694	—	191	—
9317.666	—	222	—
9318.742	—	200	—
9319.781	—	216	—
9321.805	—	154	—
9322.772	—	151	—
9323.793	—	177	—
9324.776	—	172	—

Table D-I . . . continued. . .

Br74

HJD	Phase	Radial Velocity Emission	Absorption
6041.744	—	490	—
6043.772	—	533	—
6044.706	—	583	—
6045.762	—	565	—
6047.794	—	601	—
6049.708	—	573	—
6050.696	—	528	—
6051.760	—	548	—
6052.780	—	535	—
9310.820	—	525	—
9312.837	—	554	—
9314.653	—	597	—
9316.614	—	588	—
9317.674	—	579	—
9318.793	—	527	—
9319.794	—	564	—
9322.683	—	537	—
9324.639	—	579	—

Table D-I . . . continued. . .

Br83

HJD	Phase	Radial Velocity Emission	Radial Velocity Absorption
6041.774	—	542	—
6043.796	—	575	—
6044.729	—	546	—
6045.742	—	539	—
6046.793	—	524	—
6047.774	—	528	—
6050.719	—	583	—
6051.782	—	529	—
6052.844	—	712	—
9310.862	—	593	—
9312.845	—	519	—
9314.663	—	626	—
9316.624	—	529	—
9317.686	—	618	—
9318.803	—	506	—
9319.588	—	461	—
9321.605	—	397	—
9322.604	—	519	—
9323.614	—	540	—
9324.575	—	569	—

Table D-I . . . continued. . .

Br87

HJD	Phase	Radial Velocity Emission	Radial Velocity Absorption
6041.797	—	376	—
6044.750	—	415	—
6045.727	—	418	—
6046.816	—	408	—
6047.760	—	431	—
6048.813	—	493	—
6050.739	—	387	—
6051.805	—	353	—
6052.864	—	388	—
9011.553	—	454	—
9012.553	—	458	—
9013.694	—	427	—
9014.636	—	412	—
9015.686	—	436	—
9017.673	—	438	—
9309.856	—	317	—
9310.652	—	350	—
9311.775	—	261	—
9312.814	—	287	—
9313.755	—	274	—
9314.676	—	257	—
9315.714	—	238	—
9316.635	—	314	—
9317.635	—	333	—
9318.600	—	311	—
9319.579	—	307	—
9321.628	—	227	—
9322.615	—	157	—
9323.626	—	258	—
9324.590	—	266	—

Table D-I . . . continued. . .

Br93

HJD	Phase	Radial Velocity Emission	Radial Velocity Absorption
6041.820	—	305	—
6042.847	—	168	—
6044.767	—	106	—
6045.707	—	221	—
6046.834	—	176	—
6047.735	—	135	—
6049.732	—	126	—
6050.758	—	174	—
6051.822	—	159	—
6052.801	—	192	—
9311.641	—	159	—
9313.743	—	90	—
9314.687	—	182	—
9316.644	—	143	—
9317.733	—	227	—
9318.683	—	127	—
9319.715	—	96	—
9321.786	—	154	—
9322.743	—	113	—
9323.767	—	76	—
9324.787	—	98	—

Table D-I . . . continued. . .

Br94

HJD	Phase	Radial Velocity Emission	Radial Velocity Absorption
6040.854	—	579	—
6042.693	—	588	—
6044.790	—	665	—
6045.686	—	655	—
6046.856	—	622	—
6049.757	—	632	—
6050.779	—	626	—
6051.842	—	644	—
6052.823	—	640	—
9011.553	—	538	—
9012.553	—	572	—
9013.669	—	600	—
9014.705	—	600	—
9015.710	—	634	—
9017.691	—	676	—
9309.812	—	428	—
9310.661	—	403	—
9311.729	—	453	—
9312.784	—	435	—
9313.764	—	417	—
9314.703	—	403	—
9315.741	—	391	—
9316.655	—	488	—
9317.643	—	517	—
9318.608	—	477	—
9319.597	—	509	—
9321.636	—	542	—
9322.623	—	532	—
9323.635	—	606	—
9324.599	—	616	—

Table D-I ...continued...

MG1

HJD	Phase	Radial Velocity Emission	Absorption
9311.657	—	520	—
9313.687	—	401	—
9314.714	—	437	—
9316.665	—	545	—
9317.795	—	499	—
9318.778	—	491	—
9319.742	—	440	—
9321.750	—	509	—
9322.728	—	462	—
9323.755	—	474	—
9324.724	—	437	—

Table D-I ...continued...

MG5

HJD	Phase	Radial Velocity Emission	Absorption
9311.701	—	467	—
9313.782	—	484	—
9315.770	—	574	—
9317.747	—	675	—
9318.657	—	572	—
9319.648	—	537	—
9322.636	—	508	—
9324.698	—	632	—

Table D-I ... continued...

MG6

HJD	Phase	Radial Velocity Emission	Radial Velocity Absorption
9012.553	—	460	—
9013.735	—	465	—
9014.755	—	480	—
9017.633	—	445	—
9310.673	—	206	—
9311.783	—	223	—
9313.807	—	152	—
9314.732	—	37	—
9316.682	—	240	—
9317.814	—	380	—
9318.815	—	219	—
9319.754	—	164	—
9321.718	—	179	—
9322.714	—	230	—
9323.782	—	249	—
9324.806	—	242	—

Table D-I ... continued...

AB8

HJD	Phase	Radial Velocity Emission	Radial Velocity Absorption
6040.656	0.469	69	—
6041.555	0.523	43	—
6042.564	0.584	−10	—
6043.539	0.642	−41	—
6044.549	0.703	−64	—
6045.529	0.762	−72	—
6046.527	0.822	−86	—
6047.531	0.882	−56	—
6048.532	0.943	25	—
6049.531	0.003	47	—
6050.529	0.063	141	—
6051.539	0.123	168	—
6052.539	0.183	216	—
9010.532	0.021	98	—
9011.551	0.082	132	—
9012.551	0.142	165	—
9013.551	0.203	175	—
9014.535	0.262	179	—
9015.533	0.322	191	—
9017.528	0.442	131	—
9309.556	0.999	42	—
9310.520	0.057	112	—
9311.523	0.117	239	—
9312.748	0.191	259	—
9313.531	0.238	223	—
9314.520	0.297	269	—
9315.533	0.358	220	—
9316.516	0.417	118	—
9317.509	0.477	129	—
9318.510	0.537	2	—
9319.514	0.597	−14	—
9321.511	0.717	−144	—
9322.552	0.780	−62	—
9323.556	0.840	−89	—
9324.521	0.898	−21	—

Table D-I . . . continued. . .

WR9

HJD	Phase	Radial Velocity Emission	Radial Velocity Absorption
9309.846	0.073	453	100
9310.809	0.140	481	19
9311.801	0.210	531	−59
9312.717	0.274	536	−43
9313.826	0.351	475	−37
9314.809	0.420	355	−94
9315.807	0.490	296	52
9316.800	0.559	277	55
9317.836	0.632	209	20
9318.831	0.701	144	91
9319.807	0.770	163	59
9321.839	0.912	187	−78
9322.828	0.981	280	−41
9323.828	0.051	346	−74
9324.828	0.120	417	−186

Table D-I . . . continued.

WR30a

HJD	Phase	Radial Velocity Emission	Radial Velocity Absorption
9012.554	0.948	−135	−51
9013.835	0.225	113	−92
9015.829	0.656	−258	−15
9017.814	0.085	−11	−6
9311.827	0.651	−159	239
9312.853	0.873	−167	215
9313.833	0.085	116	−41
9314.824	0.299	211	60
9315.812	0.512	−21	57
9316.805	0.727	−147	120
9317.839	0.951	−76	21
9318.844	0.168	186	−210
9319.812	0.377	169	−31
9321.846	0.817	−297	−75
9322.832	0.030	55	−146
9323.831	0.246	208	−157
9324.832	0.462	−35	−96

Appendix E

Scalar Product Evaluation with Equatorial Coordinates

Vectors expressed in equatorial coordinates (v, α, δ) can be represented in spherical coordinates (ρ, θ, ϕ). Using Figure E.1 (page a-xxxvii), the equations for conversion can be derived.

First, the angles θ and ϕ are found with

$$\theta = \frac{\pi}{12^{\mathrm{h}}}\alpha$$

and

$$\phi = \frac{\pi}{2} - \frac{\pi}{180^{\circ}}\delta,$$

where the units of θ and ϕ are radians. The vectorial magnitudes of the two coordinate systems are the same $(v \equiv \rho)$.

If x_1, y_1, z_1 and x_2, y_2, z_2 are the respective cartesian components of vectors v_1 and v_2, then the scalar product of the two is

$$\vec{v_1} \cdot \vec{v_2} = x_1 x_2 + y_1 y_2 + z_1 z_2.$$

The Cartesian components of a vector that is expressed in spherical coordinates are

$$x = \rho \sin\phi \cos\theta,$$

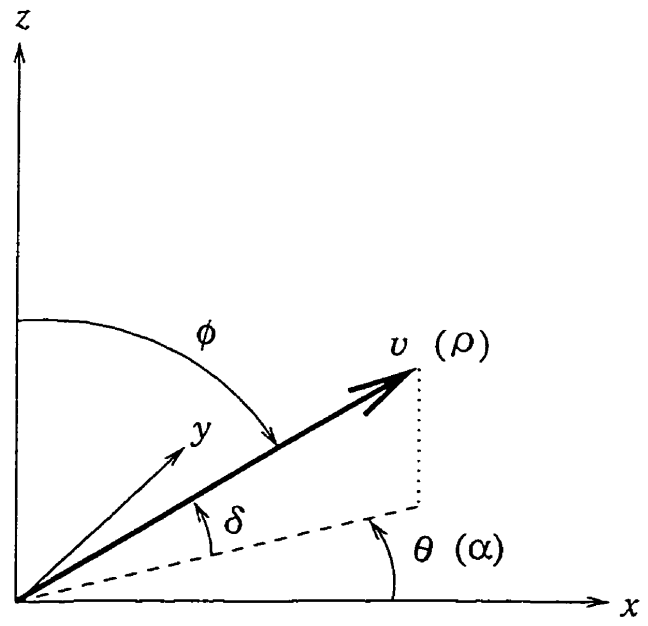

Figure E.1: *Relation between equatorial, spherical and Cartesian coordinates for a vector with equatorial coordinates* (v, α, δ) *of magnitude* $v \equiv \rho$*, forming an angle* θ *with the* x*-axis and an angle* ϕ *with the* z*-axis. The* x*-axis is in the direction of the First Point in Aries.*

$$y = \rho \sin\phi \sin\theta \qquad \text{and}$$

$$z = \rho \cos\phi.$$

It follows that

$$\begin{aligned} \vec{v}_1 \cdot \vec{v}_2 &= \rho_1 \sin\phi_1 \cos\theta_1 \, \rho_2 \sin\phi_2 \cos\theta_2 \\ &\quad + \rho_1 \sin\phi_1 \sin\theta_1 \, \rho_2 \sin\phi_2 \sin\theta_2 \\ &\quad + \rho_1 \cos\phi_1 \, \rho_2 \cos\phi_2 \end{aligned}$$

and finally

$$\begin{aligned} \vec{v}_1 \cdot \vec{v}_2 &= \rho_1\rho_2 \times (\sin\phi_1 \cos\theta_1 \sin\phi_2 \cos\theta_2 \\ &\quad + \sin\phi_1 \sin\theta_1 \sin\phi_2 \sin\theta_2 \\ &\quad + \cos\phi_1 \cos\phi_2). \end{aligned}$$

Appendix F

Wind Structure, Ionisation Strengths and WC4 Evolution

Line-width and wind structure

A negative correlation was found for the difference between the stars' average radial velocity and their milieu velocities with FWHM (Figure F.1 on page a-xl; the dashed line is for illustrative purposes and does not represent a fit). [For this and subsequent figures of this appendix, the Spearman rank-order correlation coefficient, r_s, and its t-statistic are included in the captions. As well, the statistical significance level of the correlation, P_{r_s}, is calculated using the Student's distribution probability function and is also added in the caption of each figure. In all cases where the CIII 5696 Å equivalent width is used, the values used for the stars Br22 and WR9 were those found after adjustment for WWC (see footnotes 3-IV and 3-IV of Table 3-IV).]

WC4/WO4 stars with narrower lines (*i.e.* slower winds) tend to show larger velocity excess (Δv_r). This anti-correlation cannot be due to the interception of HeI 5876 emission in the red flank of CIV 5808 for larger FWHM, since the latter would give rise to a positive correlation. A likely origin is due to enhanced P Cygni absorption effects in slower winds. For a constant mass-loss rate $\dot{M} = 4\pi r^2 \rho v$, where r is the stellar radius where the line is formed, ρ is the density

of absorbing gas and v is the wind speed, ρ will be larger for slower winds. This means that the radius from the star at which the continuum opacity τ_c (measured from the observer towards the star) is unity will be larger for a slower wind, making a wider cross-section in the CIV shell that can absorb photons. Consequently, the ratio of the absorbing region's volume (A) to the emitting region's volume (E) (within the region of the wind containing CIV ions) will be larger for slow winds (bottom right of Figure F.1). The emission line of a slower wind will have more of its blue component reduced than will one of a faster wind, making the line more red-shifted and yielding a larger Δv_r (see profiles in Figure F.1).

Line strengths, ionisation and evolution

WC-stars are expected to evolve towards the hotter WO sub-class. When this happens, there should be an increase in abundance of oxygen in the atmosphere (*e.g.* Smith & Maeder 1991). Due to their lower masses from mass loss during evolution, but smaller radii and denser structure, leading to higher escape velocities, it is nominally expected that these hotter stars will have faster winds. To test for this, the ratio of equivalent width of the CIII 5696 Å line to that of the OV 5592 Å line is plotted as a function of the FWHM of the CIV 5808 Å line in Figure F.2 on page a-xliii (the equivalent widths are determined from the average spectra taken during the Nov. 1993 mission; all data are listed in Table F-I on page a-xlv). Since a hotter star will have a greater ionisation level of the same element in its wind than a cool star, the ratio of the line strength of the OV 5592 Å line to that of the OVI 3811/34 Å line is plotted against the CIV 5808 Å line's FWHM (Figure F.3, page a-xliii).

In both of these figures, the temperature of the star seems to be negatively correlated with wind speed, so that hotter stars have higher wind velocities, yielding broader lines (the hottest stars, the WO-class Br93, AB8 and WR30a, being at the high end of the FWHM scale). There seems to be a continuous trend

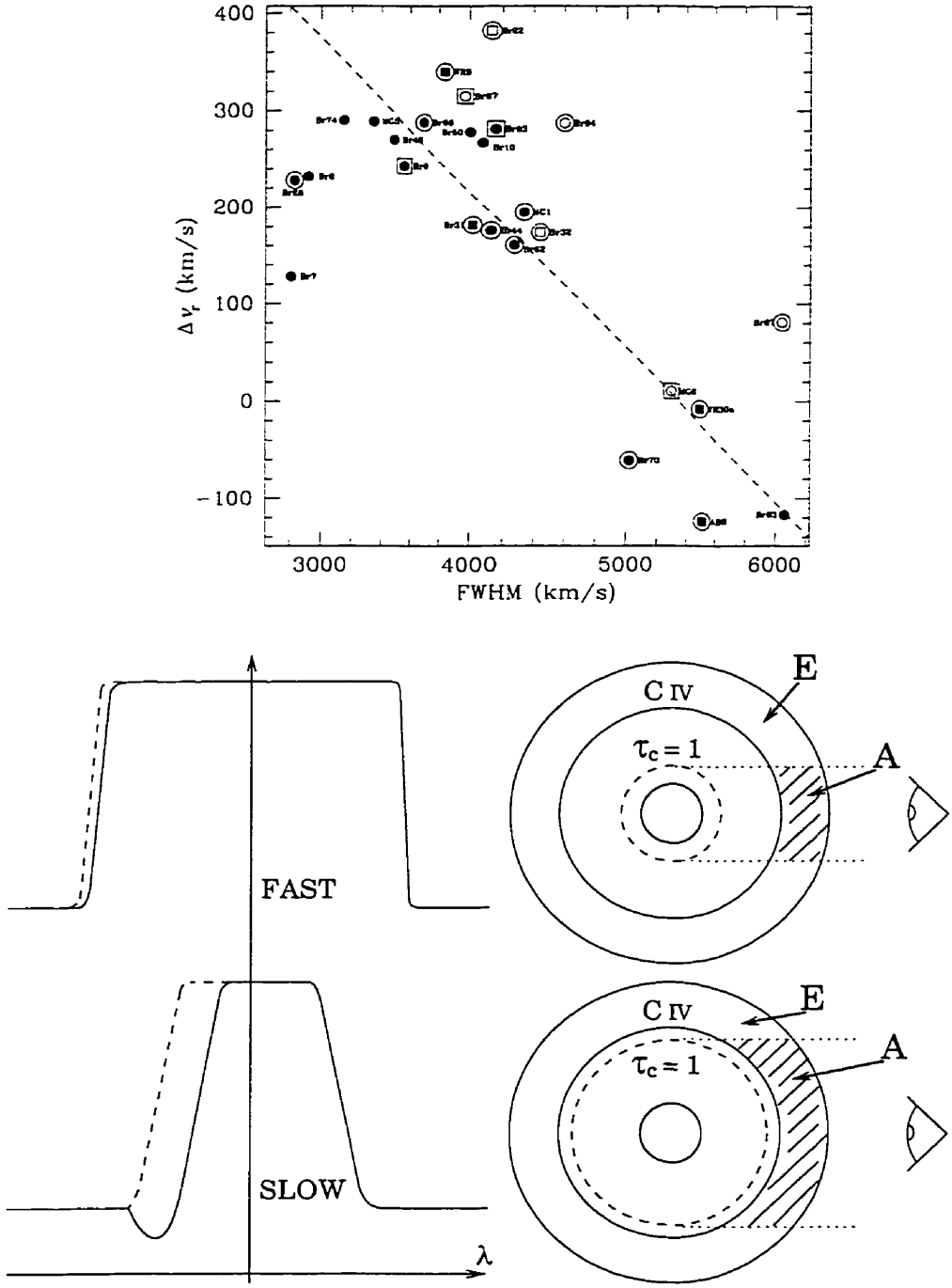

Figure F.1: *RV dispersion correlation with FWHM (top) and opacity radii with their effect on size of P Cygni absorbing region (bottom). The symbols in the top plot are as in Figure 3.4 with the dashed line indicating an apparent correlation. The bottom right diagrams show stars with different opacity radii for fast and slow winds (dashed circles) and the resulting absorption regions of the* C IV *emission region (hatched areas labelled A) and the remaining viewed emission area (E). To their left are the corresponding expected line profiles (solid lines). The dashed profile is the part of the spectral line removed by P-Cygni absorption.* $r_s = -0.57, t = -3.4, P_{r_s} = 0.0023$.

to this correlation in both plots (note dashed line, which is illustrative only and does not represent a fit). This suggests that there is a gradual evolution (implied by change in elemental abundance) within the WC4 sub-class from cooler WC4-late (which is labelled here as WC4L) to hotter WC4-early (labelled here WC4E) until, finally, the hottest: WO.

It must be noted that the very high values for the CIII/OV ratio for Br22 and WR9 do not reflect the inherent abundance of the WR-star. They are due to excess emission from CIII created by colliding stellar winds, as discussed in Chapter 5. Correcting for this does place these stars amongst the rest in Figure F.2. The correlation statistics were calculated using the excess emission adjusted values.

Such trends in abundance change (hence gradual evolution to WO) can be seen as well in a plot of the line strength ratio of CIII 5696 Å to OV 5592 Å *versus* the line strength ratio of CIV 5808 Å to OV 5592 Å. In Figure F.4 on page a-xliv, there is a gradual trend (illustrative dashed line) for the increase in carbon abundance and decrease in oxygen abundance (these apparent changes in abundance, of course, could very well be confused with changes merely in ionisation). Three stars, Br50, Br62 and Br87, lying well apart from the rest, seem not to follow this general change. Possibly the CIII/OV ratio levels off eventually for large CIV/OV.

An examination of ionisation levels, independent of species abundance, might also be useful to find further evidence of gradual evolution within the WC4 sub-class towards WO. This allows one to examine mainly the temperature. In Figure F.5 on page a-xliv ratios of line species, the OV 5592 Å to OVI 3811/34 Å line strength ratio, is plotted as a function of the CIII 5696 Å to CIV 5808 Å line strength ratio. There is a weak positive correlation between the two ratios (illustrative dashed line), with the species of highest ionisation (lowest ratios) being in the lower left-hand corner of the plot (along with two crowded stars and the highly reddenned MG5). Here, again, there is a gradual trend in ionisation.

It would appear, therefore, that there is a sub-division of class within the

WC4 stars that suggests the evolutionary scenario:

$$\text{WC4L} \rightarrow \text{WC4E} \rightarrow \text{WO}.$$

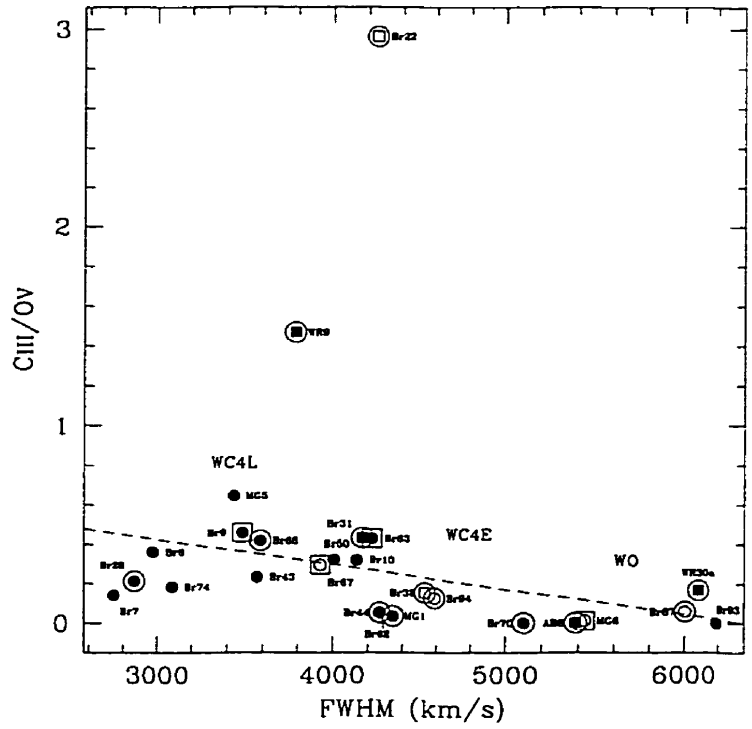

Figure F.2: *CIII/OV line strength ratio correlation with FWHM. Suggested subclassification of the WC class is labelled.* $r_s = -0.66, t = -4.3, P_{r_s} = 0.00028$.

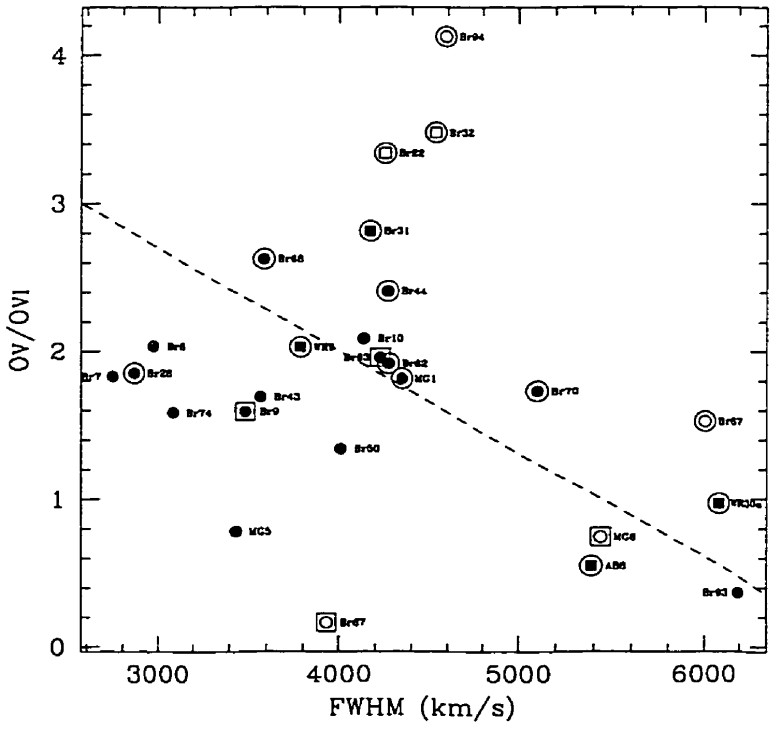

Figure F.3: *OV/OVI line strength ratio correlation with FWHM.* $r_s = -0.16, t = -0.80, P_{r_s} = 0.43$.

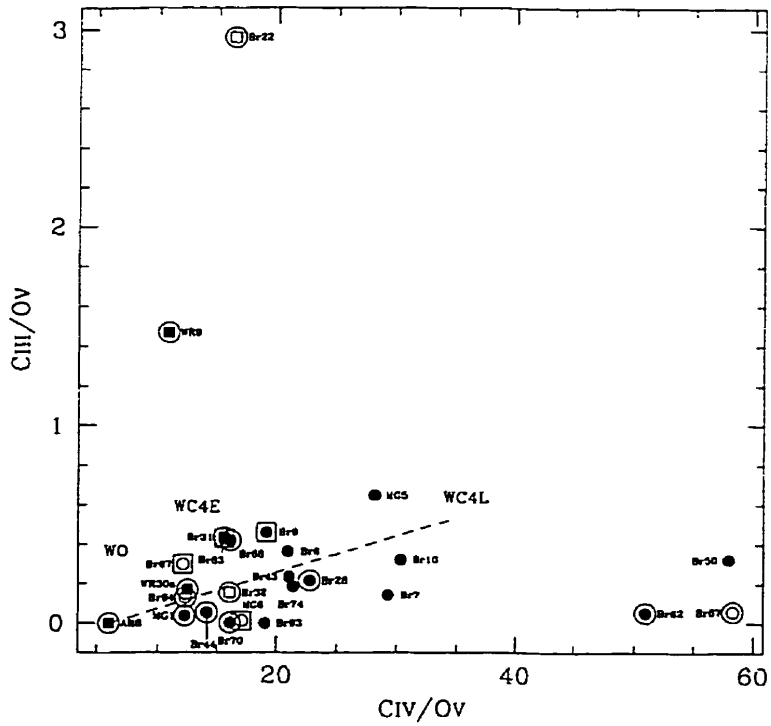

Figure F.4: *CIII/OV line strength ratio correlation with that of CIV/OV. Suggested subclassification of the WC class is labelled.* $r_s = 0.24, t = 1.2, P_{r_s} = 0.23$.

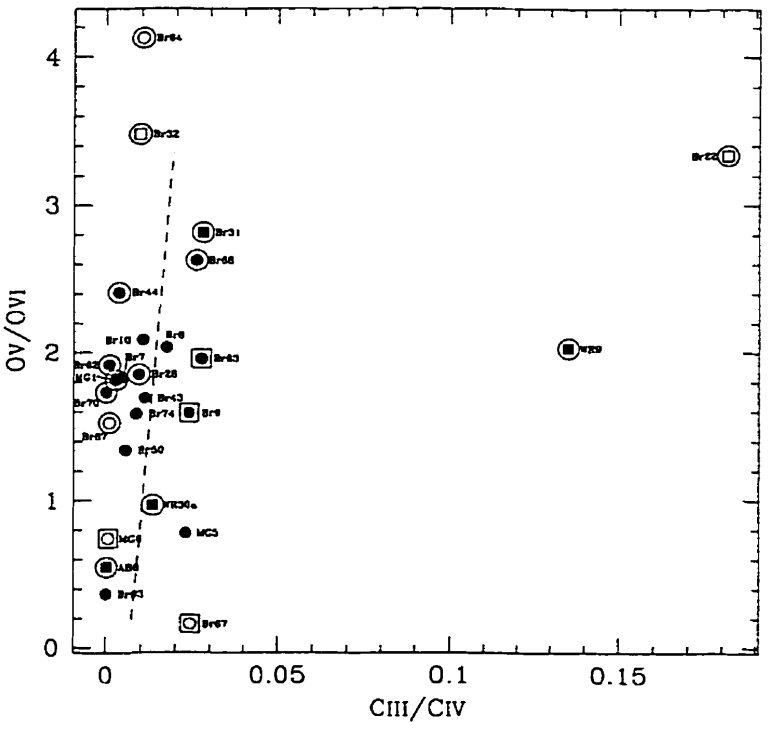

Figure F.5: *OV/OVI line strength ratio correlation with that of CIII/CIV.* $r_s = 0.33, t = 1.7, P_{r_s} = 0.10$.

Table F-I: *Equivalent widths of various ionic emission lines and the width of the* C IV *5808 Å line, from average spectra of the November 1993 mission. The FWHM is in km/s while the equivalent widths are in Å.*

Star	C IV 5808 Å	C III 5696 Å	O V 5592 Å	O VI 3811/34 Å	C IV FWHM
Br7	1800	8.9	61.4	33.5	2743
Br8	1550	26.7	73.8	36.2	2974
Br9	124	3.0	6.5	4.1	3486
Br10	1380	14.5	45.4	21.8	4137
Br22	189	34.3	11.6	3.5	4251
Br28	295	2.8	13.0	7.0	2864
Br31	90	2.5	5.8	2.1	4171
Br32	213	2.0	13.3	3.8	4533
Br43	1320	14.6	62.5	36.9	3567
Br44	498	1.9	35.3	14.7	4267
Br50	1510	8.4	26.1	19.5	4009
Br62	783	0.8	15.4	8.0	4271
Br67	69	1.7	5.7	34.5	3931
Br68	419	10.9	26.0	9.9	3586
Br70	749	0.1	46.6	26.9	5103
Br74	1400	12.1	65.4	41.2	3086
Br83	74	2.0	4.7	2.4	4226
Br87	220	0.2	3.8	2.5	6002
Br93	2150	0.1	113.0	308.0	6190
Br94	422	4.4	34.2	8.3	4589
MG1	238	0.7	19.4	10.7	4346
MG5	1200	27.5	42.6	54.5	3436
MG6	51	0.04	3.0	4.1	5435
AB8	167	0.04	27.6	50.4	5386
WR9	364	49.3	33.5	16.5	3786
WR30a	141	1.9	11.3	11.6	6081

Appendix G

Errors in Orbital Parameters

Determination of weights for radial velocity data

The errors in the radial velocity measurements of the binary stars were assumed to be about the same as those for the single stars. To determine these errors, the radial velocity standard deviation of each star, σ_{v_i}, within one epoch, was calculated (each star was designated with the index i). Neither stars classified as *Definitely SB* in Chapter 3 nor the relatively noisy spectra of the reddenned MG stars were used.

The resultant standard deviations of the same epoch were then combined to form their root mean square value, so as to have an epoch-dependent standard deviation, σ_{v_e}, found with

$$\sigma_{v_e} = \sqrt{\frac{\sum_{i=1}^{n} \sigma_{v_i}^2}{n}},$$

where n is the total number of stars that were included. Every radial velocity measurement made within the same epoch was then assigned this epoch-dependent standard deviation.

Estimating errors in the periods

The errors in the periods were estimated by determining the period interval where the confidence that the true value of the period falls within this interval is 68.3% (Press *et al.* 1992, pp. 687–690). This is defined by the periods for which the change in the reduced χ^2 from the optimum value, $\Delta\chi^2_\nu$, is not greater than one. These periods define the confidence interval. Half of this interval is taken as the error in the period, σ_P. [The reduced χ^2, χ^2_ν, is the χ^2 value of the model divided by the number of degrees of freedom of that model (the number of degrees of freedom is the number of data points minus the number of free parameters of the model).]

Acknowledgements

I must first thank my dissertation advisor, Professor A.F.J. Moffat, for his guidance and mentoring throughout my studies. He took me as his student, supported me in academic and bureaucratic matters and carried me through when I was forlorn. He also proved to me, through example, that a good physicist can be extremely intelligent without intimidating arrogance, obnoxiousness or temperamentality.

The staff of the *Complejo Astronómico El Leoncito* were most hospitable during my two observing missions. The well managed facility, the friendly assistants, the tasty meals and the care for my well-being in the observatory and in San Juan City all contributed to a pleasant stay while permiting me to carry out work crucial to my Dissertation.

The data of the Dec. 1984 mission were obtained by Professor A.F.J. Moffat, Dr. V.S. Niemela and Dr. H.G. Marraco.

The photometric observations were performed through service observing by staff members of UTSO.

Dr. R. Lamontagne developed the elliptical orbit fit programme.

Mr. L. Turbide assisted considerably with my use (at times, some called it misuse) of the computer. He would help even with the problems that he insisted happened to no one but me (devices and I just do not seem to get along). I still must disagree with him when he says that I am the problem rather than the computer.

Professor N. St-Louis generously reviewed the quality of French in the *Résumé*.

I am grateful for the financial aid provided by the Physics Department's Astronomy Group of the *Université de Montréal* from its *FCAR/équipe* grant.

I also happily acknowledge a *Bourse de production de mémoire et de thèse* from the *FICSUM* of the *Fédération des associations étudiantes du campus de l'Université de Montréal.*